POLITECHNIKA POZNAŃSKA

Politechnika Poznańska
Wydział Inżynierii Materiałowej i Fizyki Technicznej
Instytut Fizyki
Zakład Fizyki Molekularnej

ROZPRAWA DOKTORSKA

Organizacja nanocząstek złota na granicy faz i ich oddziaływanie z wybranymi związkami organicznymi

mgr inż. Beata Tim

Promotor:
prof. dr hab. Alina Dudkowiak

Promotor pomocniczy:
dr inż. Paulina Błaszkiewicz

Poznań 2026

NARODOWE CENTRUM NAUKI

Badania współfinansowane przez Narodowe Centrum Nauki w ramach grantów:
SONATA pt. „*Optymalizacja struktury nanoplatformy do powierzchniowo wzmocnionej detekcji pochodnych chlorofilu z wykorzystaniem techniki Langmuira*”, numer 2019/35/D/ST4/02037
oraz
PRELUDIUM pt. „*Fotoaktywowane nanocząstki złota jako obiecujące środki w terapii fototermicznej – badania in vitro w biomimetycznych układach błonowych*”, numer 2022/45/N/ST5/01464.

Składam wyrazy wdzięczności
Pani Promotor prof. dr hab. Alinie Dudkowiak
za życzliwość, pomoc oraz czas poświęcony mi
przez cały okres realizacji doktoratu,
w szczególności podczas przygotowywania
niniejszej rozprawy doktorskiej.

Dziękuję ***dr inż. Paulinie Błaszkiewicz***
za wszechstronną pomoc na każdym etapie:
za wsparcie merytoryczne podczas realizacji badań,
za cenne wskazówki przy interpretacji wyników
i przy redagowaniu niniejszej rozprawy doktorskiej.
Jednak największą wdzięczność pragnę wyrazić
za to, że mogłam na Ciebie liczyć w każdej,
nawet najbardziej wymagającej sytuacji.

Spis treści

Spis skrótów i oznaczeń 6
Streszczenie 8
Abstract 10
I Wstęp 12
II Forma rozprawy doktorskiej i wkład doktorantki 17
III Badane materiały oraz zastosowane techniki pomiarowe 19
IV Opis badań 23
V Podsumowanie 36
Literatura 39
Dorobek naukowy doktorantki 44
Oświadczenia współautorów publikacji naukowych 50
Przedruk publikacji [Tim, JPCC 2023] 65
Przedruk publikacji [Tim, ASS 2022] 81
Przedruk publikacji [Kotkowiak, L 2024] 93
Przedruk publikacji [Tim, JML 2025] 107

Spis skrótów i oznaczeń

A	– powierzchnia wanny Langmuira [cm^2]
Au-NPs	– nanocząstki złota
Au-NRs@PEG	– prętopodobne nanocząstki złota funkcjonalizowane poli(tlenkiem etylenu)
Au-NSs@PEG	– sferyczne nanocząstki złota funkcjonalizowane poli(tlenkiem etylenu)
Au-NSs@DDT	– sferyczne nanocząstki złota funkcjonalizowane dodekanotiolem
BAM	– mikroskopia kąta Brewstera
Chol	– cholesterol
C_s^{-1}	– moduł ściśliwości [$mN \cdot m^{-1}$]
CTAB	– bromek cetylotrimetyloamoniowy
DDT	– dodekanotiol
DLS	– dynamiczne rozpraszanie światła (ang. *Dynamic Light Scattering*)
DPPC	– 1,2-dipalmitoilo-*sn*-glicero-3-fosfocholina
DPPC:Chol (9:1)	– 1,2-dipalmitoilo-*sn*-glicero-3-fosfocholina i cholesterol, stosunek molowy 9:1
LB	– metoda (lub warstwy) Langmuira-Blodgett
LC	– stan ciekły skondensowany
LE	– stan ciekły rozprężony
LS	– metoda (lub warstwy) Langmuira-Schaefera
LSPR	– zlokalizowany powierzchniowy rezonans plazmonowy (ang. *Localized Surface Plasmon Resonance*)
PEG (PEG-SH)	– poli(tlenek etylenu) z grupą tiolową o masie cząsteczkowej 2000 (2k), 5000 (5k) lub 10000 (10k)
p-MBA	– kwas 4-merkaptobenzoesowy
PM-IRRAS	– odbiciowo-absorpcyjna spektroskopia w podczerwieni z modulacją polaryzacji (ang. *Polarization Modulation Infrared Reflection Absorption Spectroscopy*)

POPC	– 1-palmitoilo-2-oleoilo-*sn*-glicero-3-fosfocholina
POPC:Chol (4:1)	– 1-palmitoilo-2-oleoilo-*sn*-glicero-3-fosfocholina i cholesterol, stosunek molowy 4:1
QCM	– mikrowaga kwarcowa (ang. *Quartz Crystal Microbalance*)
R6G	– rodamina 6G
SAXRD	– dyfrakcja promieni rentgenowskich pod małym kątem (ang. *Small-Angle X-ray Diffraction*)
SEM	– skaningowa mikroskopia elektronowa (ang. *Scanning Electron Microscopy*)
SERS	– wzmocniona powierzchniowo spektroskopia Ramana (ang. *Surface-Enhanced Raman Spectroscopy*)
TEM	– transmisyjna mikroskopia elektronowa (ang. *Transmission Electron Microscopy*)
UV-vis	– zakres promieniowania elektromagnetycznego w obszarze ultrafioletu i światła widzialnego
π	– ciśnienie powierzchniowe [$mN \cdot m^{-1}$]

Streszczenie

W rozprawie doktorskiej przedstawiono wyniki badań dotyczące oddziaływań pomiędzy funkcjonalizowanymi (za pomocą dodekanotiolu (DDT) lub poli(tlenku etylenu) (PEG)) nanocząstkami złota (Au-NPs) o różnych kształtach (sferycznym (NSs), prętopodobnym (NRs)) w warstwach wytwarzanych na granicy faz powietrze-woda i powietrze ciało-stałe, jak również oddziaływań Au-NPs w warstwach na podłożu stałym z wybranymi molekułami (kwasem 4-merkaptobenzoesowym, rodaminą 6G) lub na subfazie wodnej z lipidami (1,2-dipalmitoilo-*sn*-glicero-3-fosfocholiną, 1-palmitoilo-2-oleoilo-*sn*-glicero-3-fosfocholiną i/lub cholesterolem). Celem przeprowadzonych badań było określenie wpływu kształtu i/lub funkcjonalizacji Au-NPs na właściwości (termodynamiczne, stabilność) i organizację (upakowanie, agregację, morfologię) cienkich warstw na granicy faz oraz na strukturę modelowych błon biologicznych.

Do tworzenia warstw i błon biomimetycznych na granicy faz powietrze-woda zastosowano technikę Langmuira oraz metody Langmuira-Blodgett, Langmuira-Schaefera do przenoszenia warstw Au-NPs na podłoża stałe. W badaniach warstw na granicy faz wykorzystano komplementarne metody spektroskopowe i mikroskopowe, w tym spektroskopię absorpcyjną UV-vis, odbiciowo-absorpcyjną spektroskopię w podczerwieni z modulacją polaryzacji, spektroskopię Ramana, mikroskopię kąta Brewstera, mikroskopię konfokalną, skaningową i transmisyjną mikroskopię elektronową. Charakterystykę hydrodynamiczną i stabilność koloidalną NPs wyznaczono odpowiednio, techniką dynamicznego rozpraszania światła i na podstawie pomiaru potencjału zeta.

Na podstawie przeprowadzonych badań stwierdzono, że funkcjonalizacja i kształt Au-NPs w istotny sposób determinują właściwości i organizacje warstw na granicy faz powietrze-woda i powietrze-ciało stałe. Wykorzystując różne metody przenoszenia warstw Langmuira Au-NSs@DDT i Au-NRs@PEG na podłoża stałe uzyskano, w określonych warunkach dobre pokrycie powierzchni i struktury agregacyjne NPs, które wykazują obszary charakteryzujące się lokalnym wzmocnieniem pola elektromagnetycznego. Wykazano, że zastosowanie techniki Langmuira stwarza możliwość projektowania i uzyskania warstw złożonych z Au-NPs, o różnym kształcie i funkcjonalizacji, o kontrolowanych i pożądanych właściwościach (w tym optycznych),

mających potencjał aplikacyjny jako podłoża do ultraczułej detekcji analitów. Pokazano również możliwość uzyskiwania warstw Au-NPs o różnym stopniu upakowania, poprzez dobór długości łańcucha polimeru oraz wykazano związek pomiędzy masą cząsteczkową polimeru wykorzystywanego do funkcjonalizacji, a stanem fizycznym, morfologią i zdolnością do agregacji NPs w warstwach na subfazie oraz na podłożu stałym.

Wnioskowano, że na strukturę modelowych błon biologicznych, ich elastyczność i stabilność na granicy faz woda-powietrze, ma wpływ anizotropia kształtu Au-NPs oraz skład lipidów. Zaobserwowano również, że obecność cholesterolu umożliwia tworzenie gęściej upakowanych i bardziej uporządkowanych monowarstw z NPs oraz zasugerowano różne sposoby oddziaływania lipidów z NPs, które mogą adsorbować na powierzchni lub częściowo wbudowywać się w warstwę lipidową, co można skorelować z kształtem NPs i/lub właściwościami fizykochemicznymi oraz składem lipidów w biomimetycznej membranie.

Przedstawione w rozprawie wyniki badań dostarczają nowej wiedzy na temat możliwości kontrolowania organizacji i oddziaływań Au-NPs w warstwach tworzonych na granicy faz. Ustalenie korelacji pomiędzy badanymi Au-NPs, warunkami procesu kompresji i metodami wytwarzania, a parametrami końcowymi otrzymywanych warstw pozwala na ich projektowanie oraz ocenę ich przydatności jako funkcjonalnych podłoży w diagnostyce biomedycznej wykorzystującej techniki spektroskopowe. Jednocześnie, analiza wpływ Au-NPs na strukturę biomimetycznych membran stanowi wkład w zrozumienie ich oddziaływań z układami biologicznymi, co jest istotne do rozwoju badań nad innowacyjnymi i bezpiecznymi nanomateriałami o potencjale aplikacyjnym.

Abstract

In the doctoral dissertation, the results of the research concerning interactions between functionalized (using dodecanethiol (DDT) or poly(ethylene oxide) (PEG)) gold nanoparticles (Au-NPs) of various shapes (spherical (NSs), rod-like (NRs)) in layers produced at the air-water and air-solid interfaces, as well as interactions of Au-NPs in layers on a solid substrate with selected molecules (4-mercaptobenzoic acid, rhodamine 6G) or on an aqueous subphase with lipids (1,2-dipalmitoyl-*sn*-glycero-3-phosphocholine, 1-palmitoyl-2-oleoyl-*sn*-glycero-3-phosphocholine and/or cholesterol) were presented. The aim of the conducted research was to determine the influence of the shape and/or functionalization of Au-NPs on the properties (thermodynamic, stability) and organization (packing, aggregation, morphology) of thin layers at the interfaces, and on the structure of model biological membranes.

The Langmuir technique was used to form layers and biomimetic membranes at the air-water interface whereas Langmuir-Blodgett and Langmuir-Schaefer methods were applied to transfer Au-NPs layers onto solid substrates. Complementary spectroscopic and microscopic methods were employed in the study of layers at interfaces, including UV-vis absorption spectroscopy, polarization modulation infrared reflection-absorption spectroscopy, Raman spectroscopy, Brewster angle microscopy, confocal microscopy, scanning and transmission electron microscopy. The hydrodynamic characteristics and colloidal stability of the NPs were determined using dynamic light scattering and zeta potential measurements, respectively.

Based on the conducted research, it was concluded that functionalization and the shape of Au-NPs significantly determine the properties and organization of their layers at the air-water and air-solid interfaces. By using various methods to transfer Langmuir layers of Au-NSs@DDT and Au-NRs@PEG onto solid substrates, under specific conditions, quite efficient surface coverage was obtained and NPs aggregate structures which possess areas characterized by local electromagnetic field enhancement were observed. It was demonstrated that the use of the Langmuir technique enables the design and production of layers composed of Au-NPs with different shapes and functionalization, with controlled and desired properties (including optical ones), having application potential as substrates for ultrasensitive analyte detection. The possibility of obtaining Au-NPs layers, with varying degrees of packing, by selecting

the polymer chain length, was also shown, and a relationship between the molecular weight of the polymer used for functionalization and the physical state, morphology, and aggregation tendency of NPs in layers on the subphase and on the solid substrate was demonstrated.

It was inferred that the shape of Au-NPs influences the structure of model biological membranes, their elasticity, and stability at the water-air interface, and this influence depends on the lipid composition and the shape anisotropy of the NPs (aspect ratio). It was also observed that the presence of cholesterol enables the formation of more densely packed and more ordered NPs monolayers. Also, different ways of lipid interacting with NPs were suggested – NPs can adsorb onto the surface or partially embed into the lipid layer, which can be correlated with their shape and/or physicochemical properties, and the lipid composition of the biomimetic membrane.

The results of the research presented in the doctoral dissertation provide new knowledge about the possibilities of controlling the organization and interactions of Au-NPs in layers created at interfaces. Establishing correlations between the studied Au-NPs, the conditions of the compression process, fabrication methods and the final parameters of the obtained layers allows for their design and assessment of their usefulness as functional substrates in biomedical diagnostics, utilizing spectroscopic techniques. Simultaneously, the analysis of the influence of Au-NPs on the structure of biomimetic membranes contributes to the understanding of their interactions with biological systems, which is important for the development of research on innovative and safe nanomaterials with application potential.

Wstęp

Przyjmuje się, że w latach 50. XX wieku zapoczątkowane zostały badania w zakresie nanotechnologii. W roku 1959, na spotkaniu American Physical Society w California Institute of Technology (Caltech), Richard Feynman [1] w wystąpieniu zatytułowanym „*There's Plenty of Room at the Bottom*" zaprezentował koncepcję miniaturyzacji urządzeń i tworzenia struktur w skali nanometrycznej. Idea ta zachęciła naukowców do poszukiwania nowych materiałów o unikalnych właściwościach, uzyskiwanych poprzez precyzyjną manipulację pojedynczymi atomami i molekułami. Rozwój badań prowadzonych w tym zakresie doprowadził do powstania nowej dziedziny nauki, którą w roku 1974 Eric Drexler nazwał „nanotechnologią", co podkreślało jej naukowy i technologiczny potencjał [2]. Obecnie nanotechnologia jest uznawana za interdyscyplinarną dziedzinę nauki i inżynierii, w ramach której prowadzi się badania nad projektowaniem, wytwarzaniem i poszukiwaniem możliwości wykorzystywania struktur charakteryzujących się co najmniej jednym wymiarem nieprzekraczającym 100 nm [3]. Dynamiczny rozwój nowych metod i technologii oraz badań prowadzonych w zakresie nanotechnologii umożliwił wykorzystanie nanomateriałów między innymi w przemyśle farmaceutycznym, kosmetycznym, medycynie, energetyce, elektronice czy inżynierii materiałowej [4–9].

Do nanomateriałów, które wzbudzają szczególne zainteresowanie w biotechnologii należą metaliczne nanocząstki, w tym nanocząstki złota (Au-NPs). Ich wyjątkowe właściwości optyczne w zakresie światła widzialnego wynikają z występowania zjawiska zlokalizowanego plazmonowego rezonansu powierzchniowego (LSPR) [10]. Polega ono na rezonansowym wzbudzeniu swobodnych elektronów promieniowaniem elektromagnetycznym o odpowiedniej długości fali. Położenie pasm(a) LSPR w widmie ekstynkcji zależy od kształtu, rozmiaru, składu chemicznego oraz funkcjonalizacji nanocząstek, co pozwala na precyzyjne projektowanie ich właściwości poprzez kontrolę warunków syntezy [11–13]. Możliwość zmiany położenia pasm(a) LSPR w funkcji kształtu Au-NPs istotnie zwiększa ich potencjał aplikacyjny. Au-NPs mogą być wykorzystane np. w celu projektowania cienkich warstw stosowanych jako podłoża do ultraczułej detekcji śladowych ilości (bio)molekuł za pomocą technik spektroskopowych, w tym powierzchniowo wzmocnionej spektroskopii Ramana (SERS) [14]. Ponadto, znalazły wiele zastosowań w medycynie, w tym diagnostyce i leczeniu,

np. jako kontrast polepszający obrazowanie promieniowaniem rentgenowskim czy nośniki dostarczające leki bezpośrednio do patologicznie zmienionych komórek lub w lokalnie selektywnej terapii fototermicznej [15–19]. Ze względu na wysoką aktywność katalityczną, Au-NPs są także wykorzystywane jako katalizatory np. w reakcjach utlenianie tlenku węgla [20].

Wytwarzanie uporządkowanych cienkich warstw, w tym monomolekularnych, o kontrolowanej architekturze jest możliwe za pomocą technik Langmuira. Rozwijanie techniki tworzenia monowarstw na powierzchni cieczy zapoczątkował Benjamin Franklin [21]. Na przełomie XIX i XX wieku Agnes Pockels opracowała metodę kompresji warstwy powierzchniowej, którą udoskonalił Irving Langmuir konstruując poziome naczynie pomiarowe, będące podstawą układu wykorzystywanego we współczesnej technice formowania warstw na granicy faz powietrze-woda [22,23]. Technika Langmuira umożliwia tworzenie monowarstw na powierzchni subfazy w kontrolowanych warunkach, pozwalając na określenie ich właściwości termodynamicznych, sposobu organizacji oraz morfologii. Utworzone warstwy mogą być przenoszone na podłoże stałe metodą Langmuira-Blodgett (LB) lub Langmuira-Schaefera (LS). Niezależnie od metody, podczas osadzania warstw utrzymywana jest stała wartość ciśnienia powierzchniowego, co pozwala na „odwzorowanie" warstwy Langmuira na podłożu stałym. Metoda LB polega na pionowym wynurzaniu i/lub zanurzaniu podłoża w czasie osadzania monowarstwy. W przypadku metody LS, ustawiona równolegle do subfazy powierzchnia podłoża jest zbliżana i styka się z monowarstwą, która zostaje przeniesiona, a następnie podłoże jest przesuwane w górę. Do wytwarzania wielowarstw częściej stosowana jest metoda LB, podczas gdy metodą LS uzyskuje się zazwyczaj pojedyncze warstwy [24]. W rozprawie doktorskiej do wytwarzania warstw Au-NPs i kontroli ich organizacji została zastosowana technika Langmuira, w tym metody LB lub LS do osadzania warstw na podłożu stałym.

Technika Langmuira może być także wykorzystywana do wytwarzania biomimetycznych układów [25–28]. Błony biologiczne są dynamicznymi strukturami, zbudowanymi głównie z podwójnej warstwy lipidów (fosfolipidów i steroli), białek i polisacharydów [29]. Ze względu na ich złożoność, badania prowadzi się często dla modelowych układów utworzonych z jednego lub wielu składników błon biologicznych [30–33]. Wykazano [34], że w określonych warunkach monowarstwy lipidowe formowane techniką Langmuira w znacznym stopniu odzwierciedlają właściwości błon

komórkowych, dlatego są wykorzystywane do badania wpływu różnych czynników na modelową strukturę oraz określania ich wzajemnych oddziaływań. Jednym z często wykorzystywanych do formowania błon biomimetycznych związków jest 1,2-dipalmitoilo-*sn*-glicero-3-fosfocholina (DPPC). DPPC jest kluczowym fosfolipidem budującym błony komórkowe ssaków i składnikiem lipidowym surfaktantu płucnego [35]. Do tworzenia modelowych układów mogą być stosowane również inne fosfolipidy (np. 1-palmitoilo-2-oleoilo-*sn*-glicero-3-fosfocholina (POPC)) i/lub sterole (w tym cholesterol (Chol)). POPC i DPPC reprezentują fosfolipidy z grupy fosfatydylocholin, jednak różnią się stopniem nasycenia łańcuchów węglowodorowych. Molekuła DPPC składa się z dwóch nasyconych łańcuchów palmitynowych, natomiast POPC składa się z nasyconego łańcucha palmitynowego i nienasyconego łańcucha oleinowego zawierającego jedno wiązanie podwójne [36]. Zastosowanie techniki Langmuira umożliwiało nie tylko tworzenie i określenie właściwości termodynamicznych jedno- i wieloskładnikowych warstw lipidowych [37,38], ale również pozwalało na badanie wpływu Au-NPs na organizację i oddziaływania w tych warstwach. W zależności od kształtu i funkcjonalizacji oraz składników modelowej błony, NPs mogą w różny sposób modyfikować właściwości fizykochemiczne warstwy, wbudowywać się w nią i oddziaływać z polarnymi lub hydrofobowymi grupami lipidów.

Pomimo rosnącego zainteresowania metalicznymi NPs i licznych doniesień literaturowych [39–43], istnieje luka badawcza w zakresie wiedzy dotyczącej korelacji pomiędzy parametrami Au-NPs (takimi jak kształt czy funkcjonalizacja), ich organizacją i warunkami tworzenia uporządkowanych cienkich warstw oraz oddziaływaniami z organicznymi molekułami, w tym barwnikami lub składnikami błon biologicznych, a pożądanymi właściwościami funkcjonalnymi pozwalającymi na znalezienie potencjału aplikacyjnego dla badanych układów.

Możliwość ultraczułej detekcji (bio)analitów metodami spektroskopii optycznej, wymaga wzmocnienia ich sygnału wykorzystując na przykład efekt lokalnego wzmocnienia pola elektromagnetycznego, prowadzący do zwiększenia wydajności zarówno procesów absorpcji i emisji promieniowania [44,45]. Pojawia się zatem pytanie o wpływ kształtu i funkcjonalizacji Au-NPs na ich optymalną organizację w warstwie, która gwarantuje pojawienie się obszarów o wysokim stopniu upakowania NPs. Wyjaśnienia wymaga również, czy właściwości termodynamiczne, odpowiednio dobrane parametry sprężania i ciśnienie powierzchniowe podczas przeniesienia warstw LB/LS,

determinują tworzenie się określonych struktur NPs oddziałujących z analitem, znajdującym się w ich bliskim otoczeniu.

Zaprojektowanie i synteza nanomateriałów jest istotną kwestią również ze względów na bezpieczeństwo stosowania NPs i ich potencjał oddziaływania na układy biologiczne. Poli(tlenek etylenu) (PEG-SH) jako biokompatybilny polimer jest powszechnie stosowany do funkcjonalizacji Au-NPs [46,47]. Jednak wpływ sfunkcjonalizowanych PEGiem NPs (o różnych kształtach) na organizację w warstwach oraz ich oddziaływanie ze składnikami modelowych błon biologicznych nie było dotychczas badane. Niewyjaśniona pozostaje również kwestia, czy istnieje określony związek pomiędzy masą cząsteczkową PEGu a stanem fizycznym monowarstw Langmuira Au-NPs@PEG, tendencją do agregacji oraz ostateczną architekturą warstw na podłożu stałym. Ponadto, interesującym wydaje się także ustalenie możliwego sposobu wbudowywania się w strukturę modelowej błony biologicznej Au-NPs@PEG, w zależności od ich kształtu oraz składu warstwy lipidowej.

Celem badań wykonanych w ramach przygotowania niniejszej rozprawy doktorskiej było określenie wpływu kształtu (sferyczne (Au-NSs), prętopodobne (Au-NRs)), funkcjonalizacji (dodekanotiol (DDT) lub polimer PEG-SH) i parametrów procesu kompresji na organizację Au-NPs w cienkich warstwach na granicy faz oraz ich oddziaływania z wybranymi związkami organicznymi (kwasem 4-merkaptobenzoesowym i/lub rodaminą 6G czy lipidami).

Motywacją do podjęcia badań było znalezienie warunków do tworzenia cienkich warstw Au-NPs (dla różnych funkcjonalizacji i kształtów) w kontekście ich potencjalnych zastosowań w ultraczułej detekcji analitów, określenie wpływu długości łańcucha polimeru użytego do funkcjonalizacji powierzchni Au-NPs na ich organizację (agregację i upakowanie) w warstwach oraz zrozumienie oddziaływań funkcjonalizowanych PEGiem Au-NPs (o różnych kształtach) z modelowymi błonami biologicznymi o ustalonym składzie lipidów.

Do badań wykorzystano komplementarne metody pomiarowe: spektroskopię absorpcyjną UV-vis, technikę SERS, mikroskopię konfokalną, skaningową (SEM) i transmisyjną (TEM) mikroskopię elektronową. Charakterystykę hydrodynamiczną i stabilność koloidalną NPs wyznaczono analizując wyniki uzyskane odpowiednio, metodą dynamicznego rozpraszania światła (DLS) i pomiarów potencjału zeta.

Wykorzystując technikę Langmuira, wyznaczono stabilność i parametry termodynamiczne monowarstw NPs i/lub lipidowych, które zobrazowano za pomocą mikroskopii kąta Brewstera (BAM). Wytworzone monowarstwy przenoszono na podłoża stałe metodami LB i LS. Oddziaływania na poziomie molekularnym pomiędzy NPs a lipidami w monowarstwach określono na podstawie analizy widm odbiciowo-absorpcyjnej spektroskopii w podczerwieni z modulacją polaryzacji (PM-IRRAS).

Uzyskane wyniki eksperymentalne umożliwiły wyjaśnienie i zrozumienie kluczowych relacji pomiędzy warunkami formowania monowarstw Langmuira, a ich właściwościami termodynamicznymi, morfologią i stabilnością. Dla Au-NPs o różnych kształtach, funkcjonalizowanych DDT lub polimerem, zidentyfikowano optymalne parametry formowania i przenoszenia odpowiednio upakowanych warstw, co pozwoliło na kontrolowane wytwarzanie obszarów o silnym wzmocnieniu pola elektromagnetycznego na podłożach stałych. Stwierdzono, że kształt Au-NPs ma znaczący wpływ na strukturę (elastyczność, stabilność i organizację) modelowych błon biologicznych, a od składu lipidów zależy czy NPs są adsorbowane na powierzchni czy częściowo wbudowują się w monowarstwę. Sposób lokalizacji NPs w warstwach lipidowych może mieć też istotne znaczenie dla zrozumienia mechanizmów oddziaływania nanomateriałów z komórkami zdrowymi lub chorobowo zmienionymi.

Wyniki badań zostały opublikowane w czterech oryginalnych artykułach naukowych, w czasopismach znajdujących się na liście *Journal Citation Reports* (JCR).

I Forma rozprawy doktorskiej i wkład doktorantki

Rozprawę doktorską pt. „*Organizacja nanocząstek złota na granicy faz i ich oddziaływanie z wybranymi związkami organicznymi*" stanowią cztery oryginalne artykuły opublikowane w recenzowanych czasopismach naukowych[*] indeksowanych na liście JCR:

1. **[Tim, JPCC 2023] B. Tim**[**], M. Kotkowiak[**], N. Kowalska, A.B. Nowicka, W. Lewandowski,
   Influence of gold nanoparticle assembly in Langmuir-Schaefer monolayers on the surface-enhanced spectroscopy response of a nanoplatform,
   Journal of Physical Chemistry C 127 (2023), 15978-15987. (IF 3,3; MNiSW 140)
2. **[Tim, ASS 2022] B. Tim**[***], P. Błaszkiewicz, A.B. Nowicka, M. Kotkowiak[**],
   Optimizing SERS performance through aggregation of gold nanorods in Langmuir-Blodgett films,
   Applied Surface Science 573 (2022), 151518-1-151518-22. (IF 6,7; MNiSW 140)
3. **[Kotkowiak, L 2024]** M. Kotkowiak[**], **B. Tim**, M. Kotkowiak, J. Musiał, P. Błaszkiewicz,
   The role of the polyethylene glycol in the organization of gold nanorods at the air-water and air-solid interfaces,
   Langmuir 40 (2024), 14561-14569. (IF 3,9; MNiSW 100)
4. **[Tim, JML 2025] B. Tim**[**], P. Błaszkiewicz, E. Coy, A. Dudkowiak,
   Interactions between functionalized PEGylated gold nanoparticles and model biological membranes,
   Journal of Molecular Liquid 428 (2025), 127501-1-127501-12. (IF 5,2; MNiSW 100)

[*] liczba punktów przyznanych dla danego czasopisma przez Ministerstwo Nauki i Szkolnictwa Wyższego (MNiSW) oraz współczynnik wpływu *Impact Factor* (IF) są zgodne z Systemem Informacji Naukowej Politechniki Poznańskiej (SIN PP),

[**] autor korespondencyjny

[***] równorzędny udział w przygotowaniu publikacji jak autor korespondencyjny,

Zgodnie z załączonymi oświadczeniami współautorów, wkład autorki rozprawy doktorskiej w powstanie publikacji był następujący:

1. **[Tim, JPCC 2023]** – wykonała przegląd aktualnej literatury dotyczącej wytwarzania warstw na granicy faz powietrze-woda i powietrze-ciało stałe sferycznych nanocząstek złota oraz ich zastosowania we wzmocnionej powierzchniowo spektroskopii Ramana (SERS). Przeprowadziła badania kontrolowanej organizacji nanocząstek złota w warstwach za pomocą techniki Langmuira i Langmuira-Schaefera (LS) oraz mikroskopii kąta Brewstera (BAM). Uczestniczyła w analizie, interpretacji i dyskusji wyników pomiarowych oraz współredagowała tekst manuskryptu.
2. **[Tim, ASS 2022] –** wykonała przegląd aktualnej literatury dotyczącej wytwarzania warstw na granicy faz powietrze-woda i powietrze-ciało stałe prętopodobnych nanocząstek złota oraz ich zastosowania w technice SERS. Wytworzyła warstwy i przeprowadziła badania za pomocą techniki Langmuira, Langmuira-Blodgett (LB) i ich charakteryzację z wykorzystaniem mikroskopii BAM oraz spektroskopii UV-vis. Uczestniczyła w analizie i dyskusji wyników eksperymentalnych oraz współredagowała tekst manuskryptu.
3. **[Kotkowiak, L 2024]** – wykonała przegląd aktualnej literatury dotyczącej warstw sfunkcjonalizowanych nanocząstek na granicy faz powietrze-woda oraz powietrze-ciało stałe. Wytworzyła warstwy i przeprowadziła badania za pomocą techniki Langmuira, LB i LS, mikroskopii BAM oraz spektroskopii UV-vis. Uczestniczyła w analizie i dyskusji wyników pomiarowych oraz współredagowała tekst manuskryptu.
4. **[Tim, JML 2025]** – wykonała przegląd aktualnej literatury dotyczącej wytwarzania modelowych błon biologicznych na granicy faz powietrze-woda składających się z lipidów oraz nanocząstek złota, opracowała koncepcję badań i sformułowała cele naukowe oraz zaplanowała strategię eksperymentalną w celu kompleksowej analizy zmian strukturalnych i oddziaływań międzyfazowych. Przeprowadziła badania za pomocą techniki Langmuira, mikroskopii BAM, techniki odbiciowo-absorpcyjnej spektroskopii w podczerwieni z modulacją polaryzacji (PM-IRRAS). Odpowiadała także za analizę i interpretację wyników eksperymentalnych oraz współredagowała tekst manuskryptu. Nadzorowała realizację projektu, koordynowała prace, zarządzała planowaniem i realizacją badań oraz pozyskała wsparcie finansowe dla projektu.

II Badane materiały oraz zastosowane techniki pomiarowe

W niniejszej rozprawie doktorskiej badano sfunkcjonalizowane sferyczne (NSs) i prętopodobne (NRs) nanocząstki złota oraz ich warstwy z wybranymi związkami organicznymi, takimi jak kwas 4-merkaptobenzoesowym (p-MBA)) i/lub rodamina 6G (R6G) czy lipidy. Nanopręty złota (Au-NRs) będące przedmiotem badań były funkcjonalizowane za pomocą poli(tlenku etylenu) z grupą tiolową (PEG-SH), o masie cząsteczkowej (Mw) odpowiednio 2000 (2k), 5000 (5k), 10000 (10k) (Au-NRs@PEG(2k), Au-NRs@PEG(5k), Au-NRs@PEG(10k)). Proces syntezy i funkcjonalizacji został przeprowadzony w laboratoriach Zakładu Fizyki Molekularnej na Wydziale Inżynierii Materiałowej i Fizyki Technicznej (WIMiFT) Politechniki Poznańskiej (PP). Szczegółowy opis przeprowadzonych reakcji wraz z parametrami syntezy, oczyszczania i funkcjonalizacji materiału, znajduje się w pracach: Błaszkiewicz i in. [48,49] oraz **[Kotkowiak, L 2024]** i **[Tim, JML 2025]**. W badaniach wykorzystano również sferyczne nanocząstki złota (Au-NSs) pokryte dodekanotiolem (DDT), które zostały przygotowane w laboratorium prof. Wiktora Lewandowskiego na Wydziale Chemii Uniwersytetu Warszawskiego, oraz Au-NSs zsyntetyzowane i sfunkcjonalizowane za pomocą PEG-SH o masie cząsteczkowej Mw ≈ 2000 (2k), otrzymane w laboratoriach Zakładu Fizyki Molekularnej na WIMiFT PP. Zastosowane procedury syntezy i funkcjonalizacji, a także parametry przeprowadzonych reakcji przedstawiono w pracy **[Tim, JPCC 2023]**. Wykorzystanie dwóch różnych ligandów do funkcjonalizacji Au-NSs pozwoliło na sprawdzenie ich potencjału aplikacyjnego. DDT jako ligand zapewniał kontrolę nad upakowaniem i zachowaniem optymalnej odległości między NSs. Jego hydrofobowa natura pozwalała na wytworzenia uporządkowanych warstw NPs, co było istotne dla uzyskania silnego sprzężenia plazmonowego na podłożach stałych i określenia możliwości wykorzystywania tych warstw w detekcji molekuł adsorbowanych na ich powierzchni, wykorzystując powierzchniowo wzmocnioną spektroskopię Ramana (SERS). Natomiast hydrofilowy PEG-SH, stosowany między innymi w produktach farmaceutycznych i spożywczych, umożliwiał nie tylko wytworzenie zagregowanych warstw sfunkcjonalizowanych NRs, które po pokryciu warstwą p-MBA testowano za pomocą techniki SERS, ale również scharakteryzowanie oddziaływań NPs z lipidami tworzącymi modelowe błony biologiczne. Warto podkreślić, że NPs funkcjonalizowane DDT charakteryzowały się

ograniczoną stabilnością koloidalną w środowisku wodnym, co sprzyjało efektywnemu tworzeniu i kontrolowaniu ich organizacji w warstwach, natomiast NPs pokryte PEG-SH wykazywały wysoką stabilność koloidalną dzięki efektowi sterycznemu oraz hydrofilowości łańcucha polimerowego, co miało kluczowe znaczenie dla prowadzonych badań, zwłaszcza w przypadku układów biomimetycznych.

Do badań nad wzmocnieniem sygnałów techniką SERS wykorzystano warstwy Langmuira-Schaefera (LS) lub Langmuira-Blodgett (LB) na podłożach stałych utworzone z sfunkcjonalizowanych Au-NPs i stosowano związki organiczne zakupione w Merck Group (p-MBA i/lub R6G), których struktury przedstawiono odpowiednio na Rys. 1 i Rys. 2.

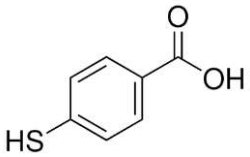

Rys. 1. Struktura kwasu 4-merkaptobenzoesowego (p-MBA) (na podstawie [50]).

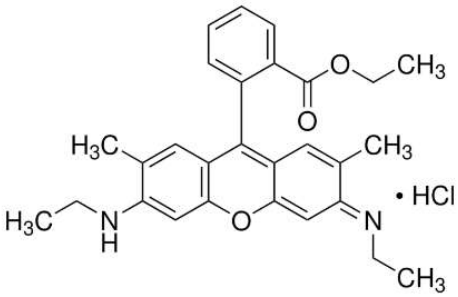

Rys. 2. Struktura rodaminy 6G (R6G) (na podstawie [51]).

W celu określenia oddziaływań Au-NRs w modelowych błonach biologicznych, do badań wybrano lipidy zakupione w Merck Group, tj. 1,2-dipalmitoilo-*sn*-glicero-3-fosfocholinę (DPPC), 1-palmitoilo-2-oleoilo-*sn*-glicero-3-fosfocholinę (POPC) i cholesterol (Chol), których struktury przedstawiono odpowiednio na Rys. 3, Rys. 4 i Rys. 5.

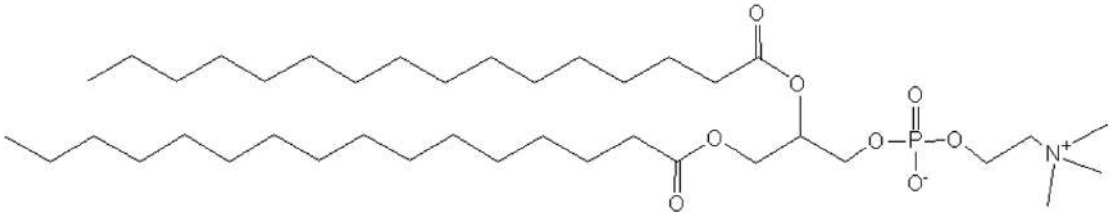

Rys. 3. Struktura 1,2-dipalmitoilo-*sn*-glicero-3-fosfocholiny (DPPC) (na podstawie [52]).

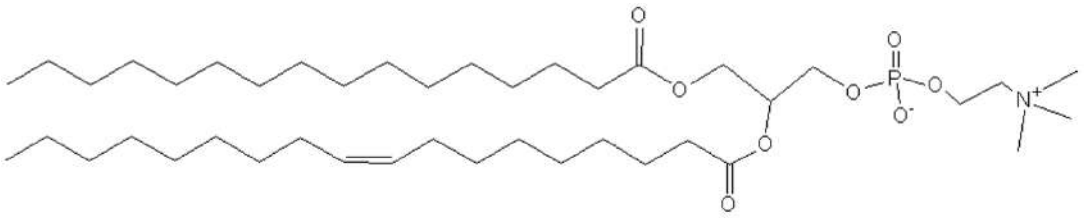

Rys. 4. Struktura 1-palmitoilo-2-oleoilo-*sn*-glicero-3-fosfocholiny (POPC) (na podstawie [53]).

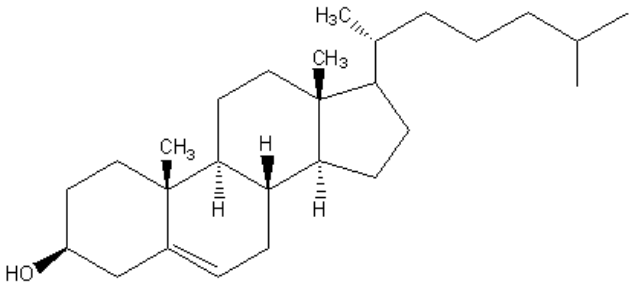

Rys. 5. Struktura cholesterolu (Chol) (na podstawie [54]).

W laboratoriach Zakładu Fizyki Molekularnej na WIMiFT PP przeprowadzono badania z wykorzystaniem techniki Langmuira. W celu wyznaczenia parametrów termodynamicznych monowarstw na powierzchni subfazy wodnej (ultraczysta woda, Milli-Q, 18,2 MΩ·cm, (71,98 ± 0,01) $mN \cdot m^{-1}$) nanoszono dyspersje Au-NPs w chloroformie (Uvasol). Po odparowaniu rozpuszczalnika organicznego wytwarzano monowarstwę poprzez zsuwanie dwóch ruchomych barier wykonanych z hydrofilowego polimeru Derlin. Podczas kompresji warstw możliwe było wykonanie pomiarów *in-situ* za pomocą spektroskopii absorpcyjnej oraz mikroskopii kąta Brewstera (BAM). Przeprowadzono również pomiary kinetyk relaksacji, które polegały na rejestracji zmian względnej powierzchni warstwy w funkcji czasu, po kompresji monowarstwy do określonego ciśnienia powierzchniowego (π).

Wytwarzane na subfazie wodnej warstwy Langmuira, po osiągnięciu zadanego ciśnienia powierzchniowego, przenoszono na podłoże stałe metodami LB lub LS. Metody te różni sposób osadzania warstwy, który polegał odpowiednio na pionowym (LB) lub poziomym (LS) przesuwaniu podłoża stałego względem subfazy.

Po przeniesieniu na podłoża stałe, właściwości spektralne warstw analizowano na podstawie widm otrzymanych metodą spektroskopii absorpcyjnej, obrazowano przy użyciu mikroskopii konfokalnej, a pokrycie powierzchni określano za pomocą mikrowagi kwarcowej (QCM). Dodatkowo, warstwy Au-NRs@PEG na podłożu stałym zobrazowano za pomocą skaningowej mikroskopii elektronowej (SEM) w Zakładzie Metaloznawstwa i Inżynierii Powierzchni na WIMiFT PP. Pomiary z wykorzystaniem

spektroskopii Ramana dotyczące oddziaływań pomiędzy związkami organicznymi a warstwami Au-NPs na podłożach stałych wykonano w Zakładzie Spektroskopii Optycznej WIMiFT PP. W Zakładzie Chemii Środowiska Uniwersytetu Jagiellońskiego, scharakteryzowano oddziaływania i morfologię warstw lipidowych z Au-NRs@PEG(2k) lub Au-NSs@PEG(2k) stosując odbiciowo-absorpcyjną spektroskopię w podczerwieni z modulacją polaryzacji (PM-IRRAS) oraz mikroskopię BAM. Dla Au-NSs@DDT (lub ich warstw), na Wydziale Chemii Uniwersytetu Warszawskiego wykonano pomiary metodami dynamicznego rozpraszania światła (DLS), dyfrakcji rentgenowskiej (SAXRD) oraz transmisyjnej mikroskopii elektronowej (TEM). Dodatkowo, w Centrum NanoBiomedycznym Uniwersytetu im. Adama Mickiewicza w Poznaniu, wykonano obrazy za pomocą mikroskopii TEM oraz pomiary potencjału zeta i DLS dla Au-NRs@PEG i Au-NSs@PEG(2k) oraz Au-NSs@PEG(2k) z lipidami.

III Opis badań

Celem badań przeprowadzonych w ramach przygotowania niniejszej rozprawy było poszerzenie wiedzy o wpływie kształtu Au-NPs na oddziaływania ze składnikami modelowych błon biologicznych oraz ustalenie optymalnych warunków otrzymywania cienkich warstw Au-NPs do detekcji śladowych ilości analitów, w kontekście potencjalnych zastosowań biomedycznych. Uzyskane wyniki pozwoliły na określenie organizacji NPs złota (różniących się funkcjonalizacją powierzchni lub kształtem) w cienkich warstwach na granicy faz oraz ich oddziaływań z wybranymi związkami organicznymi, w tym lipidami lub kwasem 4-merkaptobenzoesowym i/lub rodaminą 6G.

W pracy **[Tim, JPCC 2023]** przedmiotem badań były sferyczne złote nanocząstki, sfunkcjonalizowane hydrofobowym dodekanotiolem (Au-NSs@DDT) i ich wzajemne oddziaływania w warstwach Langmuira i Langmuira-Schaefera (LS). Ustalono korelację pomiędzy właściwościami termodynamicznymi warstw Au-NSs@DDT (w skali mikro- i nanometrycznej), a ich organizacją oraz sprawdzono możliwość wykorzystania warstw jako podłoży do badań techniką SERS.

Badane NSs@DDT charakteryzowały się pasmem LSPR przy długości fali 515 nm i wielkością (4,4 ± 0,4) nm, potwierdzoną wynikami pomiarów technikami SAXRD i TEM **[Tim, JPCC 2023, Fig. S2, S5]**. Dla warstw Langmuira Au-NSs zarejestrowano izotermy (π-A) i obliczono moduł ściśliwości (C_s^{-1}) w funkcji powierzchni wanny (A) **[Tim, JPCC 2023, Fig. 1]**. Dodatkowo, *in-situ* zobrazowano tworzone monowarstwy za pomocą mikroskopii BAM **[Tim, JPCC 2023, Fig. 2]**, co pozwoliło na monitorowanie ich morfologii w czasie rzeczywistym, na granicy faz. Zbadano również kinetyki relaksacji warstwy (zależności względnej zmiany powierzchni warstwy w funkcji czasu) **[Tim, JPCC 2023, Fig. S4]**, dla wybranych wartości ciśnienia powierzchownego (tj. π = 2, 4, 6, 12, 14 i 20 $mN \cdot m^{-1}$) i zarejestrowano histerezę sprężania/rozprężania monowarstw **[Tim, JPCC 2023, Fig. S3]**. Warstwy z subfazy przenoszono metodą LS na płytki kwarcowe przy wartościach ciśnienia powierzchniowego (tj. π = 2, 4, 6, 12, 14 i 20 $mN \cdot m^{-1}$), optymalizując prędkość zanurzania poziomego do 0,5 $mm \cdot min^{-1}$, w celu maksymalizacji pokrycia powierzchni podłoża. Morfologię i stopień pokrycia powierzchni płytek kwarcowych, w skali mikro i nanometrycznej, przeanalizowano odpowiednio na podstawie obrazów z mikroskopów konfokalnego i TEM. Dla warstw LS rejestrowano widma optyczne w zakresie UV-vis **[Tim, JPCC 2023, Fig. 4]**,

a możliwość ich stosowania jako podłoży do badań techniką SERS przetestowano wykorzystując p-MBA **[Tim, JPCC 2023, Fig. 7]**.

Zarejestrowane izotermy kompresji oraz kształt modułu ściśliwości Au-NSs@DDT w warstwach Langmuira **[Tim, JPCC 2023, Fig. 1]** wskazują na istnienie dwóch obszarów o odmiennej sprężystości warstwy, dla ciśnienia powierzchniowego poniżej i powyżej 10 $mN \cdot m^{-1}$ (i odpowiednio, powierzchni wanny pomiędzy 60 a 220 cm^2 oraz 25 a 50 cm^2). Maksimum wartości C_s^{-1} wynoszące 15 $mN \cdot m^{-1}$ sugerowało, że warstwa Langmuira utworzona z NSs@DDT znajduje się w stanie ciekłym rozprężonym (LE). Obrazy BAM warstwy NPs na powierzchni subfazy **[Tim, JPCC 2023, Fig. 2]** potwierdziły, że wraz ze wzrostem π, początkowo heterogeniczna warstwa, składająca się z izolowanych domen, przekształcała się podczas kompresji w homogeniczną warstwę o wysokim stopniu upakowania. Ponadto, zarejestrowana histereza izoterm wskazuje, że zarówno proces sprężania, jak i rozprężania przebiega w podobny sposób co oznacza, że oddziaływania pomiędzy hydrofobowo sfunkcjonalizowanymi Au-NSs@DDT w warstwie nie powodują powstawania trwałych agregatów **[Tim, JPCC 2023, Fig. S3]**.

Dla wybranych ciśnień powierzchniowych, przy których przenoszono warstwy na podłoże stałe zarejestrowano kinetyki relaksacji **[Tim, JPCC 2023, Fig. S4]**. Na ich podstawie stwierdzono, że stabilność tworzonych warstw maleje wraz ze wzrostem ciśnienia powierzchniowego, tj. podczas zwiększania upakowania Au-NSs@DDT na granicy faz. Analiza obrazów warstw Au-NSs@DDT na podłożu stałym, w skali mikroskopowej, uzyskanych za pomocą mikroskopii konfokalnej **[Tim, JPCC 2023, Fig. 5]**, wykazała liniowy wzrost pokrycia podłoża NSs w funkcji π (wybranego do depozycji warstw), co potwierdziły również wyniki obliczeń wykonane na podstawie pomiarów QCM **[Tim, JPCC 2023, Fig. S6]**. Jednakże, analiza obrazów TEM **[Tim, JPCC 2023, Fig. 6]** w skali nanometrycznej ujawniła dwa odrębne obszary organizacji NSs w warstwach LS. Dla $\pi < 9$ $mN \cdot m^{-1}$ wzrost pokrycia podłoża był stosunkowo niewielki, podczas gdy dla $\pi > 9$ $mN \cdot m^{-1}$ zaobserwowano gwałtowny, niemal dwukrotnie szybszy wzrost pokrycia wskazujący na krytyczne zbliżenie się NSs i możliwe formowanie rozległych domen o wysokim stopniu upakowania. Analiza widm absorpcji i położenia pasma LSPR **[Tim, JPCC 2023, Fig. 4]** wydaje się potwierdzać różny stopień pokrycia podłoża Au-NSs@DDT dla warstw wytwarzanych przy niższych i wyższych ciśnieniach powierzchniowych.

Pomiary dla p-MBA zdeponowanego na powierzchni warstw Au-NSs@DDT utworzonych na podłożu stałym techniką LS **[Tim, JPCC 2023, Fig. 7]** wykazały wyraźną zależność intensywności sygnału SERS od wartości ciśnienia powierzchniowego, przy którym przenoszono warstwy. W zakresie niskich ciśnień przenoszenia ($\pi < 9$ mN·m^{-1}) wzrost intensywności sygnału SERS był stosunkowo niewielki. Dla π powyżej 9 mN·m^{-1}, odpowiadających obszarowi wyższego stopnia upakowania NSs, wzrost ten był 6-krotnie większy w porównaniu z intensywnością sygnału dla warstw osadzanych w zakresie niższych ciśnień. Proces formowania warstw metodą LS, przy wartościach π przekraczających 9 mN·m^{-1}, umożliwia przeniesienie warstw Langmuira zachowując wysoki stopnień upakowania Au-NSs@DDT na podłożu stałym. Uzyskane wyniki wskazują, że wzmocnienie sygnału SERS nie jest prostą funkcją samego pokrycia, ale wynika z jakościowej zmiany w organizacji NPs. Warstwy charakteryzują się obecnością domen, w których odległości pomiędzy NSs są optymalne dla uzyskania silnego sprzężenia plazmonowego.

Analiza wyników dla Au-NSs@DDT w cienkich warstwach wytwarzanych techniką Langmuira pozwoliła na zidentyfikowanie punktu na izotermie (przy ciśnieniu powierzchniowym ok. 10 mN·m^{-1}), który rozdziela dwa obszary o różnej organizacji Au-NSs. Badania umożliwiły także skorelowanie właściwości i parametrów warstw NSs wytworzonych metodą LS ze wzmocnieniem sygnału techniką SERS. Upakowanie i wzajemne odległości NSs wpływają na uzyskanie silnego sprzężenia plazmonowego, co jest kluczowe dla wzmocnienia sygnału molekuł znajdujących się w ich pobliżu. Pokazano możliwość wykorzystania techniki Langmuira do zaprojektowania i uzyskania warstw sferycznych Au-NPs (sfunkcjonalizowanych hydrofobowym DDT) na podłożach stałych, o kontrolowanych i pożądanych właściwościach (pokryciu i upakowaniu), które mają potencjał do wykorzystania w ultraczułej detekcji molekuł.

Mając na uwadze potencjalne zastosowania biomedyczne, kluczowe wydawało się zbadanie, czy analogiczną kontrolę nad organizacją i właściwościami podłoży dla techniki SERS można osiągnąć wykorzystując NPs funkcjonalizowane polimerem, ligandem o wysokiej biokompatybilności.

W tym kontekście, w pracy **[Tim, ASS 2022]** przedmiotem badań były złote nanopręty, funkcjonalizowane hydrofilowym polimerem PEG-SH o masie cząsteczkowej 2000 (2k) (Au-NRs@PEG(2k)), w warstwach Langmuira i Langmuira-Blodgett (LB).

Sprawdzono także, czy dla Au-NRs efektywność wymiany bromku cetylotrimetyloamoniowego (CTAB) na PEG-SH podczas funkcjonalizacji i ewentualna pozostałości surfaktantu CTAB mogą w istotny sposób zakłócać proces formowania i interpretację wyników dla monowarstw na subfazie wodnej. Dla warstw Langmuira wyznaczono zależności ciśnienia powierzchniowego (π) w funkcji powierzchni wanny (A), na podstawie których obliczono moduł ściśliwości (C_s^{-1}), oraz zarejestrowano histerezę sprężania/rozprężania **[Tim, ASS 2022, Fig. 1** i **Fig. S2]**. Dodatkowo w czasie rzeczywistym (*in-situ*), dla różnych ciśnień powierzchniowych zobrazowano morfologię monowarstw za pomocą mikroskopii BAM oraz zarejestrowano widma absorpcji **[Tim, ASS 2022, Fig. 2** i **Fig. 3a]**. Wyznaczono również kinetyki relaksacji warstw Langmuira dla wybranych wartości ciśnienia powierzchownego (tj. π = 4, 8, 12, 15 i 20 $mN \cdot m^{-1}$) **[Tim, ASS 2022, Fig. S3]**. Na podstawie analizy danych eksperymentalnych i obliczeń, możliwe było określenie stopnia upakowania i rodzaj stanu, w jakim znajdują się na granicy faz oraz uzyskania informacji o organizacji sfunkcjonalizowanych PEGiem Au-NRs.

Zanim uformowano warstwy, określono stężenie CTAB pozostające w zawiesinach Au-NRs@PEG(2k) po wymianie ligandów na PEG-SH podczas procesu funkcjonalizacji NPs. Potwierdzono, że po zakończeniu procesu funkcjonalizacji Au-NRs, stężenie CTAB było znikome (rzędu 1 10^{-6}M), a analiza izoterm **[Tim, ASS 2022, Fig. 1]** wykazała, iż nie ma ono wpływu na termodynamiczne właściwości monowarstw. Dalsze badania prowadzono dla Au-NRs@PEG(2k) o średniej długości 53,2 nm i szerokości 23,6 nm.

Stwierdzono, że sfunkcjonalizowane polimerem (2k) Au-NRs tworzą stabilne monowarstwy Langmuira na subfazie wodnej. Biorąc pod uwagę kryterium wprowadzone przez Daviesa i Rideala [55] oraz maksymalną wartość C_s^{-1} określono, że stopień upakowania Au-NRs@PEG(2k) sugeruje stan ciekły rozprężony (LE) monowarstwy. Analiza obrazów BAM wskazuje, że kompresja monowarstwy prowadzi do zmiany jej morfologii, która przy niższych wartościach ciśnienia powierzchniowego jest niejednorodna, o czym świadczą liczne pasma widoczne przy π = 4 $mN \cdot m^{-1}$ **[Tim, ASS 2022, Fig. 2a]**. Wydaje się, że Au-NRs@PEG(2k) tworzą domeny na granicy faz powietrze-woda w wyniku procesu samorzutnej organizacji. Wzrost ciśnienia powierzchniowego powoduje, że Au-NRs@PEG(2k) stopniowo pokrywają dostępną powierzchnię, w konsekwencji na granicy faz powietrze-woda obserwowany jest bardziej jednorodny obraz warstwy **[Tim, ASS 2022, Fig. 2e]**. Widma absorpcji zarejestrowane

in-situ wykazały, że absorbancja przy długości fali 653 nm dla Au-NRs@PEG(2k) w warstwach Langmuira zmienia się liniowo i nie obserwuje się batochromowego przesunięcia podłużnego pasma LSPR w funkcji ciśnienia powierzchniowego **[Tim, ASS 2022, Fig. 3a,b]**. Brak zmian w położeniu pasma LSPR charakterystycznego dla badanych NRs oraz kształt histerezy dla Au-NRs@PEG(2k) **[Tim, ASS 2022, Fig. S2]**, pozwalają wnioskować, że sfunkcjonalizowane PEGiem Au-NRs nie tworzą trwałych struktur agregacyjnych na subfazie wodnej, przy ograniczaniu zajmowanej przez nie powierzchni wanny (podczas kompresji). Dla ciśnień powierzchniowych π = 4, 8, 12, 15 i 20 $mN \cdot m^{-1}$ wykonano również pomiary kinetyk relaksacji, w celu zbadania zależności między stopniem upakowania Au-NRs w monowarstwie Langmuira, a jej stabilnością. Analiza krzywych relaksacji **[Tim, ASS 2022, Fig. S3]** wykazała, że stabilność monowarstwy maleje wraz ze wzrostem ciśnienia. Podczas gdy, przy 4 $mN \cdot m^{-1}$ obserwowano niemal stałą względną zmianę powierzchni warstwy w funkcji czasu, to przy wyższych ciśnieniach (powyżej 12 $mN \cdot m^{-1}$) krytyczne naprężenia w silnie upakowanej warstwie prowadziły do nieodwracalnej zmiany stanu, w którym pierwotna struktura warstwy ulega reorganizacji.

Warstwy Au-NRs@PEG(2k) osadzono na podłożach stałych metodą LB, przy ustalonych ciśnieniach powierzchniowych (π = 4, 8, 12, 15 i 20 $mN \cdot m^{-1}$) i scharakteryzowano za pomocą mikroskopii konfokalnej oraz spektroskopii absorpcyjnej w zakresie UV-vis. Pozwoliło to określić organizację i upakowanie Au-NRs@PEG(2k) w warstwach LB, a także sprawdzić, czy oddziaływanie z podłożem wpływa na położenie pasm plazmonowych badanych NRs.

Niezależnie od ciśnienia powierzchniowego, przy którym osadzano warstwy Au-NRs@PEG(2k) na podłożu stałym, ich widma absorpcji wykazały wyraźne przesunięcie maksimum pasma podłużnego LSPR (przy 653 nm) o ok. 100 nm w kierunku dłuższych długości fali **[Tim, ASS 2022, Fig. 3c]**, w porównaniu z pasmem obserwowanym dla tych samych NRs na granicy faz powietrze-woda. Sugeruje to, że podczas procesu osadzania warstw LB może zachodzić proces agregacji Au-NRs@PEG(2k). Wydaje się, że proces ten zostaje zainicjowany w wyniku „odwadniania" warstwy w trakcie pionowego wynurzania podłoża. Zmniejszenie liczby molekuł wody w warstwie przenoszonej, w konsekwencji prowadzi do zmiany właściwości i/lub organizacji warstwy LB w odniesieniu do monowarstwy Langmuira tworzonej na subfazie wodnej. Analiza obrazów uzyskanych za pomocą mikroskopii

konfokalnej potwierdziła tworzenie agregatów o strukturze dendrytycznej **[Tim, ASS 2022, Fig. 4a-e]**. Powstawanie quasi-równoległych, dendrytycznych agregatów może wynikać z odparowywania wody z przestrzeni między NPs, co powoduje ich zbliżenie i samoorganizację. Zmiany widoczne na obrazach wskazują, że struktury tworzone przez Au-NRs@PEG(2k) zorientowane są równolegle do kierunku, w którym podłoże kwarcowe wynurza się z subfazy wodnej podczas przenoszenia warstwy Langmuira. Okazało się, że rozmieszczenie dendrytycznych struktur NPs oraz stopień pokrycia powierzchni można kontrolować przez odpowiedni dobór ciśnienia powierzchniowego, przy którym osadzane są warstwy na podłożu stałym. Analiza zależności ciśnienia powierzchniowego od stopnia pokrycia powierzchni podłoża **[Tim, ASS 2022, Fig. 4f]** wykazała, że największą jego wartość osiągnięto po przeniesieniu warstwy przy ciśnieniu 12 $mN \cdot m^{-1}$. W wyniku tworzenia się agregatów o wysokim stopniu upakowania, dochodzi prawdopodobnie do zbliżenia NPs i silnego sprzężenia plazmonowego między nimi, co uwidacznia się w widmach ekstynkcji znacznym przesunięciem maksimum pasma LSPR ku czerwieni i jego poszerzeniem. Obecność obszarów z blisko ułożonymi Au-NRs w strukturach dendrytycznych stwarza podobne możliwości, jak w przypadku Au-NSs@DDT, wykorzystania tych warstw jako aktywnych podłoży w technice SERS.

Dalsze badania pokazały, że warstwy Au-NRs@PEG(2k) mają pewien potencjał aplikacyjny w detekcji wybranych związków organicznych (p-MBA i R6G) techniką SERS, w szczególności warstwy osadzane przy ciśnieniu powierzchniowym 12 $mN \cdot m^{-1}$ (dla których współczynnik wzmocnienia SERS wynosił ok. $1{,}9 \cdot 10^5$) ze względu na najlepsze pokrycie powierzchni i tworzone struktury dendrytyczne z obszarami lokalnego wzmocnienia pola elektromagnetycznego (tzw. „hot-spotami"). Obecność tych obszarów daje szanse zastosowania techniki Langmuira do projektowania i wytwarzania warstw Au-NRs@PEG(2k) o kontrolowanych właściwościach optycznych. Warstwy te mogą być dedykowane do badania związków aktywnych biologicznie (absorbujących w różnym zakresie), dzięki możliwości syntezy nanopręt ów o różnej długości i modyfikowania położenia podłużnego pasma LSPR.

Ze względu na interesujące zastosowania warstw Au-NRs@PEG(2k) na podłożu stałym, postanowiono sprawdzić wpływ długości łańcucha PEG-SH (2k, 5k, 10k) użytego do funkcjonalizacji powierzchni Au-NRs na stabilność, właściwości termodynamiczne i morfologię monowarstw Langmuira oraz na organizację NPs na podłożu stałym

[Kotkowiak, L 2024]. Badania wykonano, podobnie jak poprzednio **[Tim, ASS 2022]**, dla Au-NRs o średniej długości 53,2 nm i szerokości 23,6 nm, które zostały scharakteryzowane za pomocą spektroskopii UV-vis oraz mikroskopii TEM **[Kotkowiak, L 2024, Fig. S2,S3]**. Pomiary DLS oraz potencjału zeta potwierdziły skuteczność funkcjonalizacji Au-NRs@PEG **[Kotkowiak, L 2024, Fig. S4, Table S1]**. Dla monowarstw Langmuira wykazano, że utworzenie stabilnej monowarstwy przez Au-NRs sfunkcjonalizowane dłuższymi łańcuchami PEG (5k, 10k) wymagało obecności CTAB w zawiesinie wyjściowej w celu stabilizacji elektrostatycznej. Pokazano, że CTAB zapobiega agregacji Au-NRs@PEG na powierzchni subfazy. Analiza izoterm π-A ujawniła wyraźny wpływ masy cząsteczkowej PEG-SH na właściwości termodynamiczne monowarstw. Izoterma dla Au-NRs@PEG(2k) charakteryzowała się stopniowym wzrostem ciśnienia od początku kompresji, podczas gdy dla Au-NRs@PEG(5k) i Au-NRs@PEG(10k) wzrost ciśnienia rozpoczynał się dopiero po znacznym ograniczeniu powierzchni wanny (do około 195 cm²) **[Kotkowiak, L 2024, Fig. 1]**. Wykorzystując kryterium wprowadzone przez Daviesa i Rideala [55], podobnie jak poprzednio **[Tim, JPCC 2023], [Tim, ASS 2022]** na podstawie modułu ściśliwości (C_s^{-1}) określono stan fizyczny monowarstw. Maksymalna wartość C_s^{-1} dla Au-NRs@PEG(2k) wyniosła 108 mN·m⁻¹ co oznacza, że monowarstwa na subfazie jest w fazie skondensowanej ciekłej (LC). Wartość modułu ściśliwości różni się od tej określonej w pracy **[Tim, ASS 2022]**, podobnie jak wartość ciśnienia powierzchniowego, przy którym następuje tzw. „collapse" warstwy. Różnice te wynikają z większej ilości CTAB zastosowanego na etapie syntezy dla Au-NRs@PEG(2k) badanych w pracy **[Kotkowiak, L 2024]**. Ponadto, na podstawie analizy krzywych kinetyk relaksacji **[Kotkowiak, L 2024, Fig. S5]** stwierdzono, że warstwy charakteryzują się większą stabilnością niż przedstawione w pracy **[Tim, ASS 2022, Fig. S3]**. Z kolei, wartości maksymalne C_s^{-1} dla Au-NRs@PEG(5k) i Au-NRs@PEG(10k) wyniosły odpowiednio 49 i 40 mN·m⁻¹, wskazując na tworzenie się znacznie bardziej elastycznych warstw, w stanie ciekłym rozprężonym (LE). Różnice te zinterpretowano biorąc pod uwagę możliwe konformacje łańcuchów, od „gęstego pędzla" (brush), w przypadku krótkiego łańcucha 2k, do „grzyba" (mushroom) dla polimeru 10k oraz prawdopodobne mniejsze upakowanie dłuższych polimerów na powierzchni Au-NRs, co zobrazowano na Rys. 6.

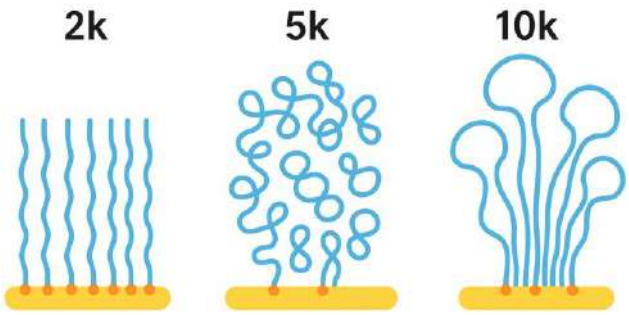

Rys. 6. Schematyczne przedstawienie zmian konformacji łańcuchów polimerowych o różnej masie cząsteczkowej (2k, 5k, 10k) na powierzchni Au-NRs.

Obrazy warstw Langmuira Au-NRs@PEG wykonane mikroskopem BAM **[Kotkowiak, L 2024, Fig. 2]** potwierdziły te wnioski, pokazując heterogeniczną strukturę monowarstwy Au-NRs@PEG(2k), jednorodną warstwę Au-NRs@PEG(5k) oraz tendencję do formowania aglomeratów przy wyższych ciśnieniach powierzchniowych – w przypadku Au-NRs@PEG(10k). Ponadto, porównując obrazy BAM zarejestrowane dla Au-NRs@PEG(2k) z pracy **[Kotkowiak, L 2024]** i obrazy uzyskane z pracy **[Tim, ASS 2022]** można stwierdzić, że CTAB wpływa na organizację tworzonych warstw, czyniąc je bardziej niejednorodnymi wraz ze wzrostem ciśnienia powierzchniowego. Następnie, wytworzone monowarstwy przeniesiono metodami LS i LB na podłoże stałe i zarejestrowano widma UV-vis **[Kotkowiak, L 2024, Fig. 3]**. Na podstawie analizy przesunięć podłużnego pasm LSPR określono stopień agregacji Au-NRs w warstwach. Zaobserwowano wyraźną korelację między masą cząsteczkową PEG, metodą depozycji, a typem tworzonej struktury. Dla Au-NRs@PEG(10k), warstwy LS deponowane przy niskich ciśnieniach (tj. $\pi = 4, 8, 15$ mN·m^{-1}) zachowywały widmo charakterystyczne dla pojedynczych, niezagregowanych NRs. Jednak przy wyższych ciśnieniach (tj. $\pi = 23, 37$ mN·m^{-1}) oraz w przypadku wszystkich warstw LB zaobserwowano silne przesunięcie pasma LSPR powyżej 750 nm, wskazujące na intensywne sprzężenie plazmonowe w domenach o zwiększonej lokalnej koncentracji NRs, tworzących prawdopodobnie agregaty. Dla Au-NRs@PEG(5k), zarówno warstwy LS, jak i LB wykazywały podobne właściwości agregacyjne, niezależnie od wartości ciśnienia powierzchniowego wybranego do przenoszenia warstw, o czym świadczyło pojawienie się dodatkowego pasma w obszarze 630-650 nm oraz przesunięcie pasma LSPR powyżej 800 nm. Natomiast, dla Au-NRs@PEG(2k) – ciśnienie powierzchniowe, przy którym przenoszono warstwy Langmuira na podłoże kwarcowe, miało wpływ na tworzenie agregatów. Przy niskich ciśnieniach obserwowano główne pasmo LSPR przy 570 nm, które ulegało przesunięciu przy wyższych ciśnieniach

przenoszenia, co wskazywałoby na stopniowe ściskanie i reorganizację Au-NRs@PEG(2k) w agregatach. Dodatkową analizę przeprowadzono wykorzystując obrazy warstw Au-NRs@PEG uzyskane za pomocą mikroskopii konfokalnej i SEM **[Kotkowiak, L 2024, Fig. 4, 5, 6, S6]**. Warstwy Au-NRs@PEG(2k) i Au-NRs@PEG(5k) tworzyły gęsto upakowane aglomeraty, których pokrycie powierzchni rosło wraz z ciśnieniem depozycji warstwy. Ponadto, warstwy uzyskane za pomocą metody LS charakteryzowały się większym pokryciem powierzchni podłoża niż w przypadku warstw LB. Dla Au-NRs@PEG(10k) zaobserwowano natomiast współwystępowanie obszarów niezagregowanych (niewidocznych w mikroskopii konfokalnej) i agregatów o charakterze „piany", co można wytłumaczyć mniejszym stopniem upakowania wynikającym z konformacji polimeru w postaci „grzyba". Oznacza to, że konformacja łańcuchów PEG na powierzchni Au-NRs ma kluczowy wpływ na proces agregacji i organizację warstw podczas osadzania. Konformacja gęstego „pędzla" w przypadku Au-NRs@PEG(2k) sprzyjała ścisłemu upakowaniu, podczas gdy objętościowa konformacja „grzyba" sugerowana dla Au-NRs@PEG(10k), przy niskich ciśnieniach, skutecznie zapobiegała zbliżeniu się metalicznych rdzeni, umożliwiając tworzenie warstw niezagregowanych. Przeprowadzone badania dowiodły, że masa cząsteczkowa PEG stanowi precyzyjne narzędzie do sterowania procesem samoorganizacji NPs na każdym etapie, tj. od stabilizacji w roztworze, przez wpływ na właściwości termodynamiczne i morfologię warstw Langmuira, po ostateczną architekturę i właściwości optyczne warstwy na podłożu stałym.

Przedstawione dotychczas badania wykazały, że PEG(2k) stanowi optymalny ligand, pozwalający na tworzenie nanostruktur złota o wysokim stopniu upakowania w cienkich warstwach. Jednak dla zastosowań bioanalitycznych, kluczowe jest zrozumienie oddziaływań Au-NPs@PEG z błoną komórkową (ważnym elementem układów biologicznych), w wyniku których mogą zostać zmodyfikowane jej właściwości i struktura. W związku z tym, przeprowadzono badania wpływ Au-NPs@PEG(2k) o różnych kształtach (sferycznym i prętopodobnym) na modelowe błony lipidowe. Wyniki badań przedstawione w pracy **[Tim, JML 2025]** dotyczą sfunkcjonalizowanych polimerem PEG-SH, sferycznych (Au-NSs@PEG(2k)) oraz prętopodobnych (Au-NRs@PEG(2k)) nanocząstek złota oraz ich wpływu na właściwości biomimetycznych błon złożonych z fosfolipidów (DPPC, POPC) i/lub cholesterolu. Wykorzystane do badań NPs były całkowicie pokryte warstwą PEG-SH co oznacza,

że stężenie CTAB było znikome w zawiesinie i nie miało wpływu na dalsze analizy oraz interpretacje wyników. Potwierdziła to kompleksowa charakterystyka NPs, przeprowadzona na podstawie obrazów TEM, widm UV-vis oraz wyznaczonych potencjałów elektrokinetycznych i rozkładów wielkości cząstek techniką DLS. Dla Au-NSs obserwowano wąskie poprzeczne pasmo LSPR zlokalizowane przy długości fali 527 nm, o szerokości połówkowej 0,1228495 eV (990,856207 cm^{-1}) **[Tim, JML 2025, Fig. S1]**, co potwierdziło uzyskanie NSs o jednorodnej wielkości. W przypadku Au-NRs **[Tim, JML 2025, Fig. S1]**, pasmo poprzeczne przy 518 nm o szerokości połówkowej 0,1228495 eV (990,856207 cm^{-1}) i odpowiednio pasmo podłużne przy 667 nm - 0,1300067 eV (1048,583394 cm^{-1}), potwierdziły monodyspersyjność i wysoki stopień czystości przygotowanych NRs. Położenie obserwowanych dla Au-NRs dwóch pasm jest również zgodne z wcześniejszymi doniesieniami literaturowymi [56,57]. Na podstawie obrazów TEM **[Tim, JML 2025, Fig. 1]** określono wielkość badanych NPs przed procesem funkcjonalizacji i dla Au-NSs, ich średnica wynosiła (15,1 ± 2,2) nm, a średnie wymiary dla Au-NRs były równe (14,3 ± 1,7) nm (szerokość) i (59,8 ± 2,6) nm (długość). Dodatkowo, dla Au-NSs@PEG(2k) można było wyznaczyć z pomiarów DLS również średnicę hydrodynamiczną, której wartość wynosiła około 64 nm. Zwiększenie średnicy NSs, w porównaniu z wynikami otrzymanymi z obrazów TEM, jest konsekwencją przeprowadzonej funkcjonalizacji, w wyniku której łańcuchy PEG-SH zostały przyłączone do powierzchni Au poprzez wiązanie kowalencyjne Au–S. Poprawność przebiegu procesu funkcjonalizacji potwierdzono również na podstawie wyników pomiaru potencjału zeta. Dla Au-NSs, ich wartość zmieniła się z -0,53 mV do -27,9 mV, odpowiednio przed i po funkcjonalizacji PEGiem. Podczas gdy, dla Au-NRs i Au-NSs@PEG(2k) wartość potencjału zeta zmieniła się odpowiednio, z 12,9 mV na -20,1 mV. Zgodnie z danymi literaturowymi [58], ujemne wartości potencjału zeta świadczą o poprawności przeprowadzonej funkcjonalizacji oraz skutecznym pokryciu powierzchni NPs łańcuchami polimeru. Na podstawie przeprowadzonej analizy można stwierdzić, że Au-NPs wykorzystane do badań oddziaływań ze składnikami modelowych błon biologicznych charakteryzowały się dobrze zdefiniowanymi właściwościami fizykochemicznymi.

Wykorzystując technikę Langmuira wytworzono monowarstwy lipidowe składające się z DPPC, POPC, DPPC:Chol (9:1) oraz POPC:Chol (4:1) oraz mieszane z NPs

(Au-NSs@PEG(2k) lub Au-NRs@PEG(2k)). Dla warstw na granicy faz powietrze-woda zarejestrowano izotermy π-A, obliczono moduły ściśliwości (C_s^{-1}) **[Tim, JML 2025, Fig. 2 i Fig. S2]** i wyznaczono charakterystyczne parametry termodynamiczne **[Tim, JML 2025, Table S1-S3]** oraz zobrazowano ich powierzchnię za pomocą mikroskopii BAM **[Tim, JML 2025, Fig. 3 i Fig. S3]**.

Podczas analizy oddziaływań w modelowych błonach interesujący aspektem badań był wpływ cholesterolu (Chol). Jego obecność prowadziła do osiągnięcia punktu załamania warstwy mieszanej DPPC:Chol przy niższym ciśnieniu powierzchniowym niż w przypadku warstwy czystego DPPC **[Tim, JML 2025, Fig. 2a, b]**. Dla monowarstw składających się z molekuł POPC, które w swojej strukturze mają nienasycone wiązanie między atomami (9 a 10) węgla, obecność Chol w warstwie POPC przesunęła izotermę w kierunku wyższych wartości powierzchni wanny w porównaniu z krzywą czystej monowarstwy POPC **[Tim, JML 2025, Fig. 2c, d]**, co wskazuje na zmniejszoną kondensację monowarstwy. Dodatek Chol do monowarstw fosfolipidowych spowodował wzrost wartości maksymalnej wartości C_s^{-1}, a w konsekwencji zmniejszenie elastyczności warstwy na powierzchni subfazy, co jest zgodne z doniesieniami literaturowymi [59,60].

Innym zagadnieniem rozpatrywanym w pracy **[Tim, JML 2025]** było określenie, jak obecność Au-NPs o różnym kształcie wpływa na właściwości (stabilność, strukturę) monowarstw lipidowych oraz w jaki sposób te nanostruktury mogą wbudowywać się w warstwy biologiczne. Okazało się, że obecność sfunkcjonalizowanych PEGiem Au-NSs i Au-NRs w monowarstwach fosfolipidowych znacząco modyfikuje ich właściwości termodynamiczne **[Tim, JML 2025, Fig. 2a]**. W monowarstwach DPPC dodatek NPs powoduje przesunięcie charakterystycznego przejścia fazowego w kierunku wyższych wartości ciśnienia powierzchniowego oraz modyfikuje wartość maksymalną C_s^{-1} **[Tim, JML 2025, Fig. 2a**, **insert]**. Uzyskane wyniki wskazują na zwiększoną elastyczność monowarstwy, co jest prawdopodobnie skutkiem zaburzenia upakowania molekuł lipidów przez NPs.

W przypadku monowarstw POPC, obecność Au-NSs@PEG i Au-NRs@PEG również obniża maksymalną wartość C_s^{-1} **[Tim, JML 2025, Fig. 2c**, **insert]**. Kluczową różnicą w porównaniu z DPPC jest jednak wyraźny wzrost ciśnienia powierzchniowego, przy którym dochodzi do załamania warstwy, co świadczy o jej zwiększonej stabilności. W układach zawierających Chol zaobserwowano dalsze modyfikacje oddziaływań,

na przykład w mieszaninie DPPC:Chol (9:1) obecność NPs prowadziła do zaniku przejścia fazowego, natomiast w układach z POPC:Chol (4:1) Au-NRs zwiększały elastyczność warstwy w większym stopniu niż NSs **[Tim, JML 2025, Fig. 2b, d]**. Sugeruje to, że Chol odgrywa kluczową rolę w upakowaniu i stabilizacji mieszanych monowarstw z udziałem NPs, prawdopodobnie dzięki tworzeniu uporządkowanych struktur stabilizowanych oddziaływaniami van der Waalsa.

Przeprowadzone badania pokazały także zmianę wartości potencjału zeta z dodatnich (dla czystych lipidów) na ujemne w obecności Au-NSs@PEG(2k), co bezpośrednio potwierdza występowanie oddziaływań elektrostatycznych pomiędzy NPs@PEG a lipidami. Analiza obrazów TEM **[Tim, JML 2025, Fig. S4]** ujawniła tendencję Au-NSs@PEG(2k) do nierównomiernej dystrybucji i tworzenia agregatów w obrębie warstwy lipidowej. Podczas, gdy obrazowanie techniką BAM **[Tim, JML 2025, Fig. 3]** potwierdziło, że kompresja monowarstw mieszanych (NPs@PEG/lipidy) prowadzi do powstawania struktur niejednorodnych, przy czym Chol powoduje tworzenie się mikroskopowych obszarów o większym zagęszczeniu lipidów, które mogą funkcjonować jako preferencyjne miejsca adsorpcji NPs.

Zarejestrowane kinetyki relaksacji monowarstw **[Tim, JML 2025, Fig. 4]** oraz widma odbiciowo-absorpcyjnej spektroskopii w podczerwieni z modulacją polaryzacji (PM-IRRAS) **[Tim, JML 2025, Fig. 5]** dostarczyły informacji o stabilności czasowej i zmianach konformacyjnych w obszarze polarnych grup lipidów. Wprowadzenie NPs do monowarstwy wpływało na jej stabilność, przy czym Au-NSs@PEG(2k) generalnie powodowały mniejsze zaburzenia stabilności niż Au-NRs@PEG(2k). Analiza widm PM-IRRAS wskazała na odmienny mechanizm oddziaływań NPs w lipidowych warstwach, w zależności od kształtu NPs oraz od typu lipidu. Kształt NPs wpływał na różny stopień hydratacji grup fosforanowych lipidów. Dla DPPC **[Tim, JML 2025, Fig. 5a]** zaobserwowano zmniejszone (w stosunku do POPC) oddziaływanie NPs z grupami polarnymi lipidu, co sugeruje, że znaczna ich frakcja pozostaje na powierzchni warstwy. W przypadku monowarstw POPC **[Tim, JML 2025, Fig. 5c]** odnotowano natomiast silniejsze oddziaływanie, prowadzące do zmian konformacyjnych, co przemawia za efektywniejszym wbudowaniem NPs w strukturę warstwy lipidowej.

Przeprowadzone badania jednoznacznie wykazały, że kształt Au-NPs oraz skład lipidowy monowarstwy są kluczowymi czynnikami determinującymi ich wzajemne oddziaływania. Obecność Au-NSs@PEG(2k) i Au-NRs@PEG(2k) w różny sposób

wpływa na elastyczność, stabilność i organizację modelowych błon komórkowych, a cholesterol dodatkowo powoduje znaczącą modyfikację warstw wpływając na jej oddziaływanie z NPs. Uzyskane wyniki pozwalają na zaproponowanie modelu, w którym NPs mogą zarówno adsorbować na powierzchni, jak i wbudowywać się w głąb lipidowej monowarstwy, w zależności od składników biomimetycznej błony i anizotropii kształtu Au-NPs.

IV Podsumowanie

W rozprawie doktorskiej zaprezentowano wyniki badań dotyczące oddziaływań pomiędzy funkcjonalizowanymi (za pomocą DDT lub PEG-SH) Au-NPs o różnych kształtach (sferycznych, prętopodobnych) w warstwach wytwarzanych na granicy faz powietrze-woda i powietrze-ciało stałe, jak również Au-NPs w warstwach na podłożu stałym z p-MBA i/lub R6G lub z lipidami (DPPC, POPC i/lub cholesterolu) na subfazie wodnej. Szczególnie istotne było określenie wpływu kształtu i/lub funkcjonalizacji Au-NPs na właściwości i organizację cienkich warstw oraz modelowych błon biologicznych. Uzyskane wyniki pozwoliły ocenić potencjał aplikacyjny badanych NPs złota jako funkcjonalnych podłoży w diagnostyce biomedycznej (w szczególności technice SERS) oraz wpływ nieorganicznych nanostruktur na strukturę biomimetycznych membran.

Na podstawie przeprowadzonych badań:

- pokazano, że funkcjonalizacja Au-NPs oraz ich kształt determinują właściwości termodynamiczne, morfologię oraz stabilność warstw Langmuira na granicy faz powietrze-woda (Au-NSs@DDT i Au-NRs@PEG(2k) podczas kompresji nie agregowały w warstwach, a stabilność tworzonych warstw malała wraz ze wzrostem ciśnienia powierzchniowego; warstwy Au-NRs@PEG(2k) charakteryzowały się większą jednorodnością niż warstwy Au-NSs@DDT i pomimo różnic w procesie formowania warstw, znajdowały się one w stanie ciekłym rozprężonym), poszerzając wiedzę z zakresu samoorganizacji nanomateriałów na powierzchniach międzyfazowych,
- wykazano, że w warstwach Au-NSs@DDT przeniesionych na podłoże stałe (powyżej ciśnienia powierzchniowego 9 $mN \cdot m^{-1}$) tworzone są domeny o wysokiej lokalnej koncentracji NPs, a odległości pomiędzy nimi są optymalne dla uzyskania silnego sprzężenia plazmonowego, co stwarza możliwość zastosowania techniki Langmuira do zaprojektowania i uzyskania warstw, które mogą być podłożami wzmacniającymi sygnał rejestrowany z wykorzystaniem spektroskopii Ramana,
- zidentyfikowano optymalną wartość ciśnienia powierzchniowego (12 $mN \cdot m^{-1}$) do przenoszenia warstwy Au-NRs@PEG(2k) na podłoże stałe, pozwalającą uzyskać zarówno dobre pokrycie powierzchni i obecność struktur dendrytycznych

z obszarami lokalnego wzmocnienia pola elektromagnetycznego, mającymi potencjał aplikacyjny do ultraczułej detekcji analitów,

- znaleziono związek pomiędzy masą cząsteczkową polimeru (PEG-SH) wykorzystywanego do funkcjonalizacji, a stanem fizycznym, morfologią i zdolnością do agregacji NRs w warstwach na subfazie oraz na podłożu stałym, który określa możliwość uzyskiwania warstw NPs@PEG o większym stopniu upakowania, w przypadku krótszych łańcuchów polimeru (PEG(2k)), lub niezagregowanych - dla dłuższych łańcuchów (PEG(10k)) oraz stwierdzono, że do utworzenia warstw Au-NRs@PEG(5k) i Au-NRs@PEG(10k) na granicy faz powietrze-woda konieczne jest użycie dodatkowego stabilizatora (CTAB),
- zaobserwowano, że kształt Au-NPs, sfunkcjonalizowanych PEG(2k), ma wpływ na strukturę modelowych błon biologicznych, przy czym Au-NRs w większym stopniu niż Au-NSs zaburzają elastyczność i stabilność warstw lipidowych na granicy faz woda-powietrze, co prawdopodobnie wynika z anizotropii kształtu,
- wnioskowano, że obecność cholesterolu sprzyja tworzeniu gęściej upakowanych i bardziej uporządkowanych monowarstw z NPs, a Au-NPs@PEG(2k) oddziałując z lipidami mogą zarówno adsorbować na powierzchni lub częściowo wbudowywać się w warstwę lipidową, przy czym warstwy POPC umożliwiają większy stopień wbudowania, podczas gdy dla DPPC dominująca wydaje się adsorpcja NPs na powierzchni warstwy.

Podsumowując, opisane w niniejszej rozprawie doktorskiej wyniki pozwoliły na scharakteryzowanie sposobu organizacji Au-NPs w warstwach Langmuira i Langmuira-Blodgett (lub Schaefera), wskazując na istotny wpływ ich kształtu i funkcjonalizacji na termodynamiczne właściwości i morfologię warstw oraz upakowanie i agregację NPs. Ustalono również warunki formowania warstw o określonych organizacji (upakowaniu) i właściwościach agregacyjnych Au-NPs, umożliwiających oddziaływanie ze związkami organicznymi tj. p-MBA i/lub R6G i wzmocnienie intensywności sygnału SERS. Pokazano, że kształt Au-NPs oraz skład monowarstw lipidowych wpływają na oddziaływanie sfunkcjonalizowanych polimerem Au-NPs z modelowymi błonami lipidowymi i na ich strukturę.

Przeprowadzone badania dostarczyły nowych informacji o właściwościach warstw Au-NPs wytwarzanych zarówno na granicy faz powietrze-woda i powietrze-ciało stałe oraz potencjalnych możliwości zastosowania wytworzonych podłoży do analiz

biomedycznych. Ponadto, pokazano możliwość wbudowywania się (lub adsorpcji) Au-NPs w modelowe błony biologiczne, co może być istotne przy projektowaniu nowoczesnych fototerapii z wykorzystaniem nanostruktur. Uzyskane wyniki wskazują na znaczenie precyzyjnego projektowania NPs złota oraz świadomego doboru ich funkcjonalizacji, stanowiąc podstawę do dalszych badań nad rozwojem innowacyjnych bionanomateriałów o potencjale aplikacyjnym.

Literatura

[1] R.P. Feynman, There's plenty of room at the bottom, Eng Sci. 23 (1960) 22–36.

[2] K.E Drexler, Nanosystems: Molecular machinery, manufacturing, and computation, ISBN: 978-0-471-57518-4, John Wiley & Sons, Inc., 1998.

[3] B. Mekuye, B. Abera, Nanomaterials: An overview of synthesis, classification, characterization, and applications, Nano Sel. 4 (2023) 486–501.

[4] J. Damodharan, Nanomaterials in medicine - An overview, Mater Today Proc. 37 (2020) 383–385.

[5] M. Roy, A. Roy, S. Rustagi, N. Pandey, An overview of nanomaterial applications in pharmacology, Biomed Res Int. 2023 (2023) 4838043.

[6] G. Fytianos, A. Rahdar, G.Z. Kyzas, Nanomaterials in cosmetics: Recent updates, Nanomater. 10 (2020) 1–16.

[7] J. Hu, M. Dong, Recent advances in two-dimensional nanomaterials for sustainable wearable electronic devices, J Nanobiotechnol. 22 (2024) 1–20.

[8] R. Thiruvengadathan, A. Wang, Nanoenergetic materials: From materials to applications, Nanomater. 14 (2024) 11–15.

[9] T. Utsev, T.M. Tiza, O. Mogbo, S. Kumar Singh, A. Chakravarti, N. Shaik, S. Pal Singh, Application of nanomaterials in civil engineering, Mater Today Proc. 62 (2022) 5140–5146.

[10] L. Bai, X. Liu, M. Li, K. Guo, M. Luoshan, Y. Zhu, R. Jiang, L. Liao, X. Zhao, Plasmonic enhancement of the performance of dye-sensitized solar cells by incorporating hierarchical TiO_2 spheres decorated with Au nanoparticles, Electrochim Acta. 190 (2016) 605–611.

[11] J.L. Li, M. Gu, Gold-nanoparticle-enhanced cancer photothermal therapy, IEEE J Sel Top Quantum Electron. 16 (2010) 989–996.

[12] C. Carrillo-Carrión, R. Martínez, M.F. Navarro Poupard, B. Pelaz, E. Polo, A. Arenas-Vivo, A. Olgiati, P. Taboada, M.G. Soliman, Ú. Catalán, S. Fernández-Castillejo, R. Solà, W.J. Parak, P. Horcajada, R.A. Alvarez-Puebla, P. del Pino, Aqueous stable gold nanostar/ZIF-8 nanocomposites for light-triggered release of active cargo iInside living cells, Angew Chem Int Ed. 58 (2019) 7078–7082.

[13] B. Pelaz, V. Grazu, A. Ibarra, C. Magen, P. Del Pino, J.M. De La Fuente, Tailoring the synthesis and heating ability of gold nanoprisms for bioapplications, Langmuir. 28 (2012) 8965–8970.

[14] B. Tim, P. Błaszkiewicz, M. Kotkowiak, Recent advances in metallic nanoparticle assemblies for surface-enhanced spectroscopy, Int J Mol Sci. 23 (2022) 291.

[15] R.S. Riley, E.S. Day, Gold nanoparticle-mediated photothermal therapy: applications and opportunities for multimodal cancer treatment, Wiley Interdiscip Rev Nanomed Nanobiotechnol. 9 (2017) 1–16.

[16] W. Li, Z. Cao, R. Liu, L. Liu, H. Li, X. Li, Y. Chen, C. Lu, Y. Liu, AuNPs as an important inorganic nanoparticle applied in drug carrier systems, Artif Cells Nanomed Biotechnol. 47 (2019) 4222–4233.

[17] M.M. Poojary, P. Passamonti, A.V. Adhikari, Green synthesis of silver and gold nanoparticles using root bark extract of Mammea suriga: characterization, process optimization, and their antibacterial activity, BioNanoSci. 6 (2016) 110–120.

[18] A. Elbagory, M. Meyer, C. Cupido, A.A. Hussein, Inhibition of bacteria associated with wound infection by biocompatible green synthesized gold nanoparticles from South African plant extracts, Nanomaterials. 7 (2017) 417.

[19] T.S. Hauck, T.L. Jennings, T. Yatsenko, J.C. Kumaradas, W.C.W. Chan, Enhancing the toxicity of cancer chemotherapeutics with gold nanorod hyperthermia, Adv Mater. 20 (2008) 3832–3838.

[20] C. Liang, J.Y. Cheong, G. Sitaru, S. Rosenfeldt, A.S. Schenk, S. Gekle, I.D. Kim, A. Greiner, Size-dependent catalytic behavior of gold nanoparticles, Adv Mater Interfaces. 9 (2022) 2100867.

[21] D.N. Wang, H. Stieglitz, J. Marden, L.K. Tamm, Benjamin Franklin, Philadelphia's favorite son, was a membrane biophysicist, Biophys J. 104 (2013) 287–291.

[22] A. Pockels, Surface tension, Nature 43 (1891) 437-439.

[23] I. Langmuir, The constitution and fundamental properties of solids and liquids. II. Liquids, J Am Chem Soc. 39 (1917) 1787–2094.

[24] M. Swierczewski, T. Bürgi, Langmuir and Langmuir-Blodgett films of gold and silver nanoparticles, Langmuir. 39 (2023) 2135-2151.

[25] G. Corucci, P. Sánchez-Puga, K.C. Batchu, N. Paracini, S. Micciulla, V. Laux, J. Carrascosa-Tejedor, M.P.K. Frewein, Y. Yamaryo-Botté, C. Botté, G. Fragneto, A. Luchini, Hydrogenous and deuterated phospholipid extracts from Escherichia coli as biomimetic cytoplasmic bacterial membranes, Chem Phys Lipids. 271 (2025) 105515.

[26] M. Rojewska, B. Tim, K. Prochaska, Interactions between silica particles and

model phospholipid monolayers, J Mol Liq. 345 (2022) 116999–117009.

[27] B. Tim, M. Rojewska, K. Prochaska, Effect of silica microparticles on interactions in mono- and multicomponent membranes, Int J Mol Sci. 23 (2022) 12822.

[28] E. Guzmán, L. Liggieri, E. Santini, M. Ferrari, F. Ravera, Influence of silica nanoparticles on phase behavior and structural properties of DPPC-Palmitic acid Langmuir monolayers, Colloids Surf A: Physicochem Eng Asp. 413 (2012) 280–287.

[29] R.C. Van Lehn, P.U. Atukorale, R.P. Carney, Y.S. Yang, F. Stellacci, D.J. Irvine, A. Alexander-Katz, Effect of particle diameter and surface composition on the spontaneous fusion of monolayer-protected gold nanoparticles with lipid bilayers, Nano Lett. 13 (2013) 4060–4067.

[30] M. Elderdfi, A.F. Sikorski, Langmuir-monolayer methodologies for characterizing protein-lipid interactions, Chem Phys Lipids. 212 (2018) 61–72.

[31] J.H. Borrell, Ò. Domènech, Critical temperature of 1-palmitoyl-2-oleoyl-sn-glycero-3-phosphoethanolamine monolayers and its possible biological relevance, J Phys Chem. B. 121 (2017) 6882–6889.

[32] C. Yuan, J. Furlong, P. Burgos, L.J. Johnston, The size of lipid rafts: An atomic force microscopy study of ganglioside GM1 domains in sphingomyelin/DOPC/cholesterol membranes, Biophys J. 82 (2002) 2526–2535.

[33] D.B. Pistonesi, M.D. Fernández-Leyes, H. Ritacco, P.S. Rivero, M.G. Sica, L.A. Benedini, M.E. Centurión, P. V. Messina, Lipid membrane-selective interactions driven by nanosilver anisotropy: Insights from prokaryotic and erythrocyte models, Langmuir. 41 (2025) 21509–21524.

[34] M. Eeman, M. Deleu, From biological membranes to biomimetic model membranes, Biotechnol Agron Soc Environ. 14 (2010) 719–736.

[35] R. Rachana, R. Banerjee, Effects of albumin and erythrocyte membranes on spread monolayers of lung surfactant lipids, Colloids Surf B: Biointerfaces. 50 (2006) 9–17.

[36] W.A.A. Sudjarwo, J.L. Toca-Herrera, Surface rheological properties and microstructures of DPPC/POPC monolayers, Langmuir. 41 (2025) 16128–16138.

[37] G. Luque-Caballero, J. Maldonado-Valderrama, M. Quesada-Pérez, A. Martín-Molina, Interaction of DNA with likely-charged lipid monolayers: An experimental study, Colloids Surf B: Biointerfaces. 178 (2019) 170–176.

[38] M. Pedrosa, A. Moncho-Jordá, M.J. Gálvez-Ruiz, M. Kanduč, Impact of cholesterol on the structure and phase separation of DPPC Langmuir monolayers: Experiments and simulations, Surfaces and Interfaces. 51 (2024) 104757.

[39] I. Hammami, N.M. Alabdallah, A. Al jomaa, M. kamoun, Gold nanoparticles: Synthesis properties and applications, J King Saud Univ - Sci. 33 (2021) 101560.

[40] W.C. Ko, S.J. Wang, C.Y. Hsiao, C.T. Hung, Y.J. Hsu, D.C. Chang, C.F. Hung, Pharmacological role of functionalized gold nanoparticles in disease applications, Molecules. 27 (2022) 1–12.

[41] N. Sarfraz, I. Khan, Plasmonic gold nanoparticles (AuNPs): Properties, synthesis and their advanced energy, environmental and biomedical applications, Chem - An Asian J. 16 (2021) 720–742.

[42] O. Maťátková, J. Michailidu, A. Miškovská, I. Kolouchová, J. Masák, A. Čejková, Antimicrobial properties and applications of metal nanoparticles biosynthesized by green methods, Biotechnol Adv. 58 (2022) 107905.

[43] B. Tim, E. Konował, A. Modrzejewska-Sikorska, Starch sodium octenylsuccinate as a new type of stabilizer in the synthesis of catalytically active gold nanostructures, Int J Mol Sci. 25 (2024) 5116.

[44] M. Li, S.K. Cushing, N. Wu, Plasmon-enhanced optical sensors: A review, Analyst. 140 (2015) 386–406.

[45] K.A. Willets, R.P. Van Duyne, Localized surface plasmon resonance spectroscopy and sensing, Annu. Rev. Phys. Chem. 58 (2007) 267–297.

[46] F. Schulz, W. Friedrich, K. Hoppe, T. Vossmeyer, H. Weller, H. Lange, Effective PEGylation of gold nanorods, Nanoscale. 8 (2016) 7296–7308.

[47] V. Bouzas, T. Haller, N. Hobi, E. Felder, I. Pastoriza-Santos, J. Pérez-Gil, Nontoxic impact of PEG-coated gold nanospheres on functional pulmonary surfactant-secreting alveolar type II cells, Nanotoxicology. 8 (2014) 813–823.

[48] P. Błaszkiewicz, M. Kotkowiak, A. Dudkowiak, Fluorescence quenching and energy transfer in a system of hybrid laser dye and functionalized gold nanoparticles, J Lumin. 183 (2017) 303–310.

[49] P. Błaszkiewicz, M. Kotkowiak, E. Coy, A. Dudkowiak, Tailoring fluorescence and singlet oxygen generation of a chlorophyll derivative and gold nanorods via a silica shell, J Phys Chem C. 124 (2020) 2088–2095.

[50] M.S. Pavan, S. Sarkar, T.N.G. Row, Exploring the rare S - H...S hydrogen bond

using charge density analysis in isomers of mercaptobenzoic acid, Acta Crystallogr B Struct Sci Cryst Eng Mater. 73 (2017) 626–633.

[51] M.F.H. Al-Kadhemy, A.A.D. Al-Zuky, H.F. Daear, Theoretical model for the effect of temperature on the fluorescence spectrum of laser dye (Rh6G) in acetone, Int Lett Chem Phys Astron. 38 (2014) 151–159.

[52] R. Panajotović, S. Ptasinska, V. Lyamayev, K. Prince, Low-energy electron damage of DPPC molecules - A NEXAFS study, Rad Applic. 1 (2016) 46–50.

[53] C. Grauby-Heywang, F. Moroté, M. Mathelié-Guinlet, I. Gammoudi, N.R. Faye, T. Cohen-Bouhacina, Influence of oxidized lipids on palmitoyl-oleoyl-phosphatidylcholine organization, contribution of Langmuir monolayers and Langmuir-Blodgett films, Chem Phys Lipids. 200 (2016) 74–82.

[54] L. Zhang, C. Hao, G. Xu, R. Sun, Effects of concentration and surface pressure on MBP interaction with cholesterol in langmuir films, Scanning. 2017 (2017) 1542156.

[55] J.T. Davies, E.K. Rideal, Interfacial phenomena, ISBN:0-12-206056-3, Academic Press, New York 1963.

[56] D. Aguilar-Ferrer, T. Vasileiadis, I. Iatsunskyi, M. Ziółek, K. Żebrowska, O. Ivashchenko, P. Błaszkiewicz, B. Grześkowiak, R. Pazos, S. Moya, M. Bechelany, E. Coy, Understanding the photothermal and photocatalytic mechanism of polydopamine coated gold nanorods, Adv Funct Mater. 33 (2023) 2304208.

[57] A. Gole, C.J. Murphy, Seed-mediated synthesis of gold nanorods: role of the size and nature of the seed, Chem Mater. 16 (2004) 3633–3640.

[58] R. Marasini, A. Pitchaimani, T. Nguyen, J. Comer, Santosh;, Influence of polyethylene glycol passivation on the surface plasmon resonance induced photothermal properties of gold nanorods, Nanoscale. 10 (2018) 13684–13693.

[59] K. Dopierała, M. Skrzypiec, Morphology, compressibility and viscoelasticity of the mixed lipid monolayers in the presence of β-carotene, Chem Phys Lipids. 213 (2018) 88–95.

[60] K. Sabatini, J.P. Mattila, P.K.J. Kinnunen, Interfacial behavior of cholesterol, ergosterol, and lanosterol in mixtures with DPPC and DMPC, Biophys J. 95 (2008) 2340–2355.

Dorobek naukowy doktorantki

Publikacje naukowe (IF – *Impact Factor*, pkt MNiSW – punkty na podstawie wykazu czasopism i wydawnictw zgodnie z bazą SIN PP):

1. **B. Tim**, P. Błaszkiewicz, M. Kotkowiak, *Recent advances in metallic nanoparticle assemblies for surface-enhanced spectroscopy*, International Journal of Molecular Sciences, 2022, 23(1), 291-1-291-24. (IF=5,6; pkt MNiSW=140)
2. **B. Tim**, P. Błaszkiewicz, A.B. Nowicka, M. Kotkowiak, *Optimizing SERS performance through aggregation of gold nanorods in Langmuir-Blodgett films*, Applied Surface Science, 2022, 573, 151518-1-121218-22. (IF=6,7; pkt MNiSW=140) **[Tim, ASS 2022]**
3. **B. Tim**, P. Błaszkiewicz, M. Kotkowiak, *Altering model cell membranes by means of photoactivated organic functionalized gold nanorods*, Journal of Molecular Liquids, 2022, 349, 118179-1-118179-7. (IF=6,0; pkt MNiSW=100)
4. M. Rojewska, **B. Tim**, K. Prochaska, *Interactions between silica particles and model phospholipid monolayers*, Journal of Molecular Liquids, 2022, 345, 116999-1-116999-10. (IF=6,0; pkt MNiSW=100)
5. **B. Tim**, M. Rojewska, K. Prochaska, *Effect of Silica Microparticles on interactions in mono- and multicomponent membranes*, International Journal of Molecular Sciences, 2022, 23, 12822-1-12822-16 (IF=5,6; pkt MNiSW=140)
6. **B. Tim**, M. Kotkowiak, N. Kowalska, A.B. Nowicka, W. Lewandowski, *Influence of gold nanoparticle assembly in Langmuir-Schaefer monolayers on the surface-enhanced spectroscopy response of a nanoplatform*, International Journal of Physical Chemistry C, 2023, 127, 15978-15987 (IF=3,3; pkt MNiSW=140) **[Tim, JPCC 2023]**
7. M. Kotkowiak, **B. Tim**, M. Kotkowiak, J. Musiał, P. Błaszkiewicz, *The role of the polyethylene glycol in the organization of gold nanorods at the air-water and air–solid interfaces*, Langmuir, 2024, 40, 14561-1-14569-9 (IF=3,9; pkt MNiSW=100) **[Kotkowiak, L 2024]**
8. **B. Tim**, E. Konował, A. Modrzejewska-Sikorska, *Starch sodium octenylsuccinate as a new type of stabilizer in the synthesis of catalytically active*

gold nanostructures, International Journal of Molecular Sciences, 2024, 25, 5116-1-5116-12 (IF=4,9; pkt MNiSW=140)

9. **B. Tim**, P. Błaszkiewicz, E. Coy, A. Dudkowiak, *Interactions between functionalized PEGylated gold nanoparticles and model biological membranes,* Journal of Molecular Liquid, 2025, 428, 127501-1-127501-12 (IF=5,2; pkt MNiSW=100) **[Tim, JML 2025]**

Udział w projektach badawczych (tytuł i numer projektu, źródło finansowania, lata i miejsce realizacji):

Kierownik

Fotoaktywowane nanocząstki złota jako obiecujące środki w terapii fototermicznej – badania in vitro w biomimetycznych układach błonowych, 2022/45/N/ST5/01464**,** PRELUDIUM, Narodowe Centrum Nauki, Wydział Inżynierii Materiałowej i Fizyki Technicznej, Politechnika Poznańska, 17.01.2023-16.01.2027, wysokość finansowania: 209 960 PLN.

Wykonawca

Optymalizacja struktury nanoplatformy do powierzchniowo wzmocnionej detekcji pochodnych chlorofilu z wykorzystaniem techniki Langmuira, 2019/35/D/ST4/02037, SONATA, Narodowe Centrum Nauki, Wydział Inżynierii Materiałowej i Fizyki Technicznej, Politechnika Poznańska, 10.2020-10.2023, wysokość finansowania: 965.760 PLN, kierujący pracą – dr inż. Michał Kotkowiak.

Staż naukowy:

09.2023-10.2023 – Zakład Chemii Środowiska, Wydział Chemii, Uniwersytet Jagielloński, Kraków (2 miesiące)

Nagrody i wyróżnienia:

03.2017-06.20217 – Stypendium Rektora Politechniki Poznańskiej dla najlepszych studentów

10.2017-02.2018 – Stypendium Rektora Politechniki Poznańskiej dla najlepszych studentów

03.2019-06.2019 – Stypendium Rektora Politechniki Poznańskiej dla najlepszych studentów

10.2019-02.2020 – Stypendium Rektora Politechniki Poznańskiej dla najlepszych studentów

03.2020-06.2020 – Stypendium Rektora Politechniki Poznańskiej dla najlepszych studentów

2022-2023 – Stypendium naukowe z Własnego Funduszu Stypendialnego Politechniki Poznańskiej dla 10% najlepszych doktorantów Szkoły Doktorskiej

2023-2024 – Stypendium naukowe z Własnego Funduszu Stypendialnego Politechniki Poznańskiej dla 10% najlepszych doktorantów Szkoły Doktorskiej

06.2025 – Wyróżnienie w konkursie na najlepszy plakat zaprezentowany na VII Interdyscyplinarnej Konferencji Nano(&)BioMateriały – od teorii do aplikacji

Szkolenia:

11.2023 – *Establishing contacts, and self-presentation of researchers* w ramach projektu STER „Towards Internationalization of Poznan University of Technology Doctoral School (INPUTDoc)" współfinansowanego przez NAWA

10.2024 – *Jak być mądrzejszym od AI? – narzędzia dla doktorantów* w ramach „PhDay – Dzień Doktoranta PP vol. 2"

10.2024 – *Skuteczne kierowanie zespołem* w ramach „PhDay – Dzień Doktoranta PP vol. 2"

10.2025 – *Design thinking: increasing creativity and teamwork* w ramach „PhDay – Dzień Doktoranta PP vol. 3"

10.2025 – *Securing grants & founding: a young scientist's guide to success PhD Students' union at the university, local and national levels* w ramach „PhDay – Dzień Doktoranta PP vol. 3"

Udział w konferencjach naukowych:

- **wystąpienia prezentowane osobiście**
  - **komunikaty ustne**

B. Tim, P. Błaszkiewicz, A. Dudkowiak, *Wpływ fotoaktywacji nanoprętów złota na błony biomimetyczne*, I Ogólnopolska Konferencja Naukowa PUTChemikon, Poznań, 05.2023

  - **plakaty**

B. Tim, M. Rojewska, K. Prochaska, *Badanie wpływu smogu na właściwości transportowe błony komórkowej organizmów żywych,* BioOrg 2019 – III Ogólnopolskie Sympozjum Chemii Bioorganicznej, Organicznej i Biomateriałów, Poznań, 12.2019

B. Tim, P. Błaszkiewicz, A.B. Nowicka, M. Kotkowiak, *Optymalizacja nanoplatformy SERS w wyniku agregacji złotych nanoprętów w warstwach Langmuira-Blodgett*, XXII Konferencja Kryształy Molekularne, Kroczyce, 09.2022

B. Tim, M. Kotkowiak, *Wpływ fotoaktywacji nanoprętów złota na organizację lipidów w modelowych błonach komórkowych*, BioOrg 2022 – IV Ogólnopolskie Sympozjum Chemii Bioorganicznej, Organicznej i Biomateriałów, Poznań, 12.2022

B. Tim, P. Błaszkiewicz, A. Dudkowiak, *Funkcjonalizowane nanopręty złota jako obiecujące środki w terapii fototermicznej – badania in vitro w biomimetycznych układach błonowych,* II Ogólnopolska Konferencja Naukowa PUTChemikon, Poznań, 05.2024

B. Tim, P. Błaszkiewicz, A. Dudkowiak, *Effect of functionalized gold nanoparticles on biological membranes in biomimetic systems*, NanoTech Poland 14th International Conference, Poznań, 06.2024

B. Tim, P. Błaszkiewicz, A. Dudkowiak, *Badanie oddziaływań funkcjonalizowanych nanocząstek złota na błony biologiczne w układach biomimetycznych*, VI Interdyscyplinarna Konferencja Nano(&)BioMateriały – od teorii do aplikacji, Toruń, 06.2024

B. Tim, E. Konował, A. Modrzejewska-Sikorska, *Oktenylobursztynian sodowy skrobi jako nowy rodzaj stabilizatora w syntezie katalitycznie aktywnych nanocząstek złota*, XI Kongres Technologii Chemicznej, Poznań, 09.2024

B. Tim, P. Błaszkiewicz, A. Dudkowiak, *Wpływ funkcjonalizowanych nanocząstek złota na organizację lipidów w wieloskładnikowych modelowych błonach biologicznych,* 66. Zjazd Polskiego Towarzystwa Chemicznego, Poznań, 09.2024

B. Tim, P. Błaszkiewicz, A. Dudkowiak, *Badanie wpływu nanocząstek złota na właściwości transportowe błon komórkowych organizmów żywych,* XXIII Konferencja Kryształy Molekularne, Poznań – Dymaczewo Nowe, 09.2024

B. Tim, P. Błaszkiewicz, A. Dudkowiak, *Effect of Cholesterol on Interactions in Mono- and Multicomponent Membranes,* I International Conference PUT STEM Day, Poznań, 01.2025

B. Tim, E. Konował, A. Modrzejewska-Sikorska, *Sodium starch octenylsuccinate as a new type of stabilizer in the synthesis of catalytically active gold nanoparticles,* 10th edition of the World Conference on Gold 2025, San Sebastian (Hiszpania), 05.2025

B. Tim, P. Błaszkiewicz, F. Giemza, W. Lewandowski, K. Załęski, A. Dudkowiak, E. Coy, *Hybrydowe złote nanocząsteczki z fotosensybilizatorem pierwszej generacji: oddziaływania z modelowymi błonami biologicznymi,* VII Interdyscyplinarna Konferencja Nano(&)BioMateriały – od teorii do aplikacji, Toruń, 06.2025

– **wystąpienia prezentowane przez współautorów**

E. Konował, A. Modrzejewska-Sikorska, **B. Tim**, G. Milczarek, *Nanostruktury złota stabilizowane solą sodową oktenylobursztynianu skrobiowego*, X Poznańska Konferencja Naukowa „Chemia - nauka i przemysł", Poznań, 12.2018

P. Koza, M. Stachowiak, J. Dlugaszewska, **B. Tim**, D. Młynarczyk, A. Dudkowiak, T. Gośliński, *Selected tribenzoporphyrazines and their liposomal formulations - photocytotoxicity study against bacteria,* 23rd International Congress of Young Medical Scientists, Poznań, 05.2023

P. Błaszkiewicz, F. Giemza, **B. Tim**, K. Kędzierski, D. Ziental, W. Lewandowski, A. Dudkowiak, E. Coy, *Hybrid gold nanoparticles with modulation of photophysical parameters as an effective platform*

for photodynamic therapy against bacteria, NanoTech Poland 14th International Conference, Poznań, 06.2024

P. Błaszkiewicz, F. Giemza, **B. Tim**, D. Ziental, W. Lewandowski, A. Dudkowiak, E. Coy, *Hybrid nanocomposites as an effective platform for combined photothermal/photodynamic therapy,* International Conference on Organic and Nanohybrid Functional Materials, Gdańsk, 06.2024

P. Błaszkiewicz, F. Giemza, **B. Tim**, W. Lewandowski, E. Coy, *Hybrid nanostructures based on gold nanoparticles as promising photoactive materials for combined therapy,* 10th edition of the World Conference on Gold 2025, San Sebastian (Hiszpania), 05.2025

Oświadczenia współautorów publikacji naukowych

Poznań, dnia 10.12.2025

prof. dr hab. Alina Dudkowiak
Wydział Inżynierii Materiałowej
i Fizyki Technicznej
Politechnika Poznańska

Oświadczenie

Oświadczam, że w niniejszej publikacji:

Beata Tim, Paulina Błaszkiewicz, Emerson Coy, Alina Dudkowiak, *Interactions between functionalized PEGylated gold nanoparticles and model biological membranes,* Journal of Molecular Liquids 428 (2025), 127501-1 - 127501-12

mój udział polegał na opracowaniu i redakcji tekstu (Writing – review & editing) oraz sprawowaniu nadzoru merytorycznego (Supervision).

Wyrażam zgodę na przedłożenie ww. pracy przez mgr inż. Beatę Tim jako część rozprawy doktorskiej w formie zbioru opublikowanych i powiązanych tematycznie artykułów naukowych.

.....
(podpis współautora)

Poznań, dnia 21.02.2024

dr inż. Paulina Błaszkiewicz
Wydział Inżynierii Materiałowej
i Fizyki Technicznej
Politechnika Poznańska,
Centrum NanoBioMedyczne
Uniwersytet im. Adama Mickiewicza

Oświadczenie

Oświadczam, że w niniejszej publikacji:

Beata Tim, Paulina Błaszkiewicz, Ariadna B. Nowicka, Michał Kotkowiak, *Optimizing SERS performance through aggregation of gold nanorods in Langmuir-Blodgett films,* Applied Surface Science 573 (2022), 151518-1-151518-22

mój udział polegał na przeprowadzeniu syntezy i funkcjonalizacji nanocząstek złota wraz z opisem procedury.

Wyrażam zgodę na przedłożenie ww. pracy przez mgr inż. Beatę Tim jako część rozprawy doktorskiej w formie zbioru opublikowanych i powiązanych tematycznie artykułów naukowych.

Paulina Błaszkiewicz
(podpis współautora)

Poznań, dnia 19.08.2024

dr inż. Paulina Błaszkiewicz
Wydział Inżynierii Materiałowej
i Fizyki Technicznej
Politechnika Poznańska,
Centrum NanoBioMedyczne
Uniwersytet im. Adama Mickiewicza

Oświadczenie

Oświadczam, że w niniejszej publikacji:

Michał Kotkowiak, Beata Tim, Mateusz Kotkowiak, Joanna Musiał, Paulina Błaszkiewicz, *The role of the polyethylene glycol in the organization of gold nanorods at the air–water and air–solid interfaces,* Langmuir 40 (2024), 14561-14569

mój udział polegał na przeprowadzeniu syntezy i funkcjonalizacji nanocząstek złota wraz z opisem procedury oraz zredagowaniu ostatecznej wersji manuskryptu.

Wyrażam zgodę na przedłożenie ww. pracy przez mgr inż. Beatę Tim jako część rozprawy doktorskiej w formie zbioru opublikowanych i powiązanych tematycznie artykułów naukowych.

Paulina Błaszkiewicz
(podpis współautora)

Poznań, dnia 17.06.2025

dr inż. Paulina Błaszkiewicz
Wydział Inżynierii Materiałowej
i Fizyki Technicznej
Politechnika Poznańska,
Centrum NanoBioMedyczne
Uniwersytet im. Adama Mickiewicza

Oświadczenie

Oświadczam, że w niniejszej publikacji:

Beata Tim, Paulina Błaszkiewicz, Emerson Coy, Alina Dudkowiak, *Interactions between functionalized PEGylated gold nanoparticles and model biological membranes,* Journal of Molecular Liquids 428 (2025), 127501-1 - 127501-12

mój udział polegał na opracowaniu i redakcji tekstu (Writing – review & editing), przeprowadzeniu badań (Investigation), pozyskaniu finansowania (Funding acquisition) oraz opracowaniu i zarządzaniu danymi badawczymi (Data curation).

Wyrażam zgodę na przedłożenie ww. pracy przez mgr inż. Beatę Tim jako część rozprawy doktorskiej w formie zbioru opublikowanych i powiązanych tematycznie artykułów naukowych.

Paulina Błaszkiewicz
(podpis współautora)

Poznań, dnia 26.08.2024

dr inż. Michał Kotkowiak
Wydział Inżynierii Materiałowej
i Fizyki Technicznej
Politechnika Poznańska

Oświadczenie

Oświadczam, że w niniejszej publikacji:

Beata Tim, Michał Kotkowiak, Natalia Kowalska, Ariadna B. Nowicka, Wiktor Lewandowski, *Influence of Gold Nanoparticle Assembly in Langmuir–Schaefer Monolayers on the Surface-Enhanced Spectroscopy Response of a Nanoplatform,* Journal of Physical Chemistry C 127 (2023), 15978-15987

mój udział polegał na opracowaniu koncepcji oraz celów badań; wykonaniu badań mikroskopowych, spektroskopowych i QCM warstw otrzymanych za pomocą techniki Langmuira-Schaefera; opisaniu uzyskanych wyników wraz z omówieniem i analizą wszystkich przeprowadzonych w tej pracy badań; przygotowaniu poprawionej wersji manuskryptu wraz z wykonaniem dodatkowych badań za pomocą techniki Langmuira–Schaefera; nadzorowaniu projektu; zarządzaniu planowaniem i realizacją badań; pozyskaniu wsparcia finansowego dla projektu.

Wyrażam zgodę na przedłożenie ww. pracy przez mgr inż. Beatę Tim jako część rozprawy doktorskiej w formie zbioru opublikowanych i powiązanych tematycznie artykułów naukowych.

.....
(podpis współautora)

Poznań, dnia 21.02.2024

dr inż. Michał Kotkowiak
Wydział Inżynierii Materiałowej
i Fizyki Technicznej
Politechnika Poznańska

Oświadczenie

Oświadczam, że w niniejszej publikacji:

Beata Tim, Paulina Błaszkiewicz, Ariadna B. Nowicka, Michał Kotkowiak, *Optimizing SERS performance through aggregation of gold nanorods in Langmuir-Blodgett films,* Applied Surface Science 573 (2022), 151518-1-151518-22

mój udział polegał na opracowaniu koncepcji oraz celów badań; wykonaniu badań mikroskopowych oraz spektroskopowych (*in situ*) warstw otrzymanych za pomocą techniki Langmuira i Langmuira-Blodgett (wraz z opisem procedury); doświadczalnym wyznaczeniu ilości CTAB w roztworach nanoprętów złota; opisaniu uzyskanych wyników (z wyłączeniem badań za pomocą techniki Langmuira) wraz z omówieniem i analizą wszystkich przeprowadzonych w tej pracy badań; współuczestniczeniu w napisaniu poszczególnych części manuskryptu tj. *abstract, introduction* i *conclusions*; przygotowaniu poprawionej wersji manuskryptu; nadzorowaniu projektu; zarządzaniu planowaniem i realizacją badań; pozyskaniu wsparcia finansowego dla projektu.

Wyrażam zgodę na przedłożenie ww. pracy przez mgr inż. Beatę Tim jako część rozprawy doktorskiej w formie zbioru opublikowanych i powiązanych tematycznie artykułów naukowych.

.....
(podpis współautora)

Poznań, dnia 26.08.2024

dr inż. Michał Kotkowiak
Wydział Inżynierii Materiałowej
i Fizyki Technicznej
Politechnika Poznańska

Oświadczenie

Oświadczam, że w niniejszej publikacji:

Michał Kotkowiak, Beata Tim, Mateusz Kotkowiak, Joanna Musiał, Paulina Błaszkiewicz, *The role of the polyethylene glycol in the organization of gold nanorods at the air–water and air–solid interfaces,* Langmuir 40 (2024), 14561-14569

mój udział polegał na opracowaniu koncepcji oraz celów badań; wykonaniu badań mikroskopowych warstw Langmuira-Schaefera i Lagmuira-Blodgett (wraz z opisem procedury), wykonaniu badań określających ilość CTAB w badanych roztworach; opisaniu uzyskanych wyników (z wyłączeniem badań wykonanych techniką Langmuira) wraz z omówieniem i analizą wszystkich przeprowadzonych w tej pracy badań; napisaniu poszczególnych części manuskryptu tj. *abstract,* części *introduction* i *conclusions*; przygotowaniu tzw. *rebuttal letter* oraz poprawionej wersji manuskryptu; redagowaniu manuskryptu na każdym etapie jego powstawania; nadzorowaniu projektu; zarządzaniu planowaniem i realizacją badań; pozyskaniu wsparcia finansowego dla projektu.

Wyrażam zgodę na przedłożenie ww. pracy przez mgr inż. Beatę Tim jako część rozprawy doktorskiej w formie zbioru opublikowanych i powiązanych tematycznie artykułów naukowych.

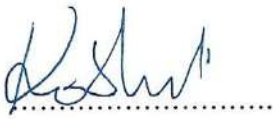

.....
(podpis współautora)

POLITECHNIKA POZNAŃSKA

WYDZIAŁ INŻYNIERII MATERIAŁOWEJ I FIZYKI TECHNICZNEJ
Instytut Badań Materiałowych i Inżynierii Kwantowej
ul. Piotrowo 3, 60-965 Poznań
tel.: +48 (61) 665 3200
e-mail: office_dtpf@put.poznan.pl
www.phys.put.poznan.pl

dr inż. Ariadna Nowicka
Zakład Spektroskopii Optycznej
Instytut Badań Materiałowych i Inżynierii Kwantowej
Wydział Inżynierii Kwantowej i Fizyki Technicznej

Poznań, 21.11.2025

Oświadczenie

Oświadczam, że w niniejszej publikacji:

Beata Tim, Michał Kotkowiak, Natalia Kowalska, Ariadna B. Nowicka, Wiktor Lewandowski, *Influence of Gold Nanoparticle Assembly in Langmuir–Schaefer Monolayers on the Surface-Enhanced Spectroscopy Response of a Nanoplatform,* Journal of Physical Chemistry C 127 (2023), 15978-15987

mój udział polegał na przeprowadzeniu pomiarów za pomocą wzmocnionej powierzchniowo spektroskopii Ramana oraz opisaniu i analizie wyników z zakresu ww. techniki oraz przeprowadzeniu badania Ramana na potrzeby poprawionej wersji manuskryptu.

Wyrażam zgodę na przedłożenie ww. pracy przez mgr inż. Beatę Tim jako część rozprawy doktorskiej w formie zbioru opublikowanych i powiązanych tematycznie artykułów naukowych.

.....
(podpis współautora)

POLITECHNIKA POZNAŃSKA

WYDZIAŁ INŻYNIERII MATERIAŁOWEJ I FIZYKI TECHNICZNEJ
Instytut Badań Materiałowych i Inżynierii Kwantowej
ul. Piotrowo 3, 60-965 Poznań
tel.: +48 (61) 665 3200
e-mail: office_dtpf@put.poznan.pl
www.phys.put.poznan.pl

dr inż. Ariadna Nowicka
Zakład Spektroskopii Optycznej
Instytut Badań Materiałowych i Inżynierii Kwantowej
Wydział Inżynierii Kwantowej i Fizyki Technicznej

Poznań, 21.11.2025

Oświadczenie

Oświadczam, że w niniejszej publikacji:

Beata Tim, Paulina Błaszkiewicz, Ariadna B. Nowicka, Michał Kotkowiak, *Optimizing SERS performance through aggregation of gold nanorods in Langmuir-Blodgett films,* Applied Surface Science 573 (2022), 151518-1-151518-22

mój udział polegał na przeprowadzeniu pomiarów za pomocą wzmocnionej powierzchniowo spektroskopii Ramana, opisaniu wyników z zakresu ww. techniki oraz przeprowadzeniu badania Ramana na potrzeby poprawionej wersji manuskryptu.

Wyrażam zgodę na przedłożenie ww. pracy przez mgr inż. Beatę Tim jako część rozprawy doktorskiej w formie zbioru opublikowanych i powiązanych tematycznie artykułów naukowych.

Nowicka
.....
(podpis współautora)

Warszawa, dnia 20.11.2025

mgr Natalia Kowalska
Wydział Chemii
Uniwersytet Warszawski

Oświadczenie

Oświadczam, że w niniejszej publikacji:

Beata Tim, Michał Kotkowiak, Natalia Kowalska, Ariadna B. Nowicka, Wiktor Lewandowski, *Influence of Gold Nanoparticle Assembly in Langmuir–Schaefer Monolayers on the Surface-Enhanced Spectroscopy Response of a Nanoplatform,* Journal of Physical Chemistry C 127 (2023), 15978-15987

mój udział polegał na przeprowadzeniu syntezy nanocząstek złota i ich charakteryzacji, wykonaniu pomiarów XRD i TEM otrzymanych warstw oraz opisaniu i analizie wyników wykonanych za pomocą techniki XRD.

Wyrażam zgodę na przedłożenie ww. pracy przez mgr inż. Beatę Tim jako część rozprawy doktorskiej w formie zbioru opublikowanych i powiązanych tematycznie artykułów naukowych.

Natalia Kowalska
(podpis współautora)

Warszawa, dnia 20.11.2025

dr hab. Wiktor Lewandowski, prof. UW
Wydział Chemii
Uniwersytet Warszawski

Oświadczenie

Oświadczam, że w niniejszej publikacji:

Beata Tim, Michał Kotkowiak, Natalia Kowalska, Ariadna B. Nowicka, Wiktor Lewandowski, *Influence of Gold Nanoparticle Assembly in Langmuir–Schaefer Monolayers on the Surface-Enhanced Spectroscopy Response of a Nanoplatform,* Journal of Physical Chemistry C 127 (2023), 15978-15987

mój udział polegał na przeprowadzaniu korekty i zredagowaniu ostatecznej wersji manuskryptu.

Wyrażam zgodę na przedłożenie ww. pracy przez mgr inż. Beatę Tim jako część rozprawy doktorskiej w formie zbioru opublikowanych i powiązanych tematycznie artykułów naukowych.

Wiktor Lewandowski; Uniwersytet Warszawski

Elektronicznie podpisany przez Wiktor Lewandowski; Uniwersytet Warszawski
Data: 2025.11.20 20:08:27 +01'00'

.....
(podpis współautora)

Poznań, dnia 3.12.2025

dr inż. Mateusz Kotkowiak
Wydział Inżynierii Materiałowej
i Fizyki Technicznej
Politechnika Poznańska

Oświadczenie

Oświadczam, że w niniejszej publikacji:

Michał Kotkowiak, Beata Tim, Mateusz Kotkowiak, Joanna Musiał, Paulina Błaszkiewicz, *The role of the polyethylene glycol in the organization of gold nanorods at the air–water and air–solid interfaces,* Langmuir 40 (2024), 14561-14569

mój udział polegał na przeprowadzeniu badań warstw Langmuira-Blodgett za pomocą techniki SEM.

Wyrażam zgodę na przedłożenie ww. pracy przez mgr inż. Beatę Tim jako część rozprawy doktorskiej w formie zbioru opublikowanych i powiązanych tematycznie artykułów naukowych.

(podpis współautora)

Poznań, 27.11.2025

dr n. farm. Joanna Musiał
Wydział Chemii
Uniwersytet im. Adama Mickiewicza w Poznaniu

Oświadczenie

Oświadczam, że w niniejszej publikacji:

Michał Kotkowiak, Beata Tim, Mateusz Kotkowiak, Joanna Musiał, Paulina Błaszkiewicz, *The role of the polyethylene glycol in the organization of gold nanorods at the air–water and air–solid interfaces,* Langmuir 40 (2024), 14561-14569,

mój udział polegał na przeprowadzeniu badań za pomocą techniki DLS wraz z opisaniem uzyskanych wyników oraz redagowaniu manuskryptu na każdym etapie jego powstawania.

Wyrażam zgodę na przedłożenie ww. pracy przez mgr inż. Beatę Tim jako część rozprawy doktorskiej w formie zbioru opublikowanych i powiązanych tematycznie artykułów naukowych.

Joanna Musiał

Poznań, dnia 16.06.2025

dr hab. inż. Emerson Coy, prof. UAM
Centrum NanoBioMedyczne
Uniwersytet im. Adama Mickiewicza
NanoBioMedical Centre
Adam Mickiewicz Univeristy

Oświadczenie

Oświadczam, że w niniejszej publikacji:

Beata Tim, Paulina Błaszkiewicz, Emerson Coy, Alina Dudkowiak, *Interactions between functionalized PEGylated gold nanoparticles and model biological membranes*, Journal of Molecular Liquids 428 (2025), 127501-1 - 127501-12

mój udział polegał na opracowaniu i redakcji tekstu (Writing – review & editing) oraz sprawowaniu nadzoru merytorycznego (Supervision).

Wyrażam zgodę na przedłożenie ww. pracy przez mgr inż. Beatę Tim jako część rozprawy doktorskiej w formie zbioru opublikowanych i powiązanych tematycznie artykułów naukowych.

Declaration

I declare that in this publication:

Beata Tim, Paulina Błaszkiewicz, Emerson Coy, Alina Dudkowiak, *Interactions between functionalized PEGylated gold nanoparticles and model biological membranes*, Journal of Molecular Liquids 428 (2025), 127501-1 - 127501-12

My contribution consisted of writing – review & editing and supervision.

I agree to submit the above work by Beata Tim, as a part of the Ph.D. dissertation in the form of a collection of published and thematically related scientific articles.

.....
(podpis współautora)
(co-author's signature)

Przedruk publikacji [Tim, JPCC 2023]

B. Tim, M. Kotkowiak, N. Kowalska, A.B. Nowicka, W. Lewandowski,

Influence of gold nanoparticle assembly in Langmuir-Schaefer monolayers on the surface-enhanced spectroscopy response of a nanoplatform,

Journal of Physical Chemistry C 127 (2023), 15978-15987. (IF 3,3; MNiSW 140)

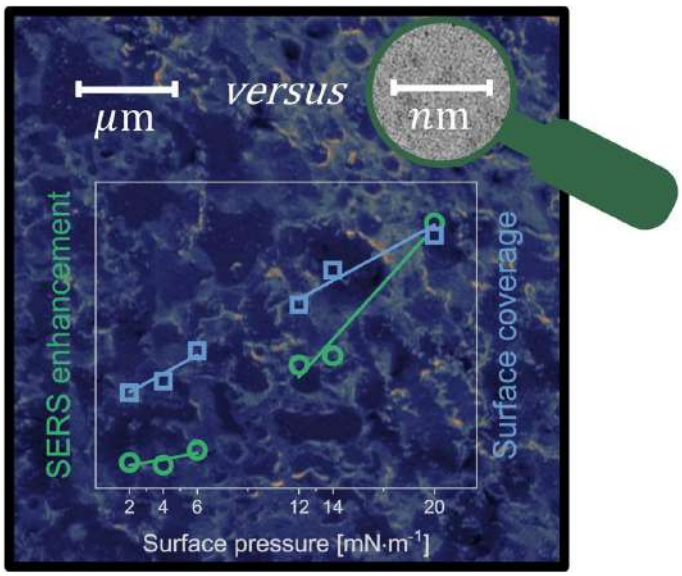

THE JOURNAL OF PHYSICAL CHEMISTRY C
A JOURNAL OF THE AMERICAN CHEMICAL SOCIETY

pubs.acs.org/JPCC

Article

Influence of Gold Nanoparticle Assembly in Langmuir–Schaefer Monolayers on the Surface-Enhanced Spectroscopy Response of a Nanoplatform

Beata Tim,* Michał Kotkowiak,* Natalia Kowalska, Ariadna B. Nowicka, and Wiktor Lewandowski

Cite This: J. Phys. Chem. C 2023, 127, 15978–15987

Read Online

ACCESS | Metrics & More | Article Recommendations | Supporting Information

ABSTRACT: Gold nanoparticles (Au-NPs) are among the most commonly used materials for increasing the sensitivity of Raman spectroscopy. This is mainly due to the strong and tunable surface plasmon resonances, which can be easily adjusted by choosing the shape and size of individual NPs. However, recent findings indicate that controlling the density of NPs in their assemblies is an equally important parameter. An efficient way to achieve such control is by using the Langmuir–Schaefer technique, which yields single-layer assemblies of NPs on a solid substrate. In this study, we correlate the density and thermodynamic properties of a monolayer of spherical Au-NPs with their performance as Raman substrates. Hence, hydrophobic NPs were synthesized and assembled into films using the Langmuir–Schaefer technique. The surface-enhanced Raman spectroscopy (SERS) showed various degrees of enhancement depending on the different ranges of transfer surface pressures employed, which almost doubled the expected SERS signal intensity at the highest deposition surface pressure. To gain greater insights into this phenomenon, we investigated the NP distribution in the Langmuir and Langmuir–Schaefer films by detailed spectroscopic and electron and optical microscopic analyses. A correlation was observed between NP enhancements on the micro- and nanoscale. The presented results demonstrated the potential of adjusting the Raman responses in ultrasensitive detection by controlling the thermodynamic properties of NP monolayers.

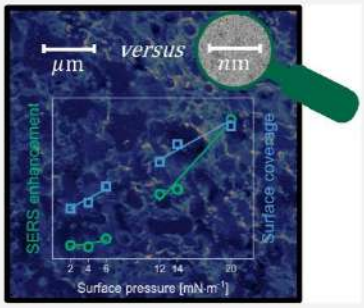

Downloaded via 91.94.109.235 on August 23, 2024 at 10:25:10 (UTC).
See https://pubs.acs.org/sharingguidelines for options on how to legitimately share published articles.

1. INTRODUCTION

Surface-enhanced Raman spectroscopy (SERS) has gained a lot of interest as a proper technique for the identification of environmental pollutants,[1] food additives,[2] and explosives,[3] strongly influencing the development of many areas such as biomedicine,[4−7] agriculture,[8−10] and public safety, just to name a few.[11] SERS analysis provides important information on the chemical structure of a compound, which allows the direct identification of various substances. However, there is a growing demand for compound detection at lower concentrations; hence, current research has focused on efficient SERS signal enhancers to decrease the detection limit even to the level of a single molecule.[12,13] One of the most promising and widely used SERS signal enhancers is metallic nanoparticles (NPs). In such a system, enhancement of SERS signals can be achieved for molecules at or close to the surfaces of the metallic NPs.[14] Gold nanoparticles (Au-NPs) are employed as enhancers in SERS due to the surface plasmon resonance, which involves collective oscillations of surface electrons of NPs. During the optimization of the performance of NP-based Raman enhancers, reports have shown that the size,[15−17] shape,[18−20] and interparticle distance[21,22] play a crucial role. However, a detailed correlation between the structure of Au-NP monolayers and their performance as SERS substrates is still not fully understood.

SERS enhancement shows a distinctive increase when NPs are compressed together to exhibit a collective enhancement of the electromagnetic field, which means that "hot spots" are formed.[23−25] Usually, such hot spots are randomly generated due to uncontrolled aggregation of NPs in dispersion. Additionally, such a process promotes aggregation, which is difficult to control and often leads to non-reproducible results, limiting its practical applicability.[26] Therefore, the creation of a controlled, self-organization of NPs method is required. The utilization of self-assembly for the fabrication of SERS substrates with controlled distribution of hot spots is desirable. In the case of thin films on solid substrates, this problem translates to controlling the degree of surface coverage by NPs. The coverage factor is crucial due to its correlation with the intensity of the registered SERS signals. For example, reposts have shown that as the surface coverage of rod-shaped Au-NPs increases, the accumulation of hot spots and the efficiency of SERS increases.[27,28] Although there is an abundance of data

Received: March 20, 2023
Revised: July 19, 2023
Published: August 8, 2023

ACS Publications

© 2023 The Authors. Published by American Chemical Society

https://doi.org/10.1021/acs.jpcc.3c01853
J. Phys. Chem. C 2023, 127, 15978−15987

related to this area of research, complete capitalization on the area to gain precise control over the assembly of NPs into a monolayer with varied densities remains a challenge. There are many techniques that produce an assembled NP monolayer. Recently, Song et al.[29] proposed a universal "lift-on" thin film technique enabled by the wetting empowered interfacial self-assembly.

One approach used to resolve the aforementioned problem is the use of the Langmuir technique. This technique is widely known as the typical method for the fabrication of 2D assemblies to study the structures and properties of substances such as lipids, proteins, and NPs.[30−36] However, the known concepts of Langmuir layer formation confirmed that layers consisting of metallic NPs show different types of interactions compared to those consisting of amphiphilic molecules. In the context of NPs, it requires the dispersion of NPs at the air−water interface, while the desired packing density, distribution, and interactions of NPs are controlled via surface pressure (π), which can be adjusted by pushing the Langmuir barriers toward each other. Monolayers of NPs can be conveniently prepared this way, as shown for nanorods[37] and nanospheres.[38] Spherical Au-NPs are one of the more common substances used as enhancers in SERS[39,40] because they are easily synthesized. Au-NPs are valued nanomaterials in SERS research due to their stability, scalable synthesis, and tunable physicochemical properties. Furthermore, produced NP monolayers can then be transferred to solid supports using Langmuir−Blodgett or Langmuir−Schaefer (LS) techniques. For example, the LS technique was used by Lafuente et al.[38] to obtain homogeneous Au-NP films that were capable of detecting rhodamine 6G in 10^{-11} M aqueous solution. One of the unexplored possibilities offered by the Langmuir method is the control of the order of NPs, which may be dependent on the range of π during monolayer transfer, which should provide means of controlling SERS signal enhancement. One of the first reports for superlattice construction with controllable interparticle distances for CdS clusters and TiO_2 nanocrystallites by means of Langmuir technique were reported by Kotov et al.[41,42] They showed that the NP arrangement can be controlled by varying the NP size or applying colloid chemical techniques. Herein, we present a detailed study on creating NP-based SERS substrates—nanoplatforms, where we explored the correlation between the surface pressure, degree of substrate coverage with NPs, inter-NP distance, and the intensity of SERS signals. Hydrophobic, spherical gold nanoparticles (Au-NPs) were utilized, assembled through the Langmuir−Schaefer technique. The formed substrates were used for the ultrasensitive analysis of 4-mercaptobenzoic acid (PMBA). SERS measurements revealed completely different Raman signal enhancements for the lower and higher π ranges. Notably, through detailed micro- and nanoscale measurements, a correlation was observed between SERS performance and Au-NP order. We carefully investigated the thermodynamic properties of hydrophobic Au-NP Langmuir monolayers (i.e., Au-NP phase state and transition points) and surface coverage of the nanoplatform. It is well-known that a Langmuir compression isotherm can be used to characterize the thermodynamics of the first-order phase transition present in the system. The presented research provides a good foundation for the future research on SERS substrates.

2. MATERIALS AND METHODS

2.1. Chemicals. Tetrachloroauric acid ($HAuCl_4$ ≥99%), dodecanethiol (DDT ≥98%), dodecylamine (≥99%), cyclohexane (99.5%), formaldehyde (37 wt% in H_2O, 10−15% methanol as the stabilizer), ethanol (95%), high-purity chloroform for spectroscopy (Uvasol®) ($CHCl_3$ >99%), isopropanol (≥99.8%), acetone (≥99.8%), and hexamethyldisilazane (HMDS ≥99%) were purchased from Merck (Darmstadt, Germany). PMBA (99%) was purchased from Sigma-Aldrich. All chemicals were used without further purification. Sulfuric acid (H_2SO_4 95%) and hydrogen peroxide (H_2O_2 solution 30%) were purchased from Chempur (Piekary Śląskie, Poland).

2.2. Chemical Synthesis of Spherical Gold Nanoparticles. Au-NP synthesis was carried out using the Wang method.[43] 7.5 g of dodecylamine was dissolved in 250 mL of cyclohexane, and 60 mL of 37% formaldehyde solution was added. After 20 min of vigorous stirring at room temperature, the mixture was centrifuged (5000 rpm over 5 min) in order to separate the organic phase, which was then washed twice with water. 100 mL of $HAuCl_4$ aqueous solution (1 g of $HAuCl_4$ in 250 mL of H_2O) was added under vigorous stirring and left for 40 min. Then, the organic phase containing the formed NPs was separated using centrifugation (5000 rpm over 5 min). Excess DDT (5 mL) was added, and the reaction was stirred overnight. The fractionation process was carried out to obtain fractions of Au-NPs with a slight size distribution. A small amount of ethanol was added to the cyclohexane NP solution until it became cloudy, which was then centrifuged (5000 rpm over 5 min), and the precipitate was redispersed in a small amount of cyclohexane. Another portion of ethanol was added to the supernatant (until it turned cloudy). This procedure was repeated, generating four fractions containing smaller and smaller NPs. The purification process was performed as follows: a small amount of acetone was added to each fraction and centrifuged (5000 rpm over 5 min), the supernatant was removed, the precipitate was redispersed in cyclohexane, and the procedure was repeated. Finally, the purified NPs were dissolved in cyclohexane. The absorption spectrum of Au-NPs in cyclohexane is shown in Figure S1 (see the Supporting Information). Au-NPs revealed a well-defined localized surface plasmon resonance (LSPR) band centered at ∼515 nm. In order to study the formation of the monolayer, Au-NPs in cyclohexane were centrifuged (6000 rpm over 30 min), producing a supernatant and a pellet. The supernatant was removed, and the pellet was evaporated using a heat plate to remove residual cyclohexane. The pellets containing Au-NPs were then dissolved in $CHCl_3$ for rapid evaporation of the solvent on the Langmuir monolayers.

2.3. Langmuir and Langmuir−Schaefer Film Preparation. The fabrication of monolayers composed of Au-NPs was carried out using a Langmuir−Blodgett balance (KSV Nima). The balance was equipped with a Langmuir trough (304 × 75 mm), two hydrophilic Delrin barriers, and a Brewster angle microscope (MicroBAM, KSV Nima). The procedure consisted of measuring the changes in π using a platinum Wilhelmy plate (instrumental accuracy 0.01 $mN{\cdot}m^{-1}$), which occurred during the symmetrical movement of the barriers at a constant speed of 5 $mm{\cdot}min^{-1}$. Before each measurement, the trough surface was prepared according to the procedure described by Tim et al.[33,37] The molecular layer was formed after Au-NPs dispersed in $CHCl_3$ (400 μL) and spread on the

https://doi.org/10.1021/acs.jpcc.3c01853
J. Phys. Chem. C 2023, 127, 15978−15987

surface of water (Milli-Q, 18.2 MΩ·cm) as the subphase using a microsyringe (Hamilton), followed by the solvent being evaporated (approx. 15 min). Compression of the monolayer caused by the movement of the barriers allowed for the recording of the π−area (A) isotherm, which was plotted as the π change as a function of the trough surface. During compression, Brewster angle microscopy (BAM) images were also recorded using a constant laser power, and image acquisition parameters remained constant. The monolayer morphology was determined, and the emerging domains were monitored, which highlighted structural changes.[30]

In the next stage of the investigation, the stability of Au-NP monolayers was determined by recording the dependence of change in the relative surface area ($A \cdot A_0^{-1}$) with time (t). For this purpose, dispersed Au-NPs in $CHCl_3$ were first spread at the air−water interface. Then, after the evaporation of $CHCl_3$, the monolayer was compressed (at a constant speed of 5 mm·min^{-1}) to π values of 2, 4, 6, 12, 14, and 20 mN·m^{-1}, and surface changes were recorded over time.

The transfer of Au-NP monolayers to a solid substrate was performed using the Langmuir−Schaefer technique. For this purpose, quartz plates (30 × 25 × 1 mm) were modified by salinization with HMDS. The cleaning of the substrates was performed according to the procedure described by Tahghighi et al.[44] The cleaned plates were immersed in HMDS for 48 h and dried at room temperature. The hydrophobicity of the plates was determined based on contact angle measurements. The contact angle of HMDS substrates was approx. 69 ± 1°. The deposition process was carried out at π values of 2, 4, 6, 12, 14, and 20 mN·m^{-1} by horizontal dipping of the hydrophobic substrate onto the surface film at an optimized speed of 0.5 mm·min^{-1}. Each experiment was carried out at a constant temperature of 21 ± 1 °C and repeated three times to ensure the reproducibility of the curves and depositions. It should be noted that reliable and repeatable transfer ratio (TR) values are difficult to obtain on hydrophobic surfaces due to the formation of the meniscus between the aqueous interface and the hydrophobic substrate. The operating software KSV Nima provides values of the TR; however, due to the relatively big dimensions of the substrate (30 × 25 mm), the value of the TR could be overestimated while using the Langmuir−Schaefer technique. Thus, during our transference, we rather focused on the visual observation of the substrate after deposition to ensure that the transferred material is deposited uniformly.

2.4. Microscopic, Spectroscopic, and Structural Measurements. The morphology and size dispersion of Au-NPs at the nanoscale were characterized by transmission electron microscopy (TEM). TEM measurements were performed using a Zeiss Libra 120 microscope with a LaB6 cathode equipped with OMEGA internal columnar filters and a CCD camera (Faculty of Chemistry University of Warsaw) and a JEOL-1400 (JEOL Co. Japan), equipped with a high-resolution digital camera CCD MORADA G2 (EMSIS GmbH, Germany) available at the Nencki Institute of Experimental Biology of Polish Academy of Sciences, Laboratory of Electron Microscopy. Au-NP monolayers were transferred to 400 mesh copper grids, which were previously mounted with Teflon tape on an HMDS-modified solid substrate. The process of deposition of the surface films on grids was conducted using the Langmuir−Schaefer technique under the same parameters as those for the deposition on HMDS-modified substrates (see Section 2.3).

The morphology of the nanoplatforms obtained via Au-NP Langmuir−Schaefer layers deposited on quartz substrates at the microscale and at different π values were generated using confocal laser scanning microscopy (LSM710, Zeiss, Germany). In the material mode (reflected light), the He−Ne laser operated at a wavelength of 543 nm. Images were collected from different Z planes using a Z stack module for the acquisition of Z stacks with a motorized focus drive. A Novascan UV Ozone cleaner was used to remove traces of organic compounds from the nanoplatforms. ImageJ processing software was used to calculate the surface coverage values and their standard deviation. ImageJ allowed us to fully verify the effect of the transfer surface pressure on the Au-NP packing. Each image was calibrated using a scale bar since a percentage is being estimated. Au-NP areas were marked using the intensity thresholding. Ten independent images at low magnification of the obtained nanoplatforms were considered in the case of the confocal microscope, typically with an area of 50 × 50 μm. For TEM analysis of surface coverage, we considered ten independent places at the sample, and the averaging area was about 300 × 300 nm.

Electronic absorption spectra of Au-NP Langmuir−Schaefer layers before and after UV ozone treatment were measured using a Varian Cary 4000 spectrometer. The in situ electronic absorption spectra of the Langmuir layers were recorded in the UV−vis range using an Ocean Optics QE65000 spectrometer, which was placed in proximity to a quartz window of the KSV Nima trough. Small-angle X-ray diffraction (SAXRD) measurements in capillary and Langmuir−Schaefer multilayers transferred at Kapton tape were performed using a Bruker Nanostar system (Cu Kα radiation, parallel beam formed by cross-coupled Goebel mirrors and a 3-pinhole collimation system, VANTEC 2000 area detector, Bruker, Billerica, MA, USA). The size of Au-NPs of 4.4 ± 0.4 nm was determined by SAXRD. TEM investigation confirmed the results obtained from SAXRD. The data for the diameter and dispersion of NPs based on SAXRD measurement were generated using the Nanofit 1.2.0.1 software. SAXRD thin layer measurements were obtained by the Langmuir Au-NPs being transferred to the Kapton tape, which was mounted on a solid substrate. The deposition process was carried out using the Langmuir−Schaefer technique for a π of 20 mN·m^{-1} by dipping the substrate into the surface film five times at an optimized speed of 0.5 mm·min^{-1}. The collected SAXRD diffractogram revealed increased scattering around the direct beam (at low angles), which was characteristic of the presence of NPs in the films. Moreover, an XRD peak was detected, which was centered at approx. 6 nm and corresponded to the center-to-center interparticle distance, see Figure S2. Given the size of the particles, NP surface-to-surface distance was 1.6 nm, which was reasonable assuming moderately interdigitating DDT ligands from neighbor particles.[45] The broadness of the peak was probably associated with the short-range correlation lengths of NP assembly, suggesting an isotropic arrangement of particles within the film.

SERS measurements were carried out using the Renishaw inVia micro-Raman system equipped with a diode laser emitting 785 nm light, which was used as an excitation source. 0.1 mM PMBA aqueous solution (prepared from 1 mM solutions in ethanol) was incubated on the surface nanoplatform overnight. The substrates were then washed with Milli-Q water and dried under nitrogen. The laser power was less than 50 mW. The laser beam was focused on the sample surface

https://doi.org/10.1021/acs.jpcc.3c01853
J. Phys. Chem. C 2023, 127, 15978−15987

using the Leica long working distance ×50 LWD objective (numerical aperture 0.5). The experiments were performed under ambient conditions using a backscattering geometry. Twelve spectra were collected in the range of 600−1800 cm^{-1}, with a spectral resolution of 2.5 cm^{-1}, from the area of 10 × 10 μm. For every sample, based on these 12 origin spectra, the average spectrum was calculated, and further calculations were performed.

3. RESULTS AND DISCUSSION

In this work, small spherical Au-NPs covered with DDT were employed. These were easily dispersible in non-polar solvents, which was crucial for the assembly of monolayers at the air−water interface. The ligands and solvent selection were based on previous studies. The ability of Au-NPs to form stable surface films at the air−water interface has already been confirmed, in which DDT or DDT/PEG-SH functionalized Au-NPs dispersed in $CHCl_3$ are often used. The selected ligands ensured the hydrophobic properties required for the formation of a monolayer on water, whereas $CHCl_3$ exhibited a high spreading factor, leading to an effective spreading of the dispersed material at the air−water interface. Au-NPs were assembled using the Langmuir technique, in which Au-NPs were drop casted at the air−water interface. To harness the ability of Au-NP Langmuir monolayer formation, the surface pressure area (π−A) isotherm was recorded during the compression of NPs (Figure 1). We noted two regions of π

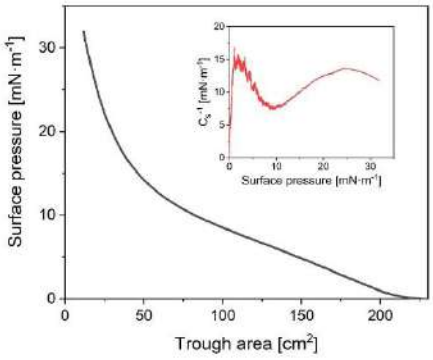

Figure 1. Surface pressure vs isotherm of the trough area of the Au-NP Langmuir monolayer; the inset graph shows the dependence of the surface compressional modulus C_s^{-1} on the surface pressure of Au-NPs.

increasing for 220 to 60 and 50 to 25 cm^2 areas. The reddish color visible on the surface of the subphase also confirmed the formation of the surface film. During Au-NP compression, the faint reddish color became more pronounced, indicating increased packing at the air−water interface. This phenomenon was previously observed by our research group for monolayers containing Au nanorods in the water subphase.[37] The ability of Au-NPs to form stable surface films at the air−water interface was confirmed by numerous reports. For example, Tahghighi et al.[44] employed spherical Au-NPs to tune SERS substrates, where Au-NPs were dispersed in $CHCl_3$ and spread on the aqueous subphase. The recorded π−A isotherms confirmed that the systems formed stable monolayers at the air−water interface. Lafuente et al.[38] also reported stable surface films consisting of Au-NPs. The systems consisted of octadecylthional-protected hydrophobic Au-NPs dispersed in chloroform. The above exmaples[38,44] showed that the use of $CHCl_3$ as a solvent generated stable dispersions that formed monolayers at the air−water interface.

The obtained isotherm was used to calculate the value of the compressibility modulus $\left(C_s^{-1} = -A\frac{d\pi}{dA}\right)$, which provided information on the elasticity and physical state of the formed film (Figure 1, inset). The maximum 15 $mN{\cdot}m^{-1}$ value of C_s^{-1} fitted into the 12.5 to 50 $mN{\cdot}m^{-1}$ range was characteristic of an expanded liquid phase state.[30] The flexible nature of the Au-NP monolayer stemmed from the transition of the formed film from the gaseous to the expanded liquid state, which was previously reported by Ishida et al.[46] In their research, hydrophobic Au-NPs were employed with polyethylene glycol (PEG-SH). The maximum reported C_s^{-1} values were higher than those presented in our research, suggesting that the use of Au-NPs of larger sizes and the presence of PEG-SH affected the compression process. Additionally, the compression isotherm of Au-NP functionalized with PEG-SH and DDT had higher values of C_s^{-1} because of the compression of the brushes upon movement of the barrier.[46] However, the surface film we obtained was characterized by a course of isotherm and elasticity, which was similar to the monolayers tested in our previous studies of Au nanorods with PEG-SH molecules.[37] Importantly, the presented studies showed that the Langmuir monolayer of the investigated Au-NPs exhibited a phase transition at approx. 10 $mN{\cdot}m^{-1}$ (see the C_s^{-1} course), which was not observed for larger-sized Au-NPs. Furthermore, this strongly impacted the obtained Langmuir−Schaefer monolayers, as presented below.

To confirm the formation of homogeneous surface films at the air−water interface, BAM imaging was performed (Figure 2). BAM analysis showed that the compression of the monolayer changed the character of the surface film from heterogeneous to more homogeneous. The apparent change in the homogeneity of the surface film during compression indicated alterations in the self-organization of the particles during the process. In the case of π = 2 $mN{\cdot}m^{-1}$, clusters of particles were visible (Figure 2a). By increasing π to 6 $mN{\cdot}m^{-1}$ (Figure 2b,c), densely packed clusters were formed. In contrast, further compression of the monolayer resulted in the formation of an increasingly homogeneous surface film (Figure 2d−f).

The compression reversibility of the Au-NP monolayer was determined, where during compression, compression/expansion hysteresis was measured in triplicate at the maximum π value (Figure S3). The comparable curves generated for both compression and expansion of the monolayer confirmed the reversibility of the process. Thus, this highlights the lack of aggregation of Au-NPs upon monolayer compression.

The determination of monolayer stability that depends on the degree of Au-NP packing is an important element in the fabrication of SERS nanoplatforms using Langmuir-like techniques. A relaxation experiment was carried out for several selected values of π, corresponding to different regions of C_s^{-1} on the π dependence curve, to obtain the optimal parameters for further transfer of the fabricated films to a solid substrate (Figure 1). Namely, measurements and deposition were performed for the first maximum of C_s^{-1} (π = 2 $mN{\cdot}m^{-1}$), in the region when C_s^{-1} decreased toward a minimum (4 and 6 $mN{\cdot}m^{-1}$), and finally in the range when C_s^{-1} again increased (12, 14, and 20 $mN{\cdot}m^{-1}$). The depositions π were carefully

https://doi.org/10.1021/acs.jpcc.3c01853
J. Phys. Chem. C 2023, 127, 15978−15987

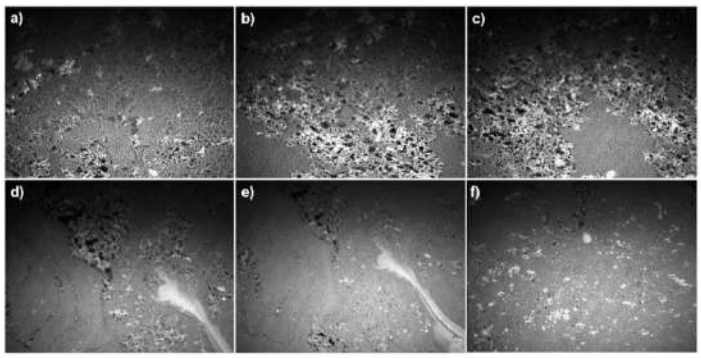

Figure 2. BAM images of the Au-NP Langmuir monolayer for surface pressures equal to 2 (a), 4 (b), 6 (c), 12 (d), 14 (e), and 20 mN·m^{-1} (f). Image width is 4000 μm.

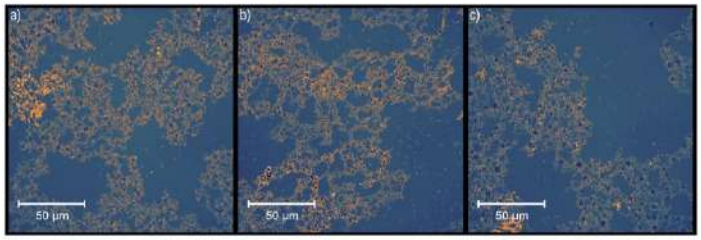

Figure 3. Confocal microscopy images of the Au-NP Langmuir–Schaefer monolayer deposited on quartz substrates for a surface pressure of 6 mN·m^{-1} and for upstroke (horizontal dipping) speeds of 0.5 (a), 1.0 (b), and 1.5 mm·min^{-1} (c).

selected based on presented thermodynamic studies. π > 20 mN·m^{-1} was not examined due to the limited stability of the monolayers for this π region, as well as the broad character of C_s^{-1} on π dependence at these π values. The relative area over time curves (Figure S4) showed higher stability for the lower π values, which was observed for less dense Au-NP packing. For the lowest tested surface pressures, $A \cdot A_0^{-1}$ values remained constant at approx. 0.97, indicating high stability of the formed monolayers. Higher pressures resulted in a single stability loss of 0.1–0.16 from the initial values. In the case of the highest tested range, the monolayers stabilized over time. These results indicated that the stability of the created layers increased with decreasing packing.

Next, the deposition parameters of the Au-NP Langmuir–Schaefer layer were optimized, where three dipping speeds of the hydrophobic substrate in the surface film were examined. Figure 3 shows examples of confocal microscopy images of Au-NP Langmuir–Schaefer layers deposited on quartz substrates for a π of 6 mN·m^{-1} at different horizontal dipping speeds. This π value was selected based on the data presented in Figure 1, in which a π of 6 mN·m^{-1} was comparable to the observed phase transitions and near the maximum value of C_s^{-1}. As shown in Figure 3a–c, upon increasing the horizontal dipping speed of the substrate (from 0.5 to 1.5 mm·min^{-1}), the surface coverage decreased from 44 ± 5 to 33 ± 6 and to 26 ± 5%. Based on the obtained surface coverages, a speed of 0.5 mm·min^{-1} was determined as the optimal deposition speed value for the deposition of Au-NPs. The comparison of the confocal microscopy images of Au-NP Langmuir–Schaefer layers (Figure 3) with BAM images of the Au-NP Langmuir monolayer (Figure 2) revealed that the transfer of monolayers to a solid substrate caused the bonding of domains that were visible on the subphase. Hence, the network formation, which may result from the dewetting process, occurred during the Langmuir monolayer transfer.

Additionally, the optical properties of the formed Au-NP monolayers were investigated using *in situ* UV–vis spectroscopy at several π values (results not shown). In all cases, the plasmonic bands characteristic of Au-NPs were observed, with a maximum at ~542 nm, and slightly red-shifted compared to Au-NP dispersion. Furthermore, the intensity recorded at the band maxima showed a linear dependence toward π. These features suggested that NPs exhibited plasmonic coupling, and the magnitude of the coupling was similar in all samples. Since the plasmonic coupling was directly related to the interparticle distance, the obtained results indicated that the interparticle distance between the adjacent NPs was independent to pressure. This was determined by the hydrophobic thick ligand shell on the surface of Au-NPs. However, it should be noted that the bands were relatively broad, limiting the possibility of detailed analysis of interparticle distance via UV–vis spectroscopy. However, Au-NPs transferred to the quartz substrate were confirmed using the Langmuir–Schaefer technique to preserve their optical properties. Therefore, UV–vis spectroscopy was used. Au-NPs did not tend to aggregate upon monolayer compression, and thus, specific dendritic structures such as that of hydrophilic Au nanorods were not visible as shown previously by Tim et al.[37] The LSPR band of the Au-NP Langmuir–Schaefer layer deposited on quartz before UV ozone treatment was localized at 536 nm (Figure 4a,b), as well as a slight red shift (by 18 nm) to 554 nm. The observed phenomena were similar to that reported by Zhong et al.,[47] where a quantitative study was conducted on the chemistry of PVP degradation during UV treatment. The

https://doi.org/10.1021/acs.jpcc.3c01853
J. Phys. Chem. C 2023, 127, 15978–15987

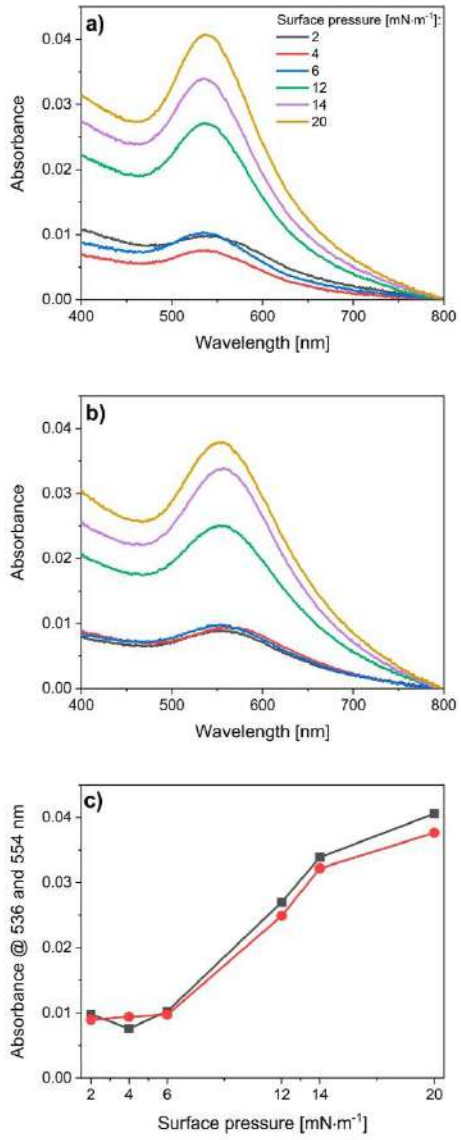

Figure 4. Absorption spectra of the Au-NP Langmuir–Schaefer layer deposited on quartz before (a) and after (b) UV ozone treatment and the dependence of the absorbance value of the LSPR peak vs surface pressure (c) before and after UV ozone treatment, black and red curves, respectively.

residual PVP underwent photochemical oxidative degradation dominated by C–C and C–N bond cleavages within the first hour of UV treatment. Further degradation decreased with an increasing degree of oxidation of the carbon skeleton and/or cross-linking reactions. Earlier studies by Zhong et al.[48] confirmed that the size and morphology of Au-NPs remained constant during UV treatment, but the intensity and position variations of the LSPR peak should indicate alternations in the coordination environment of Au-NPs. The absorbance of Au-NPs transferred on the quartz substrate remained constant for π ranging from 2–6 mN·m^{-1}, and it had a more linear character for π > 6 mN·m^{-1}. Therefore, Au-NPs were densely packed for π > 6 mN·m^{-1}, and more hot spots were present in the samples.

The Au-NP arrangement after transfer to the solid substrates was examined. To record the appropriate data at the micro- and nanoscale, confocal and TEM analyses were performed for samples transferred to the quartz substrate and copper grid, respectively (Figures 5 and 6 and Figure S5). Two maxima of

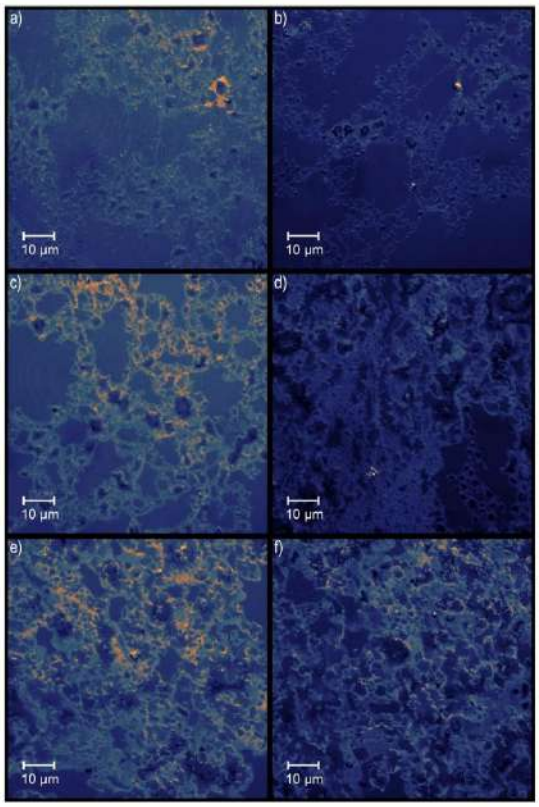

Figure 5. Confocal microscopy images of the Au-NP Langmuir–Schaefer monolayer deposited on quartz substrates for surface pressures of 2 (a), 4 (b), 6 (c), 12 (d), 14 (e), and 20 mN·m^{-1} (f).

C_s^{-1} were detected at π equal to ~2 and ~24 mN·m^{-1}. This suggested that at the beginning of Au-NP compression, the first transient assembly occurred. The structure of the assembly is shown in Figure 5, which revealed the presence of fine NP networks. The structure quickly disassembled, as indicated by the low width of the C_s^{-1} peak (FWHM ~ 4.5 mN·m^{-1}). Above 9 mN·m^{-1}, the onset of the second peak indicated that domains formed from the cracking of the first NP network were compressed. At this point, the packing was lower owing to the width of the second C_s^{-1} peak (FWHM ~ 18.0 mN·m^{-1}), and the monolayer network was much denser. The density, which included the surface coverage of the sponge-like structures, scaled linearly with π (Figure 6, blue line). The slope of the linear regression was 2.3 ± 0.3 m·mN^{-1}, R^2 = 0.93.

To examine the samples at the nanoscale, TEM images were obtained. The measured surface coverage in representative 1 ×

https://doi.org/10.1021/acs.jpcc.3c01853
J. Phys. Chem. C 2023, 127, 15978–15987

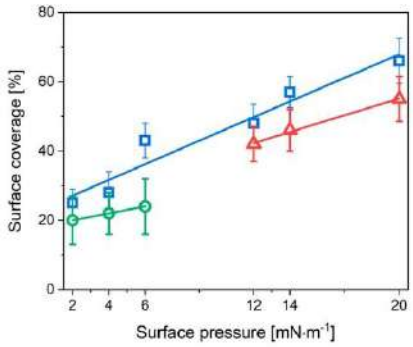

Figure 6. Dependence of the surface coverage of the Au-NP Langmuir–Schaefer layer vs the deposition surface pressure evaluated on quartz using confocal microscopy (blue symbols) and copper grids by TEM analysis for lower (green symbols) and higher (red symbols) surface pressures.

1 μm^2 areas is presented in Figure 6 (green and red symbols). As shown in Figure 6, two regions were clearly visible (green and red symbols). In the first π deposition range (π < 9 mN·m^{-1}), increased domain packing was less significant (the slope of the linear regression was 1.0 ± 0.1 m·mN^{-1}, R^2 = 0.99), while for π > 9 mN·m^{-1}, the distance between Au-NPs in the closely packed domain was more pronounced, and deposition π influenced the size of the closely packed domains, which in turn substantially increased the surface coverage (the slope of the linear regression was 1.6 ± 0.1 m·mN^{-1}, R^2 = 0.99). The behavior of the Au-NP monolayer at the nanoscale was different from that presented at the microscale. Of course, the data presented in Figure 6 (blue line) could be fitted in the lower and higher surface pressure regions; however, obtained R^2 parameters were insufficient. R^2 equal to 0.74 and 0.84 were obtained (results not shown), respectively, vs R^2 = 0.93 for both regions. The quartz crystal microbalance (QCM) technique can directly provide the estimated amount of the deposited material. It should be noted that the amount of the deposited material obtained from the QCM can be directly correlated with the surface coverage determined from confocal microscopy or TEM. To estimate surface coverage of Au-NPs at the surface of the QCM, we have performed measurements and calculations as described in the Supporting Information. The obtained surface coverage (Figure S6), calculated from QCM measurements, is a complex quantity based on few basic physical quantities; thus, its error is relatively high. However, as shown in Figure S6, we obtained good agreement between values estimated from confocal microscopy and the QCM, although the latter seems to be slightly underestimated. AFM can provide information from relatively small areas in comparison to regions reported here obtained from the TEM technique. Lafuente et al.[38] showed comprehensive characterization of SERS platforms using both SEM and AFM techniques. As emphasized by authors, the AFM images provide similar results to SEM imaging, regardless of the values of deposition surface pressure. The authors pointed out that the reproducibility in the protocol of nanoplatforms designing can be successfully assessed by the SEM technique.

The correlation between the surface coverage and π was also reported by Ishida et al.[46] According to the described SEM images, the surface coverage of Au-NPs with DDT and with or without PEG-SH at the NP surface was determined. The surface coverage values obtained in our studies for smaller Au-NPs were approx. 15% higher for π > 9 mN·m^{-1}, while below <9 mN·m^{-1}, the values were comparable. Based on this comparison, we speculated that the smaller Au-NPs were related to a greater surface coverage.

To study the influence of NP deposition on their performance as a SERS substrate, they were examined using a series of PMBA solutions. Figure 7a presents the average

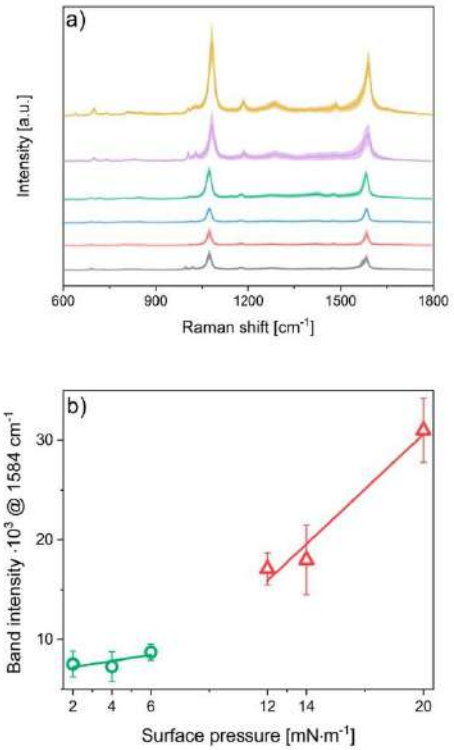

Figure 7. SERS performance of the fabricated monolayers. (a) Averaged surface-enhanced Raman spectra for various transfer surface pressures of Au-NP Langmuir–Schaefer monolayers. (b) Intensity of the peak at 1584 cm^{-1} for the spectra shown in (a); the data points presented in panel (b) were fitted with two linear regressions, for the lower (green) and higher surface pressure ranges (red symbols).

SERS spectra of PMBA adsorbed on Au-NP Langmuir–Schaefer monolayers prepared at different transfer π values. Technical details on PMBA deposition are provided in Section 2.4. For each sample, based on these 12 origin spectra, the average spectrum was calculated, and then, further calculation was performed. The relative uncertainty (standard deviation) of the obtained results resulting from the SERS measurements for PMBA determined from the average peak intensity at 1584 cm^{-1} was about 19% for different transfer surface pressures of Au-NP Langmuir–Schaefer monolayers. The spectra shown in Figure 7a represent averaged spectra with their standard deviation. However, in Figure S7, we present for example the average spectra for PMBA 10^{-4} M on Au-NP Langmuir–Schaefer monolayers deposited on quartz substrates for a surface transfer pressure of 6 mN·m^{-1}.

https://doi.org/10.1021/acs.jpcc.3c01853
J. Phys. Chem. C 2023, 127, 15978−15987

Moreover, we plotted the intensity of the peak at 1584 cm^{-1} for the spectra shown in Figure 7a versus the surface coverage of the Au-NP Langmuir−Schaefer layer, as presented in Figure S8. Both values present almost linear dependence when the intersection point (0,0) is included. The characteristic bands at PMBA at 1077 cm^{-1} in-plane ring breathing + stretching (C−S) and 1587 cm^{-1} [symmetric stretching (CC)][49] were observed. The detection limit of the investigated substrate for PMBA is about 5×10^{-8} M, results not shown. In the dependence shown in Figure 6, two regions of Au-NP domain organization were observed with either less and more significant packing. The slope ratio of the linear regression of both deposition ranges was 1.6. In general, the SERS signal was proportional to the surface coverage, but due to different processes, this dependence varied.[37,50] An even more pronounced dependence is shown in Figure 7b. In the first π deposition range (π < 9 $mN{\cdot}m^{-1}$), the slope of the linear regression was 300 ± 50 $m{\cdot}mN^{-1}$, while for π > 9 $mN{\cdot}m^{-1}$, the slope of the linear regression was 1836 ± 34 $m{\cdot}mN^{-1}$; thus, the slope ratio of the linear regression for both deposition ranges was 6.12, whereas that in Figure 6 was 1.6 (1.6 $mN{\cdot}m^{-1}{\cdot}1.0$ $mN^{-1}{\cdot}m$). The dependence shown in Figure 7b could be also interpolated using exponential function, as presented in Figure S9. Both presented scenarios are possible and mathematically correct. However, due to specific shape of the compression isotherm, a localization of phase transition point at 10 $mN{\cdot}m^{-1}$ for SERS measurements should be interpreted taking into account the thermodynamic properties of the Au-NP Langmuir monolayer. Notably, a band related to the dependence of SERS peak intensities vs π of the Langmuir−Blodgett transfer curve was not found, which would suggest limited stability of monolayers and formation of multilayer structures.[50] Thus, when using the presented parameters for the formation of Au-NP monolayers (C_s^{-1} relaxation studies and optical measurements), multilayer aggregates were not formed. Therefore, it was speculated that using a higher pressure (above 10 $mN{\cdot}m^{-1}$, the region above the phase transition point for which the gradual increase of C_s^{-1} was observed), Au-NPs tended to form well-packed structures at the micro- and nanoscale, which promoted the enhancement of Raman intensities. The obtained results indicated the importance of considering all sets of Langmuir monolayer parameters to understand the behaviors of the SERS nanoplatform.

4. CONCLUSIONS

The formation of Langmuir−Schaefer monolayers consisting of hydrophobic Au-NPs was investigated, which were used to optimize SERS performance for the ultrasensitive detection of PMBA. Au-NPs dispersed in $CHCl_3$ formed insoluble Langmuir monolayers on the ultrapure water subphase. With increasing surface pressure, the monolayers exhibited a more homogeneous nature. The compression of Au-NPs was a reversible process, and upon Langmuir monolayer compression, no aggregation of Au-NPs occurred. Relaxation studies showed that the stability of the surface film increased with decreasing surface pressure. During nanoplatform design, we optimized the horizontal dipping speed of the quartz substrate as well as the TEM copper grid to maximize the surface coverage value. For the optimized dipping speed, the dependence between the surface coverage of the substrate and the deposition pressure was linear on the microscale. However, on the nanoscale, different arrangements were observed according to the lower and higher values of the deposition surface pressure. For the first time, we correlated the thermodynamic properties of Au-NP monolayers (i.e., Au-NP phase state and transition points) with their SERS performance. The intensity of the SERS signal increased significantly after the first phase transition in the Langmuir monolayer for surface pressures greater than 12 $mN{\cdot}m^{-1}$. The results highlighted the potential of tailoring the SERS response with the thermodynamic properties of the Langmuir monolayer.

■ ASSOCIATED CONTENT

Supporting Information

The Supporting Information is available free of charge at https://pubs.acs.org/doi/10.1021/acs.jpcc.3c01853.

Absorption spectra of Au-NPs, SAXRD pattern of layers, thermodynamic properties of the Au-NP Langmuir monolayer, TEM images of layers, QCM surface coverage measurements, dependence of the surface coverage of Au-NP layer versus the deposition surface pressure, SERS spectra of layers, and intensity of the PMBA peak versus surface coverage and deposition surface pressure (PDF)

■ AUTHOR INFORMATION

Corresponding Authors

Beata Tim − *Faculty of Materials Engineering and Technical Physics, Poznan University of Technology, 60-965 Poznan, Poland*; Email: beata.tim@doctorate.put.poznan.pl

Michał Kotkowiak − *Faculty of Materials Engineering and Technical Physics, Poznan University of Technology, 60-965 Poznan, Poland*; orcid.org/0000-0001-6611-0366; Phone: +48 61 665 3182; Email: michal.kotkowiak@put.poznan.pl

Authors

Natalia Kowalska − *Faculty of Chemistry, University of Warsaw, 02-093 Warsaw, Poland*; orcid.org/0000-0001-6123-1572

Ariadna B. Nowicka − *Faculty of Materials Engineering and Technical Physics, Poznan University of Technology, 60-965 Poznan, Poland*

Wiktor Lewandowski − *Faculty of Chemistry, University of Warsaw, 02-093 Warsaw, Poland*; orcid.org/0000-0002-3503-2120

Complete contact information is available at: https://pubs.acs.org/10.1021/acs.jpcc.3c01853

Author Contributions

B.T. and M.K. have contributed equally to this work and share first authorship. **B.T.** performed Langmuir (including BAM) and Langmuir−Schaefer experiments, described results, and provided discussion of Langmuir studies (for the compression isotherm and compressional modulus, the discussion was provided in part). **M.K.** designed the concept of research and general aims of experiments; performed microscopic, spectroscopic, and QCM studies of Langmuir−Schaefer layers; described the results of performed studies together with the discussion and analysis of all performed studies within this work; prepared a revised version of the manuscript together with additional experiments (Langmuir−Schaefer experiments); supervised the project; managed research planning

https://doi.org/10.1021/acs.jpcc.3c01853
J. Phys. Chem. C 2023, 127, 15978−15987

and execution; and acquired the financial support for the project. **N.K.** synthetized gold nanoparticles and provided their characterization; performed XRD and TEM measurements; and described results and discussion of XRD. **A.B.N** measured Raman spectra; described results and discussion of Raman spectra; and performed Raman studies for a revised version of the manuscript. **W.L.** proofread and edited the final version of the manuscript. All co-authors approved the final version of the manuscript.

Notes

The authors declare no competing financial interest.

■ ACKNOWLEDGMENTS

This work was supported by the National Science Center in Poland by the project 2019/35/D/ST4/02037. We gratefully acknowledge the technical assistance of Paulina Błaszkiewicz at an early stage of the project.

■ REFERENCES

(1) Tang, H.; Zhu, C.; Meng, G.; Wu, N. Review—Surface-Enhanced Raman Scattering Sensors for Food Safety and Environmental Monitoring. *J. Electrochem. Soc.* **2018**, *165*, B3098−B3118.

(2) Zheng, J.; He, L. Surface-Enhanced Raman Spectroscopy for the Chemical Analysis of Food. *Compr. Rev. Food Sci. Food Saf.* **2014**, *13*, 317−328.

(3) Hakonen, A.; Rindzevicius, T.; Schmidt, M. S.; Andersson, P. O.; Juhlin, L.; Svedendahl, M.; Boisen, A.; Käll, M. Detection of Nerve Gases Using Surface-Enhanced Raman Scattering Substrates with High Droplet Adhesion. *Nanoscale* **2016**, *8*, 1305−1308.

(4) Cialla-May, D.; Zheng, X. S.; Weber, K.; Popp, J. Recent Progress in Surface-Enhanced Raman Spectroscopy for Biological and Biomedical Applications: From Cells to Clinics. *Chem. Soc. Rev.* **2017**, *46*, 3945−3961.

(5) Moore, T. J.; Moody, A. S.; Payne, T. D.; Sarabia, G. M.; Daniel, A. R.; Sharma, B. In Vitro and In Vivo SERS Biosensing for Disease Diagnosis. *Biosensors* **2018**, *8*, 46.

(6) Song, L.; Chen, J.; Xu, B. B.; Huang, Y. Flexible Plasmonic Biosensors for Healthcare Monitoring: Progress and Prospects. *ACS Nano* **2021**, *15*, 18822−18847.

(7) Guo, Z.; Jia, Y.; Song, X.; Lu, J.; Lu, X.; Liu, B.; Han, J.; Huang, Y.; Zhang, J.; Chen, T. Giant Gold Nanowire Vesicle-Based Colorimetric and SERS Dual-Mode Immunosensor for Ultrasensitive Detection of Vibrio Parahemolyticus. *Anal. Chem.* **2018**, *90*, 6124−6130.

(8) Pilot, R.; Signorini, R.; Durante, C.; Orian, L.; Bhamidipati, M.; Fabris, L. A Review on Surface-Enhanced Raman Scattering. *Biosensors* **2019**, *9*, 57.

(9) Yang, J.; Rorrer, G. L.; Wang, A. X. Bioenabled SERS Substrates for Food Safety and Drinking Water Monitoring. *Proc. SPIE-Int. Soc. Opt. Eng.* **2015**, *9488*, 948808.

(10) Liu, H.; Zeng, J.; Song, L.; Zhang, L.; Chen, Z.; Li, J.; Xiao, Z.; Su, F.; Huang, Y. Etched-Spiky Au@Ag Plasmonic-Superstructure Monolayer Films for Triple Amplification of Surface-Enhanced Raman Scattering Signals. *Nanoscale Horiz.* **2022**, *7*, 554−561.

(11) Rodríguez-Lorenzo, L.; Álvarez-Puebla, R. A.; De Abajo, F. J. G.; Liz-Marzán, L. M. Surface Enhanced Raman Scattering Using Star-Shaped Gold Colloidal Nanoparticles. *J. Phys. Chem. C* **2010**, *114*, 7336−7340.

(12) Zrimsek, A. B.; Chiang, N.; Mattei, M.; Zaleski, S.; McAnally, M. O.; Chapman, C. T.; Henry, A. I.; Schatz, G. C.; Van Duyne, R. P. Single-Molecule Chemistry with Surface- and Tip-Enhanced Raman Spectroscopy. *Chem. Rev.* **2017**, *117*, 7583−7613.

(13) Shiohara, A.; Wang, Y.; Liz-Marzán, L. M. Recent Approaches toward Creation of Hot Spots for SERS Detection. *J. Photochem. Photobiol., C* **2014**, *21*, 2−25.

(14) Schlücker, S. Surface-Enhanced Raman Spectroscopy: Concepts and Chemical Applications. *Angew. Chem., Int. Ed.* **2014**, *53*, 4756−4795.

(15) Pazos-Perez, N.; Wagner, C. S.; Romo-Herrera, J. M.; Liz-Marzán, L. M.; Garcíade Abajo, F. J.; Wittemann, A.; Fery, A.; Alvarez-Puebla, R. A. Organized Plasmonic Clusters with High Coordination Number and Extraordinary Enhancement in Surface-Enhanced Raman Scattering (SERS). *Angew. Chem., Int. Ed.* **2012**, *124*, 12860−12865.

(16) Shaw, C. P.; Fan, M.; Lane, C.; Barry, G.; Jirasek, A. I.; Brolo, A. G. Statistical Correlation between SERS Intensity and Nanoparticle Cluster Size. *J. Phys. Chem. C* **2013**, *117*, 16596−16605.

(17) Wustholz, K. L.; Henry, A. I.; McMahon, J. M.; Freeman, R. G.; Valley, N.; Piotti, M. E.; Natan, M. J.; Schatz, G. C.; Van Duyne, R. P. Structure-Activity Relationships in Gold Nanoparticle Dimers and Trimers for Surface-Enhanced Raman Spectroscopy. *J. Am. Chem. Soc.* **2010**, *132*, 10903−10910.

(18) San Juan, A. M. T.; Chavva, S. R.; Tu, D.; Tircuit, M.; Coté, G.; Mabbott, S. Synthesis of SERS-Active Core-Satellite Nanoparticles Using Heterobifunctional PEG Linkers. *Nanoscale Adv* **2022**, *4*, 258−267.

(19) Benz, F.; Chikkaraddy, R.; Salmon, A.; Ohadi, H.; De Nijs, B.; Mertens, J.; Carnegie, C.; Bowman, R. W.; Baumberg, J. J. SERS of Individual Nanoparticles on a Mirror: Size Does Matter, but so Does Shape. *J. Phys. Chem. Lett.* **2016**, *7*, 2264−2269.

(20) Taylor, R. W.; Lee, T. C.; Scherman, O. A.; Esteban, R.; Aizpurua, J.; Huang, F. M.; Baumberg, J. J.; Mahajan, S. Precise Subnanometer Plasmonic Junctions for SERS within Gold Nanoparticle Assemblies Using Cucurbit[n]Uril "Glue. *ACS Nano* **2011**, *5*, 3878−3887.

(21) Park, S. G.; Kang, M.; Kim, S.; Jung, H. S.; Kim, D. H. 3D-Assembled Ag Nanowires for Use in Plasmon-Enhanced Spectroscopic Sensors. *Appl. Spectrosc. Rev.* **2019**, *54*, 325−347.

(22) Jeon, T. Y.; Kim, D. J.; Park, S. G.; Kim, S. H.; Kim, D. H. Nanostructured Plasmonic Substrates for Use as SERS Sensors. *Nano Convergence* **2016**, *3*, 18.

(23) Tim, B.; Błaszkiewicz, P.; Kotkowiak, M. Recent Advances in Metallic Nanoparticle Assemblies for Surface-Enhanced Spectroscopy. *Int. J. Mol. Sci.* **2021**, *23*, 291−324.

(24) Langer, J.; Jimenez de Aberasturi, D.; Aizpurua, J.; Alvarez-Puebla, R. A.; Auguié, B.; Baumberg, J. J.; Bazan, G. C.; Bell, S. E. J.; Boisen, A.; Brolo, A. G.; et al. Present and Future of Surface-Enhanced Raman Scattering. *ACS Nano* **2020**, *14*, 28−117.

(25) Kotkowiak, M.; Dudkowiak, A. Multiwavelength Excitation of Photosensitizers Interacting with Gold Nanoparticles and Its Impact on Optical Properties of Their Hybrid Mixtures. *Phys. Chem. Chem. Phys.* **2015**, *17*, 27366−27372.

(26) Guerrini, L.; Graham, D. Molecularly-Mediated Assemblies of Plasmonic Nanoparticles for Surface-Enhanced Raman Spectroscopy Applications. *Chem. Soc. Rev.* **2012**, *41*, 7085−7107.

(27) Grzelczak, M.; Liz-Marzán, L. M.; Klajn, R. Stimuli-Responsive Self-Assembly of Nanoparticles. *Chem. Soc. Rev.* **2019**, *48*, 1342−1361.

(28) Solís, D. M.; Taboada, J. M.; Obelleiro, F.; Liz-Marzán, L. M.; García De Abajo, F. J. Optimization of Nanoparticle-Based SERS Substrates through Large-Scale Realistic Simulations. *ACS Photonics* **2017**, *4*, 329−337.

(29) Song, L.; Xu, B. B.; Cheng, Q.; Wang, X.; Luo, X.; Chen, X.; Chen, T.; Huang, Y. Instant Interfacial Self-Assembly for Homogeneous Nanoparticle Monolayer Enabled Conformal "Lift-on" Thin Film Technology. *Sci. Adv.* **2021**, *7*, No. eabk2852.

(30) Rojewska, M.; Tim, B.; Prochaska, K. Interactions between Silica Particles and Model Phospholipid Monolayers. *J. Mol. Liq.* **2022**, *345*, 116999−117009.

(31) Girardon, M.; Korchowiec, B.; Korchowiec, J.; Rogalska, E.; Canilho, N.; Pasc, A. A Way to Introducing a Hydrophilic Bioactive Agent into Model Lipid Membranes. The Role of Cetyl Palmitate in the Interaction of Curcumin with 1,2-Dioleoyl-Sn-Glycero-3-Phosphatidylcholine Monolayers. *J. Mol. Liq.* **2020**, *308*, 113040.

https://doi.org/10.1021/acs.jpcc.3c01853
J. Phys. Chem. C 2023, 127, 15978−15987

(32) Jurak, M.; Miñones, J. Interactions of Lauryl Gallate with Phospholipid Components of Biological Membranes. *Biochim. Biophys. Acta, Biomembr.* **2016**, *1858*, 1821−1832.
(33) Tim, B.; Blaszkiewicz, P.; Kotkowiak, M. Altering Model Cell Membranes by Means of Photoactivated Organic Functionalized Gold Nanorods. *J. Mol. Liq.* **2022**, *349*, 118179.
(34) Chachaj-Brekiesz, A.; Wnętrzak, A.; Włodarska, S.; Lipiec, E.; Dynarowicz-Łątka, P. Molecular Insight into Neurodegeneration − Langmuir Monolayer Study on the Influence of Oxysterols on Model Myelin Sheath. *J. Steroid Biochem. Mol. Biol.* **2020**, *202*, 105727.
(35) Tim, B.; Rojewska, M.; Prochaska, K. Effect of Silica Microparticles on Interactions in Mono- and Multicomponent Membranes. *Int. J. Mol. Sci.* **2022**, *23*, 12822.
(36) Swierczewski, M.; Bürgi, T. Langmuir and Langmuir-Blodgett Films of Gold and Silver Nanoparticles. *Langmuir* **2023**, *39*, 2135−2151.
(37) Tim, B.; Blaszkiewicz, P.; Nowicka, A. B.; Kotkowiak, M. Optimizing SERS Performance through Aggregation of Gold Nanorods in Langmuir-Blodgett Films. *Appl. Surf. Sci.* **2022**, *573*, 151518−151527.
(38) Lafuente, M.; Ruiz-Rincón, S.; Mallada, R.; Cea, P.; Pilar Pina, M. Towards the Reproducible Fabrication of Homogeneous SERS Substrates by Langmuir-Schaefer Technique: A Low Cost and Scalable Approach for Practical SERS Based Sensing Applications. *Appl. Surf. Sci.* **2020**, *506*, 144663−144671.
(39) Romo-Herrera, J. M.; Alvarez-Puebla, R. A.; Liz-Marzán, L. M.; Liz-Marzán, L. M. Controlled Assembly of Plasmonic Colloidal Nanoparticle Clusters. *Nanoscale* **2011**, *3*, 1304−1315.
(40) Indrasekara, A. S. D. S.; Paladini, B. J.; Naczynski, D. J.; Starovoytov, V.; Moghe, P. V.; Fabris, L. Dimeric Gold Nanoparticle Assemblies as Tags for SERS-Based Cancer Detection. *Adv. Healthcare Mater.* **2013**, *2*, 1370−1376.
(41) Kotov, N. A.; Meldrum, F. C.; Wu, C.; Fendler, J. H. Monoparticulate Layer and Langmuir-Blodgett-Type Multiparticulate Layers of Size-Quantized Cadmium Sulfide Clusters: A Colloid-Chemical Approach to Superlattice Construction. *J. Phys. Chem.* **1994**, *98*, 2735−2738.
(42) Kotov, N. A.; Meldrum, F. C.; Fendler, J. H. Monoparticulate Layers of Titanium Dioxide Nanocrystallites with Controllable Interparticle Distances. *J. Phys. Chem.* **1994**, *98*, 8827−8830.
(43) Chen, Y.; Wang, X. Novel Phase-Transfer Preparation of Monodisperse Silver and Gold Nanoparticles at Room Temperature. *Mater. Lett.* **2008**, *62*, 2215−2218.
(44) Tahghighi, M.; Mannelli, I.; Janner, D.; Ignés-Mullol, J. Tailoring Plasmonic Response by Langmuir−Blodgett Gold Nanoparticle Templating for the Fabrication of SERS Substrates. *Appl. Surf. Sci.* **2018**, *447*, 416−422.
(45) Bagiński, M.; Szmurło, A.; Andruszkiewicz, A.; Wójcik, M.; Lewandowski, W. Dynamic self-assembly of nanoparticles using thermotropic liquid crystals. *Liq. Cryst.* **2016**, *43*, 2391−2409.
(46) Ishida, T.; Tachikiri, Y.; Sako, T.; Takahashi, Y.; Yamada, S. Structural Characterization and Plasmonic Properties of Two-Dimensional Arrays of Hydrophobic Large Gold Nanoparticles Fabricated by Langmuir-Blodgett Technique. *Appl. Surf. Sci.* **2017**, *404*, 350−356.
(47) Zhong, R. Y.; Yang, J. W.; Hu, Z.; Xu, B. Q. Removal of Residual Poly(Vinylpyrrolidone) from Gold Nanoparticles Immobilized on SiO2 by Ultraviolet-Ozone Treatment. *ACS Appl. Nano Mater.* **2019**, *2*, 5720−5729.
(48) Zhong, R.-Y.; Sun, K.-Q.; Hong, Y.-C.; Xu, B.-Q. Impacts of Organic Stabilizers on Catalysis of Au Nanoparticles from Colloidal Preparation. *ACS Catal.* **2014**, *4*, 3982−3993.
(49) Zhang, X.-Y.; Han, D.; Pang, Z.; Sun, Y.; Wang, Y.; Zhang, Y.; Yang, J.; Chen, L. Charge Transfer in an Ordered Ag/Cu2S/4-MBA System Based on Surface-Enhanced Raman Scattering. *J. Phys. Chem. C* **2018**, *122*, 5599−5605.
(50) Tahghighi, M.; Janner, D.; Ignés-Mullol, J. Optimizing Gold Nanoparticle Size and Shape for the Fabrication of SERS Substrates by Means of the Langmuir−Blodgett Technique. *Nanomaterials* **2020**, *10*, 2264−2311.

https://doi.org/10.1021/acs.jpcc.3c01853
J. Phys. Chem. C 2023, 127, 15978−15987

Supplementary information

for

The Influence of Gold Nanoparticles Assembly in Langmuir-Schaefer Monolayers on SERS Response of Nanoplatform

Beata Tim[a,*,†], Michał Kotkowiak[a,**,†], Natalia Kowalska[b], Ariadna B. Nowicka[a], Wiktor Lewandowski[b]

[a]Faculty of Materials Engineering and Technical Physics, Poznan University of Technology, Piotrowo 3, 60-965 Poznan, Poland
[b]Faculty of Chemistry, University of Warsaw, Pasteura 1, 02-093 Warsaw, Poland

†These authors have contributed equally to this work and share first authorship

To whom correspondence should be addressed:
*E-mail: beata.tim@doctorate.put.poznan.pl (BT)
**E-mail: michal.kotkowiak@put.poznan.pl (MK)
Tel.: + 48 61 665 3182

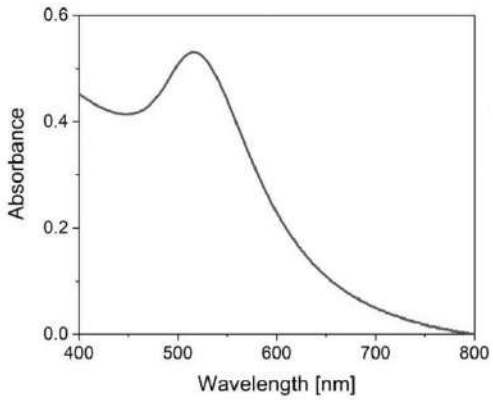

Fig. S1. Absorption spectrum of Au-NPs in cyclohexane.

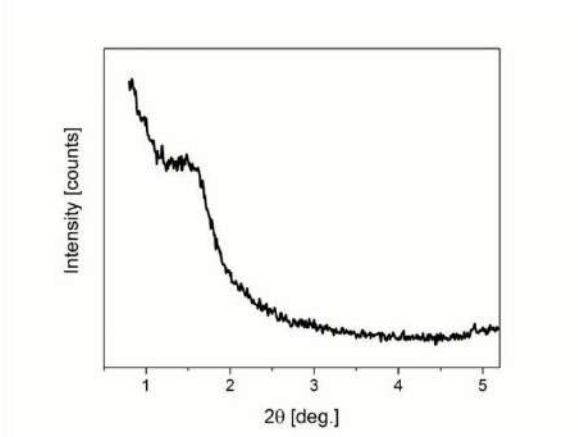

Fig. S2. SAXRD pattern of Langmuir-Schaefer multilayers of Au-NPs deposited on Kapton tape, see experimental part for details.

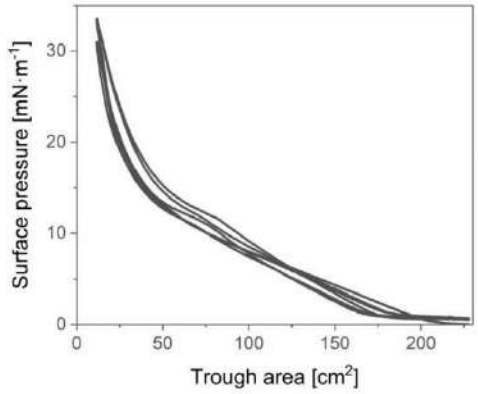

Fig. S3. The surface pressure *versus* trough area hysteresis of the Au-NPs Langmuir monolayer.

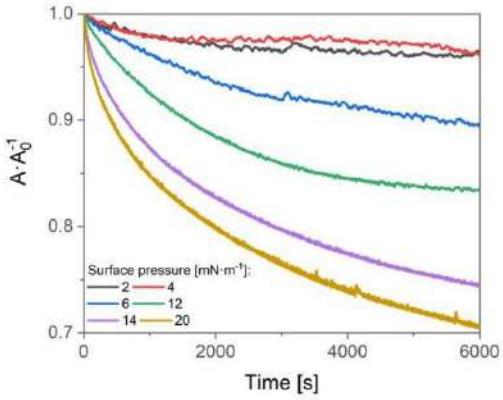

Fig. S4. Relative area changes *versus* time for a various surface pressure of the Au-NPs Langmuir monolayer.

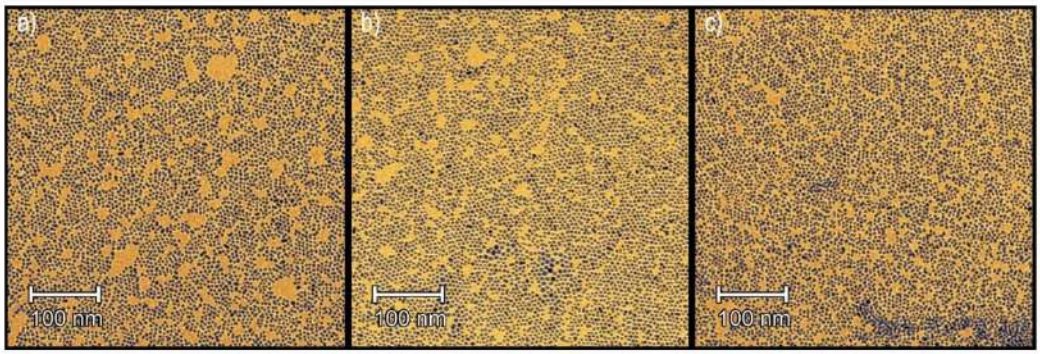

Fig. S5. Exemplary TEM images of the Au-NPs transferred at surface pressures equal to 12 **(a)**, 14 **(b)** and 20 $mN \cdot m^{-1}$ **(c).**

S1. QCM surface coverage measurements

Frequency changes (Δf) upon Au-NPs deposition were measured using openQCM Q^{-1} measuring system equipped with QCM sensor purchased from openQCM (10 MHz and 11.5 mm diameter). The known volume of Au-NPs (3.0-4.0 μL) was spread at the QCM sensors and Δf was measured as shown in Table S1. The mean Δm of the spread drop of Au-NPs was $\Delta m = 2.23 \cdot 10^{-6}$ g, as calculated from Sauerbrey equation. In order to calculate the mass of single Au-NPs we estimated the concentration of Au-NPs solution. For the known Au(0) concentration ($3.63 \cdot 10^{-4}$ M) we determined amount of gold atoms per particle from TEM measurement of particle dimensions. Dividing these numbers gave as particle concentration equal to $1.38 \cdot 10^{-7}$ M from which it was possible to determine the number of Au-NPs in a single drop. Dividing the total mass of the Au-NPs deposited on the surface of QCM by the number of Au-NPs in a single drop we obtained the mass of single Au-NPs $m = 7.91 \cdot 10^{-18}$ g/Au-NPs.

Table S1. Drop volume of Au-NPs and frequency changes (Δf) of QCM.

No.	Drop volume [μL]	Δf [Hz]
1	3.5	490
2	3.5	577
3	3.5	563
4	4.0	630
5	3.0	355
6	3.0	300
7	3.0	325
8	3.5	515
9	3.5	547
10	3.5	556
Mean	*3.4±0.1*	*486±37*

In two-dimensional space the highest-density lattice arrangement of circles is the hexagonal packing arrangement in which the centers of the circles are arranged in a hexagonal lattice and each circle is surrounded by 6 other circles. The density of this arrangement is 90.7%. Dividing

the value of QCM area by the area of Au-NPs (with DDT chain size) gave us the number of Au-NPs at the surface of QCM for 100% surface coverage ($N_{Au\text{-}NPs}=2.45\cdot10^{12}$). By multiplying $N_{Au\text{-}NPs}\cdot m$, and based on Sauerbrey equation, we obtain the frequency changes for 100% surface coverage $\Delta f_{100\%}=4216$ Hz. In the next step the Au-NPs Langmuir-Schaefer monolayer, obtained at the defined transfer surface pressure, was deposited on QCM sensor to perform Δf_{LS} measurements. Finally, we calculated the surface coverage (Table S2) from proportion taking into account $\Delta f_{100\%}$ value.

Table S2. Measured Δf_{LS} values of Au-NPs Langmuir-Schaefer monolayer for different transfer surface pressure.

Surface pressure [$mN\cdot m^{-1}$]	Δf_{LS} [Hz]
2	450
4	578
6	1345
12	1592
14	1853
20	2367

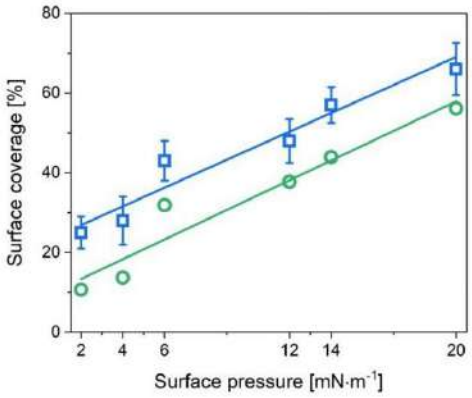

Fig. S6. Dependence of the surface coverage of Au-NPs Langmuir-Schaefer layer *vs.* the deposition surface pressure evaluated on quartz using confocal microscopy (the same dependence was presented in the manuscript) (blue symbols) and QCM (green symbols).

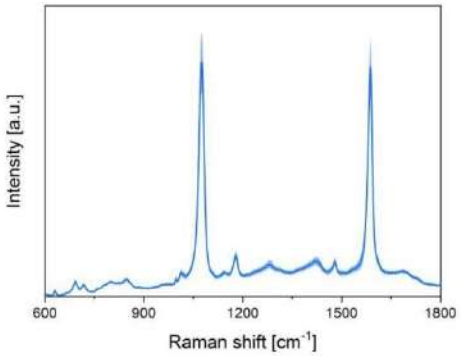

Fig. S7. SERS spectra recorded from the area (10×10 μm) for PMBA (10^{-4} M) on Au-NPs Langmuir-Schaefer monolayers for surface transfer pressures 6 mN·m^{-1}. The blue line represents the average spectrum.

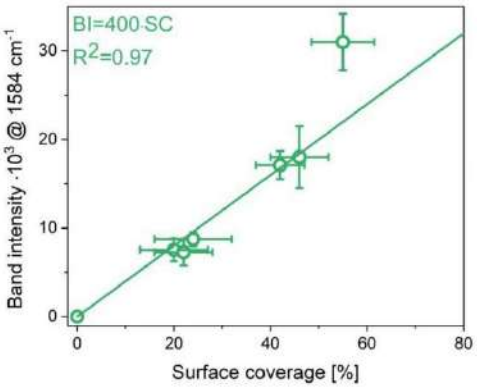

Fig. S8. Intensity of the peak at 1584 cm^{-1} for the spectra shown in Fig. 7a *versus* the surface coverage of Au-NPs Langmuir-Schaefer layer.

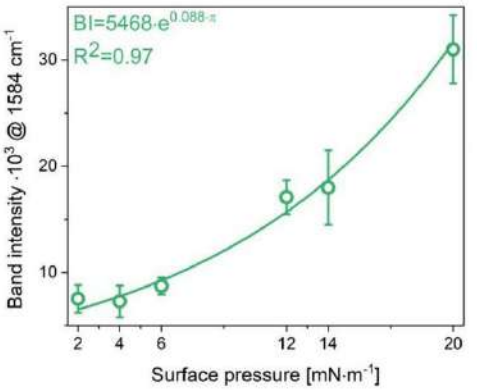

Fig. S9. Intensity of the peak at 1584 cm^{-1} for the spectra shown in Fig. 7a for various transfer surface pressures of Au-NPs Langmuir-Schaefer monolayers.

Przedruk publikacji [Tim, ASS 2022]

B. Tim, P. Błaszkiewicz, A.B. Nowicka, M. Kotkowiak,

Optimizing SERS performance through aggregation of gold nanorods in Langmuir-Blodgett films,

Applied Surface Science 573 (2022), 151518-1-151518-22. (IF 6,7; MNiSW 140)

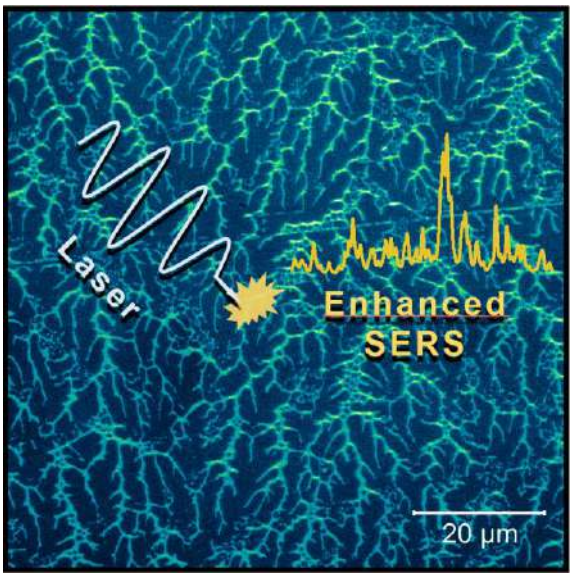

Applied Surface Science 573 (2022) 151518

Contents lists available at ScienceDirect

Applied Surface Science

journal homepage: www.elsevier.com/locate/apsusc

Full Length Article

Optimizing SERS performance through aggregation of gold nanorods in Langmuir-Blodgett films

Beata Tim [a,1], Paulina Błaszkiewicz [a], Ariadna B. Nowicka [a,b], Michał Kotkowiak [a,1,*]

[a] Faculty of Materials Engineering and Technical Physics, Poznan University of Technology, Piotrowo 3, Poznan 60-965, Poland
[b] Institute of Physical Chemistry, Polish Academy of Sciences, Kasprzaka 44/52, Warsaw 01-224, Poland

ARTICLE INFO

Keywords:
2D assembly
Air-water interface
Nanoparticles
Noble metal
Surface plasmon resonance

ABSTRACT

Nanoparticles with a high degree of anisotropy are characterized by large electromagnetic field enhancements at the single-particle level; however, their arrangement into aggregated structures does not lead to significantly better performance. Surprisingly, for nanorods a superior accumulation of hot spots is present at surface coverages above 60%, which ensures a higher efficiency for surface-enhanced Raman spectroscopy (SERS). In this study, we produced pegylated gold nanorods in Langmuir-Blodgett layers in order to optimize SERS performance for the ultrasensitive detection of molecules, by tuning plasmonic coupling and nanoparticle surface coverage. To understand the arrangement of the nanorods in Langmuir and Langmuir-Blodgett layers, we performed spectroscopic and microscopic analysis of the obtained films. Based on the compression isotherms of the nanorods, we proposed the best conditions for nanoplatform design. The Raman enhancement factor was around $2{\cdot}10^5$ with a deposition surface pressure equal to 12 $mN{\cdot}m^{-1}$. Due to the polymer's presence at the surface of the nanorods and the dewetting process, specific dendritic-like aggregates were observed on the solid substrate. The results obtained indicate the significance of further studies on the arrangement of metallic nanoparticles in monolayers, taking into account the size and shape of the nanoparticles, as well as the type of stabilizing ligands at their surface.

1. Introduction

Delocalized electrons in nanoparticles (NPs) can readily oscillate when exposed to the appropriate light frequency, and surface charge-density oscillations cause electric field enhancement near the surface of the NPs. Gold NPs deserve special attention due to the presence of surface plasmon resonance, which is responsible for their optical properties [1–3]. For metallic NPs, the resonant excitation of free electrons by electromagnetic radiation of a particular wavelength leads to strong bands characteristic of the surface plasmon in the extinction spectrum (LSPR band).

An efficient and scalable bottom-up strategy for the development of nanostructured materials can be based on the self-assembly of NPs obtained by wet chemistry methods [4,5]. A particularly versatile approach is the use of nanorods (NRs), nanotriangles, or nanostars [6–8]. Methods for the synthesis of monodisperse NPs are well-established [9]. Although the approaches proposed in literature result in stable NPs, the large size of the NPs and the types of ligands that stabilize such large structures lead to difficulty in the functionalization of the resulting NPs for specific applications [10]. Therefore, despite a significant literature on the synthesis of NPs, there is a strong need to develop a robust protocol for a more efficient method of NP functionalization.

The Langmuir technique involves the self-assembly of molecules or other hydrophobic materials into an ordered monolayer at an air–water interface and the subsequent transfer (*via* vertical or horizontal deposition) of the self-assembled monolayer onto a solid substrate. The Langmuir technique is an excellent method for depositing self-assembled systems onto surfaces. It offers homogeneity over relatively large areas, and unlike traditional self-assembled monolayers (SAMs), films of multiple layers can be obtained by successive dipping [11].

When a molecule is in close proximity to the surface of NPs, it can absorb or radiate more light than normal, since both absorption and emission occur with certain probabilities that are modified by NPs [12]. This phenomenon is widely used for the development of functional nanoplatforms for biosensing applications, since plasmon resonance

* Corresponding author.
E mail address: michal.kotkowiak@put.poznan.pl (M. Kotkowiak).
[1] These authors have contributed equally to this work and share first authorship

https://doi.org/10.1016/j.apsusc.2021.151518
Received 4 August 2021; Received in revised form 28 September 2021; Accepted 3 October 2021
Available online 10 October 2021
0169-4332/© 2021 The Author(s). Published by Elsevier B.V. This is an open access article under the CC BY-NC-ND license (http://creativecommons.org/licenses/by-nc-nd/4.0/).

enhances the scattered signals of adsorbed biomolecules [13,14]. Raman and SERS spectroscopies are commonly used methods for molecule identification [15,16]. Plasmonic effects increase by a few orders of magnitude the efficiency of an otherwise very inefficient process. The key factor related to the efficiency of SERS substrates is the presence of hot spots, the sites at which the light is trapped by plasmonic effects [15,17]. The easiest way to prepare SERS substrates is based on the formation of SAMs composed of NPs in contact with chemically modified substrates [10,18]. The main limitation of this technique is the surface coverage, which can reach up to approx. 50%, mainly due to steric hindrance. This low surface coverage reduces the hot spot density and hence the SERS response [5,16,17]. This response can be controlled by increasing and tuning a substrate's hot spot density. Besides simple strategies, more advanced protocols have recently been introduced. For example, the spacing between NPs can be tuned by NPs embedded in a thermosensitive film [19]. Alternatively, SERS substrates can be manufactured using lithographic techniques and the Langmuir-Blodgett method for mask production [20]. There are some major advantages of Langmuir monolayer formation over other methods of obtaining SAMs. After the NPs are spread at the air–water interface, their desired packing density, i.e., surface pressure, can be adjusted by moving the barriers toward each other, hence controlling the packing, arrangement, and interaction of the NPs. The surface density of hot spots can be optimized by controlling the lateral distance between NPs.

Currently, there is limited knowledge on the correlation of the packing of NPs with their experimental SERS. However, a great deal of information could be obtained from numerical simulations of SERS phenomenon. So far these simulations have been limited to relatively simple geometries or at most a few particles, but ensemble effects can be critical in the performance of actual large-scale SERS samples. A recent example for NPs with a high degree of anisotropy gave a large enhancement, even within the single-particle limit, while aggregation into dense arrays did not lead to significantly better performance. In contrast, nanospheres and NRs start out with relatively poor SERS efficiencies in dilute layers, but undergo a large boost in the accumulation of hot spots and ensuing SERS efficiency at surface coverages above ~50%. More precisely, NRs exceed the SERS enhancement of nanostars at coverages beyond ~60% [16,21,22]. Therefore, in this study we aimed at a detailed analysis of a set of aggregated pegylated gold nanorods (Au-NRs) in Langmuir-Blodgett layers in order to optimize SERS performance for ultrasensitive analysis, by tuning plasmonic coupling and nanoparticle surface coverage. The optimum conditions for nanoplatform composition were proposed, based on the compression isotherm of the Au-NRs. The thermodynamic properties of the Au-NR Langmuir monolayer were discussed and correlated with its optical properties and SERS performance.

2. Materials and methods

2.1. Chemicals

Tetrachloroauric acid ($HAuCl_4 \cdot H_2O$) (99.99%) was obtained from Alfa Aesar. Cetyltrimethylammonium bromide (CTAB) (99.00%), sodium borohydride ($NaBH_4$) (98.00%), silver nitrate ($AgNO_3$) (99.99%), ascorbic acid (99.00%), O-(2-mercaptoethyl)-O'-methylpolyethylene glycol (PEG-SH $M_w \approx 2000$) (99.99%), bromophenol blue sodium salt suitable for molecular biology (BPB), *p*-MBA (4-Mercaptobenzoic acid) (99.00%), and rhodamine 6G (99.00%) were purchased from Sigma Aldrich and were used without further purification. The chemical structure of the polymer used for the functionalization of Au-NRs is shown in Fig. S1, see supplementary material (SM). We chose the PEG-SH with $M_w \approx 2000$ to ensure thick layer formation on the surface of the Au-NRs. Spectrophotometric grade methanol was purchased from POCH S.A. (Poland). High purity chloroform for spectroscopy ($CHCl_3$) (>99%), (Uvasol®), isopropanol (≥99.8%), and acetone (≥99.8%) were purchased from Merck.

2.2. Chemical synthesis of polymer-coated gold nanorods

Au-NRs were prepared following the procedure of Nikoobakth et al. [23] with the modifications previously described by Blaszkiewicz et al. [24,25]. The PEG-SH coating was prepared using the modified method described previously [26–28], the PEG-SH being covalently grafted onto the surface of the Au-NRs. An aqueous solution of PEG-SH of the desired molecular weight was sonicated for 30 min and added to a solution of Au-NRs with vigorous stirring. The resulting solution was stirred for 24 h at room temperature to allow for complete ligand exchange with PEG-SH. Excess PEG-SH was eliminated through twice centrifuging at 6000 rpm for around 30 min. The supernatant was decanted, leaving a pellet, and refilling was carried out with ultrapure water (Milli-Q, 18.2 MΩ·cm, (71.98 ± 0.01) $mN \cdot m^{-1}$). The washing process was repeated again to remove unbound PEG-SH or other reactants, and the pellet was then transferred to methanol. Thiol groups exhibit a high affinity for gold, which results in the covalent attachment of the PEG-SH to the surface of the Au-NRs. The minimum amount of PEG-SH required to stabilize the surface of the Au-NRs was calculated based on Manson et al. [29]. To produce a PEG-SH coating on the surface of the Au-NRs, 9 μg of PEG-SH per mL of synthesized NPs was added.

2.3. Langmuir and Langmuir-Blodgett thin film preparation

Milli-Q water was used for all aqueous solutions and as the Langmuir subphase, while chloroform was used to prepare the Au-NRs dispersion, mixtures of Au-NRs with chloroform being prepared in such a way that the ratio of methanol to chloroform was 1:4 (v:v). In order to optimize dispersion in an organic solvent, thus facilitating the spread at the air–water interface, the synthetic methods proposed by Serrano-Montes et al. could be applied [30]. Experiments were carried out using a Langmuir-Blodgett (KSV Nima) balance equipped with a Langmuir trough (304 × 75 mm), two hydrophilic barriers made of Delrin polymer, and a Brewster angle microscope (MicroBAM, KSV Nima). The laser power and image acquisition parameters were kept the same during all the BAM measurements. In order to measure the surface pressure, a platinum Wilhelmy plate (instrumental accuracy 0.01 $mN \cdot m^{-1}$) was used. Au-NRs are characterized by high values of extinction coefficient, and thus it is easy to notice their presence at particular areas on the Langmuir trough because of their adsorption. During our experiments, the barriers and the Wilhelmy plate were not covered by the gold nanoparticles, as we did not observe the specific color on their surface. Before each measurement, the trough surface was cleaned with isopropanol, acetone, and ultrapure water to obtain a surface pressure value for the pure subphase (ultrapure water) below 0.2 $mN \cdot m^{-1}$ at the maximum compression.

Dispersions of Au-NRs in chloroform (4 mL) were spread onto the surface of the subphase using a microsyringe (Hamilton). After the evaporation of solvent (approx. 25 min) from the dispersion of the Au-NRs, a molecular layer was formed by the symmetrical movement of the barriers at a constant speed of 5 mm·min $^{-1}$. During the compression, the dependence of the surface pressure on the surface of the trough was recorded. Additionally, BAM images were recorded during the compression, which allowed the monitoring of structural changes in the surface film due to the presence of Au-NRs.

Relaxation experiments were performed to determine the stability of the monolayers, dispersions of Au-NRs in chloroform (4 mL) being spread onto the surface of the subphase. After evaporation of the solvent (approx. 15 min), the monolayer was compressed (at a constant speed of 5 $mm \cdot min^{-1}$) to surface pressures of 4, 8, 12, 15, and 20 $mN \cdot m^{-1}$, and the change in the relative surface area ($A \cdot A_0^{-1}$) with time (t) was recorded.

Quartz plates (25 × 25 × 1 mm) were used as substrates for surface film deposition using the Langmuir-Blodgett technique. Prior to the Langmuir monolayer deposition, the substrates were subjected to ultrasound for 20 min at 70 °C in a mixture of ultrapure water, 4%

ammonia, and 5% hydrogen peroxide, in order to remove organic residues and to make the surface strongly hydrophilic. After several rinses with ultrapure water, the hydrophilic substrates were ready for the LB film deposition. The deposition process was carried out at surface pressures of 4, 8, 12, 15, and 20 $mN{\cdot}m^{-1}$. The speed was 3 $mm{\cdot}min^{-1}$ for the upstroke. The transfer ratio for all the studied surface pressures was around 1. Each experiment was carried out at a constant temperature of (22 ± 1) °C and repeated three times to ensure the reproducibility of the curves.

2.4. Microscopic and spectroscopic measurements

The morphology and size dispersion of Au-NRs were characterized by high-resolution transmission electron microscopy (HR-TEM). Examples of HR-TEM images of Au-NRs can be found in our previous papers [24,25]. For our investigation, Au-NRs having an aspect ratio of 2.25 ± 0.23 [length (53.2 ± 1.8) nm and width (23.6 ± 1.3) nm] were chosen. The morphology of the obtained nanoplatforms, Au-NR Langmuir-Blodgett layers deposited on quartz substrates at different surface pressures, were obtained using confocal laser scanning microscopy (LSM710, Zeiss, Germany). In material mode (reflected light), the He-Ne laser operated at a wavelength of 543 nm. Images were collected from different Z planes using a Z Stack Module for the acquisition of Z-stacks with the aid of a motorized focus drive. ImageJ processing software was used to calculate the values of the surface coverage and their standard deviation. For this purpose, ten independent images of the obtained nanoplatforms were taken into consideration. Electronic absorption spectra of the Au-NR Langmuir-Blodgett layers were measured using a Varian Cary 4000 spectrometer. The *in-situ* electronic absorption spectra of the Langmuir layers were recorded in the UV–vis range with an Ocean Optics QE65000 spectrometer, which was placed in proximity to a quartz window of the KSV Nima trough. In order to measure the Raman spectra of the *p*-MBA and the model dye rhodamine 6G, Novascan UV Ozone cleaner was used to remove traces of organic compounds, including PEG-SH and CTAB molecules. We did not observe any changes in the absorption spectra of Langmuir-Blodgett layers or in their confocal microscope images after removing traces of organic compounds. Finally, 0.1 mM *p*-MBA aqueous solution (prepared from 1 mM solutions in ethanol) and 10^{-6} M rhodamine 6G aqueous solution were incubated on the surface of the Au-NR Langmuir-Blodgett layers overnight. The substrates were then washed with Milli-Q water and dried under nitrogen. SERS spectra were obtained using a Renishaw inVia micro-Raman system with instrument control software (Renishaw WiRE 3.1). All spectra were recorded with a 785 nm excitation wavelength using a diode laser with a power of less than 10 mW. The laser beam was focused on the sample surface by a Leica long working distance (LWD) 50x objective (numerical aperture 0.5). The spectra were recorded at room temperature in a range from 600 cm^{-1} to 1800 cm^{-1} for *p*-MBA and from 400 cm^{-1} to 1600 cm^{-1} for rhodamine 6G with a spectral resolution of 2.5 cm^{-1}. Due to the heterogeneous character of the substrates, the integration area of the SERS measurements was randomly selected. Typically, fifteen spectra from different places within the sample were acquired for each surface pressure. To be more precise, we randomly collected five spectra and then moved to different areas within the sample; we then collected another ten spectra from an area of 50 μm × 50 μm. For every sample, based on these fifteen original spectra, an average spectrum was calculated and further calculations carried out.

3. Results and discussion

CTAB plays an important role in the synthesis of Au-NRs, as CTAB molecules are responsible for the formation of a bilayer around the Au-NRs, which ensures their stability in aqueous solutions. It is particularly important to select the correct concentration of CTAB, because too low a concentration may cause aggregation of NRs [9]. CTAB is added in a significant amount during the production of Au-NRs, which may influence the shape of the Langmuir isotherm, due to the amphiphilic character of the CTAB molecule. We therefore decided to determine the concentration of CTAB that remained on the surface of the Au-NRs (or in the Au-NR solutions) after centrifugation and exchange with PEG-SH. According to the procedure presented by Adura et al. [31], a calibration curve for CTAB solutions was plotted, which allowed the concentration of CTAB in the synthesized Au-NRs to be determined. For this purpose, a series of solutions of CTAB in ultrapure water with concentrations of $2{\cdot}10^{-5}$ M to $1{\cdot}10^{-4}$ M were prepared. In the next step, samples consisting of 5 mL of chloroform, 1 mL of CTAB, and 1 mL of $1{\cdot}10^{-3}$ M BPB were mixed for 30 min. After 10 min from the completion of mixing, the organic phase was extracted and the visible light absorbance read with a spectrophotometer at 606 nm. The dependence of the absorbance of the organic phase *versus* CTAB concentration had a linear character as follows: A=(8535·C)–0.319, where: A – absorbance of organic phase at 606 nm, C – CTAB concentration in [M]. As a result of the 2-fold centrifugation of the Au-NRs and their exchange with PEG-SH, the amount of CTAB was reduced to a concentration of $1{\cdot}10^{-5}$ M. On the other hand, after 3-fold centrifugation, which caused aggregation of the Au-NRs, the CTAB concentration in solution was $1{\cdot}10^{-6}$ M. Moreover, incorporation of PEG-SH into solution for ligand exchange is necessary to increase the stability of the Au-NRs in non-aqueous solutions [32]. To determine the efficiency of the exchange between CTAB and PEG-SH, we decided to record the FT-IR spectrum of the supernatant (3-fold centrifugation of Au-NRs) (results not shown). As a result, it was found that a significant amount of PEG-SH was attached to the surfaces of the Au-NRs because we did not observe peaks specific for PEG-SH in the supernatant of the centrifuged Au-NRs. This small amount of PEG-SH was not able to form a Langmuir monolayer, even after spreading onto the mixture of polar and nonpolar solvents. To confirm the slight influence of the residual CTAB on the Au-NR Langmuir monolayers, isotherms were calculated for CTAB in chloroform. For this purpose, a CTAB solution was prepared with a concentration corresponding to that of CTAB in the supernatant after 3-fold centrifugation. As shown in Fig. 1, in the case of the CTAB monolayer, the course of the isotherm differed from that of the Au-NR monolayer. The CTAB isotherm was characterized by zero surface pressure over a large range of the trough surface, but the surface pressure increased rapidly at approx. 50 cm^2. This trend confirmed that the amount of CTAB remaining in the Au-NR solution after the exchange with PEG-SH was insignificant. Moreover, the shape and course of the CTAB isotherm was consistent with the studies by Dey et al. [33]. On the

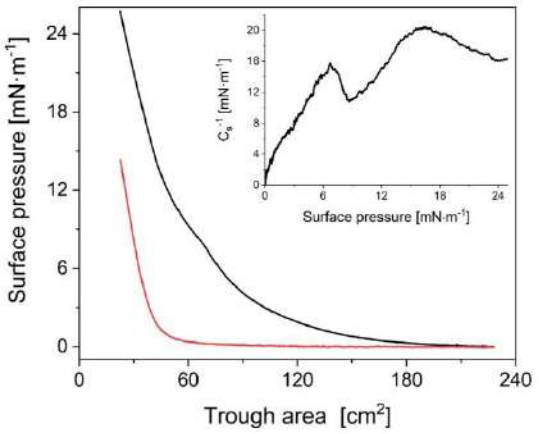

Fig. 1. The surface pressure *versus* trough area isotherm of the Au-NR Langmuir monolayer (black line) and CTAB (red line); the inset graph presents the dependence of surface compressional modulus C_s^{-1} on surface pressure of Au-NRs.

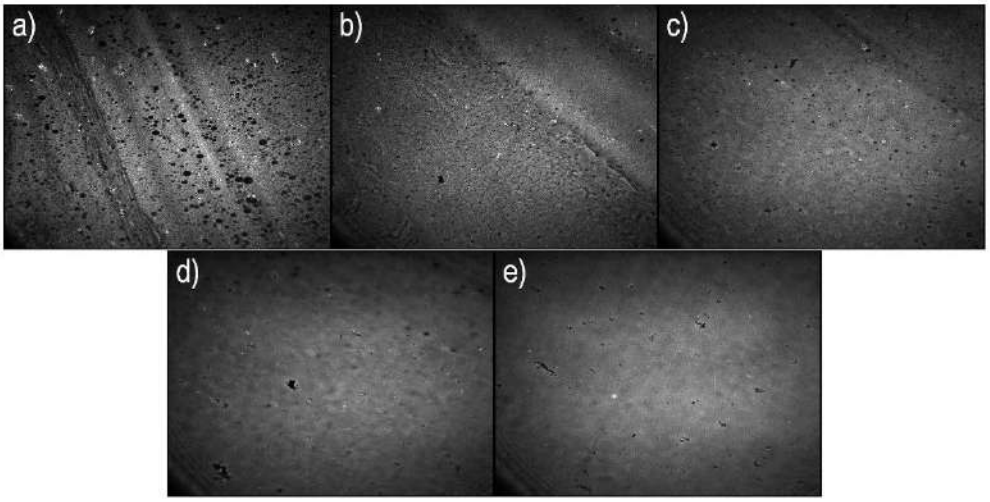

Fig. 2. Brewster angle microscope images of Au-NR Langmuir monolayer for surface pressures equal to 4 **(a)**, 8 **(b)**, 12 **(c)**, 15 **(d)**, and 20 $mN{\cdot}m^{-1}$ **(e)**.

other hand, in the case of the Au-NR isotherm, the surface pressure value increased from the start of the compression. In the area from about 220 cm^2 to about 60 cm^2, the increase in surface pressure was gradual, while for smaller values of the trough surface it was rapid. During the compression of the monolayer, a color corresponding to that of the Au-NRs was visible on the surface. On compression, this color became increasingly intense, which indicated the formation of a surface film. At the moment of starting the compression the Au-NRs monolayer was in the gaseous state (surface pressure was equal to 0 $mN{\cdot}m^{-1}$) and probably due to this fact we did not observe Au-NRs collapse. We used a medium-size Langmuir trough thus we cannot spread more Au-NRs. This could be done using a high compression trough where additional phases and collapse point of Au-NRs could be observed during compression. There are several reports showing that gold NPs are capable of forming stable monolayers. Ishida et al. [34] used gold NPs with added PEG-SH in their research, in which Langmuir isotherms showed that the presence of PEG-SH influenced the achievement of higher values of surface pressure and thus supported the formation of ordered structures. Additionally, research conducted by Lafuente et al. [35] showed that octadecylthiolate-protected gold NPs dispersed in chloroform produced systems capable of forming Langmuir monolayers. The authors showed that the long alkyl chains in the coatings of NPs tended to elongate in nonpolar solvents such as hexane, which caused aggregation between NPs. In contrast, in more polar solvents such as chloroform, the elongation of the alkyl chains was less pronounced, resulting in weaker interactions between NPs and thus allowing for the formation of more stable systems. Additionally, Fülöp et al. [36] observed a similar effect for silica-shell Au-NRs. Covering the surface of the NPs with a layer of silica prevented strong van der Waals interactions between the NPs during monolayer formation and allowed them to maintain the appropriate optical properties. In subsequent studies [37], the authors showed that the thickness of the silica coating is important, affecting the optical properties of the system, although the physicochemical behavior of the system did not change.

Additionally, during the compression of the monolayer, changes were noted to the value of the compression modulus, which is defined as follows [38]:

$$C_s^{-1} = -A\cdot\left(\frac{d\pi}{dA}\right)_T. \quad (1)$$

The analysis of the compressibility coefficient value provides information about the elasticity of the monolayer and its physical state. It is assumed that if the value of C_s^{-1} is less than 12.5 $mN{\cdot}m^{-1}$, then the monolayer is in the gaseous state (G). On the other hand, the expanded liquid state (LE) is observed when the value of the compression modulus ranges from 12.5 $mN{\cdot}m^{-1}$ to 50 $mN{\cdot}m^{-1}$. The range of C_s^{-1} values between 50 $mN{\cdot}m^{-1}$ and 250 $mN{\cdot}m^{-1}$ corresponds to the condensed liquid phase (LC), and values above 250 $mN{\cdot}m^{-1}$ correspond to the solid phase (S). The C_s^{-1} values obtained for the Au-NRs presented in Fig. 1 indicated that this monolayer, formed at the air–water interface, was in the gaseous state until the surface pressure was approx. 5 $mN{\cdot}m^{-1}$. However, the change in compressibility occurring around 6 $mN{\cdot}m^{-1}$ corresponded to the conformational changes in the PEG-SH, as confirmed by the change in the slope of the isotherm. However, for higher values of surface pressures, the monolayer was in the expanded liquid state. One of the reasons for the observed phenomenon may be the presence of a PEG-SH layer on the surface of the Au-NRs. Ishida et al. [34] showed that during the compression of a monolayer of gold NPs covered with a PEG-SH layer, it changed from a gaseous state to an expanded liquid state. As a result, the surface films containing PEG-SH were characterized by greater flexibility and stability.

In order to determine the reversibility of the compression process, the compression/expansion hysteresis of the Au-NR Langmuir monolayer was measured for the maximum value of the surface pressure and for a surface pressure equal to 15 $mN{\cdot}m^{-1}$ (the result for this value of surface pressure was omitted for clarity). The experiment also provided information on the aggregation of Au-NRs. The course of the curves (Fig. S2, see SM) showed that the compression process of the Au-NRs was reversible. Moreover, the isotherms recorded for both compression and expansion were characterized by an almost identical course, which proved the lack of aggregation of Au-NRs upon monolayer compression. We did not observe abnormal desorption of Au-NRs from the air–water interface to the water subphase within the time necessary to perform the Langmuir monolayer compression and deposition. A relaxation experiment was performed to determine the effect of the packing of the Au-NRs on monolayer stability. The film was deposited onto a solid substrate at several selected surface pressures. The criterion for selecting the surface pressures was their location on the graph showing the dependence of the surface compressional modulus C_s^{-1} on surface pressure (Fig. 1). Two values of surface pressure (4 and 12 $mN{\cdot}m^{-1}$) were selected, corresponding to half the maximum value of

C_s^{-1}. Relaxation measurements and depositions were also carried out for the maximum of C_s^{-1} (15 mN·m^{-1}). Moreover, 8 mN·m^{-1} (located after the maximum of C_s^{-1}, near the phase transition) and 20 mN·m^{-1} (located just after maximum packing of the Au-NRs) were chosen. On the basis of the relaxation curve analysis (Fig. S3, see SM), it was found that with increasing surface pressure, for which changes in the relative area over time were recorded, the stability of the monolayer decreased. In other words, the system was more compressed the more the Au-NR particles were packed on the surface of the film. In the relaxation process carried out at 4 mN·m^{-1}, the $A \cdot A_0^{-1}$ values remained constant at about 0.95. The observed stability of the surface film may have resulted from strong interactions of Au-NRs with each other. On the other hand, increasing the surface pressure to 8 mN·m^{-1} caused the relative surface value of $A \cdot A_0^{-1}$ to drop. In this case, we also noted stabilization, but only after the initial degradation of the monolayer, i.e., after approx. 75 min, when the $A \cdot A_0^{-1}$ value was at a level of approx. 0.82. A steep decrease in the $A \cdot A_0^{-1}$ value for the curve corresponding to 12 mN·m^{-1} suggested that the monolayer tended to stabilize, but this could only be achieved after a much longer time than that shown in Fig. S3, see SM. In turn, for surface pressures above 12 mN·m^{-1}, we observed film degradation, which corresponded to a decrease in the $A \cdot A_0^{-1}$ value during the entire duration of the process.

The BAM images of the Langmuir monolayer (Fig. 2), which showed changes in its structure during compression, confirmed the formation of the Au-NR surface film. The monolayer at the start of the compression was heterogeneous. For a surface pressure of 4 mN·m^{-1} (Fig. 2a), numerous bright bands were visible. They testified to the coexistence of gas and expanded liquid phases. Compression of the Au-NR Langmuir monolayer (Fig. 2b-e) gradually covered the surface, and consequently it formed a more homogeneous continuous film at the air–water interface.

To understand the arrangement of the Au-NRs in Langmuir and Langmuir-Blodgett layers, we performed spectroscopic and microscopic analysis of the obtained films, see Figs. 3-4. The easiest way to produce a Langmuir monolayer from highly hydrophilic material is to mix polar and nonpolar solvents. We obtained the best spreading conditions for PEG-SH functionalized Au-NRs dissolved in a methanol and chloroform mixture (1:4 (v:v)), see experimental section for details. Compared with the chemical graft method for the NPs' functionalization, the physical/chemical method can give rise to an amphiphilic character of the particles at the air–water interface, which aids the spreading of the particles on the water surface. However, NPs with an amphiphilic character cannot closely pack due to their relatively weak particle–particle interaction [39]. Weak particle packing influences the performance of the SERS nanoplatform. The use of alkanethiols as stabilizers provides a simple pathway for the transfer of spherical NPs to organic solvent [35,40]; however, it is not an easy task for Au-NRs due to the presence of a CTAB bilayer at the Au-NR surface. Using PEG-SH as a ligand and stabilizing agent could promote the polymer-grafted self-assembly of NPs into arrays [7,8]. The extension of the alkyl chains into a more polar solvent than hexane, such as chloroform, is less pronounced, resulting in weaker van der Waals interactions among neighboring Au-NRs and thus resulting in more stable dispersions.

To obtain information about the dispersion of the Au-NRs in the Langmuir monolayer, the *in-situ* absorption spectra were recorded at several surface pressures, see Fig. 3 panel (a) and (b). The obtained spectra were slightly redshifted compared to the spectra of the Au-NR solution (results not shown). A similar trend was recently reported for hydrophobic spherical NPs [35]. Furthermore, the position of the longitudinal LSPR peak was linearly dependent on the surface pressure, see panel (b) in Fig. 3, which confirmed the uniform character of the Au-NR

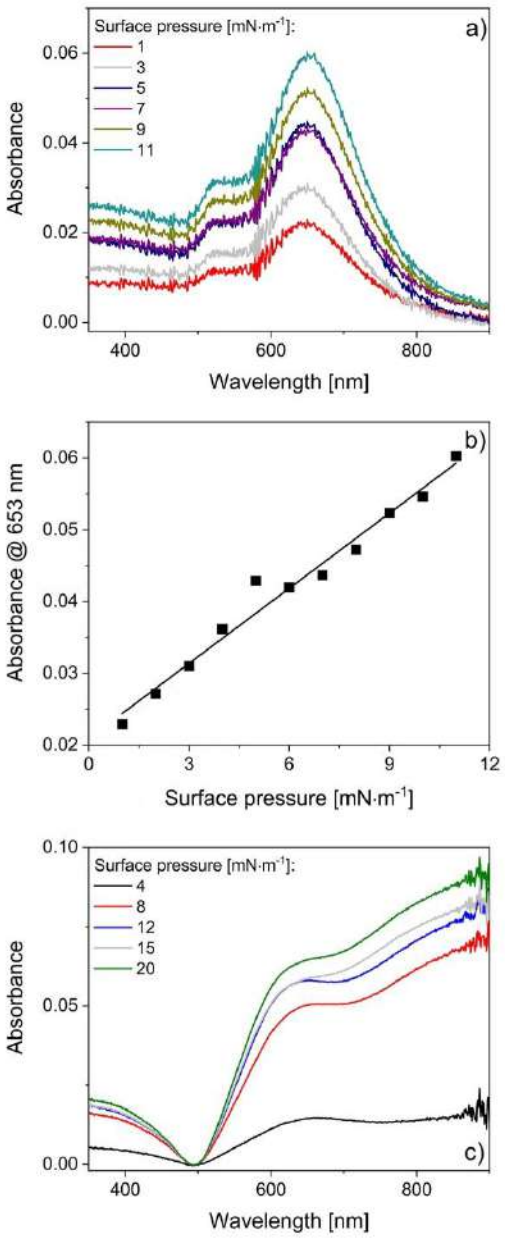

Fig. 3. *In-situ* absorption spectra of Au-NR Langmuir monolayers **(a)**, dependence of absorbance value of longitudinal LSPR peak *versus* surface pressure **(b)** obtained from (a), and the absorption spectra of the Au-NR Langmuir-Blodgett layer deposited on quartz **(c)**.

monolayer. Moreover, BAM images of the Au-NR monolayer showed the progressive increase in surface density upon layer compression, see Fig. 3. This phenomenon could be attributed to the domain formation of the Au-NRs at the air–water interface as a result of self-organization. The unchanged LSPR band position in the Au-NR Langmuir monolayer indicated that the plasmon modes could not hybridize in the range of the studied surface pressures, probably due to the presence of a relatively thick PEG-SH layer at the surface of the Au-NRs [41,42]. Upon Langmuir monolayer compression, the domains becoming closer to each other resulted in the formation of a rigid Au-NR monolayer. The same tendency was observed in previous studies by Ishida et al. [34] for hydrophobic spherical NPs. The situation was different for the Au-NR Langmuir monolayers transferred to the quartz substrates, see Fig. 3 panel (c) and Fig. 4. Due to the dewetting process during Langmuir-Blodgett depositions, the Au-NRs tended to aggregate into dendritic-like structures, as shown in Fig. 4. When the quartz substrate was pulled, the Au-NRs at the contact line were taken off the surface film and dried onto the substrate. During this step, the continuous line of nanoparticles at the water–solid interface line tended to segregate into aggregated dendritic structures. The amount of dendritic structures and the surface coverage of the Au-NRs could be tailored by controlling the deposition surface pressure, as shown in Fig. 4a-f. The obtained dendritic structures were oriented quasi-parallel to the removal direction of the quartz substrate from the aqueous subphase. Upon increasing the surface pressure, as shown in Fig. 4 panel (a) to (e), the surface coverage increased. The positive effect of the increase in the surface coverage of Au-NRs on the performance of the SERS nanoplatform was recently demonstrated by Solís et al. [21]. In the absorption spectra of the Au-NRs, a gradual increase in the absorbance was observed with an increase in the deposition surface pressure as well as with an increase in the numbers of dendritic structures, see Fig. 3c. Unfortunately, due to the lack of a spectrophotometer with a longer wavelength range, we were unable to record spectra above 900 nm. However, in a study by Serrano-Montes et al. [30], covering a homogeneous arrangement of Au-NRs, a gradually decrease in the absorbance was observed for wavelengths above 900 nm. The aggregation of the particles was the reason for the increasing magnitude of extinction. Moreover, in the absorption spectra of the Au-NRs on the quartz substrate (compare Fig. 3a with Fig. 3c), a strong redshift of the bands was observed due to the aggregation of the Au-NRs and their formation of dendritic structures. For monolayers of tightly packed Au-NRs, broad maxima resulted from a dense spectral distribution of resonances associated with the varied gap morphologies of randomly occurring gaps. Each band in the spectra was wide, and their deconvolution would be difficult to perform. Aggregation of the particles in dimers and monolayers generally produced additional redshifts of the spectral features caused by interparticle gaps, as well as an increase in the magnitude of the extinction coefficient [21]. In other words, small interparticle distances led to plasmon coupling, which was reflected in a significant redshift and the broadening of LSPR bands [30]. Plasmon coupling has been demonstrated to enhance the plasmonic features in 2D SERS active platforms. A similar behavior of the extinction spectra was observed for cube-shaped, nanoprisms NPs in polymer-grafted self-assembled layers [7,41] and for nanostars and Au-NRs [30].

To study the influence of the transfer surface pressure on the properties of the SERS nanoplatform, we analyzed standard solutions of *p*-MBA and rhodamine 6G. Fig. 5 presents the average SERS spectra of *p*-MBA (Fig. 5a) and rhodamine 6G (Fig. 5c) adsorbed on Au-NR Langmuir monolayers prepared at different transfer surface pressures. We chose several deposition surface pressures, as described above, in order to study the influence of plasmonic coupling and the surface coverage of the Au-NRs on the SERS performance. The two model molecules mentioned above were chosen as the target analytes. *p*-MBA is a molecule that chemisorbs onto the gold surface, while rhodamine 6G is a model dye which is commonly used for SERS studies [16]. Fig. 5a shows the characteristic bands for *p*-MBA at 1074 cm^{-1} and 1586 cm^{-1}, which can be assigned as in-plane ring breathing + stretching (C – S) and totally symmetric stretching (CC), respectively [43]. For rhodamine 6G

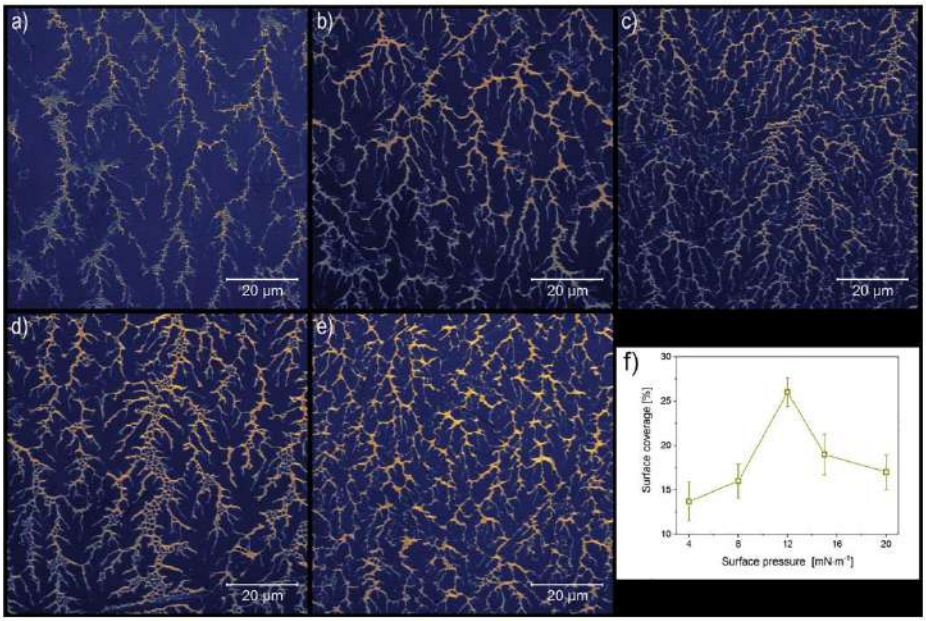

Fig. 4. Examples of confocal microscopy images of Au-NR Langmuir-Blodgett layers deposited on quartz substrates for surface pressures of 4 **(a)**, 8 **(b)**, 12 **(c)**, 15 **(d)**, and 20 $mN \cdot m^{-1}$ **(e)**. The dependence of the surface coverage of Au-NRs *versus* deposition surface pressure **(f)**. The longitudinal sides of the panels **(a)** to **(e)** represent the direction of removal of the quartz substrate from the aqueous subphase.

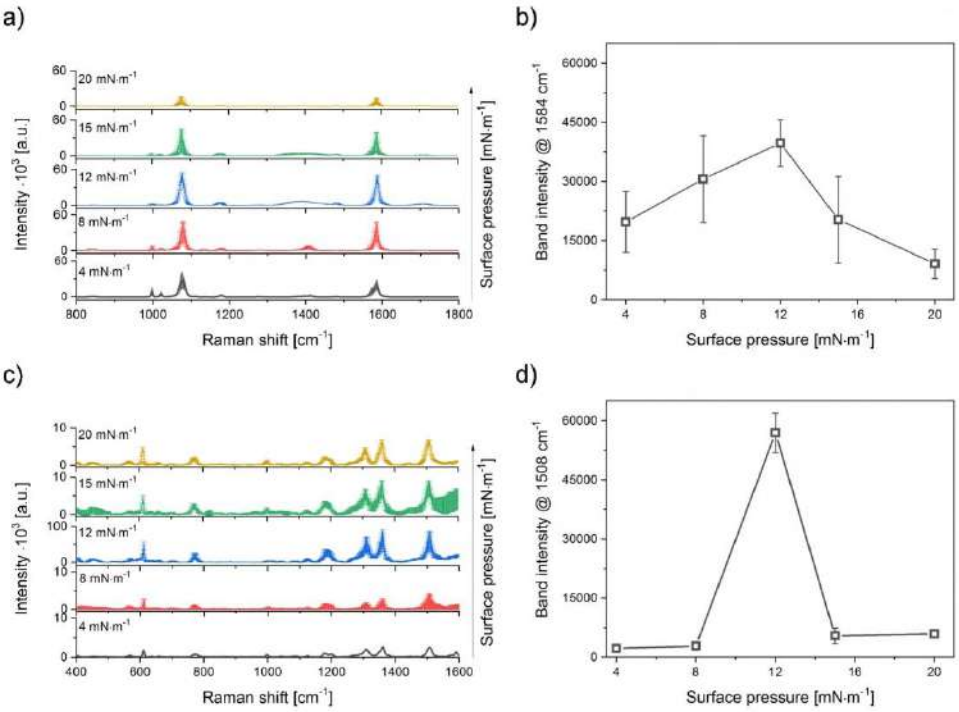

Fig. 5. Surface-enhanced Raman average spectra and average SERS peak intensity of the characteristic peak of *p*-MBA **(a)** and **(b)** and of rhodamine 6G **(c)** and **(d)**, respectively, for various transfer surface pressures of Au-NR Langmuir monolayers. The standard deviation is marked on all the plots.

we observed the characteristic bands at 610 cm^{-1} (C-C-C ring in-plane bending), 770 cm^{-1} (C–H out-of-plane bending), 1180 cm^{-1} (C-H in-plane bending), 1309 cm^{-1} (hybrid mode xanthene/phenyl rings and NHC_2H_5 group), and 1508 cm^{-1} (C-C stretching in the xanthene ring) [44]. For further analysis characteristic bands were selected: 1586 cm^{-1} for *p*-MBA and 1508 cm^{-1} for rhodamine 6G. For both *p*-MBA and rhodamine 6G, the height of the characteristic peaks at 1586 cm^{-1} (Fig. 5b) and 1508 cm^{-1} (Fig. 5d), respectively, increased with the increase in the surface pressure until it reached its maximum value at 12 $mN{\cdot}m^{-1}$. Typically, in most of the cases, only one analyte was chosen, i.e., *p*-MBA, which anchors to the surface of the gold. We decided to expand our studies to rhodamine 6G, which was not chemically attached to the surface of the nanorods. In both cases, the maximum SERS intensity was observed at 12 $mN{\cdot}m^{-1}$, and thus we showed that the performance of the nanoplatforms was not dependent on the type of analyte. Additionally, we estimated the SERS enhancement factor (EF), based on the SERS and normal Raman spectrum of *p*-MBA gathered for standard solutions and crystals of *p*-MBA, using the following equation [45]:

$$EF = \frac{I_{SERS}}{N_{SERS}} \cdot \frac{N_{Raman}}{I_{Raman}}, \quad (2)$$

where: I_{SERS} and I_{Raman} correspond to the intensity of the characteristic peak of the solution of *p*-MBA for the SERS and the Raman signal for the crystal; N_{SERS} and N_{Raman} are the numbers of *p*-MBA molecules effectively excited by the laser beam to obtain the corresponding SERS and normal Raman spectra, respectively. For 12 $mN{\cdot}m^{-1}$, the EF factor was estimated as $1.9{\cdot}10^5$. In both cases (*p*-MBA and rhodamine 6G), maximum SERS intensities were observed for Au-NRs transferred at 12 $mN{\cdot}m^{-1}$. Further compression of the Langmuir monolayer as well as increasing the C_s^{-1} value did not improve the SERS performance. Similar behavior was reported recently by Tahghighi et al. for hydrophobic spherical NPs [22] and for nanostars [46]. The authors postulated that the maximum value of the peak intensity corresponded to the limit of monolayer stability, and further compression resulted in a decrease in the hot spot density due to the formation of multilayer aggregates at both the air–water and air-sold interfaces. The Au-NRs studied herein tended not to form aggregated forms in the Langmuir monolayer, as discussed previously (Figs. 1-3a). A different situation was observed for Langmuir-Blodgett layers. We were unable to produce a nanoplatform with higher surface coverages of Au-NRs than is shown in Fig. 4f. The maximum value of surface coverage was obtained for 12 $mN{\cdot}m^{-1}$. The drop in the SERS intensities could therefore be attributed to the multilayer aggregates and the progressive decrease in hot spot density for surface pressures above 12 $mN{\cdot}m^{-1}$ for the solid substrates. As shown by Nowak et al. [47] a SERS Ag-Cu substrate with a particular microarchitecture possessed a fern-like structures which enhanced the rhodamine 6G signal and could be used as a potential support for medical diagnostics. The transfer ratio for all the studied surface pressures was around 1, meaning that whole films were transferred from the water subphase, and aggregation at the solid substrate may have induced additional hot spots due to plasmon coupling. We are aware that high SERS enhancement values from aggregated nanostructures mean that these structures are likely to generate poorly controllable and heterogeneous SERS signals to a larger degree than the cases with lower enhancement. Even though our substrates were heterogeneous due to the aggregation of Au-NRs, the randomly collected SERS spectra were characterized by a relatively low experimental error and high

repeatability. The standard mode laser spot size in the Raman system was around a few microns, so that if the Raman system was coupled with a microscope, it was possible to excite analyzed molecules in the vicinity of the dendritic structure. In order to reduce the numbers of dendritic structures of Au-NRs at the solid substrate, other variants of the substrate extraction could be used. For instance, the submerged substrate could be lifted parallel to the air–water interface, the so-called Langmuir-Schaefer layer.

4. Conclusions

The aim of the study was the formation of Langmuir-Blodgett layers consisting of pegylated Au-NRs, which were then used to optimize the SERS performance for ultrasensitive detection of model molecules (*p*-MBA and rhodamine 6G). The obtained results indicated that dispersions of pegylated Au-NRs in chloroform formed insoluble Langmuir monolayers on the ultrapure water subphase. In addition, relaxation studies showed that the stability of the surface film decreased with increasing surface pressure. It has been proved that the compression of the Au-NRs was a reversible process, and upon monolayer compression there was no aggregation of Au-NRs. A different situation was noted for Au-NRs transferred onto solid substrates. The dewetting process induced strong Au-NR aggregation, giving aggregates with dendritic structures. Upon increasing the transfer surface pressure, the aggregates became closely packed, while their orientation was quasi-parallel to the direction of removal of the quartz substrate from the aqueous subphase. Moreover, we have demonstrated that, for the arrangement of Au-NRs in dendritic structures, the enhanced SERS detection of model molecules could be tuned by taking into account plasmonic coupling and surface coverage. The optimum transfer surface pressure for SERS nanoplatform formation was 12 $mN{\cdot}m^{-1}$. The results suggest the potential of hydrophilic, pegylated Au-NR thin layers for ultrasensitive detection of molecular species. The best nanoplatform described within this study could be used for single-molecule studies in the detection of photosynthetic pigments in which the laser spot of the Raman system would be precisely localized at the hot spot of the dendritic aggregates.

CRediT authorship contribution statement

Beata Tim: Investigation, Visualization, Methodology, Data curation, Writing – original draft. **Paulina Błaszkiewicz:** Investigation, Writing – original draft. **Ariadna B. Nowicka:** Investigation, Writing – original draft. **Michał Kotkowiak:** Conceptualization, Investigation, Methodology, Visualization, Data curation, Writing – original draft, Writing – review & editing, Supervision, Funding acquisition.

Declaration of Competing Interest

The authors declare that they have no known competing financial interests or personal relationships that could have appeared to influence the work reported in this paper.

Acknowledgment

This work was supported by the National Science Center in Poland by the project 2019/35/D/ST4/02037.

Appendix A. Supplementary material

Supplementary data to this article can be found online at https://doi.org/10.1016/j.apsusc.2021.151518.

References

[1] P.K. Jain, M.A. El Sayed, Plasmonic coupling in noble metal nanostructures, Chem. Phys. Lett. 487 (4-6) (2010) 153–164.
[2] I.H. El-Sayed, X. Huang, M.A. El-Sayed, Surface plasmon resonance scattering and absorption of anti EGFR antibody conjugated gold nanoparticles in cancer diagnostics: Applications in oral cancer, Nano Lett. 5 (2005) 829–834.
[3] P. Błaszkiewicz, M. Kotkowiak, Gold-based nanoparticles systems in phototherapy – current strategies, Curr. Med. Chem. 25 (42) (2019) 5914–5929.
[4] Y. Ofir, B. Samanta, V.M. Rotello, Polymer and biopolymer mediated self-assembly of gold nanoparticles, Chem. Soc. Rev. 37 (9) (2008) 1814–1825.
[5] J. Paczesny, A. Kamińska, W. Adamkiewicz, K. Winkler, K. Sozanski, M. Wadowska, I. Dzieciclewski, R. Holyst, Three steps of hierarchical self assembly toward a stable and efficient surface enhanced Raman spectroscopy platform, Chem. Mater. 24 (19) (2012) 3667–3673.
[6] M.A. Mahmoud, R. Narayanan, M.A. El-Sayed, Enhancing colloidal metallic nanocatalysis: sharp edges and corners for solid nanoparticles and cage effect for hollow ones, Acc. Chem. Res. 46 (2013) 1795–1805.
[7] B.o. Gao, G. Arya, A.R. Tao, Self-orienting nanocubes for the assembly of plasmonic nanojunctions, Nat. Nanotechnol. 7 (7) (2012) 433–437.
[8] B. Gao, Y. Alvi, D. Rosen, M. Lav, A.R. Tao, Designer nanojunctions: orienting shaped nanoparticles within polymer thin-film nanocomposites, Chem. Comm. 49 (2013) 4382–4384.
[9] M. Grzelczak, J. Pérez-Juste, P. Mulvaney, L.M. Liz-Marzán, Shape control in gold nanoparticle synthesis, Chem. Soc. Rev. 37 (9) (2008) 1783–1791.
[10] J. Haber, K. Sokolov, Synthesis of stable citrate-capped silver nanoprisms, Langmuir. 33 (40) (2017) 10525–10530.
[11] P. Dynarowicz-Łątka, A. Dhanabalan, O.N. Oliveira, Modern physicochemical research on Langmuir monolayers, Adv. Colloid Interface Sci. 91 (2) (2001) 221–293.
[12] Y. Jeong, Y.-M. Kook, K. Lee, W.-G. Koh, Metal enhanced fluorescence (MEF) for biosensors: general approaches and a review of recent developments, Biosens. Bioelectron. 111 (2018) 102–116.
[13] P.K. Jain, K.S. Lee, I.H. El-Sayed, M.A. El-Sayed, Calculated absorption and scattering properties of gold nanoparticles of different size, shape, and composition: applications in biological imaging and biomedicine, J. Phys. Chem. B. 110 (2006) 7238–7248.
[14] S. Eustis, M.A. El-Sayed, Why gold nanoparticles are more precious than pretty gold: noble metal surface plasmon resonance and its enhancement of the radiative and nonradiative properties of nanocrystals of different shapes, Chem. Soc. Rev. 35 (2006) 209–217.
[15] R. Pilot, R. Signorini, C. Durante, L. Orian, M. Bhamidipati, L. Fabris, A review on surface-enhanced Raman scattering, Biosensors. 9 (2019) 57.
[16] J. Langer, D. Jimenez de Aberasturi, J. Aizpurua, R.A. Alvarez-Puebla, B. Auguié, J. J. Baumberg, et al., Present and future of surface-enhanced Raman scattering, ACS Nano. 14 (1) (2020) 28–117.
[17] L. Osinkina, T. Lohmüller, F. Jäckel, J. Feldmann, Synthesis of gold nanostar arrays as reliable, large-scale, homogeneous substrates for surface-enhanced Raman scattering imaging and spectroscopy, J. Phys. Chem. C. 117 (2013) 22198–22202.
[18] C. Wang, Y.i. Xu, H. Zhao, C. Gong, C. Lai, X. Liao, R. Wang, Detection and analysis of SERS effect of nano gold by self-assembly chemical plating composite method, Appl. Surf. Sci. 353 (2015) 750–756.
[19] Y.u. Lu, G.L. Liu, L.P. Lee, High-density silver nanoparticle film with temperature-controllable interparticle spacing for a tunable surface enhanced Raman scattering substrate, Nano Lett. 5 (1) (2005) 5–9.
[20] N. Marquestaut, A. Martin, D. Talaga, L. Servant, S. Ravaine, S. Reculusa, D. M. Bassani, E. Gillies, F. Lagugné-Labarthet, Raman enhancement of azobenzene monolayers on substrates prepared by Langmuir–Blodgett deposition and electron-beam lithography techniques, Langmuir. 24 (19) (2008) 11313–11321.
[21] D.M. Solís, J.M. Taboada, F. Obelleiro, L.M. Liz-Marzán, F.J. García de Abajo, Optimization of nanoparticle-based SERS substrates through large-scale realistic simulations, ACS Photonics. 4 (2) (2017) 329–337.
[22] M. Talghighi, I. Mannelli, D. Janner, J. Ignés-Mullol, Tailoring plasmonic response by Langmuir Blodgett gold nanoparticle templating for the fabrication of SERS substrates, Appl. Surf. Sci. 447 (2018) 416–422.
[23] B. Nikoobakht, M.A. El Sayed, Preparation and growth mechanism of gold nanorods (NRs) using seed-mediated growth method, Chem. Mater. 15 (10) (2003) 1957–1962.
[24] P. Błaszkiewicz, M. Kotkowiak, E. Coy, A. Dudkowiak, Laser-induced optoacoustic spectroscopy studies of inorganic functionalized metallic nanorods, J. Phys. Chem. C. 123 (44) (2019) 27181–27186.
[25] P. Błaszkiewicz, M. Kotkowiak, E. Coy, A. Dudkowiak, Tailoring fluorescence and singlet oxygen generation of a chlorophyll derivative and gold nanorods via a silica shell, J. Phys. Chem. C. 124 (3) (2020) 2088–2095.
[26] K. Rahme, L. Chen, R.G. Hobbs, M.A. Morris, C. O'Driscoll, J.D. Holmes, PEGylated gold nanoparticles: polymer quantification as a function of PEG lengths and nanoparticle dimensions, RSC Adv. 3 (2013) 6085–6094.
[27] F. Schulz, W. Friedrich, K. Hoppe, T. Vossmeyer, H. Weller, H. Lange, Effective PEGylation of gold nanorods, Nanoscale. 8 (13) (2016) 7296–7308.
[28] P. Szustakiewicz, N. Kolsut, A. Leniart, W. Lewandowski, Universal method for producing reduced graphene oxide/gold nanoparticles composites with controlled density of grafting and long-term stability, Nanomaterials. 9 (2019) 1–16.
[29] J. Manson, D. Kumar, B.J. Meenan, D. Dixon, Polyethylene glycol functionalized gold nanoparticles: the influence of capping density on stability in various media, Gold Bull. 44 (2011) 99–105.
[30] A.B. Serrano-Montes, D. Jimenez de Aberasturi, J. Langer, J.J. Giner-Casares, L. Scarabelli, A. Herrero, L.M. Liz Marzán, A general method for solvent exchange of plasmonic nanoparticles and self-assembly into SERS-active monolayers, Langmuir. 31 (33) (2015) 9205–9213.

[31] Carolina Adura, Fanny Guzman, Alejandro Álvarez-Lueje, Marcelo.J. Kogan, Ion pair method to determine the CTAB content in gold nanorods samples, J. Chil. Chem. Soc. 59 (4) (2014) 2701–2704.
[32] Z. Zhang, M. Lin, Fast loading of PEG–SH on CTAB-protected gold nanorods, RSC Adv. 4 (34) (2014) 17760–17767.
[33] B. Dey, S. Chakraborty, S. Chakraborty, D. Bhattacharjee, Inamuddin, A. Khan, S. A. Hussain, Electrical switching behaviour of a metalloporphyrin in Langmuir-Blodgett film, Org. Electron. 55 (2018) 50–62.
[34] T. Ishida, Y. Tachikiri, T. Seko, Y. Takahashi, S. Yamada, Structural characterization and plasmonic properties of two-dimensional arrays of hydrophobic large gold nanoparticles fabricated by Langmuir-Blodgett technique, Appl. Surf. Sci. 404 (2017) 350–356.
[35] M. Lafuente, S. Ruiz-Rincon, R. Mallada, P. Cea, M. Pilar Pina, Towards the reproducible fabrication of homogeneous SERS substrates by Langmuir-Schaefer technique: A low cost and scalable approach for practical SERS based sensing applications, Appl. Surf. Sci. 506 (2020) 144663–144671.
[36] E. Filop, N. Nagy, A. Deák, I. Bársony, Langmuir-Blodgett films of gold/silica core/shell nanorods, Thin Solid Films. 520 (23) (2012) 7002–7005.
[37] E. Gergely Fülöp, N. Nagy, A. Deák, Langmuir-Blodgett films of gold nanorods with different silica shell thicknesses, Period. Polytech, Chem. Eng. 59 (2) (2015) 104–110.
[38] J.T. Davies, E.K. Rideal, Interfacial Phenomena, Academic Press, 1961.
[39] C. L. Hsu, K. H. Wang, C. H. Chang, W. P. Hsu, Y. L. Lee, Surface modification of gold nanoparticles and their monolayer behavior at the air/water interface, Appl. Surf. Sci. 257 (7) (2011) 2756–2763.
[40] M. Brust, M. Walker, D. Bethell, D.J. Schiffrin, R. Whyman, Synthesis of thiol-derivatised gold nanoparticles in a two-phase Liquid-Liquid system, J. Chem. Soc. Chem. Commun. 0 (7) (1994) 801–802.
[41] D.A. Rosen, A.R. Tao, Modeling the optical properties of bowtie antenna generated by self-assembled Ag triangular nanoprisms, ACS Appl. Mater. Inter. 6 (6) (2014) 4134–4142.
[42] M. Kotkowiak, B. Grześkiewicz, E. Robak, E. Wolarz, Interaction between nanoprisms with different coupling strength, J. Phys. Chem. C. 119 (11) (2015) 6195–6203.
[43] X. Y. Zhang, D. Han, Z. Pang, Y. Sun, Y. Wang, Y. Zhang, J. Yang, L. Chen, Charge transfer in an ordered Ag/Cu2S/4-MBA system based on surface-enhanced Raman scattering, J. Phys. Chem. C. 122 (10) (2018) 5599–5605.
[44] F. Zhong, Z. Wu, J. Guo, D. Jia, Porous silicon photonic crystals coated with Ag nanoparticles as efficient substrates for detecting trace explosives using SERS, Nanomaterials. 8 (2018) 872–883.
[45] E.C. Le Ru, E. Blackie, M. Meyer, P.G. Etchegoin, Surface enhanced Raman scattering enhancement factors: a comprehensive study, J. Phys. Chem. C. 111 (2007) 13794–13803.
[46] M. Tabghighi, D. Jauner, J. Ignés-Mullol, Optimizing gold nanoparticle size and shape for the fabrication of SERS substrates by means of the Langmuir-Blodgett technique, Nanomaterials. 10 (2020) 1–11.
[47] M. Nowak, A. Trojanowska, L. Marciniak, M. Binczyk, T. Runka, B. Tylkowski, R. Jastrzab, Preparation and characterization of long-term stable SERS active materials as potential supports for medical diagnostic, Appl. Surf. Sci. 472 (2019) 93–98.

Supplementary material

for

Optimizing SERS Performance Through Aggregation of Gold Nanorods in Langmuir-Blodgett Films

Beata Tim[a,†], Paulina Błaszkiewicz[a], Ariadna B. Nowicka[a, b], Michał Kotkowiak[a,*,†]

[a]Faculty of Materials Engineering and Technical Physics, Poznan University of Technology, Piotrowo 3, 60-965 Poznan, Poland
[b]Institute of Physical Chemistry, Polish Academy of Sciences, Kasprzaka 44/52, 01-224 Warsaw, Poland

†These authors have contributed equally to this work and share first authorship

To whom correspondence should be addressed:
*E-mail: michal.kotkowiak@put.poznan.pl (M.K.)

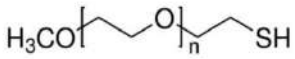

Fig. S1. Chemical structure of polymer used for gold nanorods functionalization.

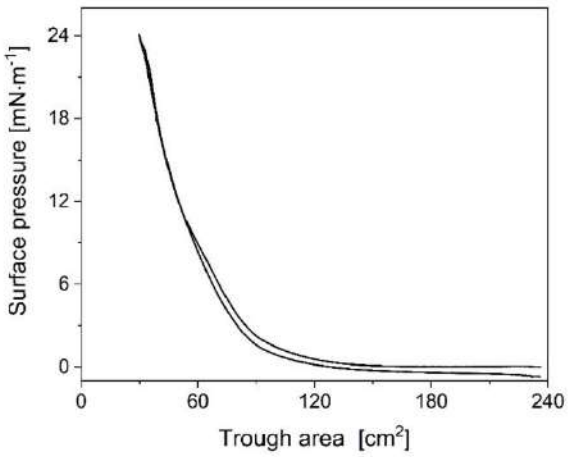

Fig. S2. The surface pressure *versus* trough area hysteresis of Au-NRs Langmuir monolayer.

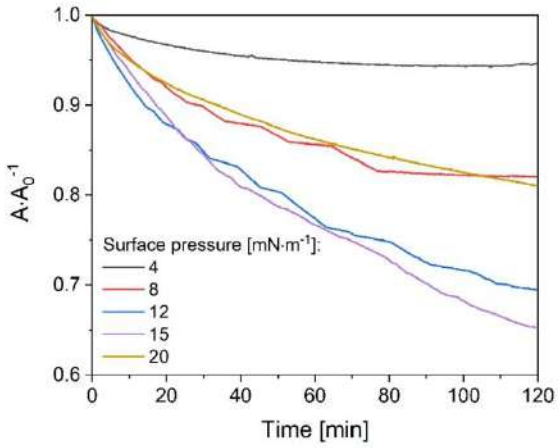

Fig. S3. Relative area changes *versus* time for a various surface pressure of Au-NRs Langmuir monolayer.

Przedruk publikacji [Kotkowiak, L 2024]

M. Kotkowiak, **B. Tim**, M. Kotkowiak, J. Musiał, P. Błaszkiewicz,

The role of the polyethylene glycol in the organization of gold nanorods at the air-water and air-solid interfaces,

Langmuir 40 (2024), 14561-14569. (IF 3,9; MNiSW 100)

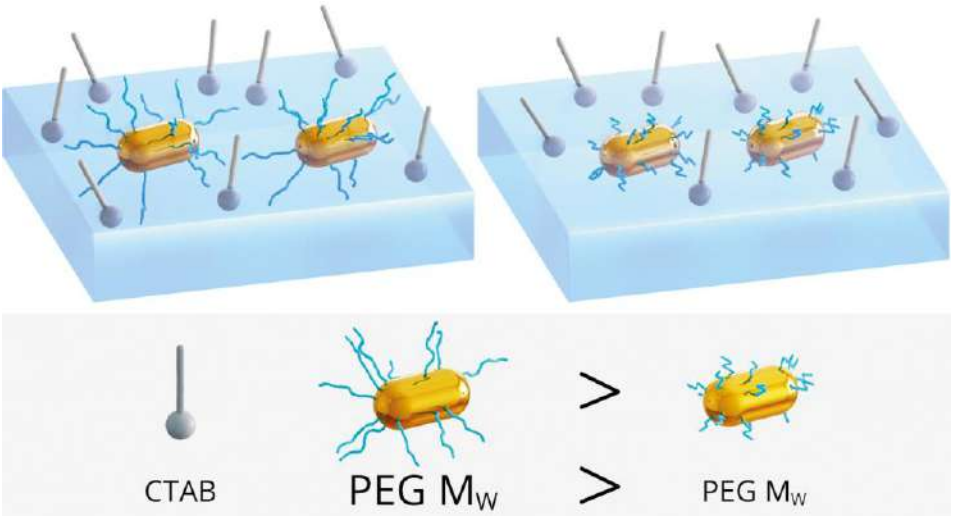

LANGMUIR

Open Access
This article is licensed under CC-BY 4.0

pubs.acs.org/Langmuir
Article

The Role of the Polyethylene Glycol in the Organization of Gold Nanorods at the Air−Water and Air−Solid Interfaces

Michał Kotkowiak,* Beata Tim, Mateusz Kotkowiak, Joanna Musiał, and Paulina Błaszkiewicz

Cite This: *Langmuir* 2024, 40, 14561−14569
Read Online

ACCESS | Metrics & More | Article Recommendations | Supporting Information

ABSTRACT: The organization of metallic nanoparticles into assembled films is a complex process. The type of nanoparticle stabilizing ligand and the method for creating an organized layer can profoundly affect the optical properties of the resulting nanoparticle assembly. Investigations of the ligand structure and nanoparticle interactions can provide a greater understanding of the design of the assembly process and the quality of the resulting materials. One of the functionalization methods in the preparation of specific gold nanorods is the utilization of thiol-terminated poly(ethylene glycol). This generates gold nanorods capable of forming stable monolayers at the air−water interface upon dispersion in a suitable organic solvent. Herein, we show that depending on the molecular weight of the poly(ethylene glycol), the structures obtained at the air−water and air−solid interfaces differ in the arrangement. The studied structures were characterized by using spectroscopic and microscopic techniques, and the structural type was correlated with the polymer type. Insoluble and stable Langmuir monolayers composed of higher-molecular-weight gold nanorods with poly(ethylene glycol) were formed only in the presence of an additional stabilizer that prevented the formation of gold nanorods in aqueous solutions. At the air−solid interface, conformational changes in poly(ethylene glycol) induced the aggregation of gold nanorods, which became closely packed under the influence of surface pressure. The presented results suggested that the arrangement of two-dimensional layers of gold nanorods could be tailored using poly(ethylene glycol) of various molecular weights.

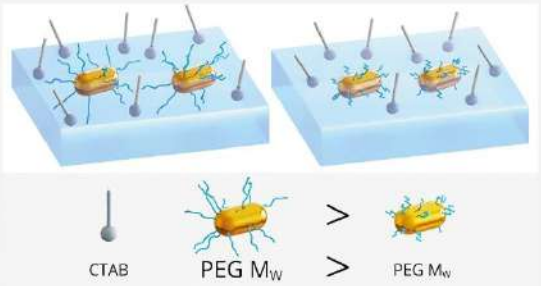

Downloaded via 91.94.109.235 on August 23, 2024 at 10:23:34 (UTC).
See https://pubs.acs.org/sharingguidelines for options on how to legitimately share published articles.

INTRODUCTION

Gold nanoparticles (Au-NPs) exhibit excellent physical, chemical, and biological properties; therefore, they have potential applications in many areas of technology.[1−3] The most crucial feature of NPs that benefits their applications is localized surface plasmon resonance (LSPR). Illumination of NPs induces charge oscillation and produces local electric field enhancement, which enhances photothermal conversion.[4] Depending on the preparation conditions, NPs with different shapes exhibiting LSPR in various spectral regions can be obtained.[5]

Spectroscopic studies of gold nanorods (Au-NRs) have two LSPRs in the transverse and longitudinal directions. The longitudinal LSPR is tunable in the spectral range from visible to near-infrared.[6] Au-NRs change their shape on the spherical surface under intense laser exposure. However, this depends on the particle's surfaces. Hence, appropriate functionalization should prevent shape deformation upon exposure to light. Additionally, control of the surface functionalization of Au-NRs is necessary for NPs to find many applications in various fields. However, difficulties arise in the exchange of the standard surface ligands, and the typical stabilizer of Au-NRs, cetyltrimethylammonium bromide (CTAB), is added, making it more challenging to promote the exchange in spherical NPs compared to sodium citrate.[7] In contrast to sodium citrate, CTAB forms a densely packed bilayer at the Au-NRs surface, and to reach the necessary stability, unbound CTAB in Au-NRs colloidal dispersion is required. Considering the toxicity of CTAB, the CTAB bilayer of Au-NRs was liganded with thiolated poly(ethylene glycol) (PEG). To reduce the cytotoxicity, Au-NRs were washed by centrifugation. However, the CTAB bilayer tends to remain on the surface of the Au-NRs, and CTAB bilayers are not covalently adsorbed on the surface. This suggests that further removal of CTAB leads to aggregation of the Au-NRs.[8] PEG was used as a linker for Au-NRs to facilitate the attachment of other functional groups to the surface of the Au-NRs via Au−S bonding. Due to its high affinity for gold, its biocompatibility, and its key role in improving the colloidal stability and dispersibility of Au-NRs in aqueous media, PEG is most commonly used in ligand

Received: April 17, 2024
Revised: June 19, 2024
Accepted: June 19, 2024
Published: July 4, 2024

ACS Publications
© 2024 The Authors. Published by American Chemical Society

https://doi.org/10.1021/acs.langmuir.4c01427
Langmuir 2024, 40, 14561−14569

exchange reactions with Au-NRs.[9] The basic method of Au-NRs PEGylation involves one-step ligand exchange. Potassium carbonate and PEG are added directly to the Au-NRs solution. Other PEGylation protocols consider the influence of pH; e.g., potassium carbonate was added under alkaline conditions. However, the use of an acidic environment at approximately pH of 3 has been reported as well.[10] PEGylation is widely applied as a surface modification method for NPs in biomedical applications to improve their biological properties, including biocompatibility and immunogenicity. The functionalization of Au-NRs with thiol-terminated PEGs yields PEGylated Au-NRs with enhanced stability and biocompatibility. The retention time of such Au-NRs in an aqueous medium is prolonged. Furthermore, PEGylated Au-NRs disperse in aqueous and several organic polar mediums, such as acetone, alcohols, acetonitrile, dimethyl sulfoxide, dimethylformamide, and phosphate-buffered saline solutions.[11] Therefore, PEGylated Au-NRs dispersed in a suitable organic solvent, e.g., chloroform, form stable monolayers at the air–water interface.[12]

The Langmuir technique is used to study nanoparticles and more complex systems, including proteins or lipids.[13] Monolayers containing NPs can be the basis for producing so-called nanoplatforms that can enhance Raman intensity. For this purpose, the monolayers produced by the Langmuir technique can be transferred to a solid substrate using the Langmuir–Blodgett (LB) or Langmuir–Schaefer (LS) techniques.[14,15] In our recent publication,[12] we described dendritic, branched structures of Au-NRs upon LB extraction and their application in the amplified detection of molecules. PEG-2k was selected to ensure a thick layer formation on the surface of Au-NRs. It was found that the thinner the layer, the more hot spots that could be induced. PEG coating is also a crucial factor in improving the biophysical properties of NPs, which is important for drug delivery systems.[16,17]

Herein, the physicochemical problem of the Au-NRs pattern formation was explored in greater detail. The PEG type in the organization of Au-NRs at the air–water and air–solid interfaces was examined. The type of formed structures was carefully characterized by using spectroscopic and microscopic techniques. Additionally, this was related to the PEG chain conformation type.

■ MATERIALS AND METHODS

Chemicals. Tetrachloroauric acid ($HAuCl_4 \cdot H_2O$) (99.99%) was obtained from Alfa Aesar. Cetyltrimethylammonium bromide (CTAB) (99.00%), sodium borohydride ($NaBH_4$) (98.00%), silver nitrate ($AgNO_3$) (99.99%), ascorbic acid (99.00%), *O*-(2-mercaptoethyl)-*O*′-methylpoly(ethylene glycol) ($M_w \approx 2000$; PEG-2k) (99.99%), *O*-[2-(3-mercaptopropionylamino)ethyl]-*O*′-methylpoly(ethylene glycol) ($M_w \approx 5000$; PEG-5k) (99.99%), and *O*-(2-mercaptoethyl)-O′-methylpoly(ethylene glycol) ($M_w \approx 10{,}000$; PEG-10k) (99.99%) were purchased from Sigma-Aldrich. Spectrophotometric grade methanol was purchased from POCH S.A. (Poland). High-purity chloroform for spectroscopy ($CHCl_3$) (>99% Uvasol), isopropanol (≥99.8%), and acetone (≥99.8%) were purchased from Merck.

Chemical Synthesis of Rod-Shaped Gold Nanoparticles and Functionalization by Polymer Coating. Aqua regia (HCl: HNO_3 3:1 (v/v)) was used to treat the glass before the synthesis of NPs. The process utilized ultrapure water (Milli-Q, 18.2 MΩ·cm, 71.98 ± 0.01 $mN \cdot m^{-1}$). Au-NRs were prepared following the procedure described by Nikoobakht et al.[18] with the modifications previously described by Blaszkiewicz et al.[19] The Au-NRs were functionalized with PEG using a modified method.[12,20] Au-NRs with a maximum absorption wavelength in the longitudinal band around 680 nm were used for the functionalization process. Their size is length (53.2 ± 1.8) nm and width (23.6 ± 1.3) nm.[19] To experimentally determine the concentration of PEGylated Au-NRs, we used inductively coupled plasma optical emission spectroscopy (ICP-OES). For this purpose, we determined the gold concentration and the gold volume per particle from the TEM measurement of particle dimensions, assuming their cylindrical shape. Dividing these numbers gave us the particle concentration. The concentrations of gold were as follows: 65 ± 4, 66 ± 4 and 61 ± 4 $mg \cdot L^{-1}$ for Au-NRs PEG-2k, 5k and 10k, respectively. The Au-NRs concentration was 7.2×10^{-10}, 7.4×10^{-10}, and 6.7×10^{-10} M for Au-NRs PEG-2k, 5k, and 10k, respectively. Au-NRs were centrifuged twice for 30 min to remove excess CTAB. Then, 10 mL of 1 mM PEG (2k, 5k, and 10k) solution was prepared and sonicated for 30 min. The centrifuged Au-NRs were redispersed in PEG solution and left stirring for 24 h at room temperature. Subsequently, the unbound PEG molecules were removed by centrifugation (twice for 30 min). The supernatant was discarded, and the Au-NRs pellet was dispersed in methanol. The functionalization reaction scheme is shown in Figure S1 (refer to the Supporting Information).

Surface Film Preparation. To obtain monolayers at the air–water interface, chloroform Au-NRs dispersions were used, according to the method described by Tim et al.[12] In the prepared mixtures of Au-NRs with chloroform, the ratio of methanol to chloroform was 1:4 (v/v). The surface films produced by the Langmuir technique were then transferred to the solid substrates (quartz plates) in two ways: using the LB and LS techniques. At the beginning of each experiment, the Langmuir trough (KSV Nima) (304 mm × 75 mm) was filled with ultrapure water, which was the subphase. Then, Au-NR dispersions were spread on the surface of the subphase and the solvent was evaporated (20 min). The layer was compressed by symmetrical movement of two Delrin polymer barriers at a constant speed of 5 $mm \cdot min^{-1}$. Changes in the surface pressure (π) values during film formation were measured using a platinum Wilhelmy plate combined with a computer-controlled Langmuir balance (KSV Nima, instrument precision of 0.01 $mN \cdot m^{-1}$). The Langmuir balance was equipped with a Brewster angle microscope (MicroBAM, KSV Nima), and the structural changes occurring during monolayer compression were recorded. The stability of the monolayer was measured using the Langmuir technique by performing relaxation experiments. For this purpose, the monolayer from Au-NRs dispersion with PEG-2k brushes was compressed (with a constant speed of 5 $mm \cdot min^{-1}$) to π equal to 4, 8, 15, 23, and 37 $mN \cdot m^{-1}$, and then the change of the relative surface area ($A \cdot A_0^{-1}$) over time (t) was recorded. In the next stage, the specific π for which relaxation experiments were performed, the monolayers were transferred to solid substrates by using LB and LS techniques. For this purpose, Au-NRs with different PEGs (2k, 5k, and 10k) were employed. Before the experiment, quartz plates (30 mm × 25 mm × 1 mm) were cleaned using an ultrasound bath for 20 min at a temperature of 70 °C in a mixture of ultrapure water, 4% ammonia, and 5% hydrogen peroxide and then rinsed in ultrapure water. In the case of the LB technique, the speed was 3 $mm \cdot min^{-1}$ for the upstroke. However, for the LS technique, it was 0.5 $mm \cdot min^{-1}$. During Langmuir monolayer deposition, the transfer ratio (TR) was monitored. For LB, the TR was around 1 in all of the analyzed cases. It should be noted that reliable and repeatable TR values are difficult to obtain for LS deposition. The operating software KSV Nima provided TR values. However, due to the relatively large dimensions of the substrate, the TR value could be overestimated using the LS technique. Thus, visual observation was prioritized during the transference to ensure that the transferred material was deposited uniformly. Each experiment was carried out in triplicate to ensure the repeatability of the curves at a constant temperature of 21 ± 1 °C.

Microscopic and Spectroscopic Measurements. The morphology of Au-NRs layers deposited on quartz substrates at different π values was determined using confocal laser scanning microscopy (LSM710, Zeiss, Germany). In the material mode (reflected light), the He–Ne laser was operated at a wavelength of 543 nm. Images were collected from Z planes using a Z Stack Module to acquire Z-stacks with a motorized focus drive. ImageJ processing software was

https://doi.org/10.1021/acs.langmuir.4c01427
Langmuir 2024, 40, 14561−14569

used to calculate the surface coverage and standard deviation. For this purpose, 10 independent images of the obtained layers were considered. Images were analyzed by using the main thresholding command in ImageJ. Electronic absorption spectra of the Au-NRs layers were measured by using a Varian Cary 4000 spectrometer. The Tescan Mira 3 scanning electron microscope (SEM) was used to investigate the Langmuir−Blodgett Au-NRs layers. Because of the thin Au layer, the acceleration voltage was equal to 12 kV. This investigation used secondary electron contrast to improve the image collection.

Dynamic Laser Scattering Measurements. The hydrodynamic diameters (HD) and the zeta potential of the PEG-coated Au-NRs were determined at 25 °C using a Malvern Zetasizer Nano ZS equipped with a laser of 632.8 nm wavelength in backward scattering mode (173°).

■ RESULTS AND DISCUSSION

The absorption spectra of Au-NRs solutions, TEM images, and DLS measurement analysis are shown in Figures S2−S4 and Table S1. The LSPR band positions of PEGylated nanorods were almost the same as those of unmodified Au-NRs. No apparent shifts were observed for the LSPR peaks (see Table S1), and a very small red shift was detected for the peaks after PEGylation. Both the red shift and blue shift of the LSPR peak have been reported after PEGylation of Au-NRs.[10]

The size of the CTAB-protected and PEGylated Au-NRs was determined using TEM and DLS. TEM micrographs showed the nanorod shape and the nanoscale size of the CTAB-protected materials (Figure S3). The longitudinal dimensions of the nanorods were from 20 to 60 nm. HD and zeta potential measurements were carried out using a dynamic laser scattering technique. Size distribution report by intensity showed two peaks (Figure S4). The peak localized at the lower size range, a few nanometers, is sometimes mistaken as the presence of small particle impurities. However, it was recently shown that it can correspond to the rotational diffusion of the nonspherical Au-NRs and should not be considered an actual particle size distribution peak.[21] This peak signifies that the rotational diffusion coefficient of the Au-NRs is equivalent to the translational diffusion coefficient of a spherical particle. The other peak, located at the higher size range, corresponds to the actual size of the solvated PEG-functionalized Au-NRs. The mean HD of PEG-2k, PEG-5k, and PEG-10k-functionalized Au-NRs was equal to 68 ± 2, 84 ± 3, and 72 ± 2 nm, respectively (Table S1). These values are in agreement with the size of CTAB-protected Au-NRs particles determined using TEM. It is important to note that DLS determines the nanoparticle size by assessing the particle's diffusion coefficient. The measurement result is HD representing the size of a solvated particle, including its electrical double layer. In addition, the diffusion coefficient is not solely influenced by the particle's mass; factors such as shape and surface chemistry also play a role.

The zeta potential of the CTAB-protected Au-NRs was equal to 34 mV, which confirms their good stability in an aqueous environment (Table S1). The positive charge stems from the cationic nature of CTAB, which, as a surfactant, forms a bilayer surrounding the nanorod. The PEGylation consisted of replacing the CTAB bilayer with PEG chains attached to the Au-NRs surface via the thiol moiety. The replacement of CTAB by thiol-PEG can be confirmed using Raman spectroscopy by registering the appearance of the Au−S band and the disappearance of the Au−Br band, which was carried out in our earlier work.[10,12] The zeta potential measured for 2, 5, and 10,000 PEG-functionalized Au-NRs was equal to 15.0, 11.4, and −10.6 mV, respectively (Table S1). These values represent the charge shielding ability of different PEG chain lengths and can be explained as follows. Upon the replacement of the positively charged CTAB bilayer by 2k or 5k PEG layer, the negative charge of the bare Au-NR is screened by neutral—and relatively short, compared to 10k PEG—loose polymer chains. However, some positively charged ions can still be attracted by the negatively charged Au-NRs and tend to form positively charged Stern and diffusion layers around the particle. In the case of 10k PEG, the polymer chains can provide a more compact shield of the Au-NRs, and the positively charged ions no longer tend to approach the particle surface. PEG molecules have a neutral to slightly negative surface charge, which may be the reason for the negative zeta potential values of the 10k PEG-functionalized Au-NRs. These results are in accordance with the literature.[8,10] Noteworthy, in addition to the attachment of the PEG chain to the Au-NR surface via the −SH moiety and electrostatic repulsion between the particles, PEG also provides steric stabilization of the materials. Sufficient PEG coating thickness prevents the aggregation of the materials caused by the van der Waals interactions and ensures good dispersion of the particles in the system.

CTAB plays many roles in Au-NRs synthesis,[22] including the organization of Au-NRs and the air−water and air−solid interfaces. The amount of CTAB in a spreading solution influences the shape of the Langmuir monolayer isotherm and its stability over time, which was previously discussed[12] and described in this work. A stable dispersion was obtained by developing a spreading solvent mixture (see the Experimental Section for details)[12] to adjust the hydrophilic character of the Au-NRs. However, for higher mass PEGs, the Langmuir monolayers should be obtained in the presence of excess CTAB, which stabilizes Au-NRs functionalized with PEG-5k and PEG-10k (results not shown). To quantify the amount of CTAB spread at the air−water interface, the procedure reported by Adura et al.[23] provided sufficient and reliable results.[12,24] Three-time centrifugation caused the aggregation of Au-NRs when CTAB concentration in solution was $(3.3 \pm 0.4) \times 10^{-6}$ M. The CTAB concentration that remained in the spreading solution was three times higher than that of PEG-2k Au-NRs.[12] Higher concentrations of CTAB have a positive influence on the Langmuir monolayers of Au-NRs. The increased CTAB content promoted stability in the Langmuir monolayer over the entire π range for PEG-2k (Figure S5), and the same effect was observed in the rest of the PEGs (results not shown). In our recent work on diketopyrrolopyrroles (DPPs)/4-octyl-4′-cyanobiphenyl (8CB) mixtures, the stability was significantly improved over time. The confocal microscopy investigation revealed almost complete removal of agglomerate structures in the DPP with 8CB.[25]

Compared to previous reports, the obtained Langmuir monolayers were more stable, as shown in Figure S5.[12] The deposition process could be more precisely and easily controlled. In this work, a higher value of CTAB was carefully selected according to the centrifugation procedure. The confirmation when using a higher amount of CTAB was also recorded for the π−A isotherm for the PEG-2k monolayer (Figure 1). In this case, higher values of π were obtained for the maximum value of surface film compression compared to published studies.[12]

Measurements of π−A isotherms carried out during the compression of the monolayers consisting of Au-NRs with

https://doi.org/10.1021/acs.langmuir.4c01427
Langmuir 2024, 40, 14561−14569

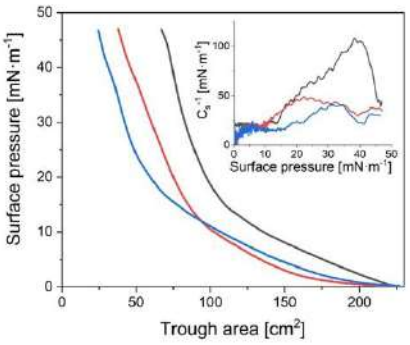

Figure 1. Surface pressure vs trough area isotherm of Langmuir monolayer for gold nanorods for different PEG: PEG-2k (black line), PEG-5k (red line), and PEG-10k (blue line); the inset graph shows the dependence of the surface compressional modulus C_s^{-1} on the surface pressure of Au-NRs.

different amounts of PEG allowed us to determine the effect of PEG chain length on the thermodynamic properties of the surface films. An increase in the molecular weight of PEG resulted in a shift of the π–A isotherm toward lower values of the trough area. Additionally, the PEG footprint increased while PEG grafting density decreased.[7] Thus, excess PEG molecules used during Au-NRs functionalization promoted the attachment of more PEG of lower molecular weight to the Au-NRs surface. Therefore, an alkyl chain of higher molecular weight was used to be more bent than the shorter one. In the case of PEG-2k, the increase in π occurred immediately after compression was started. However, for PEG-5k and PEG-10k, it occurred at the surface of the trough of 195 cm^2. Depending on the molecular weight of PEG, slight differences were observed during the course of the isotherms. For the PEG-2k, PEG-5k, and PEG-10k isotherms, the value of π increased gradually to 14, 11, and 18 $mN{\cdot}m^{-1}$, respectively. Above these values, the compression of the monolayers showed a more rapid increase in the π value.

Based on π–A isotherms, the compression modulus values (C_s^{-1}) were calculated, which was defined as $\left(C_s^{-1} = -A\frac{d\pi}{dA}\right)$. The C_s^{-1} parameter, introduced by Davies and Rideal, allowed us to determine the physical state, elasticity, and/or packing changes in a monolayer.[26] The obtained ranges of the C_s^{-1} modulus corresponded to the physical states of the monolayer. The studied monolayer was considered to be in the gaseous state (G) if the C_s^{-1} values were below 12.5 $mN{\cdot}m^{-1}$. However, the state in the liquid (LE) and condensed in the liquid (LC) had C_s^{-1} values in the ranges between 12.5–50 and 50–250 $mN{\cdot}m^{-1}$, respectively. Above 250 $mN{\cdot}m^{-1}$, the monolayer was assumed to be in the solid phase (S).[26] Analysis of the dependence of the compressibility modulus C_s^{-1} as a function of π, shown in Figure 1, proved that the molecular weight of PEG also affected the elasticity of the monolayers. For PEG-2k, the maximum value of C_s^{-1} was 108 $mN{\cdot}m^{-1}$, which corresponded to the LC phase and was characterized by reduced flexibility compared with monolayers consisting of Au-NRs coated with PEG with higher molecular weights. In the case of PEG-5k and PEG-10k, the formed films were determined as the LE phase because the maximum values of the compressibility modulus C_s^{-1} were 49 and 40 $mN{\cdot}m^{-1}$, respectively.

In the presence of PEG with a higher molecular weight, the ligand density decreased due to the larger PEG molecules that consumed more space and surface area around the anchoring thiol group. This, in turn, reduced the number of PEG molecules needed to saturate the surface and achieve a stable dispersion. Thus, when using PEG of decreasing length, a high amount of PEG was required to achieve stable PEGylated NPs and a critical stability ratio.[27]

The Langmuir monolayers were also examined by using the BAM technique (Figure 2). The obtained images provided

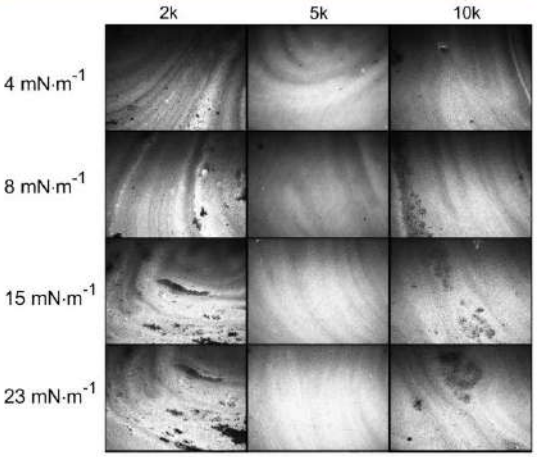

Figure 2. BAM images of gold nanorods for different PEGs and different surface pressures. The image width is 4000 μm.

data for the morphological analysis of the changes that occurred on the surface of the monolayer due to differences in PEG molecular weight. BAM images confirmed that each monolayer (PEG-2k, PEG-5k, and PEG-10k) formed a layer of Au-NRs while reducing the trough area. However, depending on the PEG used, the monolayers differed in structure. In the case of PEG-2k, the surface film exhibited the most heterogeneous structure throughout the compression period, owing to the numerous bands visible over the whole range of surface pressures. This may stem from the higher amount of CTAB present in the aqueous subphase because, according to our previous studies, the Au-NRs monolayer became more homogeneous with increasing surface pressure.[12] The effect of obtaining a homogeneous monolayer was visible on the surface film containing PEG-5k. At both low and high surface pressures, similar effects were observed, indicating the presence of nonaggregated Au-NRs on the surface of the subphase. For the monolayer containing PEG-10k, agglomerates were visible with increasing surface pressure, indicating a reduced homogeneity of the surface film. Upon monolayer compression, changes were not observed in Au-NRs Langmuir monolayer color, highlighting the nonaggregated character of Au-NRs. Moreover, for all PEGs, we recorded *in situ* absorption spectra of Langmuir monolayers (results not shown). We observed the nonaggregated character of Au-NRs spectra, and the position of the longitudinal LSPR peak was linearly dependent on the surface pressure, which confirmed the uniform character of the Au-NR monolayer.

To study the Au-NRs aggregation mechanism at the interfaces induced by the PEG brush, we performed absorption

https://doi.org/10.1021/acs.langmuir.4c01427
Langmuir 2024, 40, 14561−14569

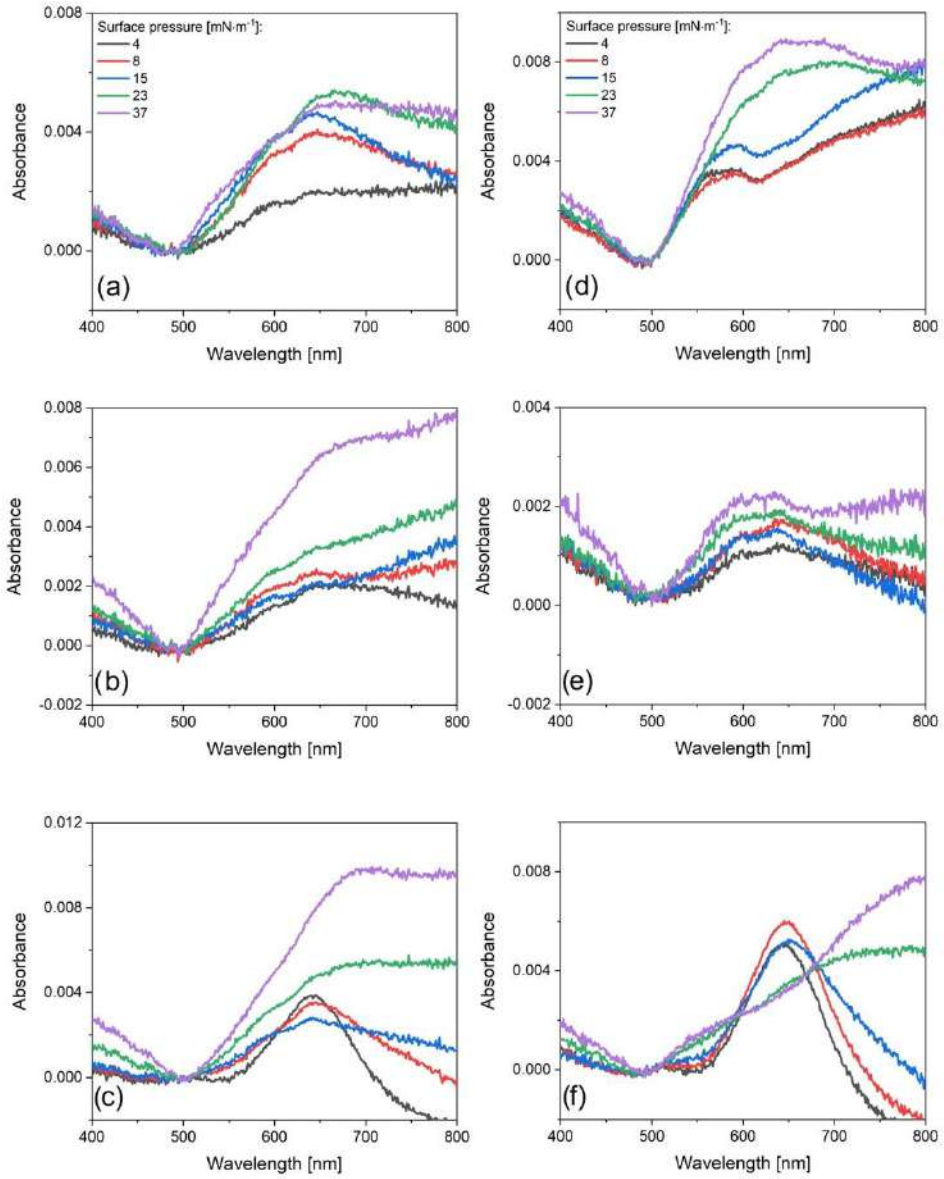

Figure 3. Absorption spectra of the Langmuir−Schaefer gold nanorods (a−c) and Langmuir−Blodgett (d−f) layers deposited on quartz for different PEG: PEG-2k (a, d), PEG-5k (b, e), and PEG-10k (c, f).

spectra measurements, confocal microscopy analysis, and surface coverage studies (Figures 3−6). NPs were used to aggregate over different processes, either spontaneous or forced.[28,29] The aggregation influenced the optical properties of individual NPs, i.e., changes in the extinction spectra observed by peak shifting or broadening. The absorption spectra of LS and LB layers shown in Figure 3 display various degrees of Au-NRs aggregation in the monolayers. Serrano-Montes et al.[30] described the homogeneous arrangement of Au-NRs, where a gradual decrease in absorbance was observed at wavelengths above 900 nm. Thus, the spectra (Figure 3) were recorded in a similar spectral region, i.e., 400−800 nm. Moreover, only the UV−vis range of electromagnetic radiation was considered in the case of film application in surface-enhanced spectroscopies.

PEG with the longest alkyl chain (PEG-10k) and the lowest π ensured nonaggregation of Au-NRs in LS monolayers (Figure 3c). The shape of the Au-NRs spectrum was similar to that observed in the Au-NRs solution. For higher π, the main peak was red-shifted. This behavior was also observed for PEG-2k and PEG-5k. The absorption peaks were broad and red-shifted upon increasing π. In both cases, two peaks were

https://doi.org/10.1021/acs.langmuir.4c01427
Langmuir 2024, 40, 14561−14569

detected at 530 and 650 nm. For PEG-5k, the third peak appeared above 800 nm. All PEGs and LS layers showed a peak at 630 nm, which suggested a red shift upon increased π. Furthermore, a different behavior was observed for LB layers (Figure 3d–f). LB deposition ensured the monomer character of Au-NRs for PEG-10k and three out of five π values (4, 8, and 15 mN·m^{-1}).

The position longitudinal LSPR for nonaggregated Au-NRs was the same as for LS and LB. The highest π of 23 and 37 mN·m^{-1} displayed a peak due to the aggregation of Au-NRs above 750 nm. A similar effect was observed for LS layers and PEG-10k. Additionally, the thickest PEGs (PEG-5k and PEG-10k) did not promote the formation of nonaggregated Au-NRs layers. PEG-5k Au-NRs formed the same type of aggregate over the whole π range, with only a small increase in absorbance observed (Figure 3e). This was also the case for PEG-2k and at $\pi \leq 15$ mN·m^{-1}, while a further increase in π modified the aggregate type due to the main peak at 570 nm for lower π being red-shifted. Similar behavior was reported by Solís et al.[31] and by Serrano-Montes et al.[30] Solís et al.[31] used state-of-the-art electromagnetic computation techniques to produce predictive simulations for a wide range of nanoparticle-based SERS substrates, including realistic configurations consisting of random arrangements of hundreds of nanoparticles. The authors stated that the aggregation of the particles in dimers and monolayers produced additional red shifts of the spectral features and broadening of LSPR bands caused by interparticle gaps as well as an increase in the magnitude of extinction. However, due to the complex character of the spectra, the authors did not perform any deconvolution to distinguish the basic plasmon modes. Moreover, Serrano-Montes et al.[30] showed a significant red shift and broadening of LSPR bands due to small interparticle distances that led to plasmon coupling. The detected characteristics of the extinction spectra also occurred in cube-shaped nanoprisms NPs in polymer-grafted self-assembled layers.[32,33]

The aggregation behavior of Au-NRs at the interfaces was also examined by microscopic slide studies using confocal microscopy (Figures 4–5). The arrangement of Au-NRs in a micrometric size scale was investigated due to the aggregation behavior of Au-NRs. Moreover, the surface coverage was calculated from the obtained data with a standard deviation for both the LS and LB layers (Figure 6). For monomer Au-NRs, satisfactory images were not recorded and are indicated in Figures 4–5 as black images. According to the spectra, PEG and LS deposition layers became more aggregated. Hence, the surface coverage and density of the aggregates were higher (Figure 6). Upon increasing π to 37 mN·m^{-1}, longitudinal aggregates were formed for PEG-5k and LS layers, which was in contrast to the other layers studied. However, they did display small micrometric aggregates at $\pi \geq 15$ mN·m^{-1}. Larger but less dense structures were observed for PEG-2k and $\pi \leq 8$ mN·m^{-1}. A new type of aggregation of PEG-2k LB layers for $\pi \geq 15$ mN·m^{-1} was clearly shown in the confocal images. Similar images were obtained for PEG-5k, while for PEG-10k and $\pi \geq 23$ mN·m^{-1}, a structural change of Au-NRs was detected as the film had a more foam-like character than that of PEG-2k. We performed SEM studies for selected Au-NR monolayers deposited at air–solid interfaces to obtain additional information about the studied systems. Results for the LB layers are shown in Figure S6, and the obtained aggregates can be seen. The aggregate formation process can

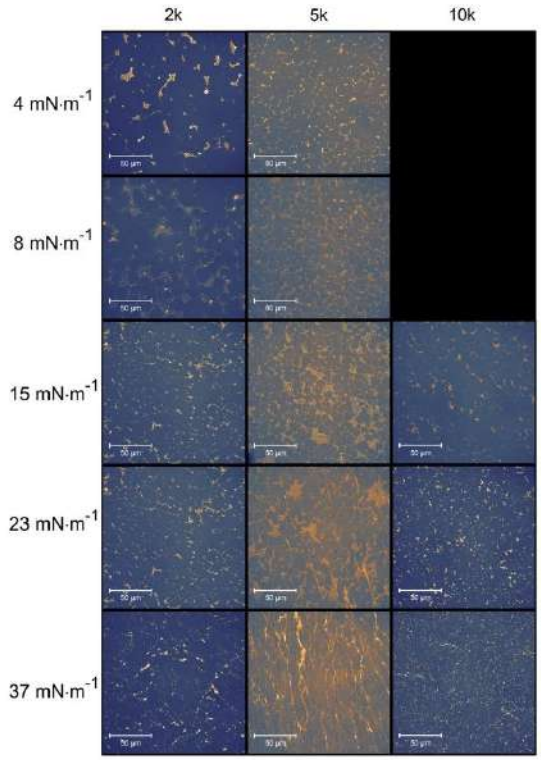

Figure 4. Examples of confocal microscopy images of Langmuir–Schaefer layers of gold nanorods functionalized with either 2, 5, or 10k PEG deposited on quartz substrates at different surface pressures. The longitudinal sides of the panels represent the longer side of the Langmuir trough.

be explained using two mechanisms. According to our previous studies for gold nanorods, the formation of aggregates at the microscale is influenced by the dewetting process that takes place during substrates pulling from the air–water interface,[12] while at the nanoscale, Au-NRs tend to form two main aggregate structures. Similar results for spherical shape NPs showed different arrangements of NPs at the micro- and nanoscale.[34] One is *end-to-end*, and the second is *side-to-side*.[35] The two types of structures dominate the shape of the spectra shown in Figure 3 and thus produce strong plasmon coupling. It was recently shown through large-scale realistic simulation for NP-arranged systems[31] that plasmon coupling leads to strongly confined resonances in Au-NRs aggregates.

The surface coverage of Au-NRs vs deposition surface pressure for the LS and LB layers is shown in Figure 6. The highest surface coverages were obtained for LS layers. Not all presented data points could be fitted to a linear plot. However, the dependence of PEG-2k and LB was linear for all π, whereas PEG-5k LS showed two regions for $\pi \leq 8$ mN·m^{-1} and $\pi > 8$ mN·m^{-1}. These results were consistent with the absorption spectra (Figure 3b) and confocal images of the PEG-5k LS layers. For $\pi > 8$ mN·m^{-1}, a new type of aggregate was formed due to the presence of a third peak in the spectrum, which red-shifted toward above 750 nm. PEG-2k and PEG-5k LB layer's surface coverage was the same in all π ranges within the experimental error. However, in PEG-10k, reduced surface

https://doi.org/10.1021/acs.langmuir.4c01427
Langmuir 2024, 40, 14561−14569

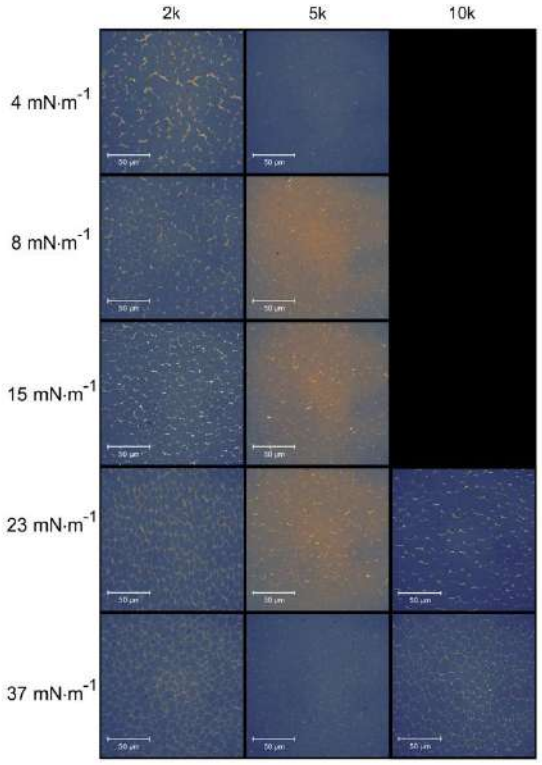

Figure 5. Examples of confocal microscopy images of Langmuir–Blodgett layers of gold nanorods functionalized with either 2, 5, or 10k PEG deposited on quartz substrates at different surface pressures. The longitudinal sides of the panels represent the longer side of the Langmuir trough.

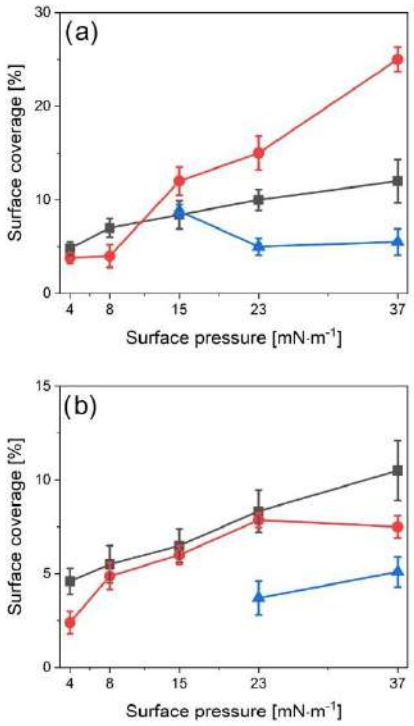

Figure 6. Dependence of the surface coverage of gold nanorods vs. deposition surface pressure for the Langmuir–Schaefer (a) and Langmuir–Blodgett (b) layers and different PEG: PEG-2k is a black line, PEG-5k is a red line, and PEG-10k is a blue line.

coverage was observed, compared to PEG-2k and PEG-5k—probably due to the coexistence of aggregated (visible in confocal microscope images) and nonaggregated (invisible in confocal microscope images) structures in LB layers. The same molecular mechanism of coexistence of two phases most likely occurred for PEG-10k and LS layers. Tim et al.[12] showed that the surface coverage did not remain as high after adding CTAB to obtain more stable Langmuir layers for all PEGs tested.

The mechanism of aggregated Au-NRs structure formation at the air–solid interfaces is a complex process. The density and optical properties of the films are influenced by many factors, mainly connected to Au-NRs synthesis and functionalization. The length of the PEG chain and its conformation at the Au-NRs surface dictated the type of aggregation. Previous studies by Rahme et al.[7] for PEG in spherical NPs showed different behaviors of NPs as a function of PEG chain length. The number of PEG molecules grafted per NP showed that the grafting density decreased in a nonlinear trend as a function of increasing PEG length due to the increased conformational entropy and the diffusion rate of free HS-PEG, which decayed exponentially with the increase of PEG M_w.[17] PEG-functionalized Au-NRs are amphiphilic; hence, only PEG-2k Au-NRs could form stable and insoluble Langmuir monolayers in the aqueous subphase without an additional stabilizer.[12] The coverage degree of PEG molecules on the Au-NPs surface can be estimated using thermogravimetric analysis.[7] We tried to perform such an analysis; however, in the case of Au-NRs, where the concentration of the final product is lower than the one for Au-NPs, estimating the PEG amount at the Au surface would be practically impossible. In this case, the presented results can be explained as follows. In the case of PEG-5k and PEG-10k Au-NRs, the Langmuir monolayers were stabilized using CTAB. The additional, constant amount of CTAB (as described at the beginning of this section) was present in all Au-NRs PEGs spreading solutions because it was not completely removed upon Au-NRs centrifugation. Different conformations of PEG chains were obtained, depending on the molecular weight and PEG grafting density at the NP surface. Starting at low values of both mentioned above, the conformation from mushroom brush to brush was changed to a more dense brush.[16] Based on the results presented in Figure 1, PEG-10k had a mushroom-brush configuration and transformed into a brush for PEG-2k due to the shifting of isotherms toward a smaller trough area. When the solid substrate was extracted from the water (in the LS or LB technique), PEG conformation controlled the aggregation process of Au-NRs at the air–solid interface. Probably, mushroom brush ensured Au-NRs in a monomer formation at low π with a tendency for stronger aggregation upon LS deposition. A denser brush with PEG chains perpendicular to the Au-NR surface ensured aggregate formation with higher packing of LS layers. On the one hand, CTAB addition allowed the generation of more stable Langmuir monolayers. On the other hand, it reduced the ability of the PEG Au-NRs to

https://doi.org/10.1021/acs.langmuir.4c01427
Langmuir 2024, 40, 14561−14569

aggregate into a more complex structure. As we reported previously, stability was improved over time in Langmuir-like layers upon a small addition of surfactant.[25] Furthermore, the dewetting process after Au-NRs deposition in such a way that the Langmuir monolayer is more stable did not affect the Au-NRs arrangement but the PEG chain conformation.

■ CONCLUSIONS

The presented study investigated the formation of Langmuir–Schaefer and Langmuir–Blodgett layers consisting of PEGylated Au-NRs with different poly(ethylene glycol) alkyl chain lengths. An interesting physicochemical problem was examined by focusing on poly(ethylene glycol)'s role in forming patterns on a solid substrate. The results indicated that insoluble and stable Langmuir monolayers on the ultrapure water subphase of Au-NRs with longer poly(ethylene glycol) formed only in the presence of an additional stabilizer. This amphiphilic stabilizer was used to prevent the aggregation of Au-NRs in aqueous solutions. It has been proven that the poly(ethylene glycol) conformation influenced the shape of the compression isotherm. Hence, specific shifts during the Langmuir monolayer compression were observed. Moreover, the conformational changes in poly(ethylene glycol) induced the aggregation of Au-NRs, resulting in aggregates with specific structures. Aggregated and nonaggregated structures could be designed without requiring two or more Au-NRs functionalization steps. When the transfer surface pressure increased, the aggregates became closely packed. Their orientation was random or quasiparallel to the direction of removal of the quartz substrate from the aqueous subphase. Moreover, we demonstrated that the degree and the type of Au-NRs aggregation could be tailored depending on the molecular weight of poly(ethylene glycol) and the addition of a stabilizer. The results suggest the potential of producing patterns of hydrophilic, PEGylated Au-NRs thin layers for photonics applications, with a particular focus on optical sensing. In this application area, plasmonic substrates with the desired optical properties are beneficial for the enhanced detection of different analytes.

■ ASSOCIATED CONTENT

Supporting Information

The Supporting Information is available free of charge at https://pubs.acs.org/doi/10.1021/acs.langmuir.4c01427.

Functionalization scheme, absorption spectra, TEM image and DLS studies of gold nanorods, relaxation studies of gold nanorods Langmuir monolayer, and SEM images of Langmuir–Blodgett layers of gold nanorods (PDF)

■ AUTHOR INFORMATION

Corresponding Author

Michał Kotkowiak – *Faculty of Materials Engineering and Technical Physics, Poznan University of Technology, 60-965 Poznan, Poland;* orcid.org/0000-0001-6611-0366; Phone: + 48 61 665 3182; Email: michal.kotkowiak@put.poznan.pl

Authors

Beata Tim – *Faculty of Materials Engineering and Technical Physics, Poznan University of Technology, 60-965 Poznan, Poland*

Mateusz Kotkowiak – *Faculty of Materials Engineering and Technical Physics, Poznan University of Technology, 60-965 Poznan, Poland*

Joanna Musiał – *Department of Rare Earths, Faculty of Chemistry, Adam Mickiewicz University, 61-614 Poznan, Poland*

Paulina Blaszkiewicz – *Faculty of Materials Engineering and Technical Physics, Poznan University of Technology, 60-965 Poznan, Poland*

Complete contact information is available at: https://pubs.acs.org/10.1021/acs.langmuir.4c01427

Author Contributions

Mic.K. designed the concept of research and general aims of experiments; performed microscopic studies of Langmuir–Schaefer and Langmuir–Blodgett layers (along with the procedure's description); experimentally determined the amount of CTAB in gold nanorods solutions; described the results of performed studies (excluding Langmuir-like studies) together with discussion and analysis of all performed studies within this work; wrote abstract, part of introduction and conclusions; prepared rebuttal letter and revised version of the manuscript; supervised the project; managed research planning and execution; and acquired the financial support for the project. **B.T.** performed Langmuir (including BAM), Langmuir–Blodgett, Langmuir–Schaefer (along with the procedure's description), and UV–vis experiments of layers; described results of Langmuir-like studies (including BAM); wrote part of introduction; and proofread rebuttal letter. **Mat.K.** performed SEM studies of Langmuir–Blodgett layers. **J.M.** performed DLS studies of gold nanorods dispersions and described the results of DLS. **P.B.** synthesized and functionalized gold nanoparticles along with the procedure's description. All coauthors approved the final version of the manuscript. **Mic.K.**, **B.T.**, and **J.M.** contributed to review and editing of all versions of the manuscript, while **Mat.K.** and **P.B.** reviewed and edited the final version of the manuscript.

Notes

The authors declare no competing financial interest.

■ ACKNOWLEDGMENTS

This work was supported by the National Science Center, Poland, under research project n° 2019/35/D/ST4/02037.

■ REFERENCES

(1) Yari, M.; Javanmardi, N. Multifunctional Gold Nanoparticle: As Novel Agents for Cancer Treatment. *Adv. Appl. NanoBio-Technol.* **2022**, *3* (2), 43–48.

(2) Sun, L.; Lin, H.; Kohlstedt, K. L.; Schatz, G. C.; Mirkin, C. A. Design Principles for Photonic Crystals Based on Plasmonic Nanoparticle Superlattices. *Proc. Natl. Acad. Sci. U.S.A.* **2018**, *115* (28), 7242–7247.

(3) Tim, B.; Błaszkiewicz, P.; Kotkowiak, M. Recent Advances in Metallic Nanoparticle Assemblies for Surface-Enhanced Spectroscopy. *Int. J. Mol. Sci.* **2022**, *23* (291), 1–24.

(4) Chiba, H.; Kodama, K.; Okada, K.; Ichikawa, Y.; Motosuke, M. Gap Effect on Electric Field Enhancement and Photothermal Conversion in Gold Nanostructures. *Micromachines* **2022**, *13* (5), 801–811.

(5) Liu, Y.; Yang, L.; Shen, Y. Hydrothermal Synthesis of Gold Nanoplates and Their Structure-Dependent LSPR Properties. *J. Mater. Res.* **2018**, *33* (18), 2671–2679.

(6) Huang, X.; Neretina, S.; El-Sayed, M. A. Gold Nanorods: From Synthesis and Properties to Biological and Biomedical Applications. *Adv. Mater.* **2009**, *21* (48), 4880−4910.
(7) Rahme, K.; Chen, L.; Hobbs, R. G.; Morris, M. A.; O'Driscoll, C.; Holmes, J. D. PEGylated Gold Nanoparticles: Polymer Quantification as a Function of PEG Lengths and Nanoparticle Dimensions. *RSC Adv.* **2013**, *3* (17), 6085−6094.
(8) Niidome, T.; Yamagata, M.; Okamoto, Y.; Akiyama, Y.; et al. PEG-Modified Gold Nanorods with a Stealth Character for in Vivo Applications. *J. Controlled Release* **2006**, *114*, 343−347.
(9) Mahmoud, N. N.; Alhusban, A. A.; Ali, J. I.; Al-Bakri, A. G.; Hamed, R.; Khalil, E. A. Preferential Accumulation of Phospholipid-PEG and Cholesterol-PEG Decorated Gold Nanorods into Human Skin Layers and Their Photothermal-Based Antibacterial Activity. *Sci. Rep.* **2019**, *9* (1), No. 5796.
(10) Zhang, Z.; Lin, M. Fast Loading of PEG−SH on CTAB-Protected Gold Nanorods. *RSC Adv.* **2014**, *4* (34), 17760−17767.
(11) Locatelli, E.; Monaco, I.; Franchini, M. Surface Modifications of Gold Nanorods for Applications in Nanomedicine. *RSC Adv.* **2015**, *5*, 21681−21699.
(12) Tim, B.; Blaszkiewicz, P.; Nowicka, A. B.; Kotkowiak, M. Optimizing SERS Performance through Aggregation of Gold Nanorods in Langmuir-Blodgett Films. *Appl. Surf. Sci.* **2022**, *573*, 151518−151527.
(13) Guzmán, E.; Liggieri, L.; Santini, E.; Ferrari, M.; Ravera, F. Influence of Silica Nanoparticles on Phase Behavior and Structural Properties of DPPC-Palmitic Acid Langmuir Monolayers. *Colloids Surf., A* **2012**, *413*, 280−287.
(14) Lee, Y. H.; Lee, C. K.; Tan, B.; Rui Tan, J. M.; Phang, I. Y.; Ling, X. Y. Using the Langmuir-Schaefer Technique to Fabricate Large-Area Dense SERS-Active Au Nanoprism Monolayer Films. *Nanoscale* **2013**, *5* (14), 6404−6412.
(15) Ishida, T.; Tachikiri, Y.; Sako, T.; Takahashi, Y.; Yamada, S. Structural Characterization and Plasmonic Properties of Two-Dimensional Arrays of Hydrophobic Large Gold Nanoparticles Fabricated by Langmuir-Blodgett Technique. *Appl. Surf. Sci.* **2017**, *404*, 350−356.
(16) Li, M.; Jiang, S.; Simon, J.; Paßlick, D.; Frey, M.-L.; Wagner, M.; Mailänder, V.; Crespy, D.; Landfester, K. Brush Conformation of Polyethylene Glycol Determines the Stealth Effect of Nanocarriers in the Low Protein Adsorption Regime. *Nano Lett.* **2021**, *21* (4), 1591−1598.
(17) Shi, L.; Zhang, J.; Zhao, M.; Tang, S.; Cheng, X.; Zhang, W.; Li, W.; Liu, X.; Peng, H.; Wang, Q. Effects of Polyethylene Glycol on the Surface of Nanoparticles for Targeted Drug Delivery. *Nanoscale* **2021**, *13* (24), 10748−10764.
(18) Nikoobakht, B.; Sayed, A. El. Preparation and Growth Mechanism of Gold Nanorods (NRs) Using Seed-Mediated Growth Method. *Chem. Mater.* **2003**, *15* (10), 1957−1962.
(19) Blaszkiewicz, P.; Kotkowiak, M.; Coy, E.; Dudkowiak, A. Laser-Induced Optoacoustic Spectroscopy Studies of Inorganic Functionalized Metallic Nanorods. *J. Phys. Chem. C* **2019**, *123* (44), 27181−27186.
(20) Szustakiewicz, P.; Kolsut, N.; Leniart, A.; Lewandowski, W. Universal Method for Producing Reduced Graphene Oxide/Gold Nanoparticles Composites with Controlled Density of Grafting and Long-Term Stability. *Nanomaterials* **2019**, *9* (4), No. 602.
(21) Schulz, F.; Friedrich, W.; Hoppe, K.; Vossmeyer, T.; Weller, H.; Lange, H. Effective PEGylation of Gold Nanorods. *Nanoscale* **2016**, *8* (13), 7296−7308.
(22) Scarabelli, L.; Sánchez-Iglesias, A.; Pérez-Juste, J.; Liz-Marzán, L. M. A "Tips and Tricks" Practical Guide to the Synthesis of Gold Nanorods. *J. Phys. Chem. Lett.* **2015**, *6* (21), 4270−4279.
(23) Adura, C.; Guzman, F.; Alvarez-Lueje, A.; Kogan, M. J. Ion Pair Method to Determine the CTAB Content in Gold Nanorods Samples. *J. Chil. Chem. Soc.* **2014**, *59*, 2701−2704.
(24) Tim, B.; Blaszkiewicz, P.; Kotkowiak, M. Altering Model Cell Membranes by Means of Photoactivated Organic Functionalized Gold Nanorods. *J. Mol. Liq.* **2022**, *349*, 118179−118186.
(25) Biadasz, A.; Rytel, K.; Kędzierski, K.; Adamski, A.; Kotkowiak, M.; Stachowiak, A.; Barszcz, B.; Jeong, H. Y.; Kim, T.-D. The Liquid Crystal Induced J-Type Aggregation of Diketopyrrolopyrrole Derivatives in Monolayer. *J. Mol. Liq.* **2019**, *285*, 598−606.
(26) Davies, J. T.; Rideal, E. K. *Interfacial Phenomena*; Academic Press, 1961.
(27) Liu, H.; Doane, T. L.; Cheng, Y.; Lu, F.; Srinivasan, S.; Zhu, J.-J.; Burda, C. Control of Surface Ligand Density on PEGylated Gold Nanoparticles for Optimized Cancer Cell Uptake. *Part. Part. Syst. Charact.* **2015**, *32* (2), 197−204.
(28) Pratap, D.; Vikas; Gautam, R.; Shaw, A. K.; Soni, S. Photothermal Properties of Stable Aggregates of Gold Nanorods. *Colloids Surf., A* **2022**, *635* (December 20), 128054.
(29) Neupane, S.; Pan, Y.; Takalkar, S.; Bentz, K.; Farmakes, J.; Xu, Y.; Chen, B.; Liu, G.; Qian, S. Y.; Yang, Z. Probing the Aggregation Mechanism of Gold Nanoparticles Triggered by a Globular Protein. *J. Phys. Chem. C* **2017**, *121* (2), 1377−1386.
(30) Serrano-Montes, A. B.; De Aberasturi, D. J.; Langer, J.; Giner-Casares, J. J.; Scarabelli, L.; Herrero, A.; Liz-Marzán, L. M. A General Method for Solvent Exchange of Plasmonic Nanoparticles and Self-Assembly into SERS-Active Monolayers. *Langmuir* **2015**, *31* (33), 9205−9213.
(31) Solís, D. M.; Taboada, J. M.; Obelleiro, F.; Liz-Marzán, L. M.; García De Abajo, F. J. Optimization of Nanoparticle-Based SERS Substrates through Large-Scale Realistic Simulations. *ACS Photonics* **2017**, *4* (2), 329−337.
(32) Gao, B.; Arya, G.; Tao, A. R. Self-Orienting Nanocubes for the Assembly of Plasmonic Nanojunctions. *Nat. Nanotechnol.* **2012**, *7* (7), 433−437.
(33) Rosen, D. A.; Tao, A. R. Modeling the Optical Properties of Bowtie Antenna Generated by Self-Assembled Ag Triangular Nanoprisms. *ACS Appl. Mater. Interfaces* **2014**, *6* (6), 4134−4142.
(34) Tim, B.; Kotkowiak, M.; Kowalska, N.; Nowicka, A. B.; Lewandowski, W. Influence of Gold Nanoparticle Assembly in Langmuir−Schaefer Monolayers on the Surface-Enhanced Spectroscopy Response of a Nanoplatform. *J. Phys. Chem. C* **2023**, *127* (32), 15978−15987.
(35) Kotkowiak, M.; Mleczko, M. In Situ Tracked Hybridization Phenomenon of Gold Nanorods in Monolayer Systems. *J. Phys. Chem. C* **2024**, *128* (14), 6065−6071.

https://doi.org/10.1021/acs.langmuir.4c01427
Langmuir 2024, 40, 14561−14569

Supplementary information

for

The Role of the Polyethylene Glycol in the Organization of Gold Nanorods at the Air-Water and the Air-Solid Interfaces

Michał Kotkowiak[a,*], Beata Tim[a], Mateusz Kotkowiak[a], Joanna Musiał[b], Paulina Błaszkiewicz[a]

[a]Faculty of Materials Engineering and Technical Physics, Poznan University of Technology, Piotrowo 3, 60-965 Poznan, Poland
[b]Department of Rare Earths, Faculty of Chemistry, Adam Mickiewicz University, 61-614 Poznan, Poland

To whom correspondence should be addressed:
*E-mail: michal.kotkowiak@put.poznan.pl (MK)
Tel.: + 48 61 665 3182

Table of contents

1. Functionalization scheme, absorption spectra, TEM image and DLS studies of gold nanorods
2. Relaxation studies of gold nanorods Langmuir monolayer
3. SEM images of Langmuir-Blodgett layers of gold nanorods

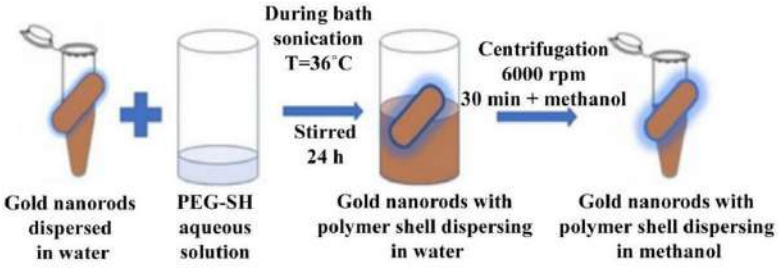

Fig. S1. Functionalization of gold nanorods by PEG coating.

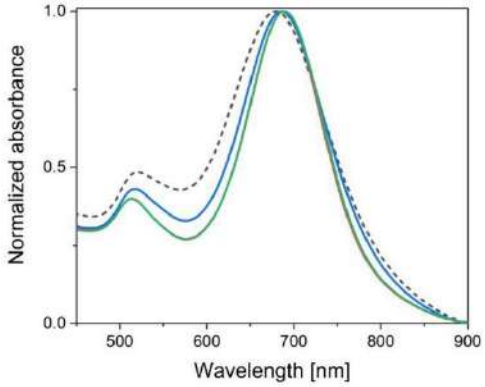

Fig. S2. Normalized absorption spectra of the gold nanorods before (dashed black line) and after PEGylation for different PEG: PEG-2k (red solid line), PEG-5k (blue), and PEG-10k (green).

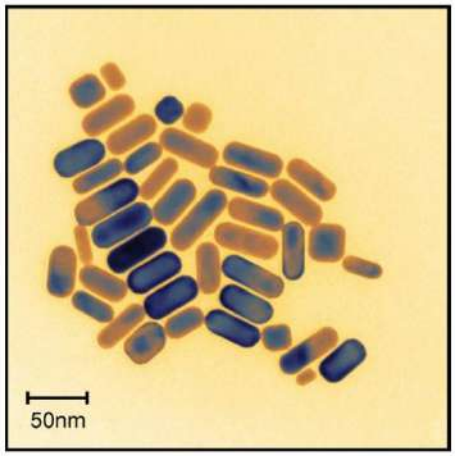

Fig. S3. Transmission electron microscopy image of the bare gold nanorods.

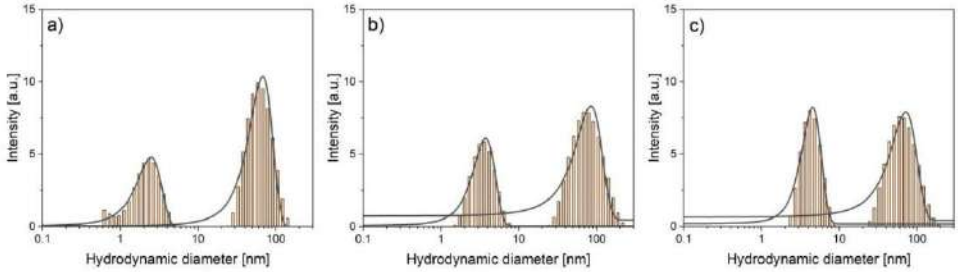

Fig. S4. Hydrodynamic diameter distribution of gold nanorods functionalized with different PEG: PEG-2k **(a)**, PEG-5k **(b)** and PEG-10k **(c)**.

Table S1. Parameters of synthesized gold nanorods functionalized with PEG

	Hydrodynamic diameter [nm]*	Zeta potential/ pH values [mV]**/[-]	LSPR localization Transverse/longitudinal [nm]
CTAB protected Au-NRs	–	34.0±0.8/7.0***	519/680
Au-NRs PEG-2k	68±2	15.0±0.4/4.8	514/688
Au-NRs PEG-5k	84±3	11.4±0.4/4.3	517/686
Au-NRs PEG-10k	72±2	-10.6±1.4/4.6	514/689

* – in methanol
** – in water/methanol mixture (9:1 v:v)
*** – in water

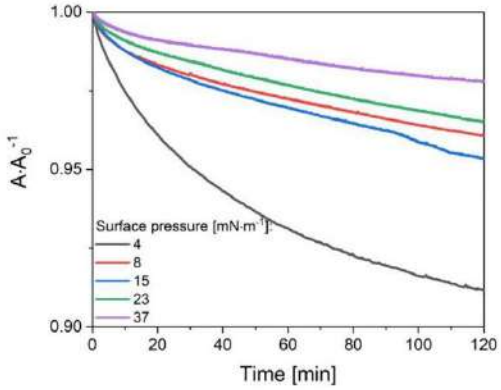

Fig. S5. Relative area changes *versus* time for a various surface pressure values of gold nanorods Langmuir monolayer functionalized with PEG-2k.

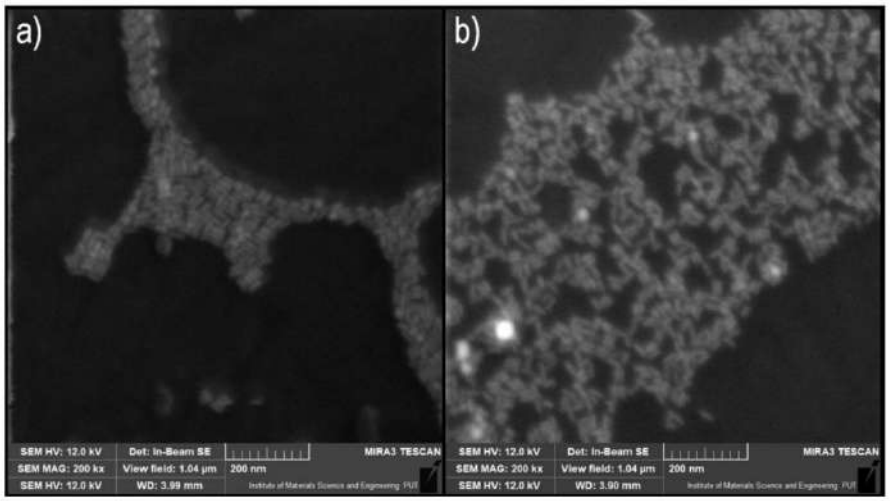

Fig. S6. Example of scanning electron microscopy images of Langmuir-Blodgett layers of gold nanorods functionalized with 2 **(a)** and **(b)** 10k-PEG, deposited on quartz substrates at surface pressures of 37 $mN \cdot m^{-1}$.

Przedruk publikacji [Tim, JML 2025]

B. Tim, P. Błaszkiewicz, E. Coy, A. Dudkowiak,

Interactions between functionalized PEGylated gold nanoparticles and model biological membranes,

Journal of Molecular Liquid 428 (2025), 127501-1-127501-12. (IF 5,2; MNiSW 100)

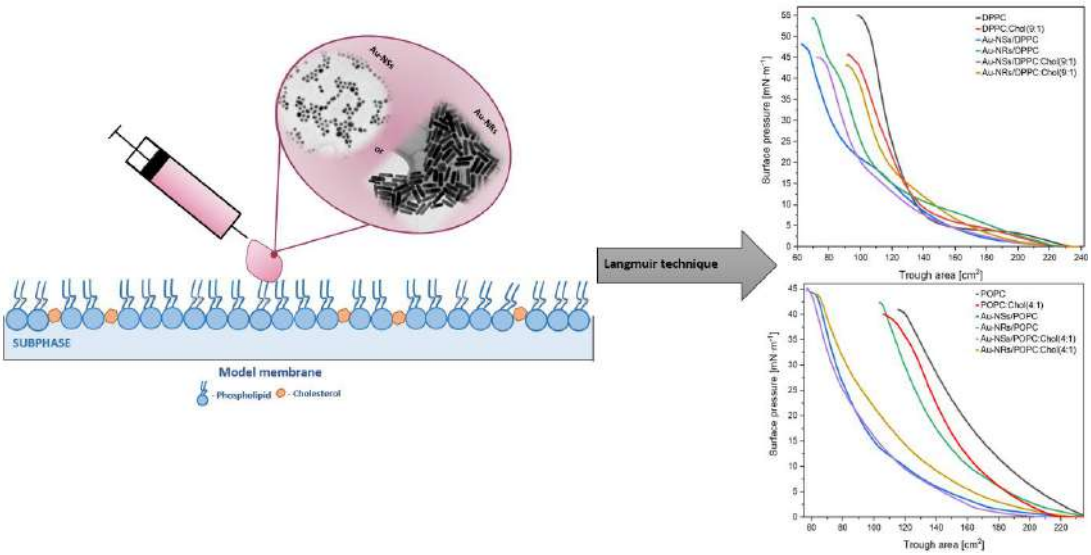

Journal of Molecular Liquids 428 (2025) 127501

Contents lists available at ScienceDirect

Journal of Molecular Liquids

journal homepage: www.elsevier.com/locate/molliq

Interactions between functionalized PEGylated gold nanoparticles and model biological membranes☆

Beata Tim [a,*], Paulina Błaszkiewicz [b], Emerson Coy [b], Alina Dudkowiak [a]

[a] Faculty of Materials Engineering and Technical Physics, Poznan University of Technology, Piotrowo 3, 60-965 Poznan, Poland
[b] NanoBioMedical Centre, Adam Mickiewicz University, Wszechnicy Piastowskiej 3, 61-614 Poznan, Poland

ARTICLE INFO

Keywords:
Cholesterol
Gold nanoparticles
Langmuir monolayer
Nanorods
Nanospheres
Phospholipids
Surface pressure isotherms

ABSTRACT

A better understanding of the interaction mechanism between functionalized gold nanoparticles and cell membrane components helps study the impact of particulate matter on biomimetic systems. The paper reports how gold nanoparticles with different geometries (spherical and rod-shaped) were synthesized with slight modifications and functionalized with polyethylene glycol. Efficient pegylation process and addition of HCl to the growth solution results in highly monodisperse nanoparticles. The obtained functionalized nanoparticles were characterized by UV–V is spectroscopy, transmission electron microscopy and dynamic light scattering. This article focuses on the effect of gold nanoparticles on the surface properties of model biological membranes consisting of phospholipids (1,2-dipalmitoyl-*sn*-glycero-3-phosphocholine (DPPC) and 1-palmitoyl-2-oleoyl-glycero-3-phosphocholine (POPC)) in the presence of cholesterol, which is an organic chemical compound, a lipid from the steroid group. The effect of the nanoparticles with different shapes on the behavior of monolayers was described using surface pressure isotherms, surface compressibility modulus, Brewster angle microscopy and polarization modulation infrared reflection absorption spectroscopy. It was shown that for all lipid systems considered, the type of nanoparticles affects the degree of condensation and the morphology of the monolayer. The studies showed that the monolayers of lipid systems containing spherical gold nanoparticles are characterized by greater stability than the monolayers containing gold nanorods. Based on the research, it can also be assumed that some of the gold nanoparticles are incorporated into lipid monolayers, while others remain on the lipid monolayer surface. The results presented may be useful to better understand the interaction between nanoparticles and the lipid components of biomembranes.

1. Introduction

Nanotechnology is a field of science with very high development potential, affecting biotechnology, transport, energy, agriculture, and industry [1]. Nanomaterials have been found to have applications in medicine for imaging and as contrast agents or drug delivery systems [2,3]. One type of such nanomaterials are metallic nanoparticles (NPs), which are widely used in medicine for diagnosis and therapy, and have been used as carriers for drugs and vaccines [4]. The use of biomimetic systems to study the influence of (bio)active agents, including NPs, on cellular organization has gained popularity in recent years.

The membrane is the first barrier that a substance must overcome to enter the cell, so it is important to determine the changes occurring at this stage of the substance introduction process [5]. Understanding the interactions that occur between gold NPs (Au-NPs) and the cell membrane is of great importance for their potential therapeutic applications. The use of Au-NPs in phototherapy or diagnostics has shown promising results, significantly increasing the effectiveness of treatment (or imaging) while reducing side effects [6,7]. Au-NPs have a unique ability to absorb and scatter near-infrared light due to the surface plasmon resonances. For this reason, Au-NPs have become the materials of choice in nanomedicine, particularly for cancer imaging and therapy, as well as for photonic sensing of biological agents and toxic compounds, e.g. in biomedical diagnostics, forensic analysis and environmental monitoring [8]. Cell membrane biomimetic technology has recently been used to give phototherapeutic pharmaceuticals with novel biological functionalities such as immune evasion, longer in vivo circulation duration, greater biocompatibility, and increased anti-tumor activity.

☆ This article is part of a special issue entitled: 'M. Jasiurkowska sp. issue' published in Journal of Molecular Liquids.

* Corresponding author.
E-mail address: beata.tim@put.poznan.pl (B. Tim).

https://doi.org/10.1016/j.molliq.2025.127501
Received 28 November 2024; Received in revised form 6 March 2025; Accepted 1 April 2025
Available online 3 April 2025
0167-7322/© 2025 Elsevier B.V. All rights are reserved, including those for text and data mining, AI training, and similar technologies.

Furthermore, phototherapy mediated by cancer and non-cancer cell membrane modified phototherapeutic drugs can boost overall antitumor immunity [9].

Biological membranes are complex dynamic structures consisting of a bilayer of lipids (e.g. phospholipids and sterols) with the presence of proteins and polysaccharides; therefore, interaction with each of their components can play an important role in the research conducted to explain the mechanism of action of metallic NPs on cells in the body. The possibility that only selected compounds are capable of entering the membrane is mainly due to the hydrophobic nature of the bilayer [10]. The lipid bilayer is the fundamental structure of membranes in living organisms. It divides the inner and exterior, defining a cell. Due to the complex structural and dynamic nature of biological membranes, research on the influence of various factors on their properties is studied in biomimetic systems using various types of membrane models, single- or multicomponent membranes [11]. One of the biomimetic systems used are phospholipid monolayers.

The Langmuir monolayers are a convenient model for monitoring and studying the changes in membrane properties caused by the presence of Au-NPs of various shapes and coating parameters [12–15]. The shapes and functionalization of Au-NPs can influence their localization, packing, arrangement, and penetration of membranes and their interactions with healthy and neoplastic cellular membrane components. That allows for a comparison of the effect of Au-NPs on monolayers composed of different lipids. The main aim is to investigate the incorporation of various Au-NPs into biomimetic systems. The obtained results will allow us to understand whether the presence of Au-NPs causes differences (and of what kind) in the organization of cellular membranes and if it can disturb their integration, and support the transport of medicinal substances, in cellular membranes.

The simplest model of a biological membrane is a layer of phospholipids, one molecule thick formed on the surface of a liquid. It has been shown that lipid monolayers under certain conditions largely reflect the properties of lipid bilayers found in cells. This makes them a good model for studying the effects of substances on biological membranes [16]. One of the main phospholipids building mammalian membranes are phosphatidylcholines (PC), which are a large group of compounds differing in the degree of chain saturation. A popular PC used to produce model biological membranes is 1,2-dipalmitoyl-*sn*-glycero-3-phosphocholine (DPPC), a derivative of palmitic acid, a basic fatty acid. DPPC consists of two palmitic acid residues [17,18]. DPPC is found, for example, in the erythrocyte membrane and is the major lipid component of the pulmonary surfactant. In addition, other phospholipids (such as 1-palmitoyl-2-oleoyl-glycero-3-phosphocholine (POPC)) and sterols (such as cholesterol (Chol)) are also added to form multicomponent systems. POPC is also a phospholipid from the PC group, but is characterized by a different degree of chain saturation than DPPC.

In turn, cholesterol, which belongs to sterols, is one of the main lipids that build mammalian membranes. Chol is responsible for among other things, altering the membrane stiffness. In the case of erythrocyte membranes, it can constitute up to 50 % of all structural lipids [19–24]. In a layer, Chol molecules are arranged so that their hydroxyl groups are near the heads of the phospholipids, and the hydrophobic rings and a side chain are located in the fatty acid chains of the interior of the membrane [19–22].

The technique of producing multicomponent model membranes allows for determining the effects of substances on cells characterized by different lipid contents. An example of this is the study of the effect of Au-NPs on the membranes of different chemical compositions. Although Au-NPs have good biocompatibility and unique optical properties, there is still a lack of data on the interaction of Au-NPs with model biological membranes [25].

In this article, the monolayers will consist of DPPC and Chol (mixed in a ratio of 9:1) (DPPC:Chol) and POPC and Chol (mixed in a ratio of 4:1) (POPC:Chol), which also allow us to determine the influence of the phospholipid structure on the interactions with Au-NPs. However, attention should be paid to the fact that interactions in Au-NPs-lipid systems are influenced not only by the type of lipid but also by the properties of Au-NPs, such as size, shape, and hydrophobicity. This was confirmed in their studies by Lin et al. [26], who investigated the influence of the shape of Au-NPs on the properties of monolayers. The change in the hydrophobicity of Au-NPs can be introduced by their appropriate functionalization by ligands [27]. Recently, a rapid procedure, based on the combination of commercially available polyethylene glycol (PEG-SH) and 1-dodecanethiol, has been proposed as a general method to transfer a wide variety of gold and silver NPs of different sizes and shapes (e.g. spherical or rods NPs, respectively, Au-NSs, Au-NRs) from an aqueous dispersion into $CHCl_3$ [23]. Moreover, the NPs functionalization step is also intended to ensure the formation of stable and highly dispersed NPs in organic solvents and to prevent agglomeration. Functionalization is also important in terms of its effect on the human body [28]. Functionalization and stabilization of nanostructures and inhibition of the shape change of NPs can be achieved by covering their surface with an in- or organic layer [29]. For example, functionalization with PEG-SH imparts the Au-NPs higher stability and better biocompatibility than pure NPs. Such NPs circulate in the blood for a long time, preventing too rapid inactivation of these systems (by the endoplasmic reticulum) and promoting their accumulation in tissues [30,31].

So far, we have conducted research on the interaction of pegylated Au-NRs@PEG with a model cell membrane composed of DPPC at the air–water interface [32]. Studies have shown that the presence of Au-NRs@PEG changes the organization of DPPC in the Langmuir monolayer by increasing the mutual distances between DPPC molecules. The results obtained for the Au-NRs@PEG/DPPC systems became the motivation to continue this type of research to determine the effect of shape on the properties of lipid components of biological membranes.

The results obtained by introducing Au nanoparticles into multicomponent lipid systems will reflect the changes that may occur as a result of the interaction of a given substance with cell membranes, depending on their type. In this article, we want to answer the question of what type of Au-NPs will be a more suitable material for further research on the use of Au-NPs in fields such as medicine or pharmacy. However, there is still a lack of knowledge of the role of the Au-NPs modification and functionalization by PEG interactions with phospholipids. For this reason, the presented work considers the influence of shape Au-NPs on Langmuir monolayers and is devoted to Au-NPs interactions into membrane models. The influence of Au-NSs and Au-NRs on the behavior of monolayers consisting of DPPC, DPPC:Chol (9:1), POPC, POPC:Chol (4:1) was described on the basis of properties of biomimetic systems (e.g. surface pressure isotherms (π) – surface area (A) and surface compressibility modulus (C_s^{-1}) – surface pressure (π) dependencies), Brewster angle microscopy (BAM) images and High-Resolution Transmission Electron Microscopy (HR-TEM). In addition, relaxation experiments were also carried out to determine the effect of the Au-NPs on the stability of model cell membranes and measurements of the infrared reflectance absorption with polarization modulated infrared reflection absorption spectroscopy (PM-IRRAS).

2. Materials and methods

2.1. Chemicals

Tetrachloroauric acid ($HAuCl_4 \cdot H_2O$) (99.99 %) from Alfa Aesar (USA), cetyltrimethylammonium bromide (CTAB) (99.00 %), sodium borohydride ($NaBH_4$) (98.00 %), silver nitrate ($AgNO_3$) (99.99 %), ascorbic acid (99.00 %), O-(2-mercaptoethyl)-O'-methylpolyethylene glycol (PEG-SH $M_W \approx 2000$ (2k) from Merck (Poland), spectrophotometric grade methanol and ethanol (EtOH) 99.80 % H_2O-free purchased from POCH S.A. (Poland) were used for the synthesis and functionalization of gold nanoparticles.

1,2-dipalmitoyl-*sn*-glycero-3-phosphocholine (DPPC) (≥99.00 %), 1-

palmitoyl-2-oleoyl-glycero-3-phosphocholine (POPC) (≥99.00 %) and cholesterol (Chol) (≥99.00 %) from Avanti Polar Lipids (USA), high-purity chloroform for spectroscopy ($CHCl_3$) (Uvasol®), isopropanol (≥99.80 %) and acetone (≥99.80 %) purchased from Merck (Poland) were used for the formation of biomimetic systems.

2.2. Chemical synthesis and functionalization of gold nanoparticles

All chemical reagents were dissolved in Milli-Q ultrapure water (18.2 MΩ·cm, 71.98 ± 0.01 $mN \cdot m^{-1}$) in glass flasks that had been treated with *aqua regia* (HCl:HNO_3 3:1 v/v) prior to use. Gold nanoparticles with different shapes (spherical (NSs) and rods (NRs)) were synthesized by a seed-mediated growth method [33,34] and used by us previously [32,35,36]. The Au-NRs were prepared in accordance with our previous procedures for further research, which are presented in this paper [37]. In this case, slight modifications were introduced. HCl was added with assisted $AgNO_3$ as a factor stimulating the growth of nanoparticles. The synthesis of the Au-NSs with PEG-SH was carried out according to the previously described procedure [35,38]. The Au-NSs were prepared by a one-step bottom-up method using a standard citrate reduction process [34]. The functionalization process of Au-NRs and Au-NSs was prepared by a modified version of a method described in a previous paper [37,39]. An aqueous solution of PEG-SH 2k was sonicated for 30 min at 40°C and added dropwise to the vigorously stirred solution of Au-NRs and Au-NSs. The mixture was left overnight with gentle stirring. The PEG-SH ligand was chosen as a capping agent to functionalize the surface of nanoparticles to ensure their stability and avoid aggregation. Even in the absence of uncapped free ligands in solution and stabilizing CTAB surfactant, the affinity of thiol groups to the gold surface ensures high stability of functionalized NPs. This allows removal of excess ligands without nanoparticle aggregation. The ligand exchange reactions were carried out using of 1 mM PEG-SH with a chain length of 2000 mers. After the functionalization process, the reaction product was properly fractionated and purified by centrifugation twice (7500 rpm for 20 min), and supernatant was removed. The precipitate was then dispersed in methanol.

2.3. Physicochemical characterization of the gold nanoparticles

The characterization of Au-NPs was performed by UV–Vis spectroscopy (Varian Cary 4000). The electrokinetic potentials and size distributions of the Au-NPs were measured using a Malvern Zetasizer Nano-ZS Dynamic Light Scattering Analyzer (Malvern Instruments Ltd.,). The morphology and size dispersion of Au-NPs were characterized by transmission electron microscopy (TEM) using a JEOL 1400 (120 kV). The TEM measurements were performed by depositing a colloidal dispersion of NPs by drop casting onto a copper grid covered with a thin carbon layer and placed on a vacuum desiccator overnight. Images were collected in a JEOL 1400 microscope working at 120 kV.

2.4. Isotherm π-A experiments

Solutions of phospholipids (DPPC, POPC) at a concentration of 0.1 $mg \cdot ml^{-1}$ and Chol at a concentration of 0.053 $mg \cdot ml^{-1}$ were prepared by dissolving the solids in $CHCl_3$. To obtain the DPPC:Chol (9:1) mixture, DPPC and Chol solutions were mixed in a molar ratio of 9:1. Similarly, a POPC:Chol (4:1) mixture was prepared. For the preparation of Langmuir monolayers, a Langmuir troughs (KSV-NIMA) with a total area of 273 cm^2 and 700 cm^2 were used. Before each experiment the Teflon trough was wiped with a tissue soaked in $CHCl_3$, followed by a tissue soaked in isopropanol. Then the trough was rinsed with plenty of MilliQ water (18.2 MΩ·cm, 71.98 ± 0.01 $mN \cdot m^{-1}$). After cleaning the trough was filled with MilliQ water which was used in the studies as the subphase. In the first stage of the research, monolayers consisting only of lipids or Au-NPs@PEG were created. For this purpose, 200 μl of lipid solutions (DPPC, POPC, DPPC:Chol (9:1), POPC:Chol (4:1)) or gold NPs@PEG (Au-NSs or Au-NRs) were applied to the surface of the subphase using a Hamilton microsyringe. To prepare layers consisting of lipids and gold NPs@PEG, 750 μl of a mixture consisting of gold NPs@PEG (Au-NSs or Au-NRs) and lipids (DPPC or POPC) or a mixture of lipids (DPPC:Chol (9:1) or POPC:Chol (4:1)), which were mixed so that the ratio of methanol to $CHCl_3$ was 1:4 (v:v). The mixtures were prepared in a similar manner to that described in our previous work [32]. 10 min after application of the solution to the subphase surface, the monolayer was compressed by the symmetrical movement of two hydrophilic barriers made of Delrin at a constant speed of 10 $mm \cdot min^{-1}$. Surface pressure was measured with a Wilhelmy-type electrobalance (KSV-NIMA). This allowed for recording changes in surface pressure (π) as a function of trough surface area (A). Each experiment was repeated three times to ensure the repeatability of the π-A curves to ± 1 $Å^2 \cdot mol^{-1}$. Measurements were performed at a constant temperature of (21.0 ± 0.1)°C, which was controlled by a Julabo F12 circulator.

2.5. Brewster angle microscopy (BAM)

BAM images were recorded during monolayer compression, which allowed visualization and monitoring changes in model membranes' morphology. BAM images were recorded for the same monolayers for which the isotherm measurements were performed. For this purpose, a Langmuir trough (KSV-NIMA) equipped with an UltraBAM from Accurion GmbH using a 50 mW laser emitting p-polarized light at a wavelength of 658 nm, a 10x magnifying lens, a polarizer, an analyzer and a CCD camera were used. The spatial resolution of the BAM was 2 μm.

2.6. Relaxation experiments

Monolayers were prepared in the same way as for the isotherm measurement – by compressing mixtures of gold NPs@PEG (Au-NSs or Au-NRs) and lipids (DPPC or POPC) or a mixture of lipids (DPPC:Chol (9:1) or POPC:Chol (4:1)) to a surface pressure of 30 $mN \cdot m^{-1}$. The pressure was kept constant on this level by the Langmuir trough software, and the relative change in surface area ($A \cdot A_0^{-1}$), i.e. the ratio of the surface area per particle (A) to its initial value (A_0), was recorded over time (t).

2.7. Polarization modulation infrared reflection absorption spectroscopy

Polarization modulated infrared reflection absorption spectroscopy (PM-IRRAS) spectra were recorded using a KSV-NIMA PM-IRRAS spectrometer (PMI 550), equipped with a polarization modulation module (ZnSe PEM-100 modulator, Hinds Instruments) and an MCT detector. The spectrometer with the Langmuir trough was mounted on an optical table equipped with an active vibration isolation system (VarioBasic 40 anti-vibration system, Halcyonics) to ensure measurement stability. The PM-IRRAS measurement is based on the constant modulation of infrared light between p and s polarization. The difference between these two signals gives the surface information, and the sum provides the reference spectrum. The spectra were collected in the wavenumber range of 700–4000 cm^{-1}, and the 850–1800 cm^{-1} range, corresponding to the head region of polar phospholipids, was analyzed. The photoelastic modulator (PEM) was set at 1500 cm^{-1} to ensure its maximum effectiveness in the polar headgroup region. The incidence angle was set on 80°. The resolution of the spectra was 8 cm^{-1}. The method used to prepare the monolayers was the same as for the relaxation measurements. After reaching 30 $mN \cdot m^{-1}$, PM-IRRAS spectra were collected.

3. Results and discussion

3.1. Characterization of the synthesized gold-nanoparticles

The potential applications of NPs depend largely on their properties and architecture, therefore the incorporation of different types of NPs

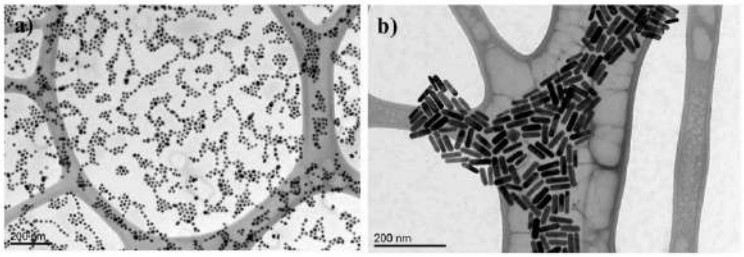

Fig. 1. Transmission electron microscopy of Au-NSs (a) and Au-NRs (b).

may differentially affect the properties of model membranes. Pegylated gold NPs (Au-NPs@PEG) of various shapes (and sizes) were used to study this issue.

To estimate the quality of the modified synthesis of Au-NPs@PEG, the extinction spectra were measured. The UV–Vis spectra of Au-NSs and Au-NRs are shown in Fig. S1 (SM). The bands of surface plasmon resonance (SPR) visible in the spectra originate from the collective oscillation of electrons in response to optical excitation. The transverse SPR band (at around 500 nm) is characteristic of Au-NSs and Au-NRs for the resonance along the short axis (perpendicular to the long axis) of the rods. The resonance parallel to the long axis of Au-NRs leads to a longitudinal SPR band, which is observed in the visible to near-infrared

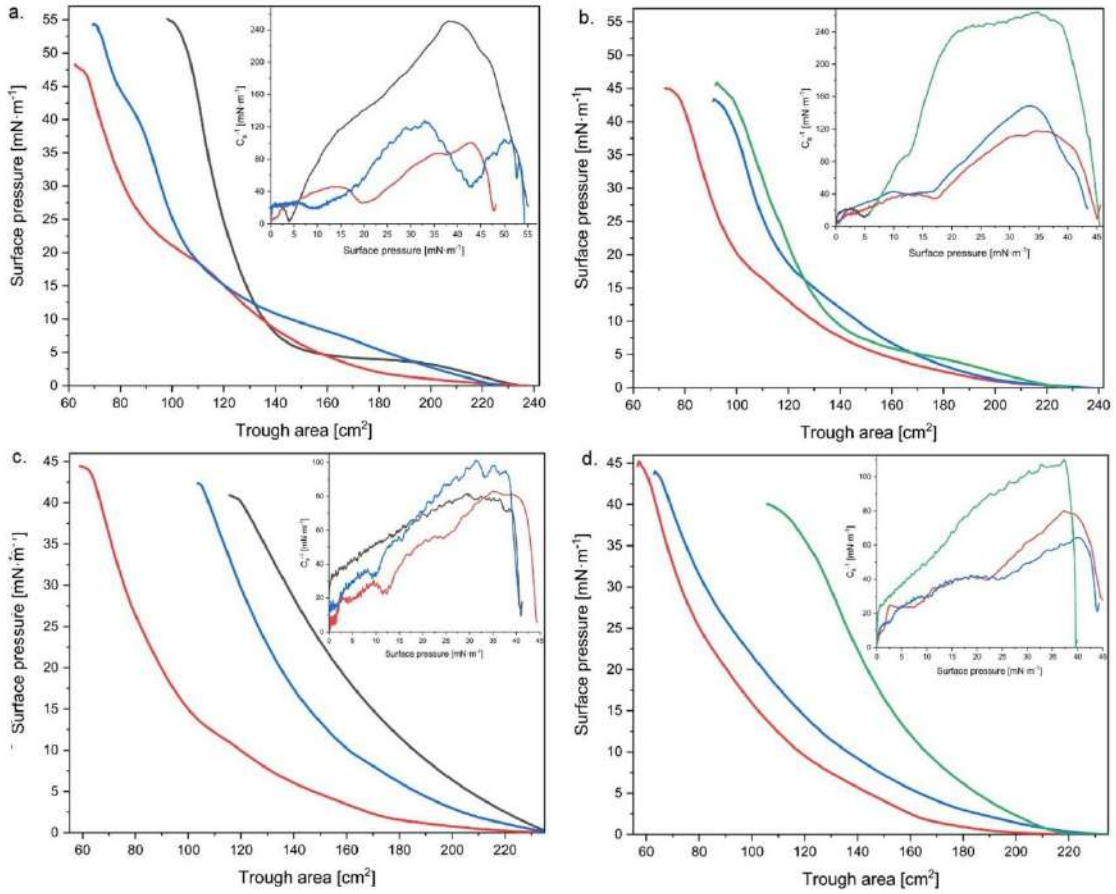

Fig. 2. π-A isotherms of the Langmuir monolayer and the surface compressibility modulus (C_s^{-1}) vs. surface pressure (π) (the inset graph) for DPPC (a), DPPC:Chol (9:1) (b), POPC (c) and POPC:Chol (4:1) (d) monolayers containing Au-NSs@PEG (red line) or Au-NRs@PEG (blue line), whereas for pure phospholipids monolayers: black line – DPPC or POPC; green line – DPPC:Chol (9:1) or POPC:Chol (4:1). (For interpretation of the references to colour in this figure legend, the reader is referred to the web version of this article.)

region of the electromagnetic spectrum. The relative intensity of both extinction bands is the yield indicator of the photochemical synthesis of Au-NRs formation [40]. The narrow peaks for the nanostructures confirm their monodispersity and the relative absence of impurities. Spectroscopic measurements showed a narrow absorption band at λ_{max} = 527 nm, confirming the formation of small and homogenous Au-NSs. The spectrum of Au-NRs is characterized by two bands located at λ_{max} = 518 nm and λ_{max} = 667 nm. Besides, the full width at half maximum (FWHM) is a measure of the gold NPs size dispersion [41]. At the beginning of the synthesis, the majority of the NPs are nanospheres and just a tiny portion are high aspect ratio NRs; hence, a substantial FWHM value is observed in the initial few minutes of the photochemical synthesis. However, as the Au-NSs grow anisotropically to form Au-NRs, the size dispersion becomes smaller. The aspect ratio of Au-NRs determines the longitudinal band wavelength, which in turn determines the quick anisotropic growth of the nuclei produced. Subsequently, the concentration of accessible gold atoms diminishes, allowing the nuclei to develop at a more controlled rate over time and create nanorods with the appropriate aspect ratio. Thus, as the photochemical synthesis proceeds, the ratio of the high aspect ratio to low aspect ratio nanorods rises, leading to a suitable longitudinal band wavelength. In our case, FWHM for Au-NSs was 0.123 eV (990.85 cm^{-1}), and for Au-NRs was 0.123 eV (990.85 cm^{-1}) and 0.130 eV (1048.58 cm^{-1}) for transverse and longitudinal bands, respectively. The values were adjusted using the Fityk program. Single and narrow peaks indicate high monodispersity and absence of impurities. The location and intensity of the band depends on the size, surface morphology and aspect ratio of the nanostructures, which is attributed to the surface plasmon resonance resulting from the collective oscillation of free conduction electrons induced by the interacting electromagnetic field. The shape and location of the spectra for Au-NSs and Au-NRs is in accordance with previous literature reports [37,42].

The size and distribution of the gold NPs were determined by means of TEM analysis (Fig. 1), which confirmed the successful synthesis of Au-NSs of the diameter of (15.1 ± 2.2) nm and Au-NRs of the average dimensions (14.3 ± 1.7) nm (width) and (59.8 ± 2.6) nm (length). The particle's diffusion coefficient is measured using DLS in order to obtain the Au-NSs size information. This explains the term "hydrodynamic dimension" applied to the particle size determined by DLS analysis. A particle's mass alone is not enough to determine its diffusion coefficient; other factors that influence the particle-solvent interactions and, consequently, the Brownian motion of the particles, include the particle's shape and surface chemistry. The mass of the NPs has less of an impact on its translational diffusion coefficient than its form and surface chemistry [43]. For prepared Au-NSs@PEG, the hydrodynamic diameter of about 64 nm was determined. The increase in diameter of the Au-NSs was due to the functionalisation process carried out, in which PEG chains were attached to the Au surface by covalent Au-S bonding. Considering the diameter obtained by TEM and comparing it with that obtained by DLS, it can be concluded that the polymeric (PEG) coating produced was more than 20 nm thick. This is an approximate value. It must also be taken into account that the PEG chains may be unevenly distributed and clumped on the surface of the nanoparticles and may form aggregates. The zeta potentials of Au-NSs changed from −0,53 mV to −27,9 mV after PEG functionalization. Au-NRs stabilized in CTAB solution exhibited cationic surfaces (12,9 mV). This resulted from the adsorbed CTAB, which possesses a hydrophilic head consisting of a quaternary amine. On the other hand, PEG-modified Au-NRs displayed a negative surface. In particular, the zeta-potential was reduced to a negative level (−20,1 mV) upon PEG modification, suggesting that PEG chains adhered to the Au-NRs and entirely covered their surface, even in the event that some CTAB remained on it. This modification was carried out without any particle fusion or aggregation. A successful coating is often proven by negative zeta potential [25].

3.2. Interactions of gold-nanoparticles with lipid monolayers

To determine the effect of Au-NPs@PEG on the lipid monolayers (DPPC, POPC, DPPC:Chol (9:1), POPC:Chol (4:1)), π-A isotherms were measured. Measurements of π-A isotherms were performed during compression of lipid or NPs@PEG monolayers, and during compression of lipid monolayers in the presence of Au-NRs@PEG and Au-NSs@PEG. Based on the π-A isotherm, it is possible to determine the surface compressibility modulus, which is defined as follows: $C_s^{-1} = -A \cdot \left(\frac{d\pi}{dA}\right)_T$ [44]. The maximum value of the surface compressibility modulus determines the degree of particle packing in the monolayer. The criterion introduced by Davies and Rideal [45] makes it possible to determine the degree of elasticity of the surface film and, indirectly, its physical state. Their proposed classification distinguishes several physical states of the monolayer such as an expanded liquid state (LE), a liquid condensed state (LC), and a solid (S) state [46]. The isotherms and surface compressibility modulus of investigated systems are shown in Figs. 2 and S2 (SM), whereas the values of the π-A isotherm parameters are given in Table S1, Table S2 and Table S3 (SM).

The first element worth paying attention to when characterizing monolayers is the addition of cholesterol to the phospholipid monolayers. The presence of Chol caused the surface film to collapse faster – this occurred at 46 $mN \cdot m^{-1}$ (Fig. 2b, Table S2, SM). This value for pure DPPC was 55 $mN \cdot m^{-1}$ (Fig. 2a, Table S2, SM). For monolayers consisting of POPC, which in its structure has an unsaturated bond between the C atom and therefore has different properties than DPPC, which is a saturated phospholipid, the presence of Chol in POPC layer shifted the isotherm (Fig. 2d) towards higher values of the trough area compared to the pure POPC monolayer curve (Fig. 2c). The addition of Chol to phospholipid monolayers resulted in an increase in the max C_s^{-1} value (Table S2, S3, SM), and consequently, the elasticity of the surface film decreased. This is in agreement with literature reports, where the authors investigated the effect of the addition of Chol on the DPPC monolayer [47,48]. In the presence of DPPC, the Chol molecule orients itself via its hydroxyl group close to the phospholipid oxygen. As a result of van der Waals interactions, interactions occur that lead to the parallel positioning of Chol molecules to the alkyl chains of the phospholipid molecules. This contributes to changes in the stability and structural order of the monolayers created by DPPC and Chol. It is well known that Chol has a condensing effect [49]. The primary effect occurring as a result of this action is the ordering of the hydrocarbon chains of adjacent DPPC molecules by the Chol ring system. In addition, there is an increase in the packing density of the monolayer consisting of DPPC and Chol [48]. This is due to the perturbation of the monolayer compression caused by the trapping of lipid particles at the phase boundary.

Another element worth paying attention to when characterizing monolayers is the addition of gold NPs@PEG (Au-NSs or Au-NRs) to lipid monolayers. For each of the tested systems the isotherm is different from the isotherms of pure Au-NSs@PEG and Au-NRs@PEG, which are presented in Fig. S2a (SM). A similar situation occurs in the case of the module, where higher values were observed for NPs systems with lipids than for pure NPs (Fig. S2b, Table S1 SM). Such results may be a confirmation of the fact that the tested nanoparticles interact with lipids to form monolayers. The presence of Au-NSs@PEG as well as Au-NRs@PEG into the DPPC monolayer significantly affects the shape of the π-A isotherm (Fig. 2a). One of the main differences is the shift of the phase transition characteristic of DPPC towards higher surface pressure values. For Au-NSs@PEG/DPPC it is seen at 18 $mN \cdot m^{-1}$, while for Au-NRs@PEG at 10 $mN \cdot m^{-1}$. The surface pressure value (47 $mN \cdot m^{-1}$) at which the Au-NSs@PEG/DPPC monolayer collapses is also lower compare to the Au-NRs@PEG/DPPC system (54 $mN \cdot m^{-1}$). Based on the data presented in Fig. 2a and in Table S2 (SM), the max C_s^{-1} value is lower for each type of nanoparticles presented in lipid monolayers than for a pure DPPC monolayer. This means that adding nanoparticles

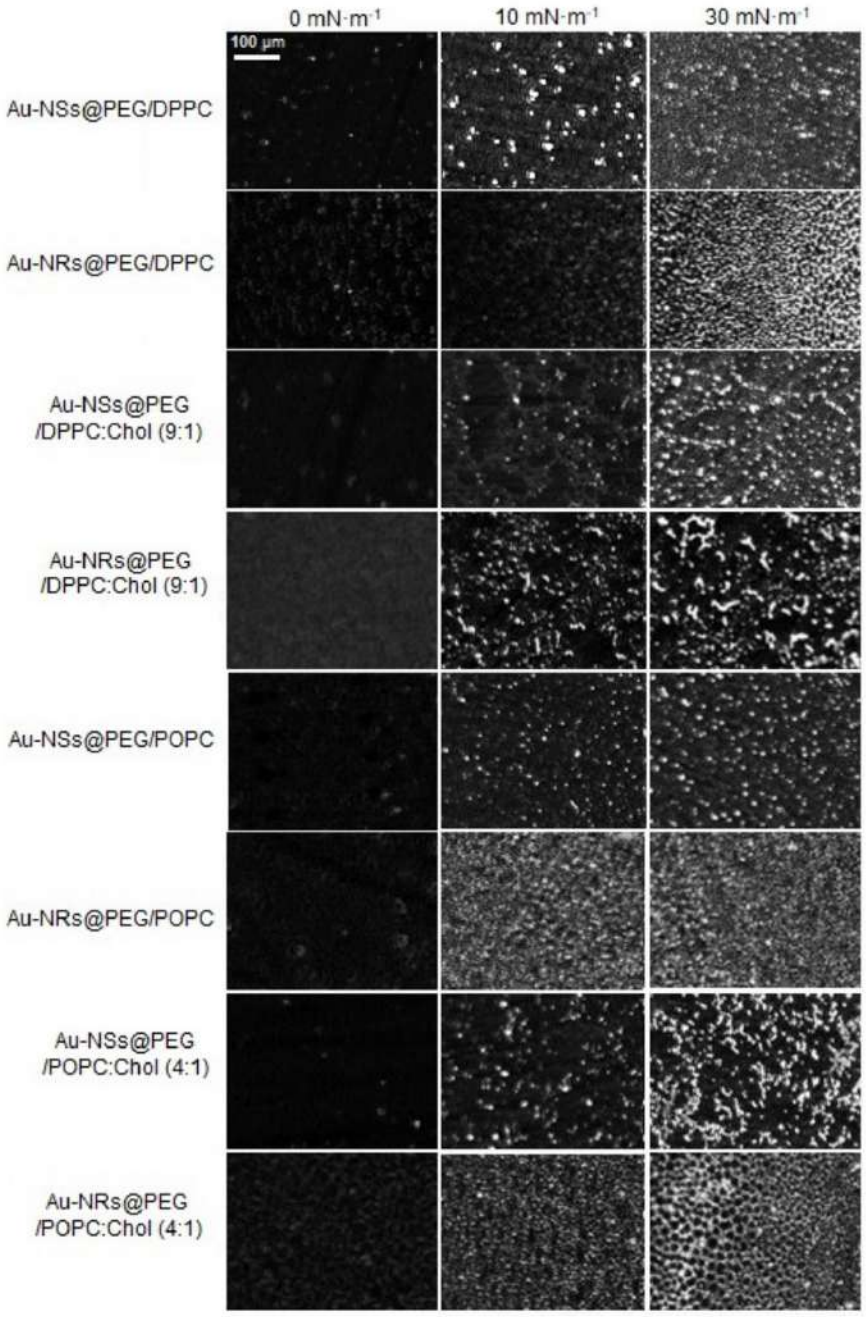

Fig. 3. Brewster angle microscopy images of DPPC, DPPC:Chol (9:1), POPC and POPC:Chol (4:1) containing Au-NSs@PEG or Au-NRs@PEG taken at different surface pressures.

reduces the surface film's stiffness. The max C_s^{-1} values indicate that both the Au-NSs@PEG/DPPC and Au-NRs@PEG/DPPC monolayer were in the LE state while the DPPC monolayer was in the LC state. The reason for the observed decrease in film stiffness may be the appearance of a spatial obstacle due to the presence of nanoparticles in the lipid monolayer [50]. However, due to the size of nanoparticles, some of them may remain on the surface of the lipid monolayer without penetrating through it. Moreover, both the surface pressure value at which the monolayer collapses and the max C_s^{-1} are different from those obtained in previous studies [32] in which we investigated DPPC monolayers with the addition of Au-NRs@PEG. However, in the studies described in this article, we used a different type of Au-NRs@PEG synthesis. Based on the data presented there, it can be concluded that depending on the method of Au-NRs@PEG synthesis, it is possible to obtain monolayers characterized by other parameters, such as collapse pressure, maximum value of the surface compressibility modulus. By comparing the values obtained for the lipid systems with Au-NSs@PEG and Au-NRs@PEG, it can be also concluded that the nanoparticles' shape affects the DPPC monolayer's properties. As seen in Fig. 2c, d and Table S3 (SM), the addition of NPs also affects the properties of the POPC monolayers. Similarly to Au-NSs@PEG/DPPC, also for Au-NSs@PEG/POPC based on the C_s^{-1}–π graph, one can conclude that a phase transition is visible at 12 mN·m^{-1}. However, in contrast to the DPPC systems, the presence of Au-NSs@PEG in the POPC monolayer increases the collapse pressure. The Au-NRs@PEG/POPC monolayer also exhibits a higher surface pressure at which the monolayer collapses compared to the POPC monolayers. The addition of both Au-NSs@PEG and Au-NRs@PEG to the DPPC:Chol (9:1) system resulted in the disappearance of the phase transition (Fig. 2b). For the Au-NSs@PEG/DPPC:Chol (9:1) and Au-NRs@PEG/DPPC:Chol (9:1) systems, the collapse pressure of the layer was about 43–45 mN·m^{-1}. Similarly, to the POPC systems, the Au-NSs@PEG/POPC and the Au-NSs@PEG/POPC:Chol (4:1) monolayers also achieved a higher surface pressure value at which the surface film collapsed (Fig. 2d, Table S3, SM). The observed increase in the monolayer collapse value for each system containing nanoparticles and POPC compared to lipid monolayers may result from interactions that may occur between POPC molecules and PEG-coated NPs. For monolayers consisting of POPC, which in its structure has an unsaturated bond between the C atom and therefore has different properties than DPPC, which is a saturated phospholipid, max C_s^{-1} value (included in Table S3, SM) indicates the LE state both for the POPC and Au-NSs@PEG/POPC monolayer. In turn, the Au-NRs@PEG/POPC monolayer is in the LC state. In this case, there was an increase in the value of max C_s^{-1}, and, consequently, a decrease in the elasticity of the surface film. In the case of the POPC:Chol (4:1) monolayer, both the addition of Au-NSs@PEG and Au-NRs@PEG caused a decrease in the max C_s^{-1} value (Table S3, SM). However, the addition of Au-NRs@PEG caused an increase in the elasticity of the layer to a greater extent than Au-NSs@PEG. The change in the elasticity of the surface film may be due to the presence of a hydrophobic sterol ring, which tends to limit contact with the aqueous subphase. Therefore, Chol molecules are usually present between phospholipid molecules. Thanks to this arrangement of molecules, the condensation of monolayers containing both Chol and Au-NPs can result from the formation of an ordered structure that is stabilized by van der Waals interactions between the sterol rings of Chol molecules and the alkyl chains of phospholipids [51]. The study by Hossain et al. [52] also showed that Chol molecules and the hydrophobic tails of amphiphilic phospholipids interact with Au-NPs. Also in our studies such an effect is possible. The interactions between Chol and the nanoparticle surface are more dominant than the phospholipid tails, which may indicate that cholesterol interacts with the PEG-coated nanoparticles. This may indicate the incorporation of more nanoparticles into the monolayer and, consequently, the presence of less nanoparticles on the lipid monolayer than in the case of DPPC systems, where lower monolayer collapse values were observed compared to pure lipid monolayers.

To investigate how the spherical nanoparticles interact with lipids, a TEM analysis (Fig. S4) was performed, which confirmed that the nanoparticles form large, unevenly distributed clusters, with an occasional tendency to form aggregates. To confirm the charge generated on the surface of the lipids and lipid-nanoparticle mixtures, the zeta potential of spherical nanoparticle systems was measured by DLS and the following values were obtained: for DPPC 2.57 mV, POPC 6.21 mV, and for the mixtures Au-NSs@PEG/DPPC −8.96 mV, Au-NSs@PEG/DPPC:Chol (9:1) −14.7 mV, Au-NSs@PEG/POPC −2.16 mV, Au-NSs@PEG/POPC:Chol (4:1) −17.1 mV. Analyzing these parameters, we can conclude that the shift to a negative potential indicates the dominant influence of the nanoparticles in the mixtures and also suggests that the nanoparticles may interact with the lipids. Au-NPs can be adsorbed onto the surface of the Langmuir monolayer by integrating with the polar head groups of the phospholipids, as well as by van der Waals interactions with the hydrophobic lipid tails. Au-NPs with a rod-like shape can induce the formation of more complex 3D structures, especially at high nanoparticle concentrations. In the case of Langmuir monolayers, gold particles can act as aggregation centers, causing DPPC and cholesterol molecules to arrange into three-dimensional clusters. This can lead to rearrangement of the lipid molecules and facilitate the formation of new structures, including aggregates. Such distribution of Au-NPs in the lipid layer affects its elasticity, as indicated by the parameters max C_s^{-1} included in Table S3, SM. Incorporation of Au-NPs can affect the packing density of the lipid molecsules, altering the overall mechanical properties, such as the surface pressure-area isotherms, which can be studied to evaluate how the nanoparticles influence the lipid layer's behavior. The penetration of such nanoparticles would only be possible with the use of additional factors, such as pressure and further encapsulation, which would enable their penetration. In our case, Au-NPs@PEG exhibit hydrophilic properties with an amphiphilic character, similar to cholesterol, which enhances the membrane stiffening effect. In addition, cholesterol also affects the electrostatic properties of the membrane, which in turn determines how negatively charged functionalized Au-NPs interact with the lipid membrane, altering the adsorption behavior of negatively charged nanoparticles.

During monolayer compression, BAM microscopy studies were also performed. The BAM technique was used to image, the morphology of monolayers formed at the air–water interface BAM images of bare lipid, bare Au-NSs@PEG and bare Au-NRs@PEG monolayers and are shown in Fig. S3 (SM). The surface pressure values were chosen to determine the changes from the moment of the onset of compression up to a surface pressure of 30 mN mN·m^{-1}, which corresponds to the pressure found in the native cell membrane [53]. In the case of DPPC layers, characteristic domains were observed which grew during compression until the entire monolayer was covered with lipid in the LC phase, which is consistent with the data reported in the literature [54].

Such changes were not observed in the case of the other lipid monolayers, which was also described in the literature [5,55]. In the case of bare Au-NSs@PEG and bare Au-NRs@PEG monolayers, with the increase in surface pressure, the formation of structures was observed, which at 30 mN·m^{-1} covered most of the surface of the monolayer.

Based on previous studies and BAM images obtained for mixtures consisting of lipids and nanoparticles (Fig. 3) and for monolayers consisting only of lipids or nanoparticles (Fig. S3, SM), it can be concluded that mixed layers are formed, the morphology of which changes with increasing surface pressure. In each monolayer, compression resulted in the formation of an increasingly heterogeneous structure that increasingly covered the surface of the layer. The presence of increasingly ordered and densely packed structures, visible in BAM images at increasing surface pressure, may indicate the presence of nanoparticles on the surface of the lipid monolayer. Cholesterol can also influence the formation of microscale regions of higher density or aggregates, which are visible in BAM microscopy images, especially at a pressure of 30 mN mN·m^{-1}. These areas serve as preferential sites for the deposition of certain nanoparticles, which can modify their interactions with cell surfaces or other components of biological systems. It also alters the

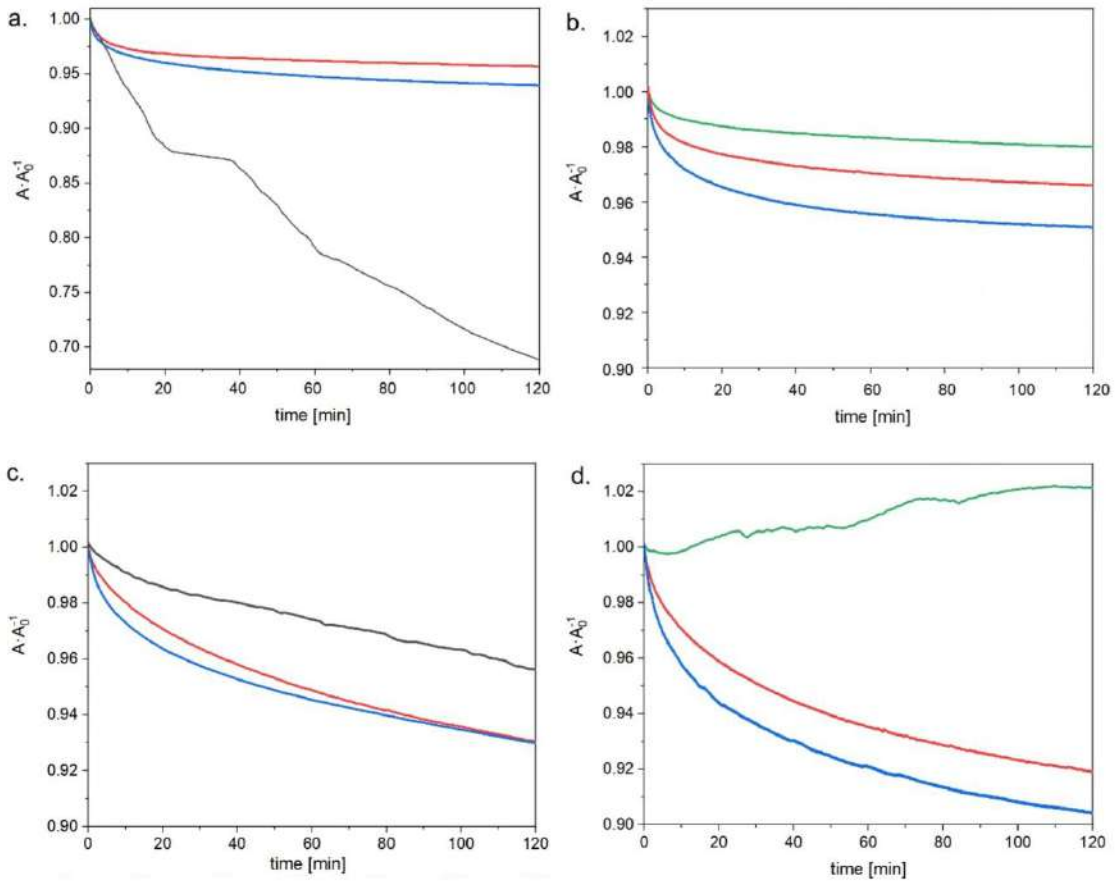

Fig. 4. Relative area vs. time curves for DPPC (a), DPPC:Chol (9:1) (b), POPC (c) and POPC:Chol (4:1) (d) monolayers containing Au-NSs@PEG (red line) or Au-NRs@PEG (blue line), whereas for pure phospholipids monolayers: black line – DPPC or POPC; green line – DPPC:Chol (9:1) or POPC:Chol (4:1). (For interpretation of the references to colour in this figure legend, the reader is referred to the web version of this article.)

dynamics of the interactions through direct interactions with the nanoparticles, as well as indirectly by influencing the properties of cell membranes or other lipid structures. These microdomains can act as 'islands' of higher order than the surrounding membrane, which can change the way nanoparticles interact with the membrane. Nanoparticles may preferentially accumulate or bind to these cholesterol-rich areas, altering their distribution within the membrane.

The relaxation measurements were carried out to determine the influence of the shape of Au-NPs@PEG on the stability of the monolayers (Fig. 4). For this purpose, all types of monolayers were compressed to 30 $mN{\cdot}m^{-1}$ and then the change in the relative surface area $A{\cdot}A_0^{-1}$ was recorded as a function of time. The incorporation of NPs resulted in a change in the $A{\cdot}A_0^{-1}$ value for each lipid monolayer. In the case of the DPPC monolayer, the addition of NPs caused an increase in the $A{\cdot}A_0^{-1}$ value, which may be due to strong NPs-NPs intermolecular interactions resulting in uneven distribution of NPs on the layer surface. In the case of the remaining lipids, the addition of NPs caused a decrease in the $A{\cdot}A_0^{-1}$ value. One of the reasons for the decrease in the value of the relative surface area may be the desorption of molecules from the phase boundary [56]. However, in the case of all Au-NPs@PEG investigated, the changes in values are small and remain above 0.9, which may indicate a small contribution of this phenomenon in monolayers. It can be seen that Au-NSs@PEG caused less destabilization of the lipid layers than Au-NRs@PEG (except for POPC lipids). The interactions between Au-NSs@PEG and lipids with or without Chol form a more stable mixed structure, probably due to their shape, uneven distribution on the monolayer surface, or incorporation into the lipid monolayer. In turn, the lower stability of Au-NRs@PEG systems may be due to the fact that Au-NRs are larger, and some amounts of them can be incorporated into the lipid monolayer, tilted to their surface, or remain on the lipid monolayer surface. Moreover, throughout the measurement period, the lowest influence of NPs shape on the relative surface area values was observed for the POPC monolayers (Fig. 4d). However, the remaining layers show that more stable layers are formed with the spherical than rods NPs. Moreover, independently of NPs shape the lowest stability in time shows the POPC:Chol monolayers. It may also indicate the incorporation of a larger number of nanoparticles into the lipid monolayer and, consequently, the presence of a smaller number of nanoparticles on the lipid monolayer surface. When interacting with nanoparticles, cholesterol can modulate the behavior of lipid systems by altering their physical properties such as elasticity and permeability. We can conclude that cholesterol stabilizes the systems, as can be seen from the increase or stability of the values of $A{\cdot}A_0^{-1}$. This behavior suggests that cholesterol acts on the system, favouring its stabilization.

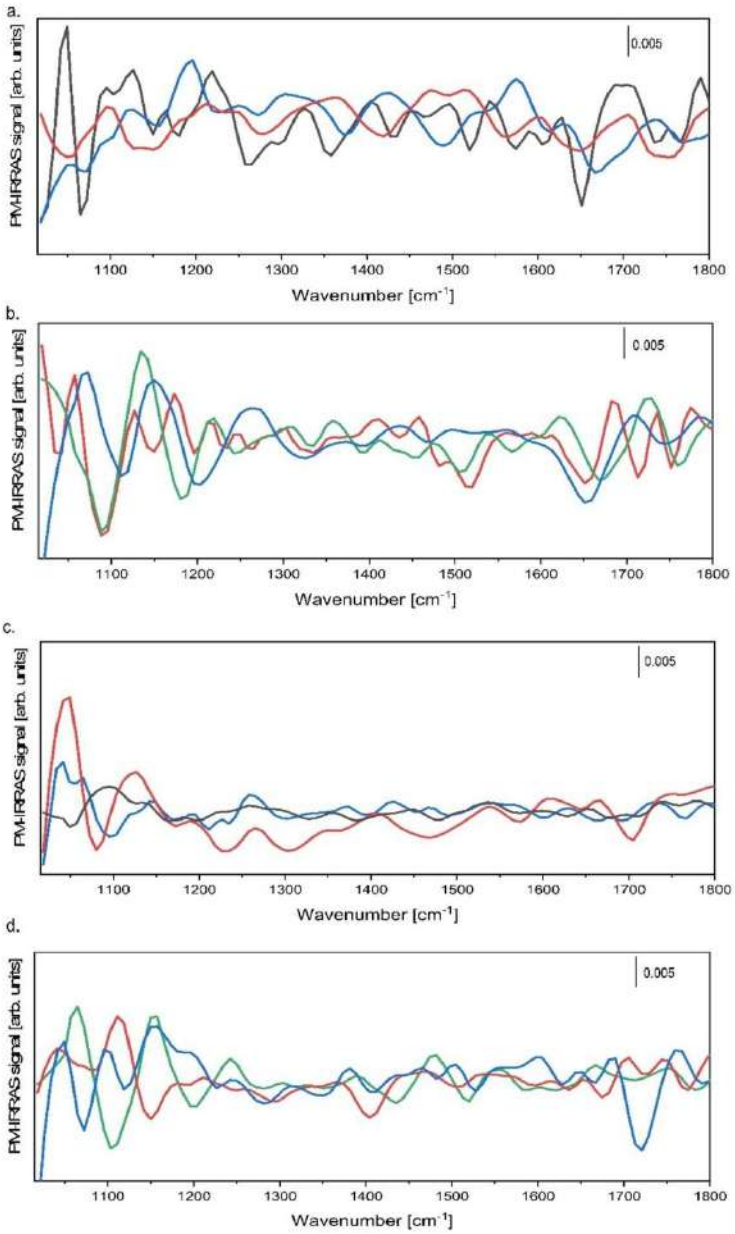

Fig. 5. PM-IRRAS spectra of DPPC (a), DPPC:Chol (9:1) (b), POPC (c) and POPC:Chol (4:1) (d) monolayers containing Au-NRs@PEG (blue line) or Au-NSs@PEG (red line) compressed to 30 mN·m^{-1}, whereas pure phospholipids' monolayers: black line – DPPC or POPC; green line – DPPC:Chol (9:1) or POPC:Chol (4:1). (For interpretation of the references to colour in this figure legend, the reader is referred to the web version of this article.)

In the next step, infrared reflectance measurements (IRRAS) were performed, which provided information on lipids' orientational and conformational properties (Fig. 5, Table 1).

For each of the systems investigated, bands corresponding to the asymmetric stretching of the single COO bond of the ester-phosphate group υ_{as}(C–O[P]) were observed. It is located at −1050 cm^{-1} [57–59]. In the case of monolayers consisting of DPPC and DPPC:Chol (9:1) (Fig. 5a, b), both the presence of Au-NSs and Au-NRs caused a decrease in the band intensity compared to the lipid monolayers. This may indicate a reduced interaction of NPs with the region of the polar head of DPPC molecules, which moves away from the surface of the monolayer as a result of the ongoing conformational changes, which

Table 1
PM-IRRAS band position (in cm^{-1}) for monolayers compressed to 30 $mN \cdot m^{-1}$.

BAND	υ_{as}(C–O [P])	$\upsilon_s(PO_2^-)$	υ_{as}(C–O–C)	$\upsilon_{as}(PO_2^-)$	υ(C=O)
DPPC	1048	1096	1219	1261	1735
DPPC:Chol (9:1)	1056	1103	1212	1264	1728
POPC	1049	1103	1224	1258	1736
POPC:Chol (4:1)	1035	1103	1212	1262	1728
Au-NSs@PEG/ DPPC	1064	1088	1213	1283	1719
Au-NRs@PEG/ DPPC	1056	1110	1226	1271	1732
Au-NSs@PEG/ DPPC:Chol (9:1)	1039	1088	1214	1264	1735
Au-NRs@PEG/ DPPC:Chol (9:1)	1033	1103	1211	1262	1728
Au-NSs@PEG/ POPC	1041	1080	1210	1256	1734
Au-NRs@PEG/ POPC	1041	1095	1227	1258	1730
Au-NSs@PEG/ POPC:Chol (4:1)	1041	1090	1233	1243	1730
Au-NRs@PEG/ POPC:Chol (4:1)	1050	1095	1226	1250	1718

may indicate a greater number of molecules on the surface of the lipid monolayer. The opposite phenomenon was observed in the case of monolayers consisting of POPC or POPC:Chol (4:1) (Fig. 5c, d). In these systems, the presence of NPs resulted in greater interaction with POPC molecules, causing conformational changes in the area of the polar head of POPC molecules, resulting in an increase in band intensity. These changes may also indicate the incorporation of more nanoparticles into the monolayer containing POPC than DPPC, which may consequently lead to a smaller number of nanoparticles on the surface of the lipid monolayer. The next vibrations observed for our systems are the symmetric vibrations $\upsilon_s(PO_2^-)$ located at ~1090 cm^{-1}. Both the localization of these vibrations and those visible ~1260 cm^{-1}, which correspond to the asymmetric vibrations of $\upsilon_{as}(PO_2^-)$, may indicate hydration of the phosphate group in the monolayers. This type of relationship was demonstrated by Zaborowska et al. [60], who studied monolayers consisting of DMPE and satins. In the case of monolayers containing Au-NSs@PEG, there was a shift in the band position towards lower wavenumber values, which was not observed in the case of monolayers containing Au-NRs@PEG. This may indicate that Au-NSs@PEG slightly induce increased hydration of phosphate groups. No significant band shifts were observed for the $\upsilon_{as}(PO_2^-)$ band. However, changes in band intensity are visible. The presence of Au-NSs@PEG and Au-NRs@PEG to the DPPC, POPC and POPC:Chol (4:1) systems increased band intensity. The exception is the Au-NRs@PEG/DPPC:Chol (9:1) monolayer, where there was a slight decrease in intensity. The increase in intensity may indicate that the phosphate group is approaching the plane of the monolayer. In the range from 1210 cm^{-1} to 1230 cm^{-1}, stretching bands υ_{as}(C–O–C) are observed in the investigated systems [61]. No clear wavenumber shifts were observed in the monolayers studied. In monolayers containing DPPC or DPPC and Chol, a decrease in band intensity is observed in the presence of Au-NRs@PEG and Au-NSs@PEG, which may indicate that the phosphate group is moving away from the plane of the monolayer. A spectral region is also associated with the ester carbonyl group υ(C=O), located at ~1700 cm^{-1}. The location of the lipid monolayer bands (Table 1) indicates the presence of ester groups that are not hydrogen-bonded. A similar conclusion can be drawn for monolayers with the addition of NPs, except for Au-NSs@PEG/DPPC and Au-NRs@PEG/POPC:Chol (4:1), where the band is shifted towards lower wavenumber values. For these monolayers, the hydration of the ester group in the presence of NPs occurred [62].

4. Conclusions

In our study, Au-NPs of two different shapes were incorporated into lipid monolayers. The schematic arrangement of the components in the investigated layers is shown in Fig. 6.

Studies have shown that monolayers containing Au-NSs@PEG are more stable than monolayers containing Au-NRs@PEG. Moreover, the conducted studies allow us to conclude that the shape of nanoparticles influences the stability of monolayers containing DPPC to a greater extent than POPC. The presence of Chol in the model lipid membrane promotes the formation of a more densely packed monolayer than in the case of a monolayer formed solely by phospholipid molecules alone. Based on the research, it can also be assumed that some of the Au-NPs are incorporated into lipid monolayers, while others remain on the lipid monolayer surface. For POPC-containing monolayers, it is possible for a larger number of nanoparticles to be incorporated into the lipid monolayer and, consequently, for fewer nanoparticles to be present on the lipid monolayer surface than for DPPC-containing monolayers. Nanoparticles can disrupt the organisation of the monolayer, possibly leading to rupture or the formation of microscale pores in the membrane. Larger nanoparticles may disrupt the integrity of the lipid layer or cause aggregation or the formation of unevenly distributed clusters, while smaller nanoparticles may integrate more easily into the layer. In such cases, nanoparticles may 'slip' inside, but not in the same way as smaller molecules, as their size prevents easy penetration. Although a single nanoparticle of about 15 nm is significantly larger than a DPPC lipid molecule (2–4 nm), it is possible that it will interact with the lipid membrane primarily on the surface, but will have difficulty penetrating directly into the interior of the monolayer.

Funding sources

This research was funded partially by the National Science Center in Poland by the project 2022/45/N/ST5/01464 (B.T.), and by the Polish Ministry of Science and Higher Education by the project No. 0512/SBAD/2420 (A.D.). P.B. also acknowledges the financial support from the National Science Center in Poland by the SONATINA grant number 2023/48/C/ST4/00067.

CRediT authorship contribution statement

Beata Tim: Writing – original draft, Visualization, Project administration, Methodology, Investigation, Funding acquisition, Data curation, Conceptualization. **Paulina Błaszkiewicz:** Writing – review & editing, Investigation, Funding acquisition, Data curation. **Emerson Coy:** Writing – review & editing, Supervision. **Alina Dudkowiak:** Writing –

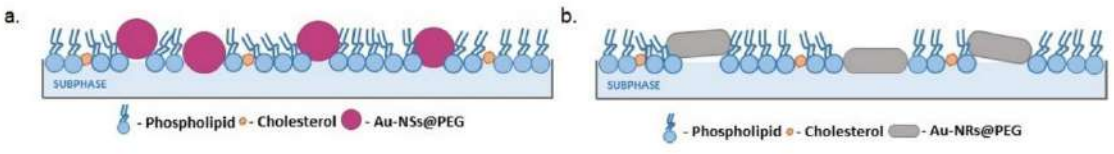

Fig. 6. Schematic arrangement of components for model Langmuir monolayer; (a) for layers with Au-NSs@PEG, (b) for layers with Au-NRs@PEG.

review & editing, Supervision.

Declaration of competing interest

The authors declare that they have no known competing financial interests or personal relationships that could have appeared to influence the work reported in this paper.

Acknowledgement

The BAM and PM-IRRAS experiments were performed at the Department of Environmental Chemistry, Jagiellonian University. The authors would like to thank Marcin Broniatowski for the opportunity to perform these measurements and for the valuable discussion of the results.

Appendix A. Supplementary data

Supplementary data to this article can be found online at https://doi.org/10.1016/j.molliq.2025.127501.

Data availability

Data will be made available on request.

References

[1] S.E. Lohse, C.J. Murphy, Applications of colloidal inorganic nanoparticles: From medicine to energy, J. Am. Chem. Soc. 134 (2012) 15607–15620, https://doi.org/10.1021/ja307589n.
[2] H. Gao, Y. Bi, X. Wang, M. Wang, M. Zhou, H. Lu, J. Gao, J. Chen, Y. Hu, Near-infrared guided thermal-responsive nanomedicine against orthotopic superficial bladder cancer, ACS Biomater Sci. Eng. 3 (2017) 3628–3634, https://doi.org/10.1021/acsbiomaterials.7b00405.
[3] E.R. Evans, P. Bugga, V. Asthana, R. Drezek, Metallic nanoparticles for cancer immunotherapy, Mater. Today 21 (2018) 673–685, https://doi.org/10.1016/j.mattod.2017.11.022.
[4] L.M. Marques Neto, A. Kipnis, A.P. Junqueira-Kipnis, Role of metallic nanoparticles in vaccinology: Implications for infectious disease vaccine development, Front. Immunol. 8 (2017) 136–143, https://doi.org/10.3389/finmu.2017.00230.
[5] B. Tim, M. Rojewska, K. Prochaska, Effect of silica microparticles on interactions in mono- and multicomponent membranes, Int. J. Mol. Sci. 23 (2022), https://doi.org/10.3390/ijms232112822.
[6] A.B. Ormond, H.S. Freeman, Gold nanoparticles therapy, Materials 6 (2013) 817–840, https://doi.org/10.3390/ma6030817.
[7] X. Huang, P.K. Jain, I.H. El Sayed, M.A. El Sayed, Plasmonic photothermal therapy (PPTT) using gold nanoparticles, Lasers Med. Sci. 23 (2008) 217–228, https://doi.org/10.1007/s10103-007-0470-x.
[8] E.C. Dreaden, A.M. Alkilany, X. Huang, C.J. Murphy, M.A. El-Sayed, The golden age: gold nanoparticles for biomedicine, Chem. Soc. Rev. 41 (2012) 2740–2779, https://doi.org/10.1039/C1CS15237H.
[9] M. Chen, Y. Sun, H. Liu, Cell membrane biomimetic nanomedicines for cancer phototherapy, Interdisciplinary Med. 1 (2023), https://doi.org/10.1002/INMD.20220012.
[10] R.C. Van Lehn, P.U. Atukorale, R.P. Carney, Y.S. Yang, F. Stellacci, D.J. Irvine, A. Alexander-Katz, Effect of particle diameter and surface composition on the spontaneous fusion of monolayer-protected gold nanoparticles with lipid bilayers, Nano Lett. 13 (2013) 4060–4067, https://doi.org/10.1021/nl401365n.
[11] M. Skrzypiec, M. Weiss, K. Dopierała, K. Prochaska, Langmuir-Blodgett films of membrane lipid in the presence of hybrid silsesquioxane, a promising component of biomaterials, Mater. Sci. Eng. C 105 (2019) 110090–110100, https://doi.org/10.1016/j.msec.2019.110090.
[12] A. Mogilevsky, R. Jelinek, Gold nanoparticle self-assembly in two-component lipid Langmuir monolayers, Langmuir 27 (2011) 1260–1268, https://doi.org/10.1021/la103718v.
[13] A.A. Torrano, Â.S. Pereira, O.N. Oliveira, A. Barros-Timmons, Probing the interaction of oppositely charged gold nanoparticles with DPPG and DPPC Langmuir monolayers as cell membrane models, Colloids Surf. B Biointerfaces 108 (2013) 120–126, https://doi.org/10.1016/j.colsurfb.2013.02.014.
[14] J. Cancino-Bernardi, P.M.P. Lins, V.S. Marangoni, H.A.M. Faria, V. Zucolotto, Difference in lipid cell composition and shaped based gold nanoparticles induce distinguish pathways in Langmuir monolayers response, Mater. Today Commun. 26 (2021) 101831, https://doi.org/10.1016/j.mtcomm.2020.101831.
[15] A.V. Rogachev, N.N. Novikova, M.V. Kovalchuk, Y.N. Malakhova, O.V. Konovalov, N.D. Stepina, E.A. Shlyapnikova, I.L. Kanev, Y.M. Shlyapnikov, S.N. Yakunin, Permeation of nanoparticles into pulmonary surfactant monolayer: In situ X-ray standing wave studies, Langmuir 38 (2022) 3630–3640, https://doi.org/10.1021/acs.langmuir.1c02179.
[16] P.U. Dynarowicz-Łątka, K. Kita, Molecular interaction in mixed monolayers at the airrwater interface, 1999. doi: 10.1016/S0001-8686(98)00064-5.
[17] S.A. Meenach, K.W. Anderson, J.Z. Hilt, R.C. McGarry, H.M. Mansour, High-performing dry powder inhalers of paclitaxel DPPC/DPPG lung surfactant-mimic multifunctional particles in lung cancer: Physicochemical characterization, in vitro aerosol dispersion, and cellular studies, Ageing Int. 15 (2014) 1574–1587, https://doi.org/10.1208/s12249-014-0182-z.
[18] J. Lin, L. Miao, G. Zhong, C.H. Lin, R. Dargazangy, A. Alexander-Katz, Understanding the synergistic effect of physicochemical properties of nanoparticles and their cellular entry pathways, Commun. Biol. 3 (2020) 1–10, https://doi.org/10.1038/s42003-020-0917-1.
[19] A. Sęk, P. Perczyk, A. Szcześ, P. Wydro, The interactions of trace amounts of ionic surfactants with mixed 1,2 dipalmitoyl sn glycero 3 phosphocholine (DPPC)/cholesterol membranes, J. Mol. Liq. 353 (2022) 1–9, https://doi.org/10.1016/j.molliq.2022.118805.
[20] P. Dynarowicz-Łątka, K. Hąc-Wydro, Interactions between phosphatidylcholines and cholesterol in monolayers at the air/water interface, Colloids Surf. B Biointerfaces 37 (2004) 21–25, https://doi.org/10.1016/j.colsurfb.2004.06.007.
[21] A. Botet-Carreras, M.T. Montero, O. Domènech, J.H. Borrell, Effect of cholesterol on monolayer structure of different acyl chained phospholipids, Colloids Surf. B Biointerfaces 174 (2019) 374–383, https://doi.org/10.1016/j.colsurfb.2018.11.040.
[22] K. Kim, C. Kim, Y. Byun, Preparation of a dipalmitoylphosphatidylcholine/cholesterol Langmuir-Blodgett monolayer that suppresses protein adsorption, Langmuir 17 (2001) 5066–5070, https://doi.org/10.1021/la0102096.
[23] A.B. Serrano-Montes, D.J. De Aberasturi, J. Langer, J.J. Giner-Casares, L. Scarabelli, A. Herrero, L.M. Liz-Marzán, A general method for solvent exchange of plasmonic nanoparticles and self-assembly into SERS-active monolayers, Langmuir 31 (2015) 9205–9213, https://doi.org/10.1021/acs.langmuir.5b01838.
[24] A. Wnętrzak, K. Łątka, P. Dynarowicz-Łątka, Interactions of alkylphosphocholines with model membranes – The langmuir monolayer study, J. Membrane Biol. 246 (2013) 453–466, https://doi.org/10.1016/j.colsurfb.2004.06.007.
[25] R. Marasini, A. Pitchaimani, T. Nguyen, J. Comer, Santosh, Influence of polyethylene glycol passivation on the surface plasmon resonance induced photothermal properties of gold nanorods, Nanoscale (2018) 13684–13693, https://doi.org/10.1039/x0xx00000x.
[26] X. Lin, Y.Y. Zuo, N. Gu, Shape affects the interactions of nanoparticles with pulmonary surfactant, Sci. China Mater. 58 (2015) 28–37, https://doi.org/10.1007/s40843-014-0018-5.
[27] T. Ishida, Y. Yanaga, S. Yamada, Y. Takahashi, A versatile method for surface functionalization and hydrophobization of gold nanoparticles, Appl. Surf. Sci. 546 (2021) 148932–148940, https://doi.org/10.1016/j.apsusc.2021.148932.
[28] Y. Xu, R. He, D. Lin, M. Ji, J. Chen, Laser beam controlled drug release from Ce6–gold nanorod composites in living cells: a FLIM study, Nanoscale 7 (2015) 2433–2441, https://doi.org/10.1039/C4NR05574H.
[29] J.R.G. Navarro, D. Manchon, F. Lerouge, N.P. Blanchard, S. Marotte, Y. Leverrier, J. Marvel, F. Chaput, G. Micouin, A.-M. Gabudean, A. Mosset, E. Cottancin, P. L. Baldeck, K. Kamada, S. Parola, Synthesis of PEGylated gold nanostars and bipyramids for intracellular uptake, Nanotechnology 23 (2012) 1–8, https://doi.org/10.1088/0957-4484/23/46/465602.
[30] F. Schulz, W. Friedrich, K. Hoppe, T. Vossmeyer, H. Weller, H. Lange, Effective PEGylation of gold nanorods, Nanoscale 8 (2016) 7296–7308, https://doi.org/10.1039/C6NR00607H.
[31] V. Bonzas, T. Haller, N. Hobi, E. Felder, I. Pastoriza-Santos, J. Pérez-Gil, Nontoxic impact of PEG-coated gold nanospheres on functional pulmonary surfactant-secreting alveolar type II cells, Nanotoxicology 8 (2014) 813–823, https://doi.org/10.3109/17435390.2013.829878.
[32] B. Tim, P. Błaszkiewicz, M. Kotkowiak, Altering model cell membranes by means of photoactivated organic functionalized gold nanorods, J. Mol. Liq. 349 (2022) 118179, https://doi.org/10.1016/j.molliq.2021.118179.
[33] B. Nikoobakth, A. El Sayed, Preparation and growth mechanism of gold nanorods (NRs) using seed mediated growth method, Chem. Mater. 15 (2003) 1957–1962, https://doi.org/10.1021/cm0207321.
[34] J. Turkevich, P.C. Stevenson, J. Hillier, A Study of the nucleation and growth processes in the synthesis of colloidal gold, Discuss. Faraday Soc. 11 (1951) 55–75, https://doi.org/10.1039/DF9511100055.
[35] P. Talarska, P. Błaszkiewicz, A. Kostrzewa, P. Wirstlein, M. Cegłowski, G. Nowaczyk, A. Dudkowiak, B.O. Grabarek, P. Głowacka-Stalmach, A. Szarpak, J. Żurawski, Effects of spherical and rod-like gold nanoparticles on the reactivity of human peripheral blood leukocytes, Antioxidants 13 (2024), https://doi.org/10.3390/antiox13020157.
[36] D. Ziental, P. Błaszkiewicz, J. Długaszewska, E. Güzel, A. Dudkowiak, L. Sobotta, Modified gold nanoparticles modulated fluorescence and singlet oxygen generation of pheophorbide a as an effective platform for photodynamic therapy against staphylococcus aureus, Eur. J. Inorg. Chem. 27 (2024), https://doi.org/10.1002/ejic.202300668.
[37] D. Aguilar-Ferrer, T. Vasileiadis, I. Iatsunskyi, M. Ziółek, K. Żebrowska, O. Ivashchenko, P. Błaszkiewicz, B. Grześkowiak, R. Pazos, S. Moya, M. Bechelany, E. Coy, Understanding the photothermal and photocatalytic mechanism of polydopamine coated gold nanorods, Adv. Funct. Mater. 33 (2023), https://doi.org/10.1002/adfm.202304208.
[38] P. Błaszkiewicz, M. Kotkowiak, A. Dudkowiak, Fluorescence quenching and energy transfer in a system of hybrid laser dye and functionalized gold nanoparticles, J. Lumin. 183 (2017) 303–310, https://doi.org/10.1016/j.jlumin.2016.11.023.
[39] P. Szustakiewicz, N. Kolsut, A. Leniart, W. Lewandowski, Universal method for producing reduced graphene oxide/gold nanoparticles composites with controlled

density of grafting and long-term stability, Nanomaterials 9 (2019) 1–16, https://doi.org/10.1002/open.201900082.
[40] J.A. Sanabria-Cala, G.R. Conde-Rodríguez, G.H. Gauthier, L.O. Ladeira, D. A. Laverde-Cataño, D.Y. Peña-Ballesteros, D. Merchan-Arenas, Gold nanoparticles formation mechanism by photochemical synthesis, Chem. Eng. Trans. 64 (2018) 403–408, https://doi.org/10.3303/CET1864068.
[41] A. Chakraborty, T. Ahmad, B.B. Abdullah, S. Bhattacharjee, Process engineering studies on synthesis of gold nanoparticles by Turkevitch method, Chem. Eng. Trans. 45 (2015) 1939–1944, https://doi.org/10.3303/CET1545324.
[42] A. Gole, C.J. Murphy, Seed-mediated synthesis of gold nanorods: role of the size and nature of the seed, Chem. Mater. 16 (2004) 3633–3640, https://doi.org/10.1021/cm0492336.
[43] H. Liu, N. Pierre-Pierre, Q. Huo, Dynamic light scattering for gold nanorod size characterization and study of nanorod-protein interactions, Gold Bull. 45 (2012) 187–195, https://doi.org/10.1007/s13404-012-0067-4.
[44] A. Kattar, E.V. Lage, M. Casas, A. Concheiro, C. Alvarez Lorenzo, Langmuir monolayer studies of non-ionic surfactants and DOTMA for the design of ophthalmic niosomes, Heliyon 10 (2024), https://doi.org/10.1016/j.heliyon.2024.e25887 e25887.
[45] J.T. Davies, E.K. Rideal, Interfacial Phenomena, Academic Press, 1961.
[46] M. Rojewska, K. Adamska, J. Kurnatowska, A. Miklaszewski, A. Bartkowska, K. Prochaska, Preparation of thin films containing modified hydroxyapatite particles and phospholipids (DPPC) for improved properties of biomaterials, Molecules 28 (2023), https://doi.org/10.3390/molecules28237843.
[47] K. Dopierała, M. Skrzypiec, Morphology, compressibility and viscoelasticity of the mixed lipid monolayers in the presence of β-carotene, Chem. Phys. Lipids 213 (2018) 88–95, https://doi.org/10.1016/j.chemphyslip.2018.04.001.
[48] K. Sabatini, J.P. Mattila, P.K.J. Kinnunen, Interfacial behavior of cholesterol, ergosterol, and lanosterol in mixtures with DPPC and DMPC, Biophys. J. 95 (2008) 2340–2355, https://doi.org/10.1529/biophysj.108.132076.
[49] A. Chachaj-Brekiesz, J. Kobierski, A. Wnętrzak, P. Dynarowicz-Latka, P. Pietruszewska, Insight into the molecular mechanism of surface interactions of phosphatidylcholines–Langmuir monolayer study compleme, J. Phys. Chem. B. 128 (2024) 1473–1482, https://doi.org/10.1021/acs.jpcb.3c06810.
[50] K. Sugikawa, K. Matsuo, A. Ikeda, Suppression of gold nanoparticle aggregation on lipid membranes using nanosized liposomes to increase steric hindrance, Langmuir 35 (2019) 229–236, https://doi.org/10.1021/acs.langmuir.8b03550.
[51] A. Alavizargar, F. Keller, R. Wedlich-Söldner, A. Heuer, Effect of cholesterol versus ergosterol on DPPC bilayer properties: insights from atomistic simulations, J. Phys. Chem. B 125 (2021) 7679–7690, https://doi.org/10.1021/acs.jpcb.1c03528.
[52] S.I. Hossain, N.S. Gandhi, Z.E. Hughes, Y.T. Gu, S.C. Saha, Molecular insights on the interference of simplified lung surfactant models by gold nanoparticle pollutants, Biochim. Biophys. Acta Biomembr. 2019 (1861) 1458–1467, https://doi.org/10.1016/j.bbamem.2019.06.001.
[53] Y. Ishitsuka, D.S. Phan, A.J. Waring, R.I. Lehrer, K.Y.C. Lee, Insertion selectivity of antimicrobial peptide protegrin-1 into lipid monolayers: Effect of head group electrostatics and tail group packing, Biochim. Biophys. Acta Biomembr. 1758 (2006) 1450–1460, https://doi.org/10.1016/j.bbamem.2006.08.001.
[54] D.S. Alvares, M.L. Fanani, J. Ruggiero Neto, N. Wilke, The interfacial properties of the peptide Polybia-MP1 and its interaction with DPPC are modulated by lateral electrostatic attractions, Biochim. Biophys. Acta Biomembr. 1858 (2016) 393–402, https://doi.org/10.1016/j.bbamem.2015.12.010.
[55] A. Tsanova, A. Jordanova, Z. Lalchev, Effects of leucin-enkephalins on surface characteristics and morphology of model membranes composed of raft-forming lipids, J. Membr. Biol. 249 (2016) 229–238, https://doi.org/10.1007/s00232-015-9862-1.
[56] K. Połeć, M. Broniatowski, P. Wydro, K. Hąc-Wydro, The impact of β-myrcene – the main component of the hop essential oil – on the lipid films, J. Mol. Liq. 308 (2020), https://doi.org/10.1016/j.molliq.2020.113028.
[57] M. Zaborowska, M. Broniatowski, P. Fontaine, R. Bilewicz, D. Matyszewska, Statin action targets lipid rafts of cell membranes: GIXD/PM IRRAS investigation of Langmuir monolayers, J. Phys. Chem. B 127 (2023) 7135–7147, https://doi.org/10.1021/acs.jpcb.3c02574.
[58] M.D. Maximino, H.S. Kavazoi, V.M. Katata, P. Alessio, Exploring the synergistic effects of amoxicillin and methylene blue on unsaturated lipid structures: A study of Langmuir monolayers and giant unilamellar vesicles, Biophys. Chem. 307 (2024) 107181, https://doi.org/10.1016/j.bpc.2024.107181.
[59] T.P. Pivetta, K. Jochelavicius, E.C. Wrobel, D.T. Balogh, O.N. Oliveira, P.A. Ribeiro, M. Raposo, Incorporation of acridine orange and methylene blue in Langmuir monolayers mimicking releasing nanostructures, Biochim. Biophys. Acta Biomembr. 1865 (2023) 184156, https://doi.org/10.1016/j.bbamem.2023.184156.
[60] M. Zaborowska, M. Broniatowski, P. Wydro, D. Matyszewska, R. Bilewicz, Structural modifications of lipid membranes exposed to statins – Langmuir monolayer and PM IRRAS study, J. Mol. Liq. 313 (2020) 1–11, https://doi.org/10.1016/j.molliq.2020.113570.
[61] T.F. Schmidt, L. Caseli, Molecular organization of dengue fusion peptide in phospholipid monolayers revealed by tensiometry and vibrational spectroscopy, Colloids Surf. B Biointerfaces 215 (2022) 112477, https://doi.org/10.1016/j.colsurfb.2022.112477.
[62] J. Huang, Y. Qiu, F. Lücke, J. Su, G. Grundmeier, A. Keller, Multiprotein adsorption from human serum at gold and oxidized iron surfaces studied by atomic force microscopy and polarization-modulation infrared reflection absorption spectroscopy, Molecules 28 (2023), https://doi.org/10.3390/molecules28166060.

Supplementary information

for

Interactions between functionalized PEGylated gold nanoparticles and model biological membranes

Beata Tim[a,*], Paulina Błaszkiewicz[b], Emerson Coy[b], Alina Dudkowiak[a]

[a] Faculty of Materials Engineering and Technical Physics, Poznan University of Technology, Piotrowo 3, 60-965 Poznan, Poland
[b] NanoBioMedical Centre, Adam Mickiewicz University, Wszechnicy Piastowskiej 3, 61-614 Poznan, Poland

To whom correspondence should be addressed:
*E-mail: beata.tim@put.poznan.pl (B.T.)

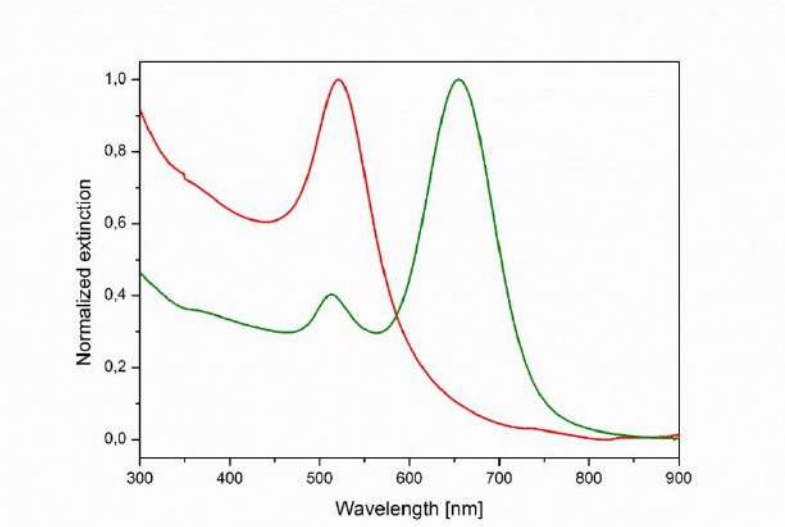

Fig. S1. Normalized extinction spectra of Au-NSs@PEG (red line) and Au-NRs@PEG (green line). Transmission electron microscope images of these nanoparticles are given in Figure 1.

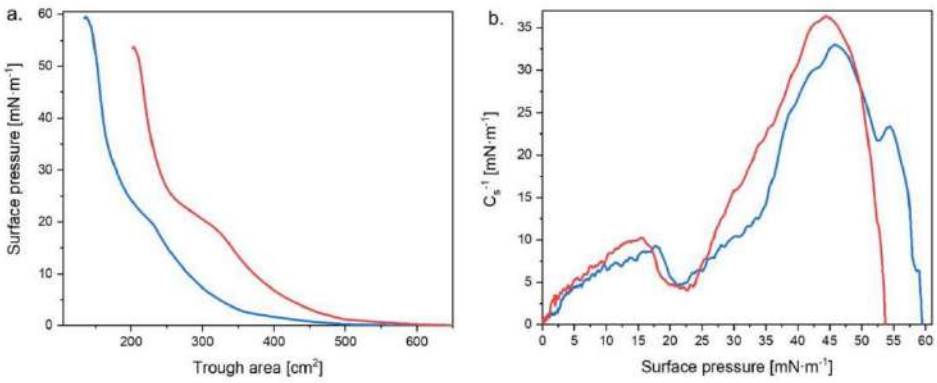

Fig. S2. π-A isotherms (a) and the compressibility modulus (C_s^{-1}) vs. surface pressure (π) (b) of the Langmuir monolayer for Au-NSs@PEG (red line) and Au-NRs@PEG (blue line).

Table S1. Characteristic parameters of the π-A isotherms for monolayers of Au-NSs@PEG, Au-NRs@PEG: $\pi_{collapse}$ – collapse pressure; max C_s^{-1} – maximum value of the compressibility modulus

	$\pi_{collapse}$ [mN·m^{-1}]	max C_s^{-1} [mN·m^{-1}]
Au-NSs@PEG	54	36
Au-NRs@PEG	59	33

Table S2. Characteristic parameters of the π-A isotherms for monolayers of DPPC and DPPC:Chol (9:1), mixture of DPPC or DPPC:Chol (9:1) with gold NPs and Au-NSs@PEG, Au-NRs@PEG: $\pi_{collapse}$ – collapse pressure; max C_s^{-1} – maximum value of the compressibility modulus

	$\pi_{collapse}$ [mN·m^{-1}]	max C_s^{-1} [mN·m^{-1}]
DPPC	55	248
Au-NSs@PEG/DPPC	47	102
Au-NRs@PEG/DPPC	54	129
	57*	177*
DPPC:Chol (9:1)	46	262
Au-NSs@PEG/DPPC:Chol (9:1)	45	119
Au-NRs@PEG/DPPC:Chol (9:1)	43	150

* data from literature [1].

Table S3. Characteristic parameters of the π-A isotherms for monolayers of POPC and POPC:Chol (4:1, mixture of POPC or POPC:Chol (4:1) with gold NPs: $\pi_{collapse}$ – collapse pressure; max C_s^{-1} – maximum value of the compressibility modulus

	$\pi_{collapse}$ [mN·m^{-1}]	max C_s^{-1} [mN·m^{-1}]
POPC	41	83
Au-NSs@PEG/POPC	44	84
Au-NRs@PEG/POPC	42	102
POPC:Chol (4:1)	40	110
Au-NSs@PEG/POPC:Chol (4:1)	45	81
Au-NRs@PEG/POPC:Chol (4:1)	44	65

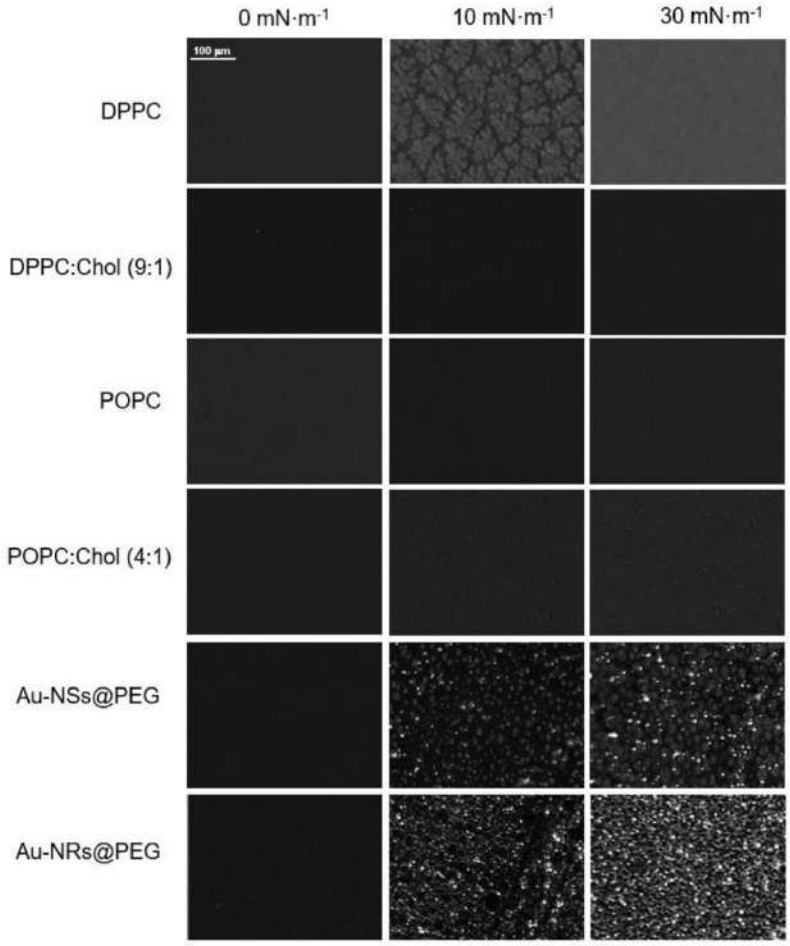

Fig. S3. BAM images for monolayers of DPPC, DPPC:Chol (9:1), POPC, POPC:Chol (4:1), Au-NSs@PEG and Au-NRs@PEG.

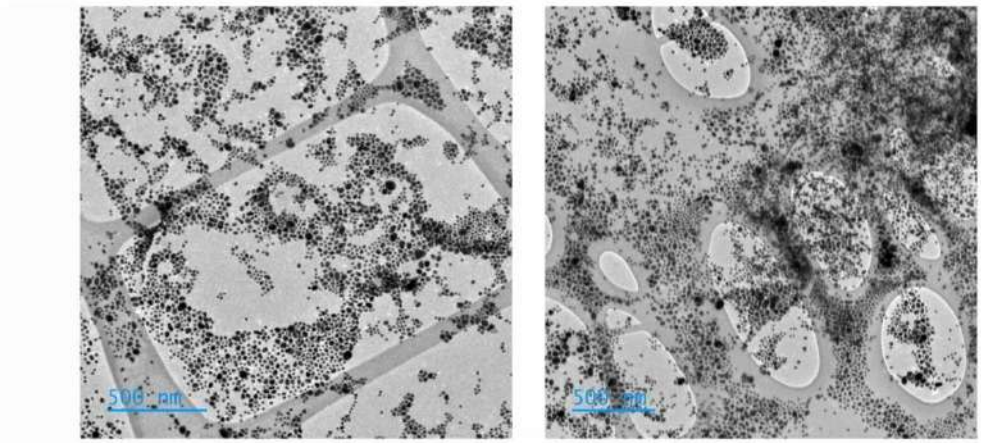

Fig. S4. Formation of unevenly distributed clusters and aggregates for Au-NSs@PEG/DPPC.

4

[1] B. Tim, P. Błaszkiewicz, M. Kotkowiak, Altering model cell membranes by means of photoactivated organic functionalized gold nanorods, J Mol Liq 349 (2022) 118179. https://doi.org/10.1016/j.molliq.2021.118179.